

ANISOTROPIC RAY TRACE

by

Wai Sze Tiffany Lam

Copyright © Wai Sze Tiffany Lam 2015

A Dissertation Submitted to the Faculty of

COLLEGE OF OPTICAL SCIENCES

In Partial Fulfillment of the Requirements

For the Degree of

DOCTOR OF PHILOSOPHY

In the Graduate College

THE UNIVERSITY OF ARIZONA

2015

THE UNIVERSITY OF ARIZONA
GRADUATE COLLEGE

As members of the Dissertation Committee, we certify that we have read the dissertation prepared by Wai Sze Tiffany Lam entitled Anisotropic Ray Trace and recommend that it be accepted as fulfilling the dissertation requirement for the Degree of Doctor of Philosophy.

Russell Chipman Date: April 23rd, 2015

Scott Tyo Date: April 23rd, 2015

Tom Milster Date: April 23rd, 2015

Final approval and acceptance of this dissertation is contingent upon the candidate's submission of the final copies of the dissertation to the Graduate College.

I hereby certify that I have read this dissertation prepared under my direction and recommend that it be accepted as fulfilling the dissertation requirement.

Dissertation Director: Russell Chipman Date: April 23rd, 2015

STATEMENT BY AUTHOR

This dissertation has been submitted in partial fulfillment of requirements for an advanced degree at the University of Arizona and is deposited in the University Library to be made available to borrowers under rules of the Library.

Brief quotations from this dissertation are allowable without special permission, provided that an accurate acknowledgement of the source is made. Requests for permission for extended quotation from or reproduction of this manuscript in whole or in part may be granted by the copyright holder.

SIGNED: Wai Sze Tiffany Lam

ACKNOWLEDGEMENTS

I would like to thank my parents and my brother who have always supported me to pursue my graduate studies.

I would like to express my appreciation and gratitude to my advisor, Professor Russell Chipman, for giving me research opportunities since my undergraduate years. His guidance and mentorship have helped me developed tremendous amount of knowledge in polarization ray tracing. His dedication to my work is very much appreciated.

I would like to thank Dr. Stephen McClain who has patiently guided me throughout the studies and algorithm development of anisotropic ray tracing. His experience in analyzing optical components with anisotropic materials has provided valuable contributions in developing analysis algorithms for anisotropic optical components.

I would like to thank Dr. Greg Smith who contributed the basic programming and provided many creative ideas in ray tracing, and shared lots of brilliant programming solutions. He has been a great listener when I ran into problems in research, and was a great teacher who always guided me toward the right direction for efficient calculations.

I would like to thank Dr. Karlton Crabtree who has provided technical advice and essential skills in solving computer problems. His knowledge and experience have helped me solved many of my technical challenges in experiment and in optical design.

I would also like to thank my committee members, Professor Scott Tyo and Professor Tom Milster for thought-provoking suggestions and general collegiality that they offered to me over the years.

I would like to thank my colleagues, fellow Polarization Lab graduate and undergraduate students, and alumni – Brain Daugherty, Garam Yun, Hannah Noble, Paula Smith, Michihisa Onishi, Kasia Sieluzicka, Tyson Ririe, Stacey Sueoka, Christine Bradley, Meredith Kupinski, Michael Dalpiaz, Alba Peinado, Lisa Li and Kyle Hawkins for their collaborations, intellectual discussions, suggestions, friendships, and cheers along the journey.

Last but not least, I would like to give special thanks to everyone who spend extra time on proofreading this dissertation.

DEDICATION

To my parents, 林健隆 and 洪德芸, and my brother 林偉軍.

TABLE OF CONTENTS

LIST OF FIGURES	11
LIST OF TABLES.....	40
ABSTRACT.....	42
CHAPTER 1 INTRODUCTION.....	46
1.1 Motivation of polarization ray trace	46
1.2 Polarization aberrations	47
1.3 Polarization ray tracing calculus.....	50
1.4 Motivation of ray tracing in anisotropic material	53
1.5 Ray tracing with anisotropic materials	57
1.6 Image formation of polarized wavefronts.....	60
1.7 Conclusions.....	66
CHAPTER 2 BASICS OF ANISOTROPIC RAY TRACING.....	68
2.1 Description of electromagnetic wave.....	68
2.2 Definition of anisotropic materials	69
2.3 Eigen polarizations in anisotropic materials.....	78
2.4 Refraction and reflections at anisotropic interface	83

2.5	External and internal refraction/reflection at a biaxial interface	92
2.6	Optical Indicatrix	100
2.7	Conclusions.....	111
CHAPTER 3 POLARIZATION RAY TRACING P MATRICES FOR ANISOTROPIC RAY TRACING		113
3.1	Purposes of polarization ray tracing P matrix.....	113
3.2	Calculation of the P matrix from the Jones matrix	115
3.3	Calculations of the P matrix from 3D polarization vectors	125
3.4	Calculating P matrices for anisotropic interfaces	128
3.4.1	Isotropic to anisotropic intercept.....	128
3.4.2	Anisotropic to isotropic intercept.....	131
3.4.3	Anisotropic to anisotropic intercept	133
3.4.4	Example.....	134
3.5	Incorporating optical path length into P matrices	135
3.6	Conclusions.....	139
CHAPTER 4 RAY TRACING A BIAXIAL PLATES WITH THE P MATRIX, AND THE CALCULATION OF DIATTENUATION AND RETARDANCE		142
4.1	Demonstrating the anisotropic ray trace with the P matrix.....	142
4.2	Ray tracing an off-axis beam through a biaxial waveplate with P matrix	143

4.3	Calculation of total P matrices with propagation effects	152
4.4	Calculation of diattenuation.....	157
4.5	Calculation of retardance and geometrical rotation	158
4.5.1	Geometrical transformation Q matrix	161
4.5.2	Calculation of retardance	164
4.6	Conclusions.....	166
CHAPTER 5 COMBINATION OF POLARIZED WAVEFRONTS.....		167
5.1	Introduction.....	167
5.2	Wavefronts and ray grids	168
5.3	Co-propagating wavefront combination	171
5.4	Sheared co-propagating wavefront combination	175
5.5	Non co-propagating wavefront combination	178
5.6	Combining irregular ray grids.....	180
5.6.1	General steps to combine misaligned ray data	180
5.6.2	Inverse-distance weighted interpolation.....	183
5.7	Conclusions.....	186
CHAPTER 6 ABERRATIONS OF CRYSTAL RETARDERS		188
6.1	Introduction to crystal waveplates	188
6.2	Angular behavior of a uniaxial A-plate	191

6.3	Polarization aberrations of a uniaxial A-plate	195
6.4	Polarization states exiting retarders	201
6.5	Conclusions.....	205
CHAPTER 7 ABERRATIONS IN THE GLAN-TAYLOR CRYSTAL POLARIZERS		
208		
7.1	Introduction to crystal polarizers	208
7.2	Polarization ray tracing of Glan-Taylor polarizer.....	210
7.2.1	Conditions of internal refraction/reflection in calcite	211
7.2.2	Nominal operation at normal incidence	213
7.2.3	Limited field of view.....	216
7.2.4	Multiple potential ray paths for off-axis operation	217
7.2.5	Multiple polarized wavefronts	222
7.3	Polarized wavefronts exiting from the polarizer.....	226
7.4	Aberrations and performance of the Glan-Taylor polarizer	229
7.5	Conclusions.....	238
CHAPTER 8 RAY TRACING ELEMENTS WITH STRESS BIREFRINGENCE ..		
240		
8.1	Introduction to stress birefringence	240
8.2	Stress birefringence in optical systems	242
8.3	Effects of stress birefringence on material properties.....	243

8.4	Ray tracing in stress birefringent components.....	245
8.4.1	Anisotropic stress model.....	246
8.4.2	Spatially varying stress.....	252
8.4.3	Refraction and reflection at stress birefringent intercepts.....	254
8.5	Polarization ray tracing P matrix for stress birefringent model.....	256
8.6	Example: Polarization ray tracing for a plastic injection molded lens	262
8.7	Conclusions.....	265
CHAPTER 9 CONCLUSIONS AND FUTURE WORK		267
9.1	Work accomplishment in Polaris-M	267
9.2	Summary of modeling optical system with anisotropic components	269
9.3	Further work.....	272
APPENDIX A	RMS FOCUS.....	275
APPENDIX B	LOCAL COORDINATE SYSTEMS	278
APPENDIX C	BIAXIAL REFRACTION AND REFLECTION PROPERTIES WITH CRYSTAL AXES ALONG XYZ AXES.....	281
REFERENCES	287

LIST OF FIGURES

Figure 1.1 A ray propagates through a birefringent material. (Top) The ray decompose into two orthogonally polarized components, called modes, x -polarized in red and y -polarized in blue. (Middle) In this example, the x -polarized light has propagated 3.25λ , and the y -polarized light has propagated 3λ . (Bottom) The incident x - and y -polarized light combine to 45° polarized light. The exiting light with a quarter wave phase difference between the x and y components is right circularly polarized.	48
Figure 1.2 The angles of incidence vary across the set of rays. (Left) A set of rays refracts through a convex lens. (Right) A grid of rays reflects from a fold mirror.	48
Figure 1.3 A skew ray (yellow) reflects from two fold mirrors, $M1$ and $M2$	52
Figure 1.4 Imaging doubling though a piece of calcite.	54
Figure 1.5 (Left) Basic setup of differential interference contrast (DIC) microscope and (right) a <i>Micrasterias furcata</i> imaged in transmitted DIC microscopy.	55
Figure 1.6 Optical layout of an optical pickups system in a CD player.	56
Figure 1.7 The off-axis aberration of the liquid crystal cell can be corrected by layers of compensating films. Layers connected by arrows compensate their variation of polarization with angle.	57
Figure 1.8 A converging beam converges through a biaxial KTP plate (left) and a uniaxial calcite plate (right). Due to ray doubling, two foci are observed, ordinary and extraordinary modes for the uniaxial plate, and fast and slow modes for the biaxial case.	60

Figure 1.9 (Left) A point object is imaged through an optical system to a point image. (Right) The entrance pupil (E) of the system is the image of the stop in the object space, so it is the spherical surface (gray surface on the left) centered at the object point. Similarly the exit pupil (X) of the system is the image of the stop in the image space; a spherical surface (gray surface on the right) centered at the object space. 61

Figure 1.10 Flow charts for coherent and incoherent imaging calculations. The pupil function P represents the wavefront function at the exit pupil of an optical system. The spatial variable of the system is x ; the wavelength of light is λ ; the focal length of the imaging system is f . The coherent point spread function is $cPSF$; the coherent transfer function is CTF ; the incoherent point spread function is $iPSF$; the optical transfer function is OTF ; the modulation transfer function is MTF ; and the phase transfer function is PSF . \mathfrak{F} is the Fourier transform operation. \star is the auto-correlation operation..... 64

Figure 1.11 The imaging calculation for polarized light. The 2×2 amplitude response matrix is the **ARM**; the 4×4 Mueller point spread matrix is the **MPSM**; the 4×4 optical transfer matrix is the **OTM**; the 4×4 modulation transfer matrix is the **MTM**; and the 4×4 phase transfer matrix is the **PTM**. 64

Figure 2.1 (Left) Principal axes for positive uniaxial material where $n_E > n_O$. (Right) Principal axes for negative uniaxial material where $n_E < n_O$ 72

Figure 2.2 (Left) Light propagating along z and polarized along x experiences the refractive index n_s . (Middle) Light propagating along z and polarized along y experiences refractive index n_M . (Right) Light propagating along x and polarized along z experiences refractive

index n_F . Thus the refractive index depends on the light polarization, not the direction of propagation.	72
Figure 2.3 Calcite CaCO_3 crystal structure with the vertical optic axis, connecting the calcium (blue) and carbon (purple) atoms.	74
Figure 2.4 Birefringence spectra of common positive uniaxial materials.	75
Figure 2.5 Birefringence spectra of common negative uniaxial materials.	75
Figure 2.6 Birefringence spectra of common biaxial materials.	75
Figure 2.7 The side and front view of the left (red) and right (blue) circularly polarized electric field propagating through an optically active material. The left circularly polarized beam propagates for three wavelengths and the right circularly polarized beam propagates for three and a half wavelengths through the material yielding one half wave of circular retardance.	77
Figure 2.8 The plane of polarization of linearly polarized light rotates at a uniform rate when propagating in an optically active medium. This one-and-a-half wave circular retarder generates 270° of optical rotation.	77
Figure 2.9 (Left) Double refraction through a calcite rhomb. (Right) A schematic of a ray splitting into two modes through a uniaxial plate. The optic axis (OA) shown is 45° from vertical. The gray line indicates a polarization state in the plane of the page, which is the extraordinary e -mode in this case. The gray dot indicates a polarization state out of the page, which is the ordinary o -mode in this example.	79

Figure 2.10 Double refraction through a calcite rhomb. When rotating the calcite, the ordinary image stays fixed while the extraordinary image rotates around it..... 79

Figure 2.11 A normally incident ray propagates through three blocks of anisotropic materials (KTP, aragonite, and mica) each with different crystal axes orientations shown as three lines inside each block. One incident ray results in eight exiting rays due to three ray splitting interfaces, each with different sequences of polarizations and different *OPLs*.
..... 81

Figure 2.12 The four configurations of anisotropic interfaces are shown with corresponding reflected rays toward the incident medium and refracted rays into the transmitting medium for a given incident ray. The black arrow represents \mathbf{S} , the Poynting vector direction, which is the direction of energy flow and is not necessarily the same as \mathbf{k} , the propagation vector direction. The transmitted and reflected modes are identified by subscripts \mathbf{ta} , \mathbf{tb} , \mathbf{rc} and \mathbf{rd} . The three gray parallel lines along each ray represent the wavefronts which are perpendicular to \mathbf{k} , but not necessarily perpendicular to \mathbf{S} . (a) A ray propagating from an isotropic medium to another isotropic medium results in one reflected ray and one refracted ray. (b-d) If the incident medium or/and the transmitted medium is/are anisotropic, ray splitting occurs and the two resultant rays in each anisotropic material have different \mathbf{k} and \mathbf{S} directions..... 85

Figure 2.13 The calculation of the *OPL* for a ray propagating through an anisotropic material where \mathbf{S} (black) and \mathbf{k} (gray) are not aligned. The wavefronts are perpendicular to the \mathbf{k} vector. The energy propagation direction is along \mathbf{S} , which determines the location of ray intercept at the next surface. The *OPL* is the number of wavelengths between the

two intercepts, the projection of the ray path ℓ onto \mathbf{k} multiplied by the refractive index of the mode..... 88

Figure 2.14 (Left) Orientations of the two optic axes of a biaxial material are perpendicular to the two circular cross sections through the index ellipsoid. (Right) A ray refracts into the direction of the biaxial optic axis. The incident polarizations distribute their Poynting vectors into a cone (the solid angle of the cone shown is exaggerated), and propagate as a cone through the biaxial crystal. The associated polarization (shown as the purple lines) rotates by π around the refracted cone. The distribution of flux around the cone depends on the distribution of incident polarization states. The fast, medium, and slow crystal axes are shown as the red, green and blue arrows. 91

Figure 2.15 A biaxial KTP crystal is setup to display conical refraction and its refracted cone is measured in an imaging polarimeter. The Mueller matrix image (left) and diattenuation orientation image (right) of the refracted cone is shown. 92

Figure 2.16 External (left) and internal (right) reflection and refraction of biaxial interface. 93

Figure 2.17 External reflection and refraction coefficients at the air/KTP interface..... 94

Figure 2.18 A fan of rays externally reflect from an air/biaxial interface. The gray arrows are the incident \mathbf{k} vectors at different incident angles. The black arrows are the corresponding reflected \mathbf{k} vectors. The blue and red arrows are the polarization ellipses, the evolution of electric field, where the arrow head indicates the start of the electric field evolution in time. In this case, all polarization ellipses shown are linearly polarized. All the

incident polarizations have the same magnitude. The length of the polarization arrow indicates the intensity of the reflected light, but are adjusted slightly for visualization... 95

Figure 2.19 A fan of rays externally refracting from an air/biaxial interface are shown in two perspectives for the four mode couplings. The gray arrows are the incident \mathbf{k} vectors. The black and brown arrows are the refracted \mathbf{S} vectors for the *slow*- and *fast*-modes, respectively. The blue, red, magenta and green arrows show the refracted polarization states in 3D and are scaled to the refracted flux. 96

Figure 2.20 Left circularly polarized incident light is sent to the air/biaxial interface. The gray, black and brown arrows are the incident, reflected and refracted rays, respectively. The purple ellipses are the incident and reflected polarizations. The red and blue arrows are the refracted *fast* and *slow*-modes. 97

Figure 2.21 Internal reflection and transmission coefficients at the KTP/air interface.... 98

Figure 2.22 A fan of rays internally reflecting from a biaxial/air interface are shown in two perspectives for all four mode couplings. The gray arrows are the incident \mathbf{k} vectors. The black arrows are the corresponding reflected \mathbf{k} vectors. The blue, red, green and magenta arrows are the polarization ellipses. 99

Figure 2.23 A fan of rays internally refracting from biaxial/air interface are shown in two perspectives for all four mode couplings. The gray arrows are the incident \mathbf{k} vectors. The black arrows are the refracted \mathbf{S} vectors for the refracted rays. The blue and red arrows are the polarization ellipses..... 100

Figure 2.24 The ray ellipsoid of biaxial (left), positive uniaxial (middle) and isotropic materials (right). The principal axes are aligned with the coordinate axes with $(x, y, z) =$

$$(E_x, E_y, E_z) / \sqrt{2u} \dots\dots\dots 101$$

Figure 2.25 The index ellipsoid of (left) biaxial, (middle) positive uniaxial, and (right) isotropic materials. Their principal axes are aligned with the coordinate axes with $(x, y, z) =$

$$=(D_x, D_y, D_z) / \sqrt{2u} \dots\dots\dots 102$$

Figure 2.26 (Left) A ray normally incident to a block of uniaxial material. (Right) The index ellipsoid in the system coordinates where the optic axis is shown rotated by α from the z axis in the y - z plane. The blue ellipse goes through the optic axis. The red circle is perpendicular to the optics axis..... 103

Figure 2.27 (Left) For a ray with propagation vector \mathbf{k} (purple) propagating through a negative uniaxial crystal, the ray index ellipse (light purple disk in the y - z plane) is the intersection of the plane normal to \mathbf{k} and the optical indicatrix. (Right) The minor and major axes of the index ellipse correspond to the \mathbf{D} field directions of the o - and e -modes, and the lengths of these two axes are the refractive indices..... 104

Figure 2.28 The index ellipse (light purple disk) in the x - y plane is normal to \mathbf{k} (purple arrow). \mathbf{D}_e (pink arrow) is on the pink plane in the y - z plane containing both the optic axis (dashed brown line) and the \mathbf{k} vector. \mathbf{D}_o (blue arrow) is on the blue plane in the x - z plane orthogonal to the pink \mathbf{D}_e plane. The three planes are orthogonal to each other, and both \mathbf{D}_o and \mathbf{D}_e are lying on the purple index ellipse in the x - y plane. The brown ellipse is the great ellipse containing the optic axis..... 104

- Figure 2.29 Several possible index ellipses (blue) in a positive uniaxial index ellipsoid (yellow) are shown. (Left) The index ellipses shown contain the x axis. (Middle) The index ellipses shown contain the z axis. (Right) The index ellipses shown contain an axis 45° from the x axis in the x - z plane. 105
- Figure 2.30 (Left) A ray propagating in the y - z plane has an index ellipse (purple disk) lying in a plane orthogonal to \mathbf{k} and containing the x axis. \mathbf{k} lies at an angle θ from the optic axis along the z axis. (Right) The projected length of the index ellipse is the magnitude of $n_e(\theta)$ 105
- Figure 2.31 The K -surfaces and their cross sections for the o -mode (red, sphere) and the e -mode (blue, ellipsoid). The optic axis (dashed brown line) lies on the k_z/k_o axis..... 107
- Figure 2.32 The K -surfaces are oriented for the example in Figure 2.26, where the optic axis is rotated by α from the z axis. The Poynting vectors are normal to the k -surface. 108
- Figure 2.33 (Left) The Poynting vectors are normal to the K -surface in 2D. (Right) The incident energy divides into \mathbf{S}_e and \mathbf{S}_o direction. Their wavefronts \mathbf{D} , shown as the three parallel lines, are orthogonal to \mathbf{k} and skewed from \mathbf{S} 108
- Figure 2.34 The K -surface for refraction from an isotropic material to a uniaxial material at normal incidence. 109
- Figure 2.35 S -surface for positive (left) and negative (right) uniaxial material. Blue for e -mode, and red for o -mode. The optic axis (brown) is oriented vertically. 110
- Figure 2.36 The K -surface and S -surface of the extraordinary mode in a positive uniaxial material. 111

- Figure 2.37 A ray tree for one incident ray refracting through three uniaxial interfaces, where the ordinary mode is o and the extraordinary mode is e 112
- Figure 3.1 A ray is normally incident on a surface with $\mathbf{k} = (0, 0, 1)$ and reflects off the surface with $\mathbf{k}' = (0, 0, -1)$. The transverse plane (yellow) of the rays contains a pair of local basis (\hat{s}, \hat{p}) for the incident ray and (\hat{s}', \hat{p}') for the reflected ray. The s - and p -polarized incident electric fields $\bar{\mathbf{E}}_s$ and $\bar{\mathbf{E}}_p$ reflect to $\bar{\mathbf{E}}_s'$ and $\bar{\mathbf{E}}_p'$ 114
- Figure 3.2 A ray with incident \mathbf{k} and electric field \mathbf{E} refracts through an optical interface with surface normal $\boldsymbol{\eta}$. The refracted ray propagates in \mathbf{k}' with electric field \mathbf{E}' . The plane of incidence contains \mathbf{k} , \mathbf{k}' and $\boldsymbol{\eta}$ 116
- Figure 3.3 Fresnel coefficients, amplitude (left) and phase (right), for transmission and reflection at an air/glass interface. For external reflection from refractive index 1 to refractive index 1.5, the Brewster's angle is 56.31° . At normal incidence, the reflected s - and p -polarizations have a Fresnel π phase shift due to a coordinate flip during reflection. 117
- Figure 3.4 The incident and exiting s - p - k basis for refraction (left) and reflection (right) are shown. The plane of incidence (PoI) is the blue plane containing \mathbf{k} , \mathbf{p} , and $\boldsymbol{\eta}$ 118
- Figure 3.5 A converging grid of rays at 765nm reflects from a gold fold mirror with refractive index $0.718 + 4.749i$ 121
- Figure 3.6 Fresnel coefficients, amplitude (left) and phase (right), for reflection at an air/gold interface. At normal incidence the s - and p -polarizations have a Fresnel π phase shift due to a coordinate flip during reflection. 121

- Figure 3.7 Phase change of electric field upon reflection at an air/gold interface. At normal incidence, the s - and p -polarizations are degenerate. 123
- Figure 3.8 (Left) A half wave plate has its fast axis (pink line) oriented at α from the x_{local} axis. (Right) The plate is tilted 10° from the z axis. A normal incident ray (brown arrow) passes through the tilted waveplate in the global xyz coordinate systems. 123
- Figure 3.9 The incident electric field \mathbf{E}_s (magenta) and \mathbf{E}_p (blue) passes through a half wave plate shown in Figure 3.8 and rotates to \mathbf{E}_s' and \mathbf{E}_p' 124
- Figure 3.10 The incident and refracted \mathbf{E} (gray), \mathbf{D} (pink), \mathbf{k} (red) and \mathbf{S} (black) field orientations of an isotropic/isotropic (left) and a birefringent/birefringent (right) interface. Only p -polarization coupling to p -polarization is shown refracting through the isotropic interface. Only e -mode coupling to e -mode is shown refracting through the birefringent interface..... 125
- Figure 3.11 Mode coupling in refraction through an isotropic/anisotropic interface. The incident ray with orthogonal modes, labeled as n (red) and m (blue), splits into two exiting modes as v (pink) and w (green) in two directions. In biaxial and uniaxial materials, \mathbf{E}_v and \mathbf{E}_w are linearly polarized. In optically active materials, \mathbf{E}_v and \mathbf{E}_w are circularly polarized. Given a ray with a specific pair of \mathbf{k}'_v and \mathbf{S}'_v in an anisotropic material, the ray can only be polarized in \mathbf{E}_v , so the orthogonal state $\mathbf{E}_{v\perp}$ (dashed arrow) has zero amplitude..... 129
- Figure 3.12 Mode coupling in refraction through an anisotropic/isotropic interface. The incident ray is polarized along \mathbf{E}_m (blue) and has a zero amplitude component \mathbf{E}_n (red,

dashed arrow). The incident polarization couples to the s - and p -states in the isotropic medium which are \mathbf{E}_v (pink) and \mathbf{E}_w (green) and propagate in the same direction \mathbf{S}' 132

Figure 3.13 Mode coupling in refraction through an anisotropic/anisotropic interface. The incident ray propagating in \mathbf{S} is polarized along \mathbf{E}_m (blue) and has a zero amplitude component \mathbf{E}_n (red, dashed arrow). It splits into two exiting modes as v (green) and w (pink) in two directions. Their orthogonal states $\mathbf{E}_{v\perp}$ and $\mathbf{E}_{w\perp}$ (dashed arrows) both have zero amplitude..... 133

Figure 3.14 An incident ray refracts through two anisotropic interfaces to two branches of rays. A ray starts from an isotropic medium, splits into o - and e -modes, and refracts into oi - and ei -modes..... 134

Figure 4.1 A ray propagates with $\hat{\mathbf{k}} = \hat{\mathbf{S}}$ from air into a KTP biaxial crystal (in pink). The entrance surface and the exit surface have the same surface normal $\hat{\mathbf{n}} = (0, 0, 1)$. The KTP crystal splits the ray in two at the exit surface with direction $\hat{\mathbf{S}}'_{\text{tf}}$ and $\hat{\mathbf{S}}'_{\text{ts}}$ which are parallel in air. The plane that contains the PoI and the doubled rays is highlighted in gray. 143

Figure 4.2 The polarizations of the two ray paths are shown from two different perspectives. The s - and p -polarized components are shown as red and blue arrows, respectively. Part of the ray reflects with a π phase shift on both s - and p -polarizations. The refracted light splits into two modes where the s -polarization couples to *fast*-mode, and p -polarization couples to refracted *slow*-mode in this configuration. With two different propagation directions, the two modes exit the plate with a phase delay between them. 152

Figure 4.3 (a) A collimated wavefront refracts through a birefringent plate. Two partially overlapping collimated beams exit the plate in the same direction. (b) Two rays of the incident wavefront are traced through the plate, where the *s*-mode (red) from the upper incident ray overlaps with the *f*-mode (blue) from the lower incident ray. (c) The resultant split rays have a displacement of \bar{a} between the two exiting modes, which contributes to the *OPL* difference between the two modes outside of the waveplate. 153

Figure 4.4 **P** matrices of individual ray intercepts, cumulative **P** matrices, and *OPLs* of the split ray paths for the two modes are represented in the figure. The refraction **P** matrices at the entrance surface are \mathbf{P}_{tf} and \mathbf{P}_{ts} , shown in boxes. The refraction **P** matrices for the exit surface are \mathbf{P}'_{tf} and \mathbf{P}'_{ts} , shown in boxes at the exit interface. The cumulative **P** matrices with the *OPLs* right after the entrance are $\mathbf{P}_{tf,total}^+$ and $\mathbf{P}_{ts,total}^+$, respectively. The cumulative **P** matrices right before the exit surface with the corresponding *OPLs* are $\mathbf{P}_{tf,total}^-$ and $\mathbf{P}_{ts,total}^-$, respectively. Finally the cumulative **P** matrices after the exit surface are $\mathbf{P}_{tf,total}^+$ and $\mathbf{P}_{ts,total}^+$ 154

Figure 4.5 Physical retardance: (a) Linearly polarized light passes through a waveplate and becomes elliptically polarized. (b) Linearly polarized light reflect from a metal surface and becomes elliptically polarized..... 159

Figure 4.6 (a) Linear polarization, represented by green arrows, rotates 120° after three total internal reflections within a solid corner cube. (b) Six incident rays incident at different regions of the entrance surface follow different paths within the corner cube, and the corresponding exiting states have a different amount of polarization rotations. (c)

Circular retardance induced by the corner cube alters the absolute phase of circular incident light. The amount of circular retardance depends on the ray path inside the corner cube. (d) The rotation associated with the induced circular retardance are 0° , 120° , 240° , 360° and so on around the exit surface. 160

Figure 4.7 Horizontally polarized light propagates through a dove prism which rotates about the incident direction by 0° , 30° and 60° . Then the resultant polarization rotates 0° , 60° and 120° about the exiting direction. 160

Figure 4.8 Elliptically polarized light propagates through a dove prism which is rotated about the incident direction by 0° , 30° and 60° . The major axis of the resultant polarization ellipse rotates by 0° , 60° and 120° with a change of helicity. 160

Figure 4.9 (a) A ray propagates through three prisms and exits in the same incident direction, $\mathbf{k}=(0, 0, 1)$. The surface normal of these six surfaces are $(0, -0.423, 0.906)$, $(0, 0.423, 0.906)$, $(0.366, 0.211, 0.906)$, $(-0.366, -0.211, 0.906)$, $(-0.380, 0.198, 0.903)$ and $(0.378, -0.201, 0.903)$. (b) Two orthogonal polarizations propagate through the three prisms and rotate slightly due to the geometry of the ray path..... 163

Figure 5.1 The point source on the left emits spherical wavefronts (gray surfaces) which are represented by a grid of rays (blue arrows) propagating towards the lens (light blue). 168

Figure 5.2 A collimated wavefront passes through a lens and converges through a birefringent plate. The optic axis (black line) of the birefringent plate lies in the plane of the page. Two aberrated wavefronts (red and blue) exit the birefringent plate and pass a

series of planes labeled from A to F . The ray positions from the two modes overlap on those planes are spaced differently. 170

Figure 5.3 (Left) Illumination pattern created from a light focusing through a glass of water. The wavefront contains many bright lines which are the caustics. (Right) The caustics are highlighted in red. 171

Figure 5.4 (a) A normal incident collimated beam with a planar wavefront (purple) incident onto a birefringent plate. The disks in the plot indicate the start of each period of the oscillating electric fields. The incident beam splits into two wavefronts (red and blue) with a phase delay between them and reaches an observation plane. (b) Electric fields of the two orthogonal eigenstates for a ray passing through the plate. Red for y -polarized and blue for x -polarized. (c) Both electric field oscillations are plotted in one plane to show that the x -polarized mode goes through 3 periods while the y -polarized mode goes through 3.25 periods traversing the plate. 172

Figure 5.5 The resultant polarization states as a function of ΔOPL 175

Figure 5.6 One off-axis collimated ray grid propagates through a birefringent plate splits into two collimated wavefronts. They partially overlap each other on plane A and plane B 176

Figure 5.7 The two resultant wavefronts are horizontally (blue) and vertically (red) polarized. The overlapping area of the two orthogonal modes is 45° polarized. 177

Figure 5.8 Two individual wavefronts, one horizontally and one vertically polarized, are laterally sheared by the waveplate. They partially overlap each other. The polarization of

the overlapping region depends on the phase difference of the individual wavefront. Showing from left to right, the relative phases are (0, 0.15, 0.25, 0.35, 0.5) waves. 177

Figure 5.9 Two collimated wavefronts (red and blue) exiting a PBS into the same direction. 179

Figure 5.10 Resultant polarization states with spatially varying ΔOPL across the beam. 180

Figure 5.11 Three grids of rays corresponding to three modes reach a 2D plane. (a) The location of the rays are shown as dots. (b) The ray data are resampled in a regular grid with zeros values (gray dots) outside the region of the three beams. 182

Figure 5.12 (Left) An unevenly spaced ray grid at locations ($\mathbf{r}_{E1}, \mathbf{r}_{E2}, \dots, \mathbf{r}_{Ea}, \dots, \mathbf{r}_{EA}$) are shown in red. The evenly spaced grid ($\mathbf{r}_1, \mathbf{r}_2, \dots, \mathbf{r}_b, \dots, \mathbf{r}_B$) for resampling is shown in black. (Right) Interpolation involves weighting contributions from nearest neighbors. Five closest data location ($\mathbf{r}_{c1}, \mathbf{r}_{c2}, \mathbf{r}_{c3}, \mathbf{r}_{c4}, \mathbf{r}_{c5}$) to \mathbf{r}_b are shown. 183

Figure 5.13 Seven data points (red) are interpolated using equation (5.10). The resultant interpolation functions are shown in blue for five different p 185

Figure 5.14 Two non-zero data point (blue) are interpolated using equation (5.10). The resultant 2D interpolated functions shown in orange for the different p reveal the influence function for the different p 185

Figure 6.1 A ray of an incident beam refracts into a uniaxial plane parallel plate and splits into two rays in two directions. After these two rays refract out of the crystal, they both propagate in the same direction as the incident ray, but are displaced by Δr 190

Figure 6.2 Negative uniaxial A-plate such as calcite with a y -oriented optic axis delaying the o -modes with respect to the e -mode.	191
Figure 6.3 (a) n_e at wavelength $0.5 \mu\text{m}$ in a y -oriented calcite A-plate as a function of incident angle (θ_x, θ_y) in air. (b) The shear displacement Δr between the two exiting modes through the quarter wave calcite A-plate, measured transverse to the \mathbf{k} vector.	192
Figure 6.4 Three incident rays at $0.5 \mu\text{m}$ along the principal section with incident angles 0° , 30° , and 45° pass through a quarter wave A-plate, and experience different birefringence Δn and ΔOPL	192
Figure 6.5 (Left) Sagittal and (right) tangential ray bundles ($\pm 45^\circ$) in the focal region are shown with o -rays in red and e -rays in blue. A thick waveplate is used to make the aberrations easily visible.	193
Figure 6.6 (a) and (b) show the OPL of the o - and e -wavefronts after the A-plate. (c) shows the OPL values in the tangential and sagittal planes.	194
Figure 6.7 (a) o - and e -polarizations are shown on the exiting wavefronts in Figure 6.5 , thus the slight rotation. The arrow locations indicate phase. (b) Retardance magnitude through the quarter wave A-plate.	195
Figure 6.8 A beam with 0.5NA is simulated by a grid of rays which focuses through a quarter wave calcite A-plate with optic axis oriented along y . The incident ray grid splits into two ray grids, one for the ordinary mode (red), and one for the extraordinary mode (blue).	195

Figure 6.9 The o - and e -wavefronts at the exit pupil of the quarter wave calcite A-plate for 0.5 NA at 0.5 μm	196
Figure 6.10 The maximum (red) o - and (blue) e - ΔOPL calculated from ray tracing at the exit pupil for six different plate thickness t	196
Figure 6.11 The P matrices of the o - and e -wavefronts at the exit pupil. The magnitude (left 3 \times 3 panels) and phase in radians (right 3 \times 3 panels) of the (a) e -mode's and (b) o -mode's P matrices.....	197
Figure 6.12 The Jones pupil of the o - and e -wavefronts at the exit pupil. The magnitude (left 2 \times 2 panels) and phase in radians (right 2 \times 2 panels) of the (a) e -mode's and (b) o -mode's Jones pupils.	197
Figure 6.13 The amplitude of the 2 \times 2 ARMs of the o - and e -wavefronts. Zero amplitude in gray, medium amplitude in red, and highest amplitude in yellow.....	198
Figure 6.14 The ARM amplitude of the o - and e -wavefronts with 0.5NA for various A-plate thicknesses.....	199
Figure 6.15 The amplitude of ARM of the combined o - and e -wavefronts with 0.5NA for various A-plate thicknesses.....	200
Figure 6.16 (Left) The maximum amplitude and (right) the 50% encircled energy (EE) for $ARM_{e,yy}$ calculated from ray tracing results at six different plate thickness t	200
Figure 6.17 MPSM of the combined o - and e -wavefronts with 0.5NA for various A-plate thicknesses.	201

- Figure 6.18 (a) A 45° linearly polarized wavefront is simulated for a circular grid of rays. (b) The circular grid of rays with $\pm 25^\circ$ incident angle propagate through a 1st order quarter waveplate whose optic axis is oriented along y . (c) The exiting wavefronts are circularly polarized with small aberrations. The locations of the arrows indicate the phase of each rays..... 202
- Figure 6.19 The grid locations on a spherical surface where the fields and *OPLs* will be combined..... 202
- Figure 6.20 Fit functions for the **E** field components and the *OPL* for the two exiting modes through the 1st order quarter waveplate. The dots are the discrete ray data, and the smooth surfaces are the fit 203
- Figure 6.21 The polarization ellipses over $\pm 25^\circ$ after the $1\frac{1}{4}\lambda$, $3\frac{1}{4}\lambda$, and $5\frac{1}{4}\lambda$ waveplates. 204
- Figure 6.22 (Left) The polarization ellipse on the transverse plane of a wavefront with 15° NA after a $50\frac{1}{4}\lambda$ thick waveplate. (Right) The polarization ellipses plotted on a 2D plane. 204
- Figure 6.23 Exiting Stoke parameters for unpolarized, horizontally polarized, vertically polarized, 45° linearly polarized, 135° linearly polarized, right circularly polarized and left circularly polarized incident light for the quarter wave A-plate..... 206
- Figure 6.24 Exiting Stoke parameters for unpolarized, horizontally polarized, vertically polarized, 45° linearly polarized, 135° linearly polarized, right circularly polarized and left circularly polarized incident light for the 3.5 wave A-plate. 206

Figure 6.25 Exiting Stoke parameters for unpolarized, horizontally polarized, vertically polarized, 45° linearly polarized, 135° linearly polarized, right circularly polarized and left circularly polarized incident light for the 17.5 wave A-plate. 207

Figure 7.1 (Left) A Wollaston prism is made of two blocks of calcite which have orthogonal optic axes (light blue lines inside crystals). It directs two orthogonal modes into two directions, due to the different refractive index associated to each mode. (Right) A Glan-Taylor polarizer is also made of two blocks of calcite with the same optic axes orientation. It transmits the *e*-mode (blue arrows) while redirect the *o*-mode (red arrows) at the interface..... 208

Figure 7.2 (a) Glan-Taylor polarizer consists of two calcite right-triangular pieces separated by an air gap with vertically oriented optic axes (black arrows inside the two blocks). (b) The geometry of the crystal polarizer is defined by θ_A , H , L , and C . The combination of the two crystal blocks forms a rectangular cube. The entrance surface has an area $H \times H$. The length of the crystal is $L = H \tan \theta_A$. The air gap has a thickness C . . 211

Figure 7.3 The properties of internal refraction at a calcite/air interface as a function of incident angle at the air-gap interface. (a) The refractive index as a function of ray angle in calcite. (b) The refraction angle as a function of incident angle, the *o*- mode critical angle is 37.08° and *e*-mode critical angle is 42.22° . (c) The intensity transmission as function of incident angle, where the maximum *e*-transmission occurs at 34.54° 212

Figure 7.4 *o*- and *e*-rays internally refracts through a calcite/air interface. The incident and exiting polarization orientations are shown at the start and at the end of each ray. (a) The

o-mode is orthogonal to the optic axis (purple arrow) and (b) the *e*-mode is in the plane of the optic axis. The length of the polarization state represents the transmission coefficient which is also plotted in Figure 7.3 (c). This figure cannot represent the rays with rapidly changing intensity in a small range close to the critical angle..... 213

Figure 7.5 For a normal incident ray, the *o*-mode (red) undergoes TIR at the air gap, while the *e*-mode (blue) transmits to the exit surface as vertically polarized light. The *o*-mode either exits through the top surface or is absorbed by a black coating on the top surface. The partial reflections associated with small amplitude are not shown here, for example the partial reflection of the *e*-mode at the hypotenuse..... 214

Figure 7.6 (a) The angle of refraction for the *o*- and the *e*-modes at the 1st air gap interface as a function of the incident angle (θ_x , θ_y) at the polarizer's entrance surface. The false color scale indicates the refraction angle, where gray denotes TIR. At the critical angle, light refracts at 90° (light blue). The vertical shift between these two functions for *oi*- and *ei*-modes, is the basis of operation for the Glan-Taylor polarizer, indicating the incident angles where the *o*-mode TIRs while the *e*-mode partially transmits. This shift is responsible for the highly efficient performance of the Glan-Taylor. (c) The intended field for the Glan-Taylor polarizer shown ensures the *o*-mode will TIR at the interface, while the *e*-mode transmits through the polarizer. At $\theta_x=0$, the polarizers field along θ_y ranges from -4.5° to +3.5°..... 216

Figure 7.7 A ray tree of all possible ray paths of a ray propagating through a Glan-Taylor polarizer with different mode combinations. The incident ray splits into *o*- and *e*-modes at the entrance surface. Without loss of generality, at the 1st surface of the air gap, both modes

can refract through the gap or TIR back to the 1st crystal. For light reflected from the hypotenuse, the rays split further into *oo*- and *oe*-modes or *eo*- and *ee*-modes. These modes may escape through the top surface. Rays transmitted through the air gap further split into *oio*- and *oie*- or *eio*- and *gie*-modes, and exit the polarizer. Up to four exiting modes may occur for a given incident ray, but depending on the incident ray propagation direction, some of these modes have zero amplitude..... 218

Figure 7.8 Ray traces of several incident angles. Only rays associated with TIR and transmitted through the air-gap are shown. The top left is normal incidence. The incident rays for the top two ray trace on the right are tilted along the *y* axis with incident $\mathbf{k}=(0, 0.087, 0.996)$ in air and $(0, -0.122, 0.993)$. The incident rays in the third row are tilted in both the *x* and *y* directions with incident $\mathbf{k}=(0.104, -0.104, 0.989)$ and $(0.104, 0.104, 0.989)$. All incident beams are 45° linearly polarized with amplitude of one. The resultant *gie*- (blue), *eio*- (green), *oie*- (magenta), *oio*- (red), *ee*- (light blue) and *oo*- (orange), *eo*- (green), and *oe*-(coral) polarizations are shown with their corresponding amplitude..... 219

Figure 7.9 Ray paths for a ±45° fan of rays in the *y-z* plane. Details ray paths for five circularly polarized incident rays in the *y-z* plane are shown for refraction and TIR. (To keep the figures simple, the partial reflection are not shown.) The resultant *gie*- (blue), *oio*- (red), *ee*- (light blue) and *oo*-(orange) polarizations are shown with their corresponding electric field amplitude. 221

Figure 7.10 A ±45° *x-z* fan of rays through a Glen-Taylor polarizer. Individual rays in the *x-z* plane at different incident angles with circularly polarized incident ray (purple) with incident angle θ_{in} and an amplitude of 1. The resultant *gie*- (blue), *eio*- (green), *ee*- (light

blue), *oo*- (orange), *eo*- (light green), and *oe*- (coral) polarizations are shown with their corresponding electric field amplitudes. 221

Figure 7.11 (Top) An incident spherical wavefront (yellow) is ray traced for a grid of rays (gray lines) shown within a $\pm 45^\circ$ cone. The wavefront focuses at the entrance of the Glan-Taylor polarizer and diverges into the crystal. Due to ray doubling, four resultant modes, shown in separate colors, pass through the polarizer, exit, and overlap unevenly. The *eie*-mode is blue, *eio*-mode is green, *oie*-mode is red, and *oio*-mode is magenta. (Middle row) The grid of rays for each refracted modes are plotted separately. The exiting polarization states are determined in 3D. Note that only the bottom half of the rays transmit through. The polarization ellipses of each rays are shown in at the end of the ray. (Bottom row) The 3D polarization states scaled by their amplitudes viewed after the crystal. 223

Figure 7.12 The distribution of the electric field amplitudes for each exiting modes in Figure 7.11 as function of exiting angle. The numerical aperture (NA) of the incident beam for each rows are (top) $0.088 = \sin 5^\circ$, (middle) $0.259 = \sin 15^\circ$ and (bottom) $0.707 = \sin 45^\circ$ 224

Figure 7.13 The overlap between the four exiting modes for 0.707NA (the bottom row of Figure 7.12), as function of exiting angle. 225

Figure 7.14 *OPL* of each modes corresponds to the amplitude shown in Figure 7.12, and relative to the *OPL* of the on-axis *eie*-ray. 226

Figure 7.15 The resultant intensity distribution for Figure 7.12 and Figure 7.14. The incident NA for each of them are (left) 0.088, (middle) 0.259 and (right) 0.707. Light pink is chosen to represent the lower intensity.	227
Figure 7.16 Polarimeter measurement of a Glan-Taylor polarizer with a 0.1NA microscope objective pair. (Left) Measured irradiance, (middle) normalized Mueller matrix image, and (right) diattenuation image.....	229
Figure 7.17 The <i>OPL</i> function for the <i>ieie</i> -mode from ray tracing to a flat surface; defocus dominates.	229
Figure 7.18 Wavefront of <i>ieie</i> -mode after removing piston, tilt and defocus.....	231
Figure 7.19 Polarizer configurations for calculating extinction of Glan-Taylor polarizers. (Left) A normal incident ray propagates through the (top) cross and (bottom) co-polarized systems. (Right) An off-axis ray with $\theta_y=3^\circ$ incident angle propagates through the two systems, where light leaks through the cross-polarized system while more rays split through the co-polarized system.....	232
Figure 7.20 A ray propagates through a co-polarized system with 4 crystals. Beyond $\theta_y=-10^\circ$, one incident ray produces 16 exiting rays.	233
Figure 7.21 (Left) A grid of rays with 0.05NA propagates through the cross and co-polarized systems, where rays leak through for non-normal incident rays. (Right) The exiting modes are divided into groups by different colors and are plotted as function of exiting angles. In the co-polarized system, <i>ieieieie</i> -mode dominates the center of the field.	234

- Figure 7.22 Polarization amplitudes through the cross-polarized system with 0.05NA for each resultant mode expressed in the exiting angle coordinates..... 235
- Figure 7.23 Polarization amplitudes through the co-polarized system with 0.05NA for each resultant mode in exiting angle coordinates..... 235
- Figure 7.24 Resultant electric field intensity at the exit surface of the (left) co and (right) cross- polarized systems with 0.05NA..... 236
- Figure 7.25 The intensity distribution at the center $\pm 3^\circ$ in the far field for the (left) co and (right) cross-polarized systems. The Maltese cross pattern represents the light leakage from off-axis rays in the cross-polarized system. The co-polarized system has decreasing amplitude toward the $+y$ direction. 236
- Figure 7.26 Extinction ratio map for $\pm 3^\circ$ square illumination. The highest extinction ratio is at normal incidence, and along the x and y directions..... 237
- Figure 7.27 Analysis for a $\pm 6^\circ$ incident beam. (Top) The mode overlapped after the co and cross-polarized systems. (Bottom, left & middle) The exiting intensity within $\pm 6^\circ$ exiting angle for the co- and cross-polarized systems. (Bottom, right) Overlapping mode is visible in the extinction ratio plot. 238
- Figure 8.1. The colors in these plastic cup, plastic tape dispenser, and prescription eye glasses placed between crossed polarizers indicate large amounts of spatially varying stress..... 241
- Figure 8.2 (a) An isotropic glass plate placed in an optical mount and viewed between crossed polarizers. (b) The same glass plate as a screw is tightened against the glass at the

bottom. Due to the stress created, induced birefringence has caused significant leakage between crossed polarizers. 241

Figure 8.3 Stress on an object results in compressive stress and tensile stress. (Left) The original shape of an object. (Right) When stress is applied to the object, the shape of the object deformed. The deformation of the object shown is exaggerated to visualize the effect of compressive and tensile stress. 244

Figure 8.4 The change of refractive index Δn plotted as a function of material stress-optic coefficient C for 15MPa applied stress, where $\Delta n = C \cdot \text{Stress}$. Glasses such as N-BK7 and SF4 have $C < 5$. Polymers, such as Polymethylmethacrylate (PMMA), Polystyrene (PS), and Polycarbonate (PC), have larger C which vary in a large range with temperature.. 244

Figure 8.5 Refractive index change Δn and its corresponding ray split $\Delta \theta$ as a function of applied stress for glass N-BK7 (left) and polymer polycarbonate (right). The ray split is calculated with algorithms presented in Chapter 2. 245

Figure 8.6 The 3×3 stress tensor distribution of an injection molded lens. Red indicates tension, blue indicates compression, and gray indicates zero stress. The plastic entered the lens mold from the bottom at the region called the gate. The cylinder of plastic extending from the bottom of the lens is for handling the lens, which will be removed by a robotic saw. When the cylinder is removed, the lens falls into packaging for delivery. 254

Figure 8.7 (a) A tetrahedron element has four vertices (1, 2, 3, and 4) and four surfaces (I, II, III, and IV). (b) and (c) are surface plots of two different injection molded lens structures. The surfaces are represented by surface triangles. 255

Figure 8.8 Refraction through an injection molded lens uses surface triangles and Snell's law to calculate ray intercepts. The figure shows a simulation of collimated rays converging through the lens.....	256
Figure 8.9 A tetrahedron element defined by four corners (top row, left column) is reduced to one data point, shown as a red point at the center of the element. Eleven tetrahedrons shown in the middle row are reduced to eleven data locations. The last row shows all 95,656 tetrahedrons of an object are reduced to 95,656 data locations, each of them are associated with a stress tensor.....	257
Figure 8.10 Two views of the stress tensor coefficient σ_{xx} from the CAD file of an injection molded lens.....	258
Figure 8.11 Stress tensor maps for the 9 components are plotted across an object cross section in color scale.....	258
Figure 8.12 For a single ray, a spatially varying biaxial material (left) can be simulated as a stack of constant biaxial slabs (right). A different stack is calculated for each ray.....	259
Figure 8.13 The ray path inside the spatially varying biaxial material is divided into steps. Interpolation is used to obtain stress information at each step. (a) A ray passes near many stress data points shown in light blue along its ray path. (b) The ray path is then divided into steps shown as orange parallel lines along the ray path. (c) It is unlikely that the step exactly intersects any data point. (d) The N closest data points, three are highlighted in purple, are used to interpolate the stress for the step. (e) A \mathbf{P} matrix is calculated for the step from the stress tensor, the ray direction, and the step length.	260

Figure 8.14 The stress images of the injection molded lens (the same lens as in Figure 8.11) with a cut away through the CAD variation file.	262
Figure 8.15 Retardance magnitude, retardance orientation, and polariscope images from a polarization ray trace for an injection molded lens of Figure 8.14. The gate of the lens is located at the top of the lens shown.	263
Figure 8.16 Stress induced retardance of a DVD pick up lens across the pupil.	264
Figure 8.17 Point spread functions of polarized light through the un-stressed lens (left) and the stressed lens (right) in log scale.	264
Figure 8.18 Point spread functions of polarized light refracting through a stressed lens with 10, 100, and 1000 times the stress shown in Figure 8.17.	265
Figure 9.1 Ray tree for system with two anisotropic surfaces. The incident ray split into two modes at the 1 st intercept. These two modes split again at the 2 nd anisotropic interface and result in four exiting modes. The surface interactions are represented by \mathbf{P}_{if} , \mathbf{P}_{is} , \mathbf{P}_{ff} , \mathbf{P}_{fs} , \mathbf{P}_{sf} , and \mathbf{P}_{ss} . The phase changes due to propagation are represented by \mathbf{P}_f , \mathbf{P}_s . The polarization of the first exiting mode is represented by the \mathbf{P} matrices along the first ray path, which is the matrix multiplication of $\mathbf{P}_{ff} \mathbf{P}_f \mathbf{P}_{if}$	270
Figure 9.2 Summary of anisotropic ray tracing and imaging analysis of multiple polarized wavefronts. Subscript m indicates the m^{th} eigen-polarized wavefront. The total \mathbf{MPSM} is the summation of \mathbf{ARM}_m of all the overlapped modes.	271
Figure A.1 A collimated beam focuses through a lens. Due to aberrations, none of the ray coincides at a single point. (Left) On-axis beam. (Right) Off-axis beam.	275

- Figure A.2 The ray intercepts on the last surface before focus are shown in yellow. The average of these ray intercets \mathbf{r}_{Mean} is shown in red. The average axis \mathbf{S}_{Mean} is shown as pink line passing through \mathbf{r}_{mean} . (Left) On-axis beam. (Right) Off-axis beam. 276
- Figure A.3 Potential planes of focus (light blue) orthogonal to average axis (pink). (Left) On-axis beam. (Right) Off-axis beam. 276
- Figure A.4 Ray intercepts (colored points) of the grid on rays on each potential planes of best focus (blue). (Left) On-axis beam. (Right) Off-axis beam. 277
- Figure B.1 Dipole coordinates have local x and y axes along the latitude and longitude of a spherical wavefront. 278
- Figure B.2 Double pole local coordinates with one double singularity at $-z$. (Left) Viewing toward the opposite end of the singular double pole, the basis vectors have a nice nearly uniform distribution. (Right) At around the double pole, the basis vectors rotate rapidly by 720° 279
- Figure C.1 External (left) and internal (right) reflection and refraction of biaxial interface. 281
- Figure C.2 Reflection and transmission coefficients at the air/KTP interface. 282
- Figure C.3 A fan of rays externally reflect from an air/biaxial interface. The gray arrows are the incident \mathbf{k} vectors. The black arrows are the corresponding reflected \mathbf{k} vectors. The blue and red arrows are the polarization ellipses, showing the evolution of the electric field, where the arrow head indicates the start of the electric field evolution in time. All the

incident polarizations have the same magnitude. The length of the polarization arrows indicate the intensity of the reflected light, but are adjusted slightly for visualization. ... 283

Figure C.4 A fan of rays externally refract through an air/biaxial interface. The gray arrows are the incident \mathbf{k} vectors. The black and brown arrows are the refracted \mathbf{S} vectors for the *slow*- and *fast*-modes. The blue and red arrows are the polarization ellipses of *p-slow* couplings and *s-fast* couplings. 288

Figure C.5 Left circularly polarized light is incident on the air/biaxial interface. The gray, black and brown arrows are the incident, reflected and refracted rays, respectively. The purple ellipses are the incident and reflected polarizations. The red and blue arrows are the refracted *fast*- and *slow*-modes. 284

Figure C.6 Internal reflection and transmission coefficients at the KTP/air interface. 285

Figure C.7 A fan of rays internally reflect from a biaxial/air interface. The gray arrows are incident \mathbf{k} vectors. The black arrows are reflected \mathbf{k} vectors. The blue arrows are the incident and reflected polarizations of *slow*-modes. The red arrows are the incident and reflected polarizations of *fast*-modes. 285

Figure C.8 A fan of rays internally refract through a biaxial/air interface. The gray arrows are incident \mathbf{k} vectors. The black arrows are refracted \mathbf{k} vectors. The blue arrows are the incident and refracted polarizations of *slow*-modes. The red arrows are the incident and reflected polarizations of *fast*-modes. 286

LIST OF TABLES

Table 1.1 Ray parameters for polarization ray trace.....	59
Table 1.2 Parameters of anisotropic interface.....	59
Table 2.1 Polarization ellipses evolving in time for three polarization vectors.....	69
Table 2.2 Properties of biaxial, uniaxial and isotropic materials when the principal axes are aligned with the global coordinate system. (Yellow) The biaxial crystal has principal refractive indices n_S , n_M , and n_F . (Green) The uniaxial crystal has principal refractive indices n_O and n_E . (Blue) The isotropic material has one refractive index n	71
Table 2.3 Mode labeling for exiting rays in different types of anisotropic interfaces. The s - and p -polarizations in isotropic material have the same propagation directions and are grouped to one mode, <i>isotropic</i>	82
Table 2.4 Ray tracing parameters to be calculated for each anisotropic ray intercept to characterize each exiting ray.....	83
Table 3.1 The polarization states for calculating the \mathbf{P} matrices for an uncoated interface. (m , n , v , w) are defined in equation (3.13). ' indicates exiting mode. The split eigenmodes in an anisotropic material are described by two \mathbf{P} matrices. However, the two \mathbf{P} matrices for s' and p' exiting states can be combined (\Rightarrow) to one \mathbf{P} matrix.....	128
Table 3.2 Summary of the intermediate \mathbf{P} matrices for incorporating <i>OPL</i>	139
Table 4.1 Ray parameters at the entrance surface (external reflection/refraction).	148
Table 4.2 Ray parameters at the exit surface (internal reflection/refraction)	150

Table 4.3 Eigenanalysis of \mathbf{M}_R of the \mathbf{P} and \mathbf{Q} matrices for the three prisms example in Figure 4.9.	165
Table 5.1 Steps to reconstruct wavefront from wavefront combination.....	181
Table 7.1 Resultant e -mode \mathbf{P} matrices and electric fields for a normally incident ray through a Glan-Taylor polarizer.	215
Table 7.2 Resultant transmittance and transmission of ie -mode from normal incident is calculated. t_p is the Fresnel coefficient and T_p is the Fresnel transmission.....	215
Table 7.3 Zernike coefficients for the ie -wavefront for system with 0.088NA.....	230
Table 8.1 Refractive index n_o , strain optic coefficients (p_1 and p_2), Young's modulus E , Poisson's ratio ν , and stress optic tensor coefficients (C_1 and C_2) for glasses and plastics at 633nm.	249

ABSTRACT

Optical components made of anisotropic materials, such as crystal polarizers and crystal waveplates, are widely used in many complex optical systems, such as display systems, microlithography, biomedical imaging and many other optical systems, and induce more complex aberrations than optical components made of isotropic materials. The goal of this dissertation is to accurately simulate the performance of optical systems with anisotropic materials using polarization ray tracing. This work extends the polarization ray tracing calculus to incorporate ray tracing through anisotropic materials, including uniaxial, biaxial and optically active materials.

The 3D polarization ray tracing calculus is an invaluable tool for analyzing polarization properties of an optical system. The 3×3 polarization ray tracing \mathbf{P} matrix developed for anisotropic ray tracing assists tracking the 3D polarization transformations along a ray path with series of surfaces in an optical system. To better represent the anisotropic light-matter interactions, the definition of the \mathbf{P} matrix is generalized to incorporate not only the polarization change at a refraction/reflection interface, but also the induced optical phase accumulation as light propagates through the anisotropic medium. This enables realistic modeling of crystalline polarization elements, such as crystal waveplates and crystal polarizers. The wavefront and polarization aberrations of these anisotropic components are more complex than those of isotropic optical components and can be evaluated from the resultant \mathbf{P} matrix for each eigen-wavefront as well as for the overall image.

One incident ray refracting or reflecting into an anisotropic medium produces two eigenpolarizations or eigenmodes propagating in different directions. The associated ray parameters of these modes necessary for the anisotropic ray trace are described in Chapter 2. The algorithms to calculate the \mathbf{P} matrix from these ray parameters are described in Chapter 3 for anisotropic ray tracing. This \mathbf{P} matrix has the following characteristics:

- (1) Multiple \mathbf{P} matrices are calculated to describe the polarization of the multiple eigenmodes at an anisotropic intercept.
- (2) Each \mathbf{P} matrix maps the orthogonal incident basis vectors $(\hat{\mathbf{E}}_{\mathbf{m}}, \hat{\mathbf{E}}_{\mathbf{n}}, \hat{\mathbf{S}})$ before the optical interface into three orthogonal exiting vectors $(a_m \hat{\mathbf{E}}'_{\mathbf{m}}, a_n \hat{\mathbf{E}}'_{\mathbf{n}}, \hat{\mathbf{S}}')$ after the interface, where a_m and a_n are the complex amplitude coefficients induced at the intercept.

The ray tracing algorithms described in this dissertation handle three types of uncoated anisotropic interfaces isotropic/anisotropic, anisotropic/isotropic and anisotropic/anisotropic interfaces.

- (3) The cumulative \mathbf{P} matrix associated with multiple surface interactions is calculated by multiplying individual \mathbf{P} matrices in the order along the ray path.

Many optical components utilize anisotropic materials to induce desired retardance. This important mechanism is modeled as the optical phase associated with propagation.

- (4) The optical path length OPL of an eigenpolarization along an anisotropic ray path is incorporated into the calculation of each \mathbf{P} matrix.

Chapter 4 presents the data reduction of the \mathbf{P} matrix of a crystal waveplate. The diattenuation is embedded in the singular values of \mathbf{P} . The retardance is divided into two parts: (A) The physical retardance induced by *OPLs* and surface interactions, and (B) the geometrical transformation induced by geometry of a ray path, which is calculated by the geometrical transform \mathbf{Q} matrix. The \mathbf{Q} matrix of an anisotropic intercept is derived from the generalization of *s*- and *p*-bases at the anisotropic intercept; the *p* basis is not confined to the plane of incidence due to the anisotropic refraction or reflection.

Chapter 5 shows how the multiple \mathbf{P} matrices associated with the eigenmodes resulting from propagation through multiple anisotropic surfaces can be combined into one \mathbf{P} matrix when the multiple modes interfere in their overlapping regions. The resultant \mathbf{P} matrix contains diattenuation induced at each surface interaction as well as the retardance due to ray propagation and total internal reflections.

The polarization aberrations of crystal waveplates and crystal polarizers are studied in Chapter 6 and Chapter 7. A wavefront simulated by a grid of rays is traced through the anisotropic system and the resultant grid of rays is analyzed. The analysis is complicated by the ray doubling effects and the partially overlapping eigen-wavefronts propagating in various directions. The wavefront and polarization aberrations of each eigenmode can be evaluated from the electric field distributions. The overall polarization at the plane of interest or the image quality at the image plane are affected by each of these eigen-wavefronts.

Isotropic materials become anisotropic due to stress, strain, or applied electric or magnetic fields. In Chapter 8, the \mathbf{P} matrix for anisotropic materials is extended to ray

tracing in stress birefringent materials which are treated as spatially varying anisotropic materials. Such simulations can predict the spatial retardance variation throughout the stressed optical component and its effects on the point spread function and modulation transfer function for different incident polarizations.

The anisotropic extension of the \mathbf{P} matrix also applies to other anisotropic optical components, such as anisotropic diffractive optical elements and anisotropic thin films. It systematically keeps track of polarization transformation in 3D global Cartesian coordinates of a ray propagating through series of anisotropic and isotropic optical components with arbitrary orientations. The polarization ray tracing calculus with this generalized \mathbf{P} matrix provides a powerful tool for optical ray trace and allows comprehensive analysis of complex optical system.

CHAPTER 1 INTRODUCTION

1.1 Motivation of polarization ray trace

Polarization is an important property of light utilized in many scientific studies and sophisticated optical systems, for example astronomical studies, atmospheric sciences, advanced remote sensing satellites, telecommunication systems, microlithography systems, liquid crystal displays, 3D cinema, and numerous other products. As these technologies have advanced rapidly in the last decade, there has been an increasing need to develop tools for accurate modeling of polarized light, to understand the sources of polarization aberrations, and to estimate the magnitude of the polarization effects on image quality.

The capability of accurately ray tracing through anisotropic materials is not fully developed in current commercial ray tracing software. The goal of this dissertation is to develop systematic polarization ray tracing algorithms that are easy to use and understand. The result will assist scientists and engineers in designing better polarizers, waveplates, polarizing beam splitters with new choices of optical thin films, and ultimately produce optical systems with better performance, in particular better control of polarized light.

This dissertation developed three-dimensional ray tracing algorithms to polarization ray trace through the principal types of anisotropic materials: uniaxial, biaxial and optically active materials. These algorithms and methods for anisotropic analysis are programmed in a polarization ray tracing program, Polaris-M, which has been developed and is in use at the Polarization Laboratory at the University of Arizona. All the ray tracing

examples, polarization analysis, and the image formation simulations shown in this dissertation are generated using Polaris-M.

1.2 Polarization aberrations

The aberration of an optical system is its divergence from ideal performance. For an imaging system with a point source object, the ideal output is a spherical wavefront with uniform amplitude and polarization state.

There are several types of aberrations. Wavefront aberrations are deviations from a spherical wavefront, and result from the variations of optical path length (*OPL*) across the wavefront. These variations are due to the geometry of the optical surfaces, and the laws of reflection and refraction. Amplitude aberrations are deviations from constant amplitude, and arise from the differences in transmitted flux due to reflection, refraction, and absorption between rays. Amplitude variations are usually referred to as apodization.

Polarization aberrations are variations of polarizations properties of an optical system. Polarization change occurs at each light-surface interaction because reflection and transmission are functions of polarization states. For example, the *s* and *p* components of the light at an isotropic interface, or the ordinary and extraordinary eigenpolarizations at an anisotropic interface, have different reflection and transmission coefficients. Another example is the polarization change along ray paths when light propagates through anisotropic material, as shown in Figure 1.1. In this example, the anisotropic material decomposes light into orthogonal polarization components, which then have different *OPLs* as they passed through the anisotropic medium.

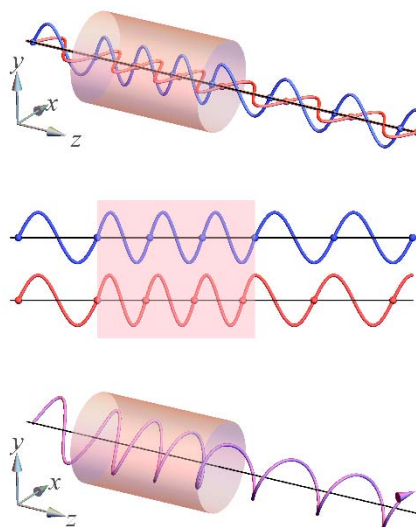


Figure 1.1 A ray propagates through a birefringent material. (Top) The ray decompose into two orthogonal polarized components, called modes, x -polarized in red and y -polarized in blue. (Middle) In this example, the x -polarized light has propagated 3.25λ , and the y -polarized light has propagated 3λ . (Bottom) The incident x - and y -polarized light combine to 45° polarized light. The exiting light with a quarter wave phase difference between the x and y components is right circularly polarized.

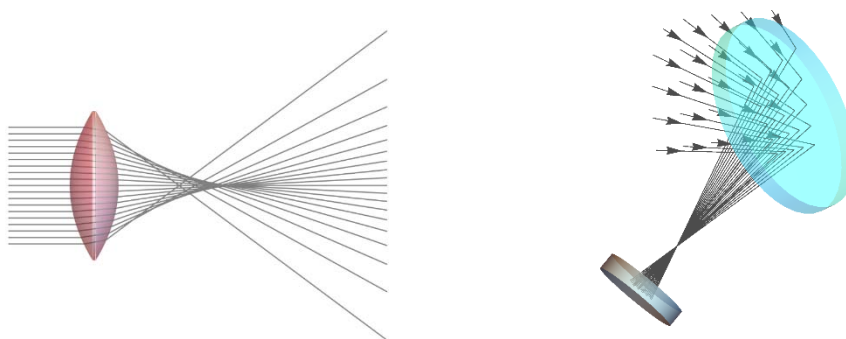


Figure 1.2 The angles of incidence vary across the set of rays. (Left) A set of rays refracts through a convex lens. (Right) A grid of rays reflects from a fold mirror.

The polarization change is function of incident angle. Across a set of rays, as shown in Figure 1.2, the angle of incidence at an optical surface varies, so a uniformly polarized input beam has polarization variations when exiting the system^{1,2,3}. The desired output light of many optical systems is constant polarization across the beam with zero polarization change occurring. This ideal condition is associated with a set of identity Jones matrices

for every rays ray path. Deviations from these identity matrices are one common definition for the polarization aberration of an optical system.

Wavefront aberration, which is calculated in all commercial ray tracing programs, is the most important aberration, because variations of *OPL* of small fractions of a wavelength can greatly reduce the image quality. The variations of amplitude and polarization cause much less change to the image quality than the wavefront aberrations. However, in high performance systems, for example when imaging and measuring polarization of exoplanets^{4,5}, or focusing light through a system with high numerical aperture (NA) in microlithography^{6,7}, these amplitude and polarization effects can no longer be ignored.

Polarization aberration refers to the polarization variation across the wavefront. “Fresnel aberration” is polarization aberration due to uncoated interfaces and is calculated from the Fresnel equations^{1,8,9,10,11}, such as when converging or diverging beam reflects from metal coated mirrors, and collimated beam refracts through uncoated lenses. Surfaces associated with anisotropic materials and multilayer-coated surfaces produce polarization aberrations with similar functional forms to the wavefront aberrations, since they arise from similar geometrical considerations of surface shape and angle of incidence variation^{12,13,14,15,16,17,18,19,20,21}. Polarization aberrations which arise from propagation through anisotropic materials are more complex than those from isotropic materials due to ray doubling and multiple exiting wavefronts.

The aberrations of an optical system can be measured using interferometers and polarimeters. The interferograms of an optical system measured by an interferometer show

the wavefront deviation from an ideal wavefront. Polarization aberrations can be measured by placing an optical system in the sample compartment of an imaging polarimeter and measuring images of the Jones matrices and/or Mueller matrices for a collection of ray paths through the optical system^{22,23}.

1.3 Polarization ray tracing calculus

Polarization aberrations result from polarization variations across exit pupil of an optical system and affect image quality. In microlithography system with high numerical aperture, for example, the quality of the point spread function is affected by the polarization aberration to a magnitude which can affect the performance goals. These variations result from polarization change upon light-surface interaction characterized by Fresnel coefficients (complex amplitude coefficients of the eigenpolarizations) at each ray intercept, or light-matter interaction as light propagates through material.

The polarization properties along the ray paths can be calculated by polarization ray tracing, which requires many extra ray parameters be calculated beyond those carried in conventional geometrical ray trace. Traditionally, geometrical ray trace calculates the optical path length (*OPL*) to determine phase in the exit pupil and image, which is a scalar function. *OPL* alone is insufficient to describe variation of polarization. Since polarization is fundamentally tied to the directional properties of light's electric field relative to the optical materials, a higher level of ray tracing algorithm is required to effectively operate on the vector form of light. One example is the Jones calculus.

The Jones calculus incorporates polarization changes as a 2×2 Jones matrix. Thus it naturally can represent the polarization element. Polarized light is described by a 2×1

Jones vector the Jones matrix operates on to represent the change of polarization²⁴. The Jones matrix characterizes each light-surface or light-matter interaction and can be used to trace the evolution of polarization along a ray path. To interpret the polarization aberration associated with a ray path, the Jones matrix can be divided into diattenuation, which is polarization dependent reflection or transmission, and retardance, which is polarization dependent *OPL* difference. These properties can be calculated from the Jones matrix²⁵ for each or a series of light-surface or light-matter interactions.

However, the Jones calculus has some problems simulating complex systems with high NA. It does not describe the change of direction of the light, only the polarization change from the transverse plane of an incident ray to the transverse plane of an exiting ray. The 2D nature of the Jones calculus becomes inconvenient for light propagating in 3D. For example, “horizontal” and “vertical” are insufficient to fully describe the polarization transformation in 3D. To use the Jones matrix in ray tracing, it is necessary to separately carry a set of incident and exiting local coordinate systems to define and specify the Jones matrix at every interaction. These local coordinates define the incident and exiting transverse planes relative to the global coordinate system in order to perform exact 3D ray trace. Chapter 3 shows how easily confusion can arise when using Jones matrices to describe simple interactions, such as normal reflection and transmission through a half-waveplate. Another polarization calculus, the Polarization Ray Tracing Calculus was recently developed to avoid the troublesome transformations between 2D and 3D during ray tracing, the polarization ray tracing calculus more succinctly represents the polarization evolution through optical systems in 3D. This calculus facilitates the polarization ray

tracing of light propagating in arbitrary directions. The polarization ray tracing calculus^{26,27,28,29} is explained in detail in Chapter 3. In the polarization ray tracing calculus, each polarization element is represented by a 3×3 polarization ray tracing (\mathbf{P}) matrix. These \mathbf{P} represents transformation of the 3×1 polarization vector (\mathbf{E}). \mathbf{P} also describes the changing ray direction directly in 3D. For system with many reflections or refractions which folds around in 3D, such as system with multiple fold mirrors shown in Figure 1.3, the polarization ray tracing calculus provides a straightforward method to handle the arbitrary propagations.

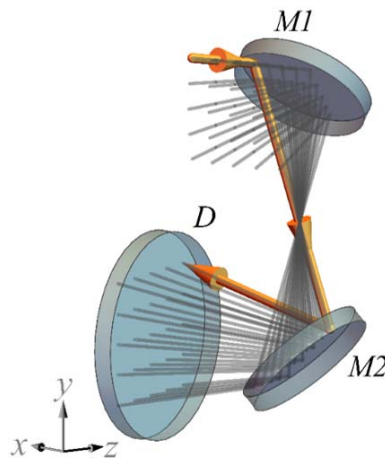


Figure 1.3 A skew ray (yellow) reflects from two fold mirrors, $M1$ and $M2$.

Similar to Jones matrices, the diattenuation and retardance properties of a ray can be calculated from the \mathbf{P} matrix. Since the \mathbf{P} matrix represents not only the physical change of the polarized light, but also the geometrical change of a ray path in 3D, the retardance calculated for ray paths from the \mathbf{P} matrix will be further divided into physical retardance and geometrical transformation as described in Chapter 4. The physical retardance results from polarization dependent variation of OPL . The geometrical transformation arises from the geometry of the ray path and mathematically takes the form of circular retardance. It is

a rotation of polarization state from the entrance space to the exit space of an optical system, similar to circular retardance, but no retardance is actually involved. This variation of geometrical transformation across the exit pupil is called the skew aberration^{6,30,31}.

This dissertation extends the established methods of polarization ray tracing to optical system with anisotropic materials. At each anisotropic interface, ray doubling occurs. An incident ray divides into orthogonal polarizations during refraction and reflection. These resultant polarizations propagate in different directions, follow different ray paths and experience different polarization changes through the optical system. The reflection and refraction of the polarized light at anisotropic interfaces will be described in Chapter 2. Then a ray tracing method through anisotropic materials using polarization ray tracing calculus will be shown in Chapter 3 and Chapter 4.

1.4 Motivation of ray tracing in anisotropic material

The light-surface interaction and light-matter interaction associated with the anisotropic materials are different from those associated with the isotropic materials. The exiting rays at anisotropic interface have properties depending on the direction and polarization state of the incident light. Also, the *OPL* associated with light propagation within anisotropic material is a function of polarization state. Anisotropic materials provide optical phenomena which cannot be generated by isotropic material, and are essential in many optical systems.

Uniaxial materials are the most common anisotropic materials. They are used as retarders, polarizing optical components which generate phase shift between polarization states. Uniaxial materials are also used to construct polarizers, which divide wavefronts

based on polarization and redirect these components into different directions. The special properties of uniaxial crystals were first described by Erasmus Bartholin who in 1669 discovered double refraction, as shown in Figure 1.4, when light transmitted through the crystal Iceland spar, which is one of the names for calcite³². In 1690, Christiaan Huygens developed his revolutionary wave optics theory which included a law of refraction for the extraordinary ray in calcite. E. L. Malus in 1808 described the image doubling through calcite in terms of polarized light and confirmed Huygens' extraordinary refraction result^{33,34}.



Figure 1.4 Imaging doubling through a piece of calcite.

Anisotropic materials have been used to make polarization components, such as polarizers, polarizing beam splitter, and retarders. The first polarizer made from a uniaxial material was the Nicol prism, invented in 1828 by William Nicol^{35,36}. Since then a series of high performance crystal polarizers have been developed, including the Glan-Foucault prism, the Glan-Thompson prism, and the Glan-Taylor prism^{37,38,39,40,41}. Another class of polarizing prisms are the beam splitting prisms which divide the wavefront into two different direction for the two polarization components; examples include the Rochon prism^{42,43} and the Wollaston prism⁴⁴. Multiple crystal waveplates are often cemented together to achieve achromatic^{45,46,47,48,49,50} and athermalized^{46,51,52,53} retarder performance.

The Lyot filter is another anisotropic component which utilizes many birefringent plates to produce a narrow bandpass filter. The Lyot filter can be modified to an electrically tunable filter by rotating plates or with the use of liquid crystals to tune the transmitted wavelength. Uniaxial plates are often used in optical cavities for laser tuning.

Anisotropic components play important roles in modern optical system and can be found in polarimeters, ellipsometers, interferometers, microscopes, medical imaging systems, projectors, display technologies and most other complex systems. For example, Figure 1.5 shows a differential interference contrast (DIC) microscope layout which contains two Wollaston prisms for dividing and recombining polarized wavefronts. DIC greatly enhances the contrast of (unstained) transparent specimens, because the image intensity is a function of the gradient of optical path length of the sample, and otherwise invisible effect.

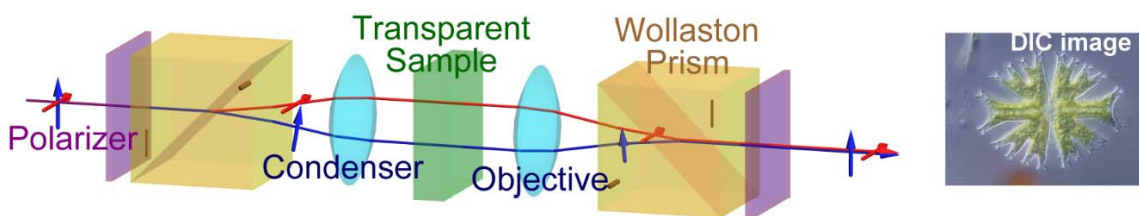


Figure 1.5 (Left) Basic setup of differential interference contrast (DIC) microscope and (right) a *Micrasterias furcata* imaged in transmitted DIC microscopy⁵⁴.

Polarized light is also used in ophthalmology for medical diagnostics, because retinal cell layers tend to have a regular structure which yields measurable differences in the magnitude and phase of polarized light upon interaction⁵⁵. The birefringence of the retinal Henle fibers (photoreceptor axons that go radially outward from the fovea) provides a reliable detection of strabismus and anisometric amblyopia⁵⁶. Also, the Laser

Diagnostics GDx (a scanning laser polarimeter) measures the birefringence of the optic nerve fiber layer which indirectly quantify its thickness, and is used in the assessment and monitoring of glaucoma.

Plastic lens are commonly used in consumer products, such as cell phone camera lenses and in CD and DVD pick up devices as shown in Figure 1.6. Plastic lenses are cheaper and easier to make compared to optical glass. However, plastic lenses suffer from greater stress induced birefringence from the injection molding manufacturing process. In the CD pick up system shown in Figure 1.6, any birefringence in the plastic pick up lens affects the size of the point image formed on the disk. Some stress will always be present in molded plastic lenses, so this stress induced birefringence needs to be carefully controlled in order to meet specifications and produce a sufficiently small image to accurately read the data stored on the disk.

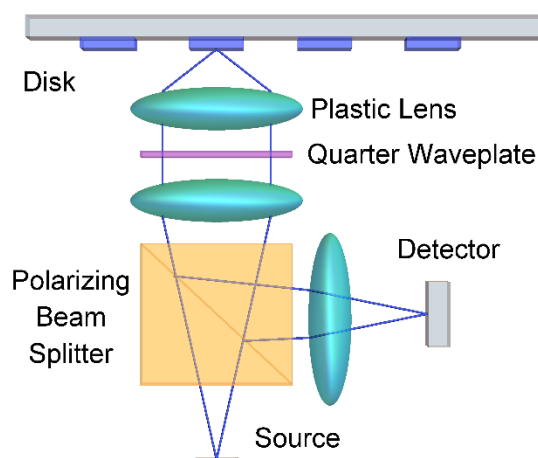


Figure 1.6 Optical layout of an optical pickups system in a CD player⁵⁷.

To maximize the field of view (FOV) of liquid crystal displays, multilayer biaxial thin films are used to enhance the desired contrast for off-axis viewing. As shown in Figure

1.7, the off-axis aberrations of the liquid crystal cell can be compensated by layers of biaxial films. The aberrations are corrected by matching pairs of LC cell layers and compensating film layers.

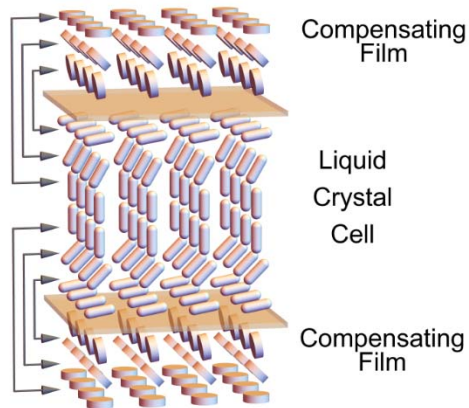


Figure 1.7 The off-axis aberration of the liquid crystal cell can be corrected by layers of compensating films. Layers connected by arrows compensate their variation of polarization with angle.

Many anisotropic optical systems have limited FOV. As the technology advanced, the anisotropic components are modified to incorporate larger FOV. To optimize the performance of these anisotropic components, accurate simulations are needed to calculate the on-axis and off-axis behaviors.

1.5 Ray tracing with anisotropic materials

Conventional ray tracing algorithm primarily calculates the *OPL* of a set of rays, the wavefront aberration, which is a scalar function. Polarization ray tracing algorithm calculates the amplitude, phase, *OPL* and polarization changes of a set of rays, which is a multi-dimensional calculation, an eight dimensional function if Jones matrices are used. The light-matter interaction (refraction or reflection) at anisotropic materials divides the incident ray into two eigenpolarizations or eigen-*modes* with distinct refractive indices and

mutually orthogonal polarizations propagating in two different directions. So polarization ray tracing through anisotropic materials results in multiple sets of exiting rays.

In optical ray trace, a ray with wavelength λ is launched in a direction specified by the Poynting vector \hat{S} (direction of energy) and its wavefront (constant phase) propagating in direction \hat{k} , and a ray segment begins. As the ray propagates within a material for a certain distance, light-matter interaction took place along this ray segment, and the *OPL* associated with the ray increases. As this ray encounters an optical surface, light-surface interaction occurs at the ray intercept. The interaction changes the direction, the polarization (amplitude, phase, and orientation), and the associated refractive index of the ray. Next a ray with the new ray parameters is launched and proceeds toward the next ray intercept. If the light-surface interaction involves anisotropic material, ray doubling might occur, then the interaction could produce two new ray segments in transmission or reflection. Table 1.1 and Table 1.2 list the ray parameters and material properties necessary to polarization ray trace through anisotropic materials. The directional properties of anisotropic materials are described by 3×3 tensors rather than the one refractive index in isotropic material.

Table 1.1 Ray parameters for polarization ray trace

Propagation vector:	$\hat{\mathbf{k}}$
Poynting vector:	$\hat{\mathbf{S}}$
Ray refractive index:	n
Electric field vector:	$\hat{\mathbf{E}}$
Magnetic field vector:	$\hat{\mathbf{H}}$
Electric field amplitude (reflection or refraction) coefficient:	a

Table 1.2 Parameters of anisotropic interface

Dielectric and gyrotropic tensor of incident medium:	$\boldsymbol{\varepsilon}_1$ and \mathbf{G}_1
Dielectric and gyrotropic tensor of exiting medium:	$\boldsymbol{\varepsilon}_2$ and \mathbf{G}_2
Surface normal:	$\hat{\boldsymbol{\eta}}$

Many researchers have published algorithms for calculating light-matter interactions with anisotropic materials. Ray tracing algorithms for uniaxial interface were published by Stavroudis⁵⁸, Swindell⁵⁹, Simon^{60,61}, Liang⁶², and Wang⁶³. Algorithms which include biaxial interfaces were developed by Zhang⁶⁴, Laudry⁶⁵, Chen⁶⁶, and Wang⁶⁷. A general algorithm for anisotropic interfaces handling homogeneous uniaxial, biaxial and optically active materials was developed by McClain^{68,69}. Since McClain's algorithm is developed with 3×1 vector electromagnetic fields, it interacts easily with the 3×3 \mathbf{P} matrix. This set of algorithm will be used as the basis for the anisotropic ray tracing extension to the polarization ray tracing calculus in Chapter 3.

To simulate the propagation of a wavefront through an optical systems, a large number of rays are traced to sample the shape, amplitude, and polarization over a wavefront. For each anisotropic element, one incident wavefront yields two exiting wavefronts in transmission. So a system with N anisotropic elements can have 2^N exiting wavefronts. Figure 1.8 shows two example grids of rays refracting through a biaxial and

uniaxial plates, splitting into two polarized wavefronts. Each of the wavefronts focuses at a different location, has different polarization state variation, and differing amounts of wavefront aberrations. The ray tracing result of these wavefronts are stored in the **P** matrices. Then the properties of these wavefronts, such as the wavefront aberrations, polarization aberrations including diattenuation and retardance, and the image quality are calculated from the **P** matrices.

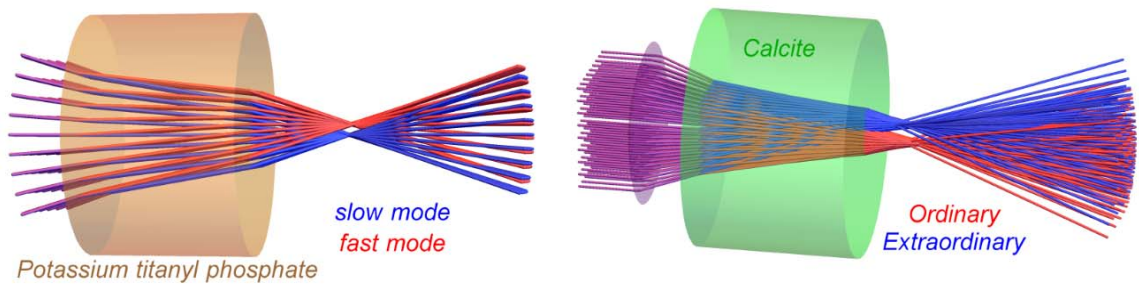


Figure 1.8 A converging beam converges through a biaxial KTP plate (left) and a uniaxial calcite plate (right). Due to ray doubling, two foci are observed, ordinary and extraordinary modes for the uniaxial plate, and fast and slow modes for the biaxial case.

1.6 Image formation of polarized wavefronts

The image quality of an imaging system can be calculated by diffraction theory using the wavefront calculated by polarization ray tracing. This section outlines the generalization of the diffraction image formation algorithms from scalar diffraction to wavefronts with polarization aberrations by the vector extensions to diffraction theory. These calculations will be utilized in Chapter 6 and Chapter 8 to evaluate the point spread functions and the image polarizations of optical systems with anisotropic materials.

Consider a point object imaged through an optical system to a point image, as shown Figure 1.9 (left). The incident spherical wavefront is simulated by a grid of rays. These incident rays are traced to the image point, or for system with aberrations, the rays

are traced to the best focus which could be where the exiting beam has the smallest RMS spot (Appendix A).

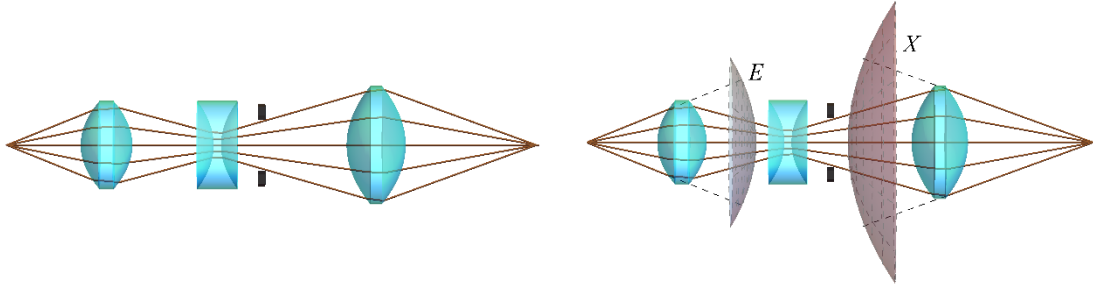


Figure 1.9 (Left) A point object is imaged through an optical system to a point image. (Right) The entrance pupil (E) of the system is the image of the stop in the object space, so it is the spherical surface (gray surface on the left) centered at the object point. Similarly the exit pupil (X) of the system is the image of the stop in the image space; a spherical surface (gray surface on the right) centered at the object space.

To evaluate the wavefront aberrations and their effect on image quality, the ray trace calculates the *OPLs* of the ray paths from the entrance pupil in the object space to the exit pupil in the image space (Figure 1.9 right). These pupils are used because the light fields have well defined edges with nearly constant and slowly varying electric fields. Any surfaces other than the pupils will have large amplitude oscillation due to Fresnel diffraction. Therefore, the image quality of the lens is best evaluated by using ray tracing from the entrance to exit pupil, then by diffraction theory from the exit pupil to the image.

Conventional wavefront aberration $W(\rho, \varphi)$ is a scalar function describing the distribution of *OPL* across the exit pupil,

$$e^{i \frac{2\pi}{\lambda} W(\rho, \varphi)}, \quad (1.1)$$

where (ρ, φ) are polar coordinate for the exit pupil. An ideal wavefront with zero aberration has constant *OPL*, and produces an ideal Airy disk image. This scalar aberration function

needs to be generalized to an aberration matrix for representing the phase, amplitude, and polarization change of polarized states.

Using the polarization ray tracing method in this dissertation, the wavefront at the exit pupil is also described by a grid of \mathbf{P} matrices. The light-surface and light-matter interactions for each ray are combined in an overall \mathbf{P} matrix which contains: (1) the phase of light propagation, which is the *OPL* in the traditional geometrical ray trace, and (2) the phase and amplitude change due to light-surface interactions, calculated from the Fresnel equations for uncoated isotropic interface or the thin film equations for coated surface. The calculations of the end-to-end \mathbf{P} matrix for homogeneous anisotropic materials will be described in Chapter 3 and Chapter 4.

Although it is advantageous to perform the ray trace using 3D algorithms, it is also useful to analysis the wavefront and polarization aberrations on two dimensional surfaces (the surface transverse to the grid of exiting rays). To do this, the grid of \mathbf{P} matrices cumulated at the exit pupil are converted into a Jones pupil representation $\mathbf{J}_{\text{pupil}}$, a grid of Jones matrices defined on a pair of spherical surfaces at the entrance and exit pupils^{12,13},

$$\begin{aligned}
 \mathbf{J}_{\text{pupil}}(r) &= \begin{pmatrix} J_{xx}(r) & J_{yx}(r) \\ J_{xy}(r) & J_{yy}(r) \end{pmatrix} \\
 &= \begin{pmatrix} j_{xx}(r) & j_{yx}(r) \\ j_{xy}(r) & j_{yy}(r) \end{pmatrix} e^{i\frac{2\pi}{\lambda}OPL(r)} \quad , \\
 &= \begin{pmatrix} A_{xx}(r)e^{i\phi_{xx}(r)} & A_{yx}(r)e^{i\phi_{yx}(r)} \\ A_{xy}(r)e^{i\phi_{xy}(r)} & A_{yy}(r)e^{i\phi_{yy}(r)} \end{pmatrix}
 \end{aligned} \tag{1.2}$$

where r is the pupil coordinate. In the conversion from \mathbf{P} to $\mathbf{J}_{\text{pupil}}$, a set of local coordinate systems need to be defined for the Jones matrices. Two common sets of local coordinate systems for spherical wavefronts are shown in Appendix B.

The Jones pupil represents the variations of polarization coupling from the incident wavefront to the exiting wavefront across the exit pupil for any set of incident polarized light. It represents the polarization couplings of two orthogonal incident states (x, y) to two orthogonal exiting states (x', y') in the form of a 2×2 matrix: $\begin{pmatrix} x \rightarrow x' & y \rightarrow x' \\ x \rightarrow y' & y \rightarrow y' \end{pmatrix}$. Each of the J_{xx} describes the couplings of x -polarized incident light to x -polarized exiting light, and J_{xy} describes the x -polarized incident light couples to y -polarized exiting light. These x - and y -polarized basis states are defined in the local coordinate system of the incident and exiting wavefronts.

When the optical system involves anisotropic materials, ray doubling occurs and results in multiple polarized wavefronts represented by multiple Jones pupils. Each of them contains different polarization and wavefront aberrations. In the example shown in Figure 1.8, two $\mathbf{J}_{\text{pupil}}$ are needed to represent the two exiting wavefronts. The algorithms for combining these wavefronts are presented in Chapter 5.

<p>⟨Coherent imaging⟩</p> $pupil = P$ $\downarrow \mathfrak{F}$ $cPSF = h = \mathfrak{F}[P]_{\xi=\frac{x}{\lambda f}}$ $\downarrow \mathfrak{F}$ $CTF = \frac{\mathfrak{F}[h]}{ \mathfrak{F}[h] } = H \propto P$	<p>⟨Incoherent imaging⟩</p> $pupil = P$ $\downarrow \mathfrak{F}$ $iPSF = cPSF ^2 = h ^2 = \left \mathfrak{F}[P]_{\xi=\frac{x}{\lambda f}} \right ^2$ $\downarrow \mathfrak{F}$ $OTF = \frac{\mathfrak{F}[h ^2]}{ \mathfrak{F}[h ^2] } = H \star H^*$ $= MTF \exp(iPTF)$
--	---

Figure 1.10 Flow charts for coherent and incoherent imaging calculations. The pupil function P represents the wavefront function at the exit pupil of an optical system. The spatial variable of the system is x ; the wavelength of light is λ ; the focal length of the imaging system is f . The coherent point spread function is $cPSF$; the coherent transfer function is CTF ; the incoherent point spread function is $iPSF$; the optical transfer function is OTF ; the modulation transfer function is MTF ; and the phase transfer function is PTF . \mathfrak{F} is the Fourier transform operation. \star is the auto-correlation operation.

⟨Imaging polarized light⟩

$$Jones\ pupil = \mathbf{J}_{pupil}$$

$$\downarrow \mathfrak{F}$$

$$\mathbf{ARM} = \mathfrak{F}[\mathbf{J}_{pupil}] \rightarrow \mathbf{MPSM}$$

$$\downarrow \mathfrak{F}$$

$$\mathbf{OTM} = \mathbf{MTM} \exp(i\mathbf{PTM})$$

Figure 1.11 The imaging calculation for polarized light. The 2×2 amplitude response matrix is the **ARM**; the 4×4 Mueller point spread matrix is the **MPSM**; the 4×4 optical transfer matrix is the **OTM**; the 4×4 modulation transfer matrix is the **MTM**; and the 4×4 phase transfer matrix is the **PTM**.

The flow charts of the algorithms for coherent and incoherent imaging of scalar waves, and for the imaging of system with polarization aberrations are compared in Figure 1.10 and Figure 1.11. In conventional optics, the amplitude response function at the image is the Fourier transform of the pupil function. To incorporate polarization aberration, the amplitude response function is generalized to the amplitude response matrix **ARM**, which

is the impulse response of the Jones pupil to coherent light, the 2×2 Fourier transform (\mathfrak{F}) of $\mathbf{J}_{\text{pupil}}(r)$,

$$\mathbf{ARM}(r') = \begin{pmatrix} ARM_{xx}(r') & ARM_{yx}(r') \\ ARM_{xy}(r') & ARM_{yy}(r') \end{pmatrix} = \begin{pmatrix} \mathfrak{F}[J_{xx}(r)] & \mathfrak{F}[J_{yx}(r)] \\ \mathfrak{F}[J_{xy}(r)] & \mathfrak{F}[J_{yy}(r)] \end{pmatrix}, \quad (1.3)$$

where r' is the image plane coordinate. From the grid of ray parameters, the **ARM** is calculated by discrete Fourier transform from the Jones pupil. Each component of the $\mathbf{J}_{\text{pupil}}$ is a 2D array of electric field values cumulated at the pupil, and each component of the **ARM** is a 2D array characterizing the impulse response at the image plane. For coherent imaging, an x -polarized incident illumination produces an image with an x -polarized $\mathfrak{F}[J_{xx}(r)]$ and a y -polarized $\mathfrak{F}[J_{xy}(r)]$ amplitude response functions. The corresponding intensity point spread function is $|\mathfrak{F}[J_{xx}]|^2 + |\mathfrak{F}[J_{xy}]|^2$, which can also be calculated with the Mueller point spread matrix **MPSM**, demonstrated in Chapter 6.

For a point object imaged through an optical system with N anisotropic interfaces, there are 2^N wavefronts, and thus 2^N component of **ARMs**. Each of these wavefronts is ray traced separately. When their resultant **ARMs** overlap, they are combined. There are two ways to calculate the resultant image for anisotropic systems: (1) Combine the wavefronts in equation (1.2), then the total impulse response is calculated as in equation (1.3). Or, (2) keep the Jones pupils of each polarized wavefronts separate from each other, then calculate their impulse response separately using equation (1.3). These separate responses reside on top of each other. So, the total response will be the summation of the separated **ARMs**. Both of these routes give the same resultant **ARM**. For incoherent light or partially

polarized and unpolarized light source, the **ARM** is converted to 4×4 Mueller point spread matrix **MPSM**, which is done in the same fashion as converting a Jones matrix to a Mueller matrix⁷⁰. Then the image of an incoherent point source specified by a set of four Stokes parameters is calculated by matrix multiplying the Stokes parameters to the **MPSM**, yielding the image of the point spread function in the form of Stokes parameters.

1.7 Conclusions

This chapter provides an overview of performing polarization ray tracing through isotropic and anisotropic materials using 3D polarization ray tracing calculus^{71,72}. Using the ray tracing results, the polarization aberrations can be studied at individual optical surface, and also for a series of optical surfaces. This dissertation extends the polarization ray tracing calculation to optical system with anisotropic materials. Due to the ray doubling behavior of the anisotropic materials, the algorithm for polarization ray tracing is further generalized to handle the exponentially increasing number of ray segments as the number of anisotropic elements increased.

The image quality of an imaging system with anisotropic materials is calculated by diffraction theory from the polarization ray tracing result. In this dissertation, the diffraction image formation of the multiple polarization-aberrated beams is handled by the vector extensions to diffraction theory^{12,13,73,74,75,76} which was discussed in section 1.6. Then the image quality is evaluated by the polarization impulse response function and the polarization point spread function.

The modeling method provided in this dissertation can assist optical designers and engineers to accurately simulate the performance of optical systems with anisotropic

components, to gain insight of polarization variations through the system, to perform tolerance, and to improve the overall image quality^{14,15,77}.

CHAPTER 2 BASICS OF ANISOTROPIC RAY TRACING

2.1 Description of electromagnetic wave

Light is a transverse electromagnetic wave, an oscillating electric and magnetic field propagating at the speed of light $c=3\times 10^8 m/s$ in vacuum. It is characterized by its electric field \mathbf{E} , its magnetic field \mathbf{H} , its displacement field \mathbf{D} , and its induction field \mathbf{B} by Maxwell's equations⁹. The electromagnetic fields of a monochromatic plane wave in space \mathbf{r} and time t with wavelength λ are

$$\begin{aligned}\mathbf{E}(\mathbf{r},t) &= \mathcal{Re} \left\{ \mathbf{E} \exp \left[i \left(\frac{2\pi n}{\lambda} \hat{\mathbf{k}} \cdot \mathbf{r} - \omega t \right) \right] \right\}, \\ \mathbf{H}(\mathbf{r},t) &= \mathcal{Re} \left\{ \mathbf{H} \exp \left[i \left(\frac{2\pi n}{\lambda} \hat{\mathbf{k}} \cdot \mathbf{r} - \omega t \right) \right] \right\}, \\ \mathbf{D}(\mathbf{r},t) &= \mathcal{Re} \left\{ \mathbf{D} \exp \left[i \left(\frac{2\pi n}{\lambda} \hat{\mathbf{k}} \cdot \mathbf{r} - \omega t \right) \right] \right\}, \text{ and} \\ \mathbf{B}(\mathbf{r},t) &= \mathcal{Re} \left\{ \mathbf{B} \exp \left[i \left(\frac{2\pi n}{\lambda} \hat{\mathbf{k}} \cdot \mathbf{r} - \omega t \right) \right] \right\}.\end{aligned}\tag{2.1}$$

The propagation vector in a medium with refractive index n is $\mathbf{k} = \frac{2\pi n}{\lambda} \hat{\mathbf{k}}$. In an absorptive material, the complex refractive index is $n+i\kappa$, so the magnitude of the fields decay exponentially as light propagates. The angular frequency of the light is ω with unit rad/s, which is equivalent to $2\pi\nu$ where ν is the frequency in Hz.

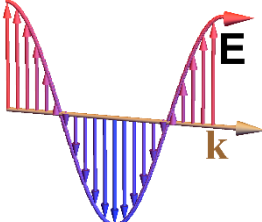

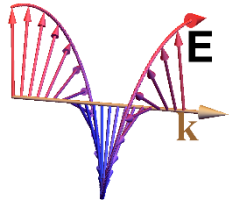
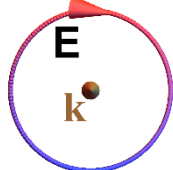
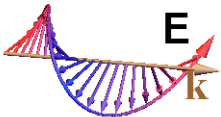
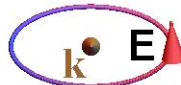
The polarization vector is a 3×1 vector defined as

$$\mathbf{E} = E_o e^{i\phi_o} \hat{\mathbf{E}} = E_o e^{i\phi_o} \begin{pmatrix} E_x \\ E_y \\ E_z \end{pmatrix} = E_o e^{i\phi_o} \begin{pmatrix} |E_x| e^{i\phi_x} \\ |E_y| e^{i\phi_y} \\ |E_z| e^{i\phi_z} \end{pmatrix}\tag{2.2}$$

which describes the polarization states in 3D. The field has an absolute complex magnitude $E_0 e^{i\phi_x}$ and complex components (E_x, E_y, E_z) , where $\hat{\mathbf{E}} \cdot \hat{\mathbf{E}}^* = |E_x|^2 + |E_y|^2 + |E_z|^2 = 1$.

Table 2.1 shows electric field oscillations in time for three example polarization vectors.

Table 2.1 Polarization ellipses evolving in time for three polarization vectors.

Polarization vector	Viewing \mathbf{E} propagating in time	Viewing \mathbf{E} towards \mathbf{k}	
$\mathbf{E} = \begin{pmatrix} 1 \\ 0 \\ 0 \end{pmatrix}$			Linear polarization
$\mathbf{E} = \begin{pmatrix} i \\ 1 \\ 0 \end{pmatrix}$			Right circular polarization (evolving clockwise in time as one looks into the beam)
$\mathbf{E} = \begin{pmatrix} 1 \\ 0.5i \\ 0 \end{pmatrix}$			Left Elliptical polarization (evolving counter-clockwise in time as one looks into the beam)

2.2 Definition of anisotropic materials

The types of anisotropic materials treated in this chapter are uncoated homogeneous biaxial, uniaxial, and optically active materials. Each of these anisotropic materials is

described by a dielectric tensor $\boldsymbol{\varepsilon}$ and a gyrotropic tensor \mathbf{G} . The gyrotropic tensor is zero for biaxial and uniaxial materials and non-zero for optically active materials.

The dielectric tensor $\boldsymbol{\varepsilon}$ relates the variation of refractive index with the light's polarization state by relating \mathbf{E} to \mathbf{D} as^{78,79}

$$\mathbf{D} = \boldsymbol{\varepsilon} \mathbf{E} = \begin{pmatrix} D_x \\ D_y \\ D_z \end{pmatrix} = \begin{pmatrix} \varepsilon_{XX} & \varepsilon_{XY} & \varepsilon_{XZ} \\ \varepsilon_{YX} & \varepsilon_{YY} & \varepsilon_{YZ} \\ \varepsilon_{ZX} & \varepsilon_{ZY} & \varepsilon_{ZZ} \end{pmatrix} \begin{pmatrix} E_x \\ E_y \\ E_z \end{pmatrix}. \quad (2.3)$$

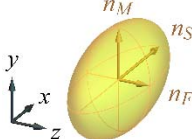
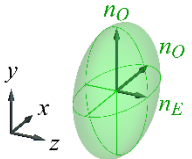
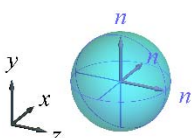
When an \mathbf{E} field is applied to a crystal, the response of the material depends on the atomic configuration of the crystal. Under the influence of the light field, the charges respond and contribute to the \mathbf{E} field. The result is the \mathbf{D} field which includes the light's field and a contribution from dipoles induced in the material. This relationship is described by the 3×3 dielectric tensor.

The tensor $\boldsymbol{\varepsilon}$ can always be rotated into a diagonal form,

$$\boldsymbol{\varepsilon}_{\mathbf{D}} = \begin{pmatrix} \varepsilon_X & 0 & 0 \\ 0 & \varepsilon_Y & 0 \\ 0 & 0 & \varepsilon_Z \end{pmatrix} = \begin{pmatrix} (n_X + i\kappa_X)^2 & 0 & 0 \\ 0 & (n_Y + i\kappa_Y)^2 & 0 \\ 0 & 0 & (n_Z + i\kappa_Z)^2 \end{pmatrix} \quad (2.4)$$

where n_X , n_Y , and n_Z (capital subscripts) are the principal refractive indices associated with three orthogonal principal axes or crystal axes (CA) and κ_X , κ_Y and κ_Z are the associated absorption coefficients along those three axes. Table 2.2 shows $\boldsymbol{\varepsilon}_{\mathbf{D}}$ of isotropic, uniaxial and biaxial materials with their principal axes aligned with the xyz axes of a global coordinate system.

Table 2.2 Properties of biaxial, uniaxial and isotropic materials when the principal axes are aligned with the global coordinate system. (Yellow) The biaxial crystal has principal refractive indices n_S , n_M , and n_F . (Green) The uniaxial crystal has principal refractive indices n_O and n_E . (Blue) The isotropic material has one refractive index n .

Material	Principal Label	Principal Refractive index	Diagonal Dielectric Tensor ϵ_D
Biaxial	<i>Slow</i>	(n_S, n_M, n_F) 	$\begin{pmatrix} \epsilon_S & 0 & 0 \\ 0 & \epsilon_M & 0 \\ 0 & 0 & \epsilon_F \end{pmatrix} = \begin{pmatrix} n_S^2 & 0 & 0 \\ 0 & n_M^2 & 0 \\ 0 & 0 & n_F^2 \end{pmatrix}$
	<i>Medium</i>		
	<i>Fast</i>		
Uniaxial	<i>Ordinary</i>	(n_O, n_E) 	$\begin{pmatrix} \epsilon_O & 0 & 0 \\ 0 & \epsilon_O & 0 \\ 0 & 0 & \epsilon_E \end{pmatrix} = \begin{pmatrix} n_O^2 & 0 & 0 \\ 0 & n_O^2 & 0 \\ 0 & 0 & n_E^2 \end{pmatrix}$
	<i>Extraordinary</i>		
Isotropic	<i>Isotropic</i>	n 	$\begin{pmatrix} \epsilon & 0 & 0 \\ 0 & \epsilon & 0 \\ 0 & 0 & \epsilon \end{pmatrix} = \begin{pmatrix} n^2 & 0 & 0 \\ 0 & n^2 & 0 \\ 0 & 0 & n^2 \end{pmatrix}$

Biaxial materials, such as mica and topaz, have three different principal refractive indices — n_S for the largest index, n_M , and n_F for the smallest index. The refractive index experienced by the light varies with the direction of the light's electric field, not its propagation direction. Uniaxial materials, such as calcite and rutile, have two equal principal refractive indices n_O as the principal ordinary index, and n_E as the principal extraordinary index, as shown in Figure 2.1. By definition a negative uniaxial crystal, such as calcite, has $n_O > n_E$ while a positive uniaxial crystal has $n_O < n_E$. An isotropic material can be considered a special case of an anisotropic material with $\epsilon_X = \epsilon_Y = \epsilon_Z = \epsilon$. Optical glasses are isotropic, as are air, water, and vacuum. The dielectric tensor of an isotropic material is proportional to the identity matrix; light experiences the same refractive index

n regardless of propagation direction and polarization state. Materials also become anisotropic due to stress, strain, or applied electric or magnetic fields.

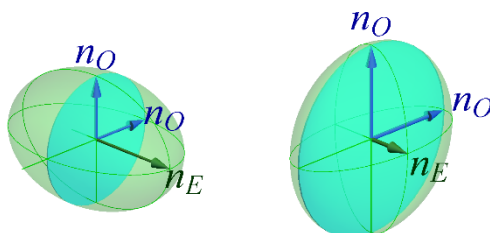


Figure 2.1 (Left) Principal axes for positive uniaxial material where $n_E > n_O$. (Right) Principal axes for negative uniaxial material where $n_E < n_O$.

The refractive index experienced by a light ray depends on its electric field orientation relative to the principal axes of the material. Light linearly polarized with its electric field along each of the three principal axes is depicted in Figure 2.2, which shows that the refractive index of the light depends on its polarization, not the direction of propagation. The refractive index characterizes how strongly the electrons in a material oscillate in response to an electromagnetic wave, and governs how fast the ray propagates.⁸⁰

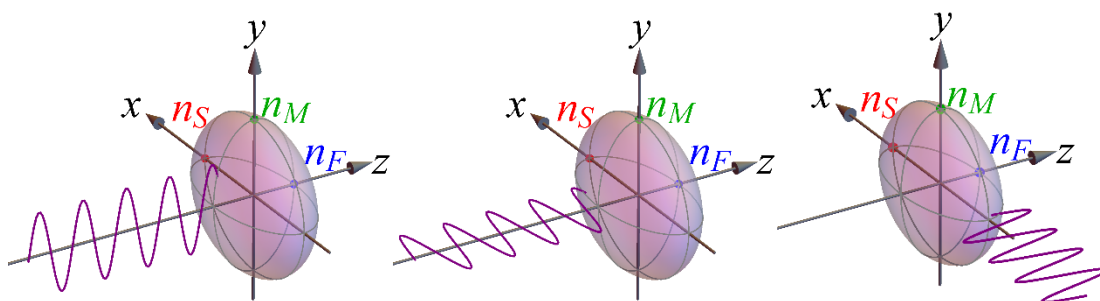


Figure 2.2 (Left) Light propagating along z and polarized along x experiences the refractive index n_s . (Middle) Light propagating along z and polarized along y experiences refractive index n_M . (Right) Light propagating along x and polarized along z experiences refractive index n_F . Thus the refractive index depends on the light polarization, not the direction of propagation.

An optic axis of an anisotropic material is a direction of propagation in which the light experiences zero birefringence. When light propagates along the optic axis, the refractive index is the same for all the \mathbf{E} field components in the transverse plane. Uniaxial materials, including crystallized minerals in the tetragonal, hexagonal, and trigonal crystal systems⁷⁸, have a single optic axis, hence the name uniaxial. Inside the crystal, the response of the material to the light field oscillation depends on the field orientation relative to the different chemical bonds. In a uniaxial calcite crystal CaCO_3 , all the calcium-carbon bonds are oriented in one direction, which is the extraordinary principal axis. The three carbon-oxygen bonds in the carbonate radical are oriented in the perpendicular plane, shown in Figure 2.3. The response of the ionic calcium-carbon bond to the \mathbf{E} field is dissimilar to the response of the covalent bonds in the carbonate group. Therefore driving charges along the calcium-carbon bond generates a different refractive index than driving charges in the plane of the carbonate bonds. When light propagates along the extraordinary principal axis of uniaxial calcite, the electric field components in the transverse plane with the three-fold symmetry of the carbon oxygen bonds can only experience the ordinary refractive index n_o ; the two eigenmodes are degenerate. Therefore, the optic axis of a uniaxial material is the extraordinary principal axis.

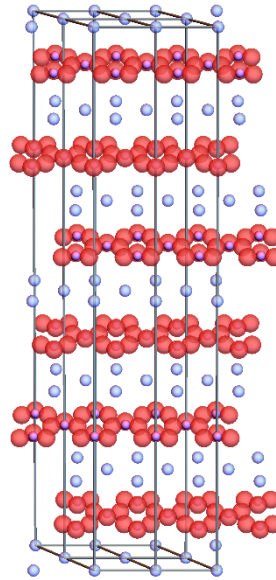


Figure 2.3 Calcite CaCO_3 crystal structure with the vertical optic axis, connecting the calcium (blue) and carbon (purple) atoms.

On the other hand, a biaxial material has three distinct principal indices, and there are four directions along two axes within the material having degenerate eigenpolarizations, as is explained in section 2.4. So, unlike a uniaxial material, a biaxial material has two optic axes.

The birefringence Δn is the refractive index difference between two eigenpolarizations propagating the same direction in an anisotropic material. The maximum birefringence of various biaxial and uniaxial material, $n_S - n_F$ and $n_E - n_O$, as a function of wavelength are shown in Figure 2.4, Figure 2.5 and Figure 2.6^{81,82,83,84,85,86}.

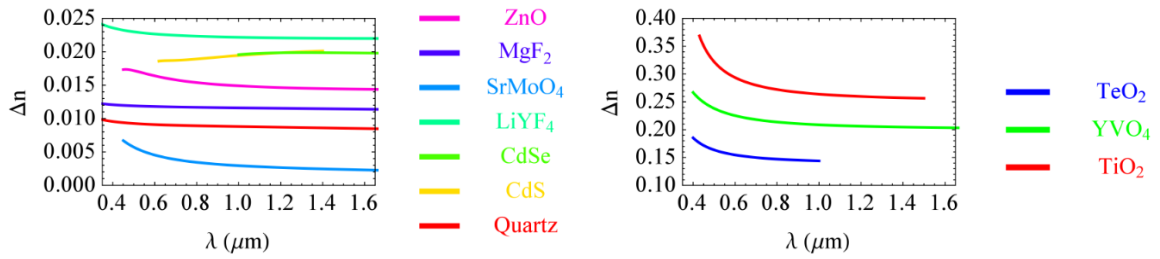


Figure 2.4 Birefringence spectra of common positive uniaxial materials.

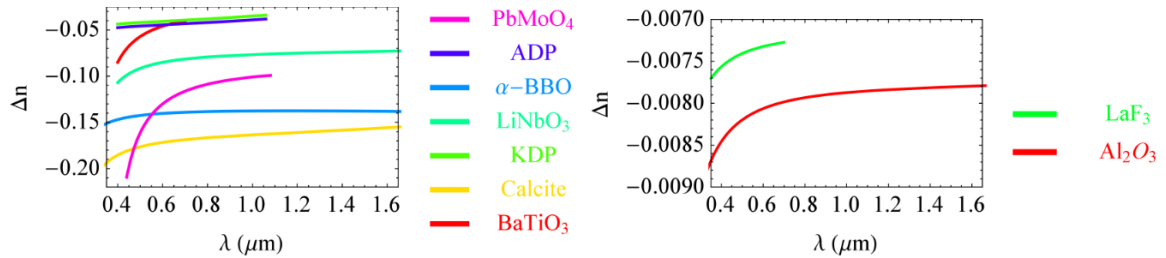


Figure 2.5 Birefringence spectra of common negative uniaxial materials.

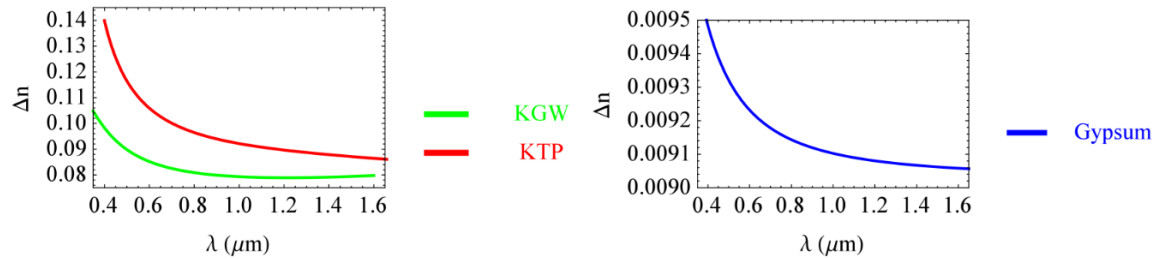


Figure 2.6 Birefringence spectra of common biaxial materials.

Optically active materials have a molecular structure that induces a rotation of the plane of the \mathbf{E} field oscillations as light passes through the material. The effect of optical activity is described by the gyrotropic tensor \mathbf{G} in the constitutive relation,

$$\mathbf{D} = \boldsymbol{\varepsilon} \mathbf{E} + i \mathbf{G} \mathbf{H} \quad \text{and} \quad \mathbf{B} = \boldsymbol{\mu} \mathbf{H} - i \mathbf{G} \mathbf{E}, \quad (2.5)$$

where $\boldsymbol{\mu}$ is the magnetic permeability tensor^{9,87}. Organic liquids such as glucose and sucrose solutions are common examples of isotropic optically active liquids which induce birefringence, or a phase shift between left and right circularly polarized light. The two

circularly polarized eigenmodes have slightly different refractive indices n_R and n_L . Thus optical activity is a source of circular birefringence. The difference between these two indices is often characterized by the optical rotatory power α which is related to the gyrotropic constant g ,

$$\alpha = \frac{2\pi}{\lambda} g = \frac{\pi}{\lambda} |n_R - n_L|. \quad (2.6)$$

The corresponding gyrotropic tensor \mathbf{G} for an optically active liquid is a diagonal tensor,

$$\mathbf{G} = \begin{pmatrix} g & 0 & 0 \\ 0 & g & 0 \\ 0 & 0 & g \end{pmatrix}. \quad (2.7)$$

In general, \mathbf{G} is a symmetric tensor with 6 independent coefficients,

$$\mathbf{G} = \begin{pmatrix} g_{11} & g_{12} & g_{13} \\ g_{12} & g_{22} & g_{23} \\ g_{13} & g_{23} & g_{33} \end{pmatrix}. \quad (2.8)$$

The majority of biaxial and uniaxial materials have no optical activity, so the gyrotropic tensor is zero. A few crystals combine uniaxial or biaxial properties with optical activity, such as Mercury Sulfide. In general, molecules which lack mirror symmetry are optically active, i.e. a molecule which cannot be superposed on its mirror image, such as left shoe and right shoe.

Crystalline quartz has both uniaxial and optically active characteristics. In quartz, the optical activity is only significant when the light propagates near the uniaxial optic axis, so \mathbf{G} for quartz has two dependent values⁶⁹,

$$\mathbf{G} = \begin{pmatrix} g_O & 0 & 0 \\ 0 & g_O & 0 \\ 0 & 0 & g_E \end{pmatrix}, \quad (2.9)$$

where $g_O = \frac{1}{2} (n_R - n_L) = 3 \times 10^{-5}$ and $g_E = -1.92g_O$ at 589nm.

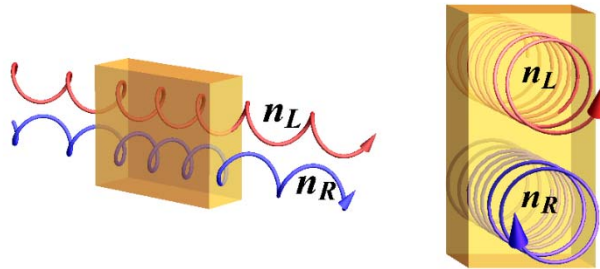


Figure 2.7 The side and front view of the left (red) and right (blue) circularly polarized electric field propagating through an optically active material. The left circularly polarized beam propagates for three wavelengths and the right circularly polarized beam propagates for three and a half wavelengths through the material yielding one half wave of circular retardance.

A schematic of the electric field for the two circularly polarized modes propagating in an optically active material are shown in Figure 2.7. When linearly polarized light passes through the optically active material, its plane of polarization rotates steadily through the medium, as shown in Figure 2.8, and it exits the material with rotated orientation but still linearly polarized.

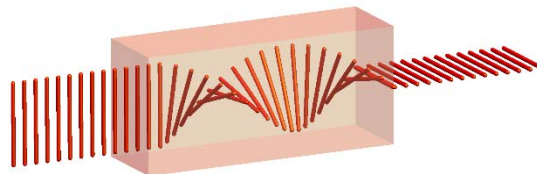


Figure 2.8 The plane of polarization of linearly polarized light rotates at a uniform rate when propagating in an optically active medium. This one-and-a-half wave circular retarder generates 270° of optical rotation.

For a system defined in global xyz coordinates, the principal axes of an anisotropic component do not need to align with the axes. The non-diagonal dielectric and gyrotropic tensors of the anisotropic component are calculated by matrix rotation of the diagonal tensor. For principal refractive indices (n_A, n_B, n_C) with principal axis orientations specified by unit vectors $(\mathbf{v}_A, \mathbf{v}_B, \mathbf{v}_C)$, the dielectric tensor is

$$\boldsymbol{\varepsilon} = \begin{pmatrix} v_{Ax} & v_{Bx} & v_{Cx} \\ v_{Ay} & v_{By} & v_{Cy} \\ v_{Az} & v_{Bz} & v_{Cz} \end{pmatrix} \cdot \begin{pmatrix} n_A^2 & 0 & 0 \\ 0 & n_B^2 & 0 \\ 0 & 0 & n_C^2 \end{pmatrix} \cdot \begin{pmatrix} v_{Ax} & v_{Bx} & v_{Cx} \\ v_{Ay} & v_{By} & v_{Cy} \\ v_{Az} & v_{Bz} & v_{Cz} \end{pmatrix}^{-1}. \quad (2.10)$$

2.3 Eigen polarizations in anisotropic materials

Ray tracing through anisotropic materials results in multiple rays with different polarizations. Within anisotropic materials, only certain polarization states can propagate in a given direction without change of polarization. These polarization states are the eigenpolarizations or *eigen-modes*. When light refracts into an anisotropic material, its energy divides into orthogonally polarized eigenmodes in a process of double refraction or ray splitting. An example of this ray splitting is Figure 2.9 showing the image of the text “POLARIS” seen through a calcite crystal. The two images have orthogonally linear polarization states, so either image can be selected by rotating a linear polarizer in front of the crystal.

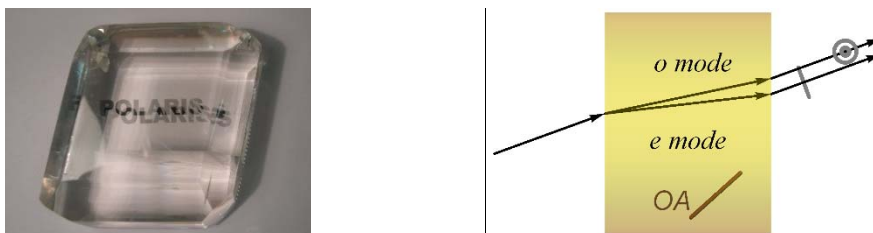


Figure 2.9 (Left) Double refraction through a calcite rhomb. (Right) A schematic of a ray splitting into two modes through a uniaxial plate. The optic axis (OA) shown is 45° from vertical. The gray line indicates a polarization state in the plane of the page, which is the extraordinary e -mode in this case. The gray dot indicates a polarization state out of the page, which is the ordinary o -mode in this example.

The direction of image doubling rotates as the crystal rotates, since the principal section is fixed with the crystal. As the crystal rotates, the principal section also rotates; the ordinary mode image remains fixed while the extraordinary mode image rotates around the ordinary image.

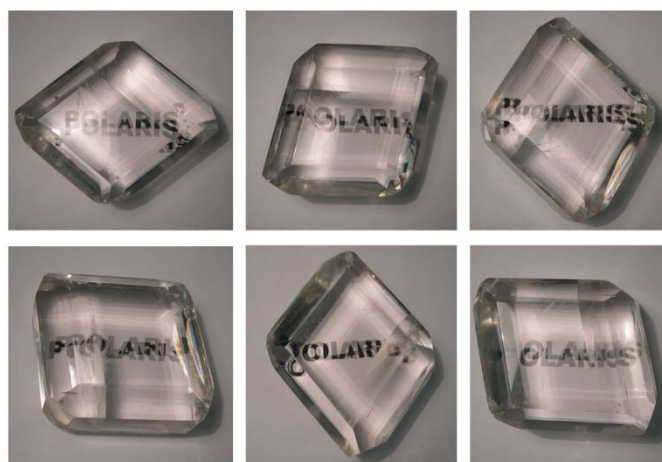


Figure 2.10 Double refraction through a calcite rhomb. When rotating the calcite, the ordinary image stays fixed while the extraordinary image rotates around it.

Figure 2.9 (right) shows the schematic of a ray refracting into a uniaxial plate in the principal section of the crystal, which is the plane of ray splitting. The two resultant eigenmodes are the ordinary o -mode and the extraordinary e -mode. The refractive indices associated with these two modes are n_o and n_e . The lower case subscripts are associated

with the ray refractive indices as opposed to the upper case subscripts for the principal refractive indices of the material. Light polarized orthogonal to the optic axis, for example in the carbonate plane of calcite, is the *o*-mode and has an ordinary refractive index n_o which is always equal to the material principal refractive index n_o . The *e*-mode is polarized perpendicular to the *o*-mode, in a plane containing the optic axis, and experiences the extraordinary refractive index n_e which has a value between n_E and n_o . The birefringence of a ray in a uniaxial material is the refractive index difference between these two modes, $n_e - n_o$. Due to the refractive index difference, the two modes refract into the anisotropic material in different directions. The division of flux between these two modes is a function of the incident polarization state.

Consider a ray propagating through an example anisotropic system shown in Figure 2.11. A ray refracts from air into a biaxial KTP (Potassium titanyl phosphate, KTiOPO_4) crystal, where the light divides into two modes, labeled as *fast* (f_1) and *slow* (s_1), due to double refraction. The *fast*-mode has a lower refractive index while the *slow*-mode has a higher refractive index. These two modes then refract into another biaxial crystal, aragonite, which has different crystal axes than the KTP. The f_1 ray couples into two modes, f_2 and s_2 , and similarly the s_1 -mode couples into f_2 and s_2 -modes. The collective mode labels after propagating through KTP and Aragonite are *fast-fast* ($f_1 f_2$), *fast-slow* ($f_1 s_2$), *slow-fast* ($s_1 f_2$), and *slow-slow* ($s_1 s_2$). This ray doubling continues into the third biaxial crystal, mica. When the incident ray exits the three blocks of crystals, eight modes emerge as *fff*, *ffs*, *fsf*, *fss*, *sff*, *sfs*, *ssf*, and *sss*. Each *f* and *s* represent distinct electric field orientations along separate ray segments. The exiting polarization state and phase is found from the addition

(superposition) of eight waves. The optical path length, OPL , has eight different values for the eight partial waves, a term for the component waves derived from one incident wave.

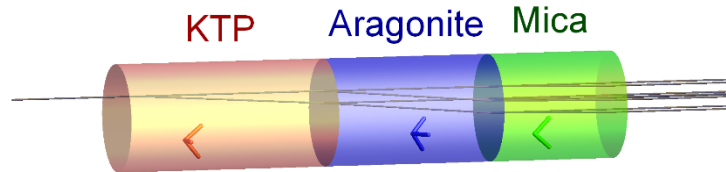


Figure 2.11 A normally incident ray propagates through three blocks of anisotropic materials (KTP, aragonite, and mica) each with different crystal axes orientations shown as three lines inside each block. One incident ray results in eight exiting rays due to three ray splitting interfaces, each with different sequences of polarizations and different OPL s.

The symbols indicating eigenmodes in different types of anisotropic material are listed in Table 2.3. When refracting into an isotropic material, both refracted modes (s - and p -states) share the same Poynting vector direction \hat{S} and propagation vector direction \hat{k} ; thus the transmitted modes are degenerate with the same refractive index. Similarly for the reflected modes. So, after refraction, the s - and p -modes are combined and treated as a single mode i , denoting an isotropic mode. In isotropic optically active materials, the two modes are the right circularly r and left circularly l polarized modes.

Table 2.3 Mode labeling for exiting rays in different types of anisotropic interfaces. The s - and p -polarizations in isotropic material have the same propagation directions and are grouped to one mode, *isotropic*.

Anisotropic material	Descriptions of eigenmodes	Mode Label
Biaxial	Mode with smaller n	f -mode; <i>fast</i> -mode
	Mode with larger n	s -mode; <i>slow</i> -mode
Uniaxial	Ordinary ray	o -mode
	Extraordinary ray	e -mode
Optically active	Left circularly polarized	l -mode; <i>left</i> -mode
	Right circularly polarized	r -mode; <i>right</i> -mode
Isotropic	Polarized in plane of incidence	p -polarization
	Polarized out of the plane of incidence	s -polarization
	Combined s - and p -states	i -mode
General anisotropic material		
Transmission	Transmitted rays	ta, tb
Reflection	Reflected rays	rc, rd

In general, ray doubling occurs each time a beam enters into or reflects toward a birefringent medium, unless the polarization is aligned exactly such that only one mode is excited with energy. An incident ray refracting through N anisotropic interfaces results in a potential of 2^N separate exiting rays with 2^N different mode sequences. Each of these modes takes a different path and has its own amplitude, polarization, and OPL . To retrieve the properties of each of these modes, a list of ray parameters, presented in Table 2.4, are calculated for each ray segment during the polarization ray trace through an optical system. Mode label is an additional ray parameter needed for tracking ray doubling at each birefringent interface. The collective mode label of a resultant ray at the exit pupil describes the evolution of polarization along that specific ray path. Polarization ray tracing a grid of incident rays emerging from an incident wavefront through N anisotropic surfaces produces

2^N separate wavefronts at the exit pupil. The exiting rays with the same mode label represent one of these wavefronts. By studying the properties of these rays at the exit pupil, one mode at a time, the wavefront aberrations (amplitude aberration, defocus, spherical aberration, coma, astigmatism, etc.) of each mode sequence can be analyzed and the effects of overlapping these wavefronts calculated.

Table 2.4 Ray tracing parameters to be calculated for each anisotropic ray intercept to characterize each exiting ray.

Parameter	Symbol
Coordinate of ray intercept	\mathbf{r}
Propagation vector	$\hat{\mathbf{k}}$
Poynting vector	$\hat{\mathbf{S}}$
Normal to surface	$\hat{\mathbf{n}}$
Mode label	$f, s, o, e, l, r, \text{ or } i$
Mode refractive index	$n_f, n_s, n_o, n_e, n_l, n_r, \text{ or } n$
Optical path length	OPL
Electric field vector or polarization vector	$\hat{\mathbf{E}}$
Magnetic field vector	$\hat{\mathbf{H}}$
Amplitude reflection or transmission coefficient	a
Polarization ray tracing matrix for a ray intercept	\mathbf{P}
Geometrical transformation for a ray intercept	\mathbf{Q}

2.4 Refraction and reflections at anisotropic interface

When light strikes an optical interface, part of its energy refracts and part reflects. At an anisotropic intercept, the energy of the light divides into eigenmodes. The division of energy and the exiting ray parameters shown in Table 2.4 are calculated from the incident ray parameters, and the material properties before and after the interface. The algorithms to calculate the exiting ray parameters for polarization ray tracing in refraction and reflection for each exiting modes at an anisotropic intercept are described in this section.

These resultant ray parameters will be used in Chapter 3 to calculate their polarization ray tracing matrices, \mathbf{P} , which represent polarization properties of one or a series of ray intercepts. The type of uncoated anisotropic interfaces described in this section include isotropic/anisotropic, anisotropic/isotropic, and anisotropic/anisotropic interfaces. Depending on the type of the interface, the number of exiting rays varies. The resultant fields behave differently, but the calculations are similar and can be generalized.

The four combinations of isotropic and anisotropic interfaces along with the corresponding ray splitting configurations are depicted in Figure 2.12⁶⁹. The incident, refracted, and reflected ray parameters are distinguished by their subscripts *inc*, *t*, and *r* respectively.

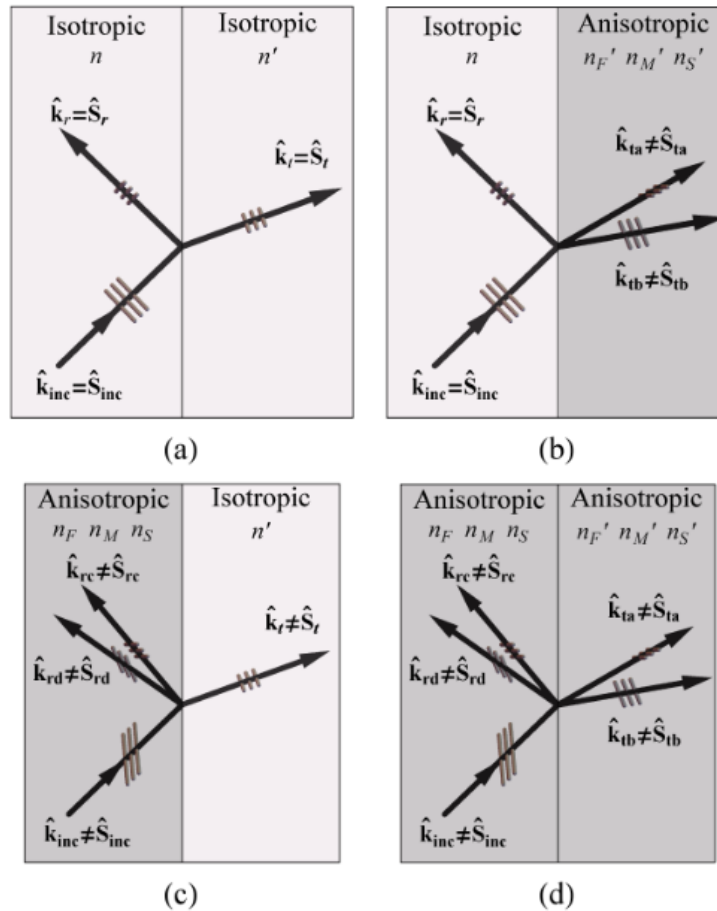


Figure 2.12 The four configurations of anisotropic interfaces are shown with corresponding reflected rays toward the incident medium and refracted rays into the transmitting medium for a given incident ray. The black arrow represents \mathbf{S} , the Poynting vector direction, which is the direction of energy flow and is not necessarily the same as \mathbf{k} , the propagation vector direction. The transmitted and reflected modes are identified by subscripts **ta**, **tb**, **rc** and **rd**. The three gray parallel lines along each ray represent the wavefronts which are perpendicular to \mathbf{k} , but not necessarily perpendicular to \mathbf{S} . (a) A ray propagating from an isotropic medium to another isotropic medium results in one reflected ray and one refracted ray. (b-d) If the incident medium or/and the transmitted medium is/are anisotropic, ray splitting occurs and the two resultant rays in each anisotropic material have different \mathbf{k} and \mathbf{S} directions.

In an isotropic material, the refractive index remains constant and is independent of the polarization of the ray. The \mathbf{k} and \mathbf{S} vectors of the *s*- and *p*-polarizations are parallel and one incident ray produces one reflected and one refracted ray. In this case, the reflected and refracted constant phase wavefronts are perpendicular to the energy propagation

direction. In anisotropic materials, the surfaces of constant phase (the wavefronts) are not generally perpendicular to the direction of energy propagation; \mathbf{k} and \mathbf{S} are not aligned in the same direction. At anisotropic intercepts, one incident ray may result in up to four exiting rays, two reflected and two refracted.

The essential steps of the anisotropic ray tracing algorithm, following McClain^{68,69}, are as follows. The electromagnetic fields and tensors are represented by 3×1 vectors and 3×3 matrices, respectively; all calculations are directly performed in 3D. The normalized refracted or reflected propagation vector $\hat{\mathbf{k}}$ at an anisotropic material is

$$\hat{\mathbf{k}} = \frac{n\hat{\mathbf{k}}_{\text{inc}} + \left(-n\hat{\mathbf{k}}_{\text{inc}} \cdot \hat{\boldsymbol{\eta}} \pm \sqrt{n^2 (\hat{\mathbf{k}}_{\text{inc}} \cdot \hat{\boldsymbol{\eta}})^2 + (n'^2 - n^2)} \right) \hat{\boldsymbol{\eta}}}{\left\| n\hat{\mathbf{k}}_{\text{inc}} + \left(-n\hat{\mathbf{k}}_{\text{inc}} \cdot \hat{\boldsymbol{\eta}} \pm \sqrt{n^2 (\hat{\mathbf{k}}_{\text{inc}} \cdot \hat{\boldsymbol{\eta}})^2 + (n'^2 - n^2)} \right) \hat{\boldsymbol{\eta}} \right\|}, \quad (2.11)$$

where n and n' are the refractive index for the incident and the exiting rays, $\hat{\mathbf{k}}_{\text{inc}}$ and $\hat{\mathbf{k}}$ are the normalized incident and exiting propagation vectors, and the sign of the square root is + for refraction and – for reflection. The solution is complicated by the fact that $\hat{\mathbf{k}}$ is a function of n' . By combining the constitutive relations in equation (2.5) with Maxwell's equations, the eigenvalue equations for the exiting \mathbf{E} fields are formed,

$$\left[\boldsymbol{\varepsilon}' + (n' \mathbf{K}_t + i \mathbf{G}')^2 \right] \mathbf{E}_t = 0 \quad \text{and} \quad \left[\boldsymbol{\varepsilon} + (n \mathbf{K}_r + i \mathbf{G})^2 \right] \mathbf{E}_r = 0 \quad (2.12)$$

for refraction and reflection respectively, where

$$\mathbf{K} = \begin{pmatrix} 0 & -k_z & k_y \\ k_z & 0 & -k_x \\ -k_y & k_x & 0 \end{pmatrix} \quad (2.13)$$

and $\hat{\mathbf{k}} = (k_x, k_y, k_z)$. For a non-zero exiting \mathbf{E}_t and \mathbf{E}_r , the determinant of equation (2.12) has to be zero,

$$\left| \boldsymbol{\varepsilon}' + (n' \mathbf{K}_t + i \mathbf{G}')^2 \right| = 0 \quad \text{and} \quad \left| \boldsymbol{\varepsilon} + (n' \mathbf{K}_r + i \mathbf{G})^2 \right| = 0. \quad (2.14)$$

Equations (2.11) and (2.14) are solved simultaneously for n' and \mathbf{k} . The exiting \mathbf{E} fields are calculated by equation (2.12) through singular value decomposition. The exiting \mathbf{H} and \mathbf{S} fields are calculated by equation (2.15) and (2.16).

$$\mathbf{H}_t = (n_t \mathbf{K}_t + i \mathbf{G}') \mathbf{E}_t \quad \text{and} \quad \mathbf{H}_r = (n_r \mathbf{K}_r + i \mathbf{G}) \mathbf{E}_r \quad (2.15)$$

$$\hat{\mathbf{S}}_t = \frac{\mathcal{R}e[\mathbf{E}_t \times \mathbf{H}_t^*]}{\|\mathcal{R}e[\mathbf{E}_t \times \mathbf{H}_t^*]\|} \quad \text{and} \quad \hat{\mathbf{S}}_r = \frac{\mathcal{R}e[\mathbf{E}_r \times \mathbf{H}_r^*]}{\|\mathcal{R}e[\mathbf{E}_r \times \mathbf{H}_r^*]\|} \quad (2.16)$$

Then the \mathbf{E} , \mathbf{D} , \mathbf{B} , \mathbf{H} and \mathbf{S} fields are calculated for all exiting modes. Since highly transparent materials are preferred in optical systems, the absorption is assumed negligibly small. Extension of these methods to absorbing and dichroic materials is included in references 63, 64, 67, and 88.

The equation for *OPL* in anisotropic materials is generalized from its definition for isotropic materials in equation (2.17). *OPL* describes the phase accumulated along a ray path between optical element interfaces, and is calculated separately for each mode. The

physical ray path is along \mathbf{S} which is the direction of energy flow, while the phase increases along \mathbf{k} . Therefore the *OPL* for the ray segment is

$$OPL = n \ell \hat{\mathbf{k}} \cdot \hat{\mathbf{S}} \quad (2.17)$$

as shown in Figure 2.13.

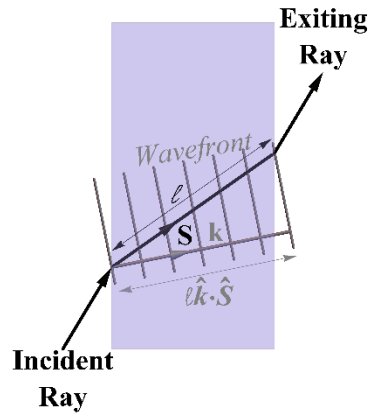


Figure 2.13 The calculation of the *OPL* for a ray propagating through an anisotropic material where \mathbf{S} (black) and \mathbf{k} (gray) are not aligned. The wavefronts are perpendicular to the \mathbf{k} vector. The energy propagation direction is along \mathbf{S} , which determines the location of ray intercept at the next surface. The *OPL* is the number of wavelengths between the two intercepts, the projection of the ray path ℓ onto \mathbf{k} multiplied by the refractive index of the mode.

The fraction of the incident energy which couples into each of the four modes is described by the amplitude transmission coefficients (t_a and t_b) and the amplitude reflection coefficients (r_c and r_d), where subscripts a , b , c , and d are labels for the four split modes. These coefficients at an isotropic/isotropic intercept are the conventional Fresnel coefficients for the s - and p -polarizations. By matching the boundary conditions at the interface for \mathbf{E} and \mathbf{H} fields, all four exiting amplitude coefficients at the intercept are calculated using equations (2.18) through (2.22):

$$\mathbf{A} = \mathbf{F}^{-1} \cdot \mathbf{C}, \quad (2.18)$$

where

$$\mathbf{A} = (t_a, t_b, r_c, r_d)^T, \quad (2.19)$$

$$\mathbf{F} = \begin{pmatrix} \mathbf{s}_1 \cdot \hat{\mathbf{E}}_{ta} & \mathbf{s}_1 \cdot \hat{\mathbf{E}}_{tb} & -\mathbf{s}_1 \cdot \hat{\mathbf{E}}_{rc} & -\mathbf{s}_1 \cdot \hat{\mathbf{E}}_{rd} \\ \mathbf{s}_2 \cdot \hat{\mathbf{E}}_{ta} & \mathbf{s}_2 \cdot \hat{\mathbf{E}}_{tb} & -\mathbf{s}_2 \cdot \hat{\mathbf{E}}_{rc} & -\mathbf{s}_2 \cdot \hat{\mathbf{E}}_{rd} \\ \mathbf{s}_1 \cdot \mathbf{H}_{ta} & \mathbf{s}_1 \cdot \mathbf{H}_{tb} & -\mathbf{s}_1 \cdot \mathbf{H}_{rc} & -\mathbf{s}_1 \cdot \mathbf{H}_{rd} \\ \mathbf{s}_2 \cdot \mathbf{H}_{ta} & \mathbf{s}_2 \cdot \mathbf{H}_{tb} & -\mathbf{s}_2 \cdot \mathbf{H}_{rc} & -\mathbf{s}_2 \cdot \mathbf{H}_{rd} \end{pmatrix}, \quad (2.20)$$

$$\mathbf{C} = (\mathbf{s}_1 \cdot \hat{\mathbf{E}}_{inc}, \mathbf{s}_2 \cdot \hat{\mathbf{E}}_{inc}, \mathbf{s}_1 \cdot \mathbf{H}_{inc}, \mathbf{s}_2 \cdot \mathbf{H}_{inc})^T, \quad (2.21)$$

with subscript **inc** for incident fields,

$$\mathbf{s}_1 = \hat{\mathbf{k}} \times \hat{\boldsymbol{\eta}} \quad \text{and} \quad \mathbf{s}_2 = \hat{\boldsymbol{\eta}} \times \mathbf{s}_1. \quad (2.22)$$

$\mathbf{s}_1 \cdot \mathbf{V}$ and $\mathbf{s}_2 \cdot \mathbf{V}$ operate on vector \mathbf{V} to extract the tangential and normal components of \mathbf{V} .

Therefore the transmitted electric field is the superposition of the two transmitted modes:

$$\mathbf{E}_t(\mathbf{r}, t) = \mathcal{R}e \left[E_{inc} \left(t_a \hat{\mathbf{E}}_{ta} e^{i \left(\frac{2\pi}{\lambda} n_{ta} \hat{\mathbf{k}}_{ta} \cdot \mathbf{r} \right)} + t_b \hat{\mathbf{E}}_{tb} e^{i \left(\frac{2\pi}{\lambda} n_{tb} \hat{\mathbf{k}}_{tb} \cdot \mathbf{r} \right)} \right) e^{-i\omega t} \right], \quad (2.23)$$

and the reflected electric field is

$$\mathbf{E}_r(\mathbf{r}, t) = \mathcal{R}e \left[E_{inc} \left(r_c \hat{\mathbf{E}}_{rc} e^{i \left(\frac{2\pi}{\lambda} n_{rc} \hat{\mathbf{k}}_{rc} \cdot \mathbf{r} \right)} + r_d \hat{\mathbf{E}}_{rd} e^{i \left(\frac{2\pi}{\lambda} n_{rd} \hat{\mathbf{k}}_{rd} \cdot \mathbf{r} \right)} \right) e^{-i\omega t} \right]. \quad (2.24)$$

For the isotropic-to-isotropic interface, ($n_{ta}=n_{tb}$, $\hat{\mathbf{k}}_{ta} = \hat{\mathbf{k}}_{tb}$, $\hat{\mathbf{E}}_{ta} \perp \hat{\mathbf{E}}_{tb}$) and ($n_{rc}=n_{rd}$, $\hat{\mathbf{k}}_{rc} = \hat{\mathbf{k}}_{rd}$, and $\hat{\mathbf{E}}_{rc} \perp \hat{\mathbf{E}}_{rd}$). Thus, equations (2.23) and (2.24) reduce to

$$\mathbf{E}_t(\mathbf{r}, t) = \mathcal{Re} \left[E_{inc} (t_s \hat{\mathbf{E}}_{ts} + t_p \hat{\mathbf{E}}_{tp}) e^{i \left(\frac{2\pi}{\lambda} n_t \hat{\mathbf{k}}_t \cdot \mathbf{r} - \omega t \right)} \right] \text{ and} \quad (2.25)$$

$$\mathbf{E}_r(\mathbf{r}, t) = \mathcal{Re} \left[E_{inc} (r_s \hat{\mathbf{E}}_{rs} + r_p \hat{\mathbf{E}}_{rp}) e^{i \left(\frac{2\pi}{\lambda} n_r \hat{\mathbf{k}}_r \cdot \mathbf{r} - \omega t \right)} \right]. \quad (2.26)$$

For rays refracting into a uniaxial medium, the a and b -modes are the o - and e -modes in equation (2.23). For rays refracting into an optically active medium, the resultant two modes are l and r -modes. It is important to note that equations (2.23) and (2.24) must be repeated for the orthogonally polarized incident modes to yield the four refracting or four reflecting modes (i.e., for biaxial-to-biaxial: ff , fs , sf , ss -modes; for uniaxial-to-uniaxial: oo , oe , eo , ee -modes).

The light intensity I of a given \mathbf{E} is calculated by multiplying $|\mathbf{E}|^2$ with the cross-section scaling factor, $n_2 \cos \theta_{s2} / n_1 \cos \theta_{s1}$, at a ray intercept as

$$I = \frac{n_2 \cos \theta_{s2}}{n_1 \cos \theta_{s1}} |\mathbf{E}|^2, \quad (2.27)$$

where θ_s is the angle of the Poynting vector, subscript 1 for parameters before the interface, and subscript 2 for parameters after the interface.

When equation (2.11) yields a ray with complex \mathbf{k} , the corresponding mode is an evanescent wave. The mode is totally internal reflected for a complex \mathbf{k}_t and all the energy is reflected with zero transmission⁸⁹. In an anisotropic material, inhibited reflection occurs when the reflected ray has a complex \mathbf{k}_r ; then all the energy transmits with zero reflection

The algorithms above based on McClain explain the calculation for uncoated anisotropic interfaces. The calculations for layered of anisotropic slabs and anisotropic coatings are discussed by Mansuripur⁹¹, Abdulhalim^{92,93} and others^{94,95}.

Finally, conical refraction is a complex phenomenon in biaxial materials where light refracts into a continuous cone of light, not just into two modes in two directions. It only happens when light propagates along one of the two optic axes^{9,96,97} in a biaxial material as shown in Figure 2.14 (left). The optic axes of a biaxial material do not correspond to any of the principal axes. When conical refraction occurs, the eigenmodes experience the same refractive index⁹⁸, and the solution to Maxwell's equations becomes degenerate with a family of \mathbf{k} and \mathbf{E} pairs. The associated refracted energy forms a hollow cone of light as shown in Figure 2.14 (right).

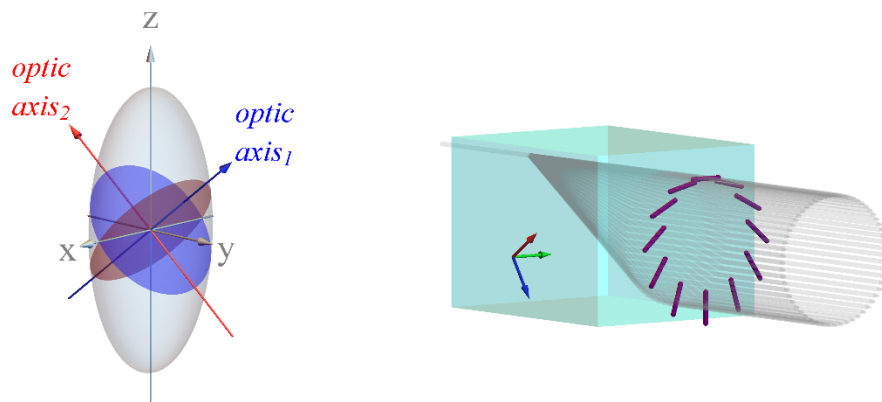


Figure 2.14 (Left) Orientations of the two optic axes of a biaxial material are perpendicular to the two circular cross sections through the index ellipsoid. (Right) A ray refracts into the direction of the biaxial optic axis. The incident polarizations distribute their Poynting vectors into a cone (the solid angle of the cone shown is exaggerated), and propagate as a cone through the biaxial crystal. The associated polarization (shown as the purple lines) rotates by π around the refracted cone. The distribution of flux around the cone depends on the distribution of incident polarization states. The fast, medium, and slow crystal axes are shown as the red, green and blue arrows.

Figure 2.15 shows measurements of conical refraction in a KTP crystal. The distribution of the energy depends on the incident polarization; the corresponding polarization state rotates around the cone through 180° and forms a ring on the next interface. Thus, due to conical refraction special care is required when ray tracing near the optic axes^{99,100}. For example, the cone of light can be modeled as a cone of rays.

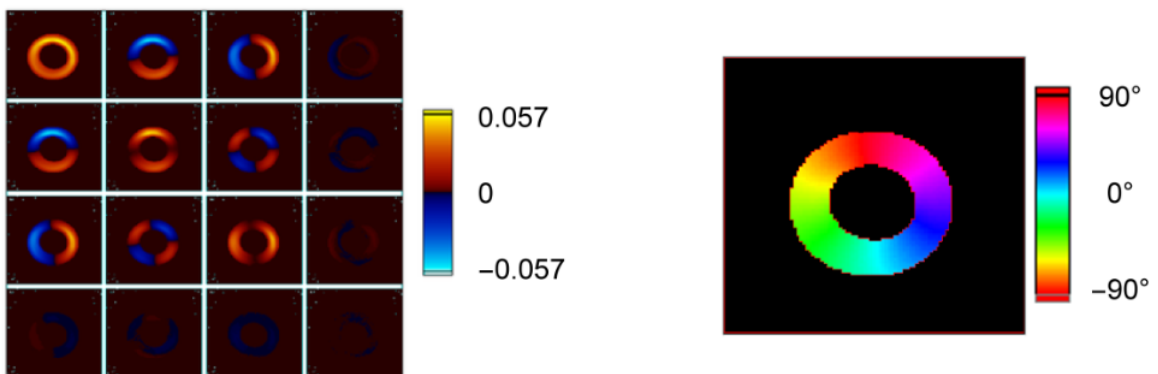


Figure 2.15 A biaxial KTP crystal is setup to display conical refraction and its refracted cone is measured in an imaging polarimeter. The Mueller matrix image (left) and diattenuation orientation image (right) of the refracted cone is shown.

2.5 External and internal refraction/reflection at a biaxial interface

The transmission and reflection for an example anisotropic surface are shown in this section. Consider a KTP biaxial crystal with principal refractive indices $(n_F, n_M, n_S) = (1.786, 1.797, 1.902)$ whose principal axes are oriented along $(0.690, 0.55, 0.48)$, $(-0.03, 0.68, -0.73)$ and $(0.73, -0.49, -0.49)$, as shown in Figure 2.16. A similar analysis of this example KTP crystal with principal axes along global xyz axes is included in Appendix C for reference.



Figure 2.16 External (left) and internal (right) reflection and refraction of biaxial interface.

The external and internal reflection and refraction properties are calculated using the algorithms of section 2.4 for a wavelength of 500 nm across a range of incident angles. The external reflection and refraction are isotropic/anisotropic interactions of a ray propagating from air to KTP. The ray reflects back to air with s - and p -polarizations, and refracts into KTP as $fast$ - and $slow$ -modes in different propagation directions, as depicted in Figure 2.16 (left). The internal reflection and refraction, shown in Figure 2.16 (right), are anisotropic/isotropic interactions of an eigenmode propagating from KTP to air. The ray reflects back into KTP with $fast$ - and $slow$ -modes having different propagation directions, and the ray refracts to air with s - and p -polarized components propagating in the same direction. These refracted and reflected modes inside the biaxial crystal do not necessarily lie in the plane of incidence (PoI) due to the crystal's anisotropic structure, but the effect in this example is small due to the small birefringence of KTP.

In general, the incident s - and p -polarizations can both couple to the refracted $fast$ - and $slow$ -modes in external refraction. Similarly for internal reflection, the incident $fast$ - and $slow$ -modes can both couple to the reflected $fast$ - and $slow$ -modes. The intensity of these mode couplings depends highly on the orientation of the crystal axes. As shown in

Appendix C, the crystal axes can be adjusted so that p -polarization couples entirely to the $slow$ -mode and s -polarization couples entirely to the $fast$ -mode or vice versa.

First, consider the external interaction. The intensity coefficients of the air/KTP interface, as plotted in Figure 2.17, are the result of external dielectric reflection and refraction. In reflection, both s - and p -polarized states have the same reflectance at normal incidence. The reflectance of the s -polarization increases with angle, while the reflectance of the p -polarization decreases to zero at about 60° corresponding to the Brewster's angle. As both states approach the Brewster's angle, the difference of their reflectance increases, thus reflected diattenuation also increases. In refraction, the p -polarization couples mostly to the $fast$ -mode and the s -polarization couples mostly to the $slow$ -mode. The intensity of s - $fast$ and p - $slow$ couplings are relatively low and appear as orthogonally polarized ghosts or leakage when compared with the s - $slow$ and p - $fast$ modes.

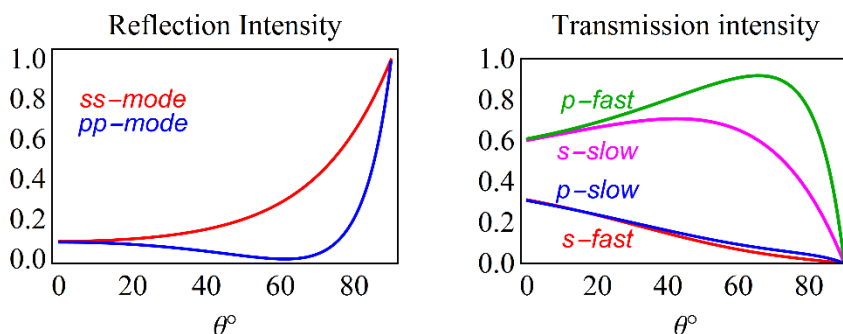


Figure 2.17 External reflection and refraction coefficients at the air/KTP interface.

Figure 2.18 shows a fan of incident rays, from 0° to 70° reflecting from the air/KTP interface. At normal incidence, the s - and p -states are degenerate and both have a π phase shift. The intensity of the s -state increases with angle, while the intensity of the p -state

decreases with angle and turns around, switching to in-phase with the incident state when passing through Brewster's angle with zero reflectance.

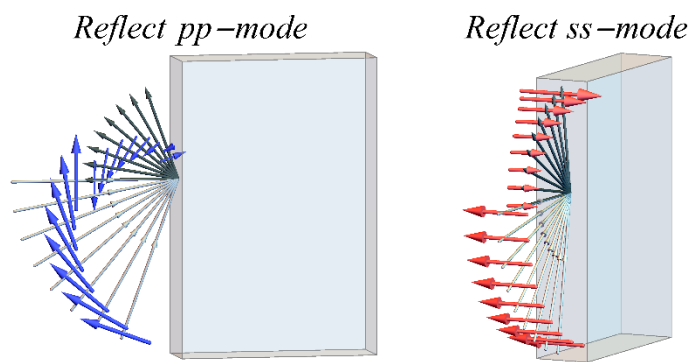


Figure 2.18 A fan of rays externally reflect from an air/biaxial interface. The gray arrows are the incident \mathbf{k} vectors at different incident angles. The black arrows are the corresponding reflected \mathbf{k} vectors. The blue and red arrows are the polarization ellipses, the evolution of electric field, where the arrow head indicates the start of the electric field evolution in time. In this case, all polarization ellipses shown are linearly polarized. All the incident polarizations have the same magnitude. The length of the polarization arrow indicates the intensity of the reflected light, but are adjusted slightly for visualization.

In refraction, the crystal axis orientation of this example biaxial KTP allows energy to couple to both *fast*- and *slow*-modes from both *s*- and *p*-incident states. The transmitted *fast*- and *slow*-modes have slightly different \mathbf{S}_t and lie close to, but not exactly in the PoI. The phase of the polarization is unchanged upon refraction for the uncoated surface, as shown in Figure 2.19; thus the refracted retardance is zero. As the incident angle increases, the transmission decreases, as opposed to increasing reflection. The *p-fast* and *s-slow* modes are polarized close to the incident *p*- and *s*-polarizations, respectively. The *p-slow* and *s-fast* modes with lower transmission have larger polarization rotations due to the biaxial structure.

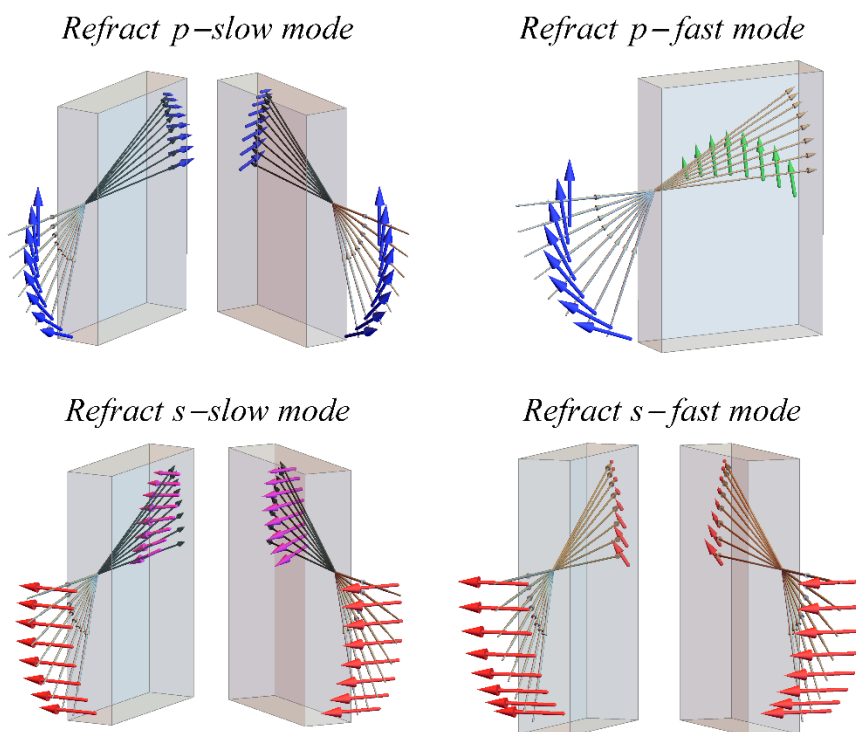


Figure 2.19 A fan of rays externally refracting from an air/biaxial interface are shown in two perspectives for the four mode couplings. The gray arrows are the incident \mathbf{k} vectors. The black and brown arrows are the refracted \mathbf{S} vectors for the *slow*- and *fast*-modes, respectively. The blue, red, magenta and green arrows show the refracted polarization states in 3D and are scaled to the refracted flux.

Consider left circularly polarized light incident on the example air/KTP interface at various angles, as shown in Figure 2.20. The reflected electric fields are circularly/elliptically polarized. Around normal incidence, the incident and reflected polarizations evolve in the same direction when viewing in 3D; left circularly polarized[§] light reflects as right circularly polarized light. As the incident angle approaches Brewster's angle, the reflected polarization elongates towards the *s*-polarized state. When it reaches

[§] The left and right circular polarizations are demonstrated in Table 2.1.

Brewster's angle, the reflected p component is zero, and the reflected light is completely s -polarized. Above the Brewster's angle, the reflected polarization becomes elliptical again, but with the opposite helicity than below the Brewster's angle; left circularly polarized light reflects as left circularly polarized light. Both refracted modes are linearly polarized, and they both rotate slightly with the refraction angle.

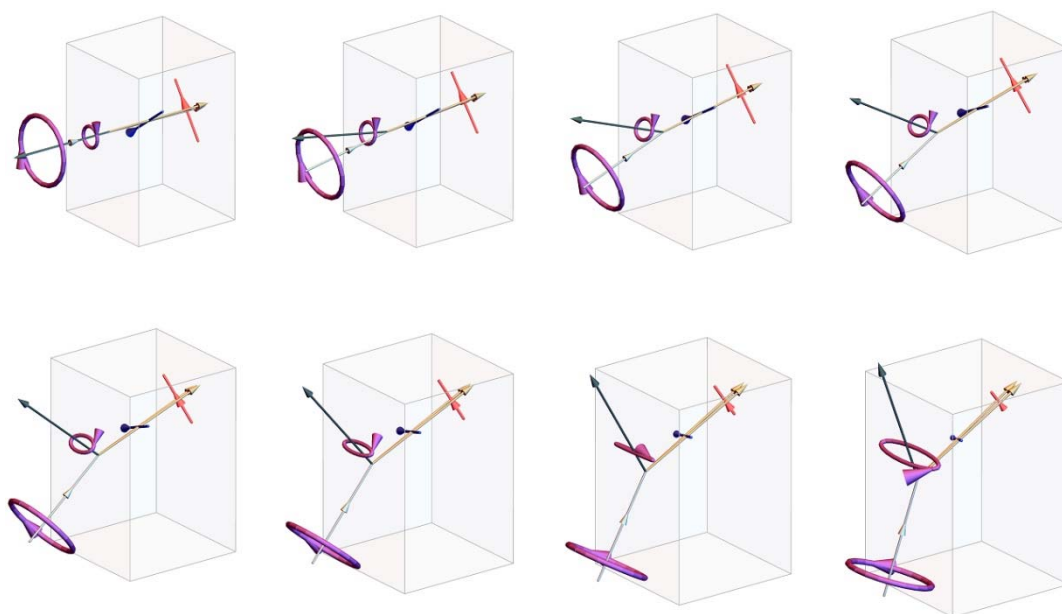


Figure 2.20 Left circularly polarized incident light is sent to the air/biaxial interface. The gray, black and brown arrows are the incident, reflected and refracted rays, respectively. The purple ellipses are the incident and reflected polarizations. The red and blue arrows are the refracted *fast* and *slow*-modes.

As light propagates from inside the crystal back into air, it is subject to internal light-surface interactions. The internal reflection/refraction coupling coefficients of the example KTP/air interface are shown in Figure 2.21. The *fast*- and *slow*-modes couple to both reflected *fast*- and *slow*-modes. The critical angle is about 32° , where no light transmitted and all four reflected modes have about 50% couplings.

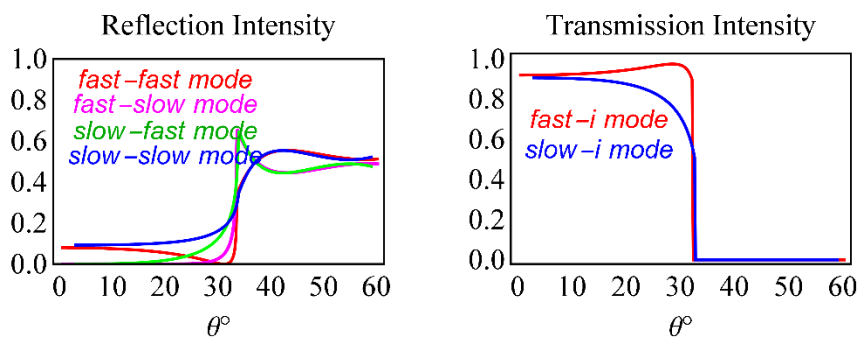


Figure 2.21 Internal reflection and transmission coefficients at the KTP/air interface.

The polarizations resulting from the internal reflection are shown in Figure 2.22. The incident *fast*- and *slow*-modes lie in the plane transverse to incident **S**, but are not in or orthogonal to the PoI. Below the critical angle, most of the light transmits, and the reflected light has a π phase change upon reflections. Above the critical angle, the reflected intensity increases drastically due to total internal reflection with a changing phase shift as function of reflection angle.

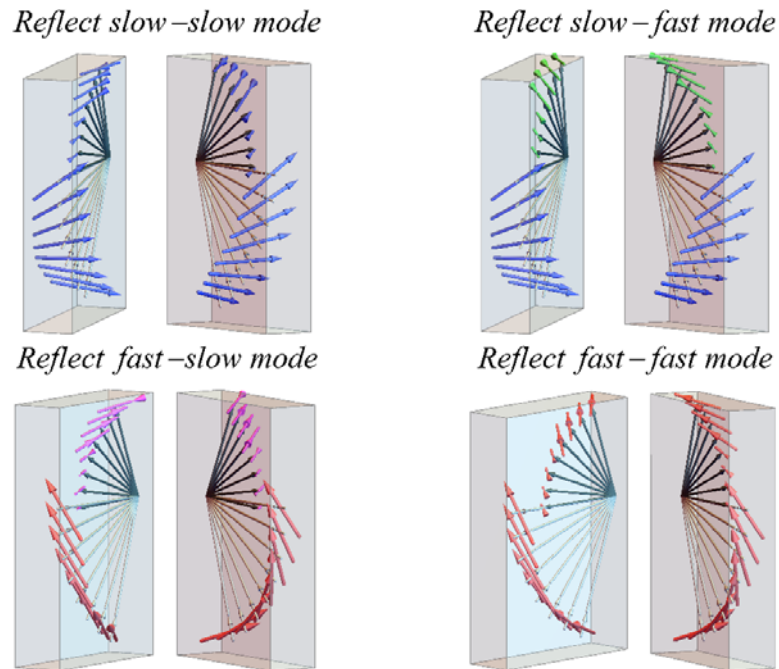


Figure 2.22 A fan of rays internally reflecting from a biaxial/air interface are shown in two perspectives for all four mode couplings. The gray arrows are the incident \mathbf{k} vectors. The black arrows are the corresponding reflected \mathbf{k} vectors. The blue, red, green and magenta arrows are the polarization ellipses.

The refracted polarization in air shown in Figure 2.23 has non-zero s and p components which are coupled from both *fast*- and *slow*-modes. Since refraction through an uncoated dielectric surface induces zero phase change, the refracted light of a linearly polarized incident state is linearly polarized in between the s - and p -polarized states.

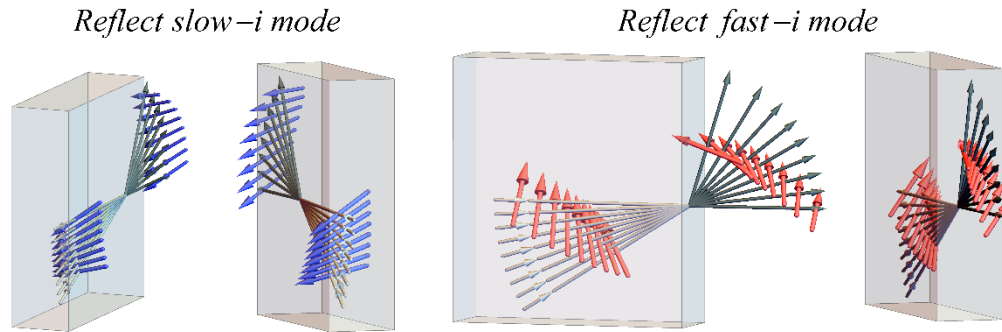


Figure 2.23 A fan of rays internally refracting from biaxial/air interface are shown in two perspectives for all four mode couplings. The gray arrows are the incident \mathbf{k} vectors. The black arrows are the refracted \mathbf{S} vectors for the refracted rays. The blue and red arrows are the polarization ellipses.

2.6 Optical Indicatrix

The refraction and reflection at anisotropic interface can be understood by a geometrical construction rather than the algebraic algorithm in Section 2.4. In this geometrical approach, the calculation of ray parameters is visualized using the index ellipsoid and optical indicatrix, which are very helpful for understanding wavefront aberrations.

The \mathbf{E} and \mathbf{D} vectors are related by the dielectric tensor, and the energy density u in the electromagnetic wave,

$$\mathbf{D} = \boldsymbol{\varepsilon} \mathbf{E} \quad \text{and} \quad u = \frac{1}{2} \mathbf{E} \cdot \mathbf{D} \quad (2.28)$$

In the principal coordinates, the dielectric tensor is diagonal and the three principal axes are aligned with the xyz axes,

$$\begin{pmatrix} D_x \\ D_y \\ D_z \end{pmatrix} = \begin{pmatrix} n_x^2 & 0 & 0 \\ 0 & n_y^2 & 0 \\ 0 & 0 & n_z^2 \end{pmatrix} \begin{pmatrix} E_x \\ E_y \\ E_z \end{pmatrix}, \quad (2.29)$$

then

$$u = \frac{1}{2} \left(n_x^2 E_x + n_y^2 E_y + n_z^2 E_z \right). \quad (2.30)$$

So

$$1 = \frac{\left(\frac{E_x}{\sqrt{2u}} \right)^2}{(1/n_x)^2} + \frac{\left(\frac{E_y}{\sqrt{2u}} \right)^2}{(1/n_y)^2} + \frac{\left(\frac{E_z}{\sqrt{2u}} \right)^2}{(1/n_z)^2}. \quad (2.31)$$

The solutions for the electric field vector in equation (2.31) can be represented as an ellipsoid with semi-axes $1/n_x$, $1/n_y$, and $1/n_z$, as shown in Figure 2.24.

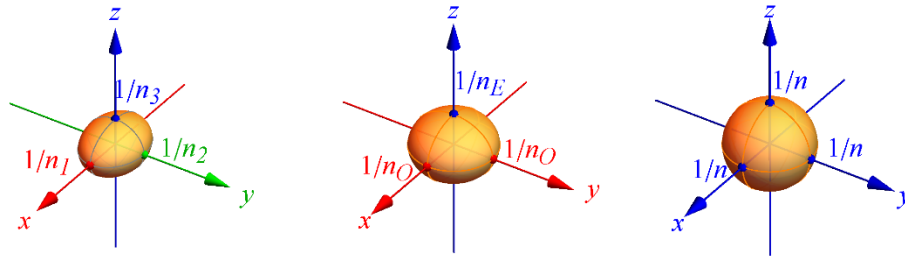


Figure 2.24 The ray ellipsoid of biaxial (left), positive uniaxial (middle) and isotropic materials (right). The principal axes are aligned with the coordinate axes with $(x, y, z) = (E_x, E_y, E_z) / \sqrt{2u}$

On the other hand, the electric field can be expressed in terms of the displacement field as

$$\mathbf{E} = \boldsymbol{\varepsilon}^{-1} \mathbf{D} \quad \text{or} \quad \begin{pmatrix} E_x \\ E_y \\ E_z \end{pmatrix} = \begin{pmatrix} 1/n_x^2 & 0 & 0 \\ 0 & 1/n_y^2 & 0 \\ 0 & 0 & 1/n_z^2 \end{pmatrix} \begin{pmatrix} D_x \\ D_y \\ D_z \end{pmatrix} \quad (2.32)$$

where the inverse of $\boldsymbol{\varepsilon}$ is the impermeability tensor

$$\boldsymbol{\varepsilon}^{-1} = \begin{pmatrix} 1/n_x^2 & 0 & 0 \\ 0 & 1/n_y^2 & 0 \\ 0 & 0 & 1/n_z^2 \end{pmatrix}. \quad (2.33)$$

Then the energy density is

$$u = \frac{1}{2} \mathbf{E} \cdot \mathbf{D} = \frac{1}{2} \left(\frac{D_x^2}{n_x^2} + \frac{D_y^2}{n_y^2} + \frac{D_z^2}{n_z^2} \right) \quad (2.34)$$

and

$$1 = \frac{\left(\frac{D_x}{\sqrt{2u}} \right)^2}{(n_x)^2} + \frac{\left(\frac{D_y}{\sqrt{2u}} \right)^2}{(n_y)^2} + \frac{\left(\frac{D_z}{\sqrt{2u}} \right)^2}{(n_z)^2}. \quad (2.35)$$

With equation (2.35), the dielectric tensor is visualized as an index ellipsoid shown in Figure 2.25, whose semi-axes are the principal refractive indices in the principal coordinates. The index ellipsoid is variously called the ellipsoid of wave normals, reciprocal ellipsoid, or index indicatrix.^{9,81,101,102,103}

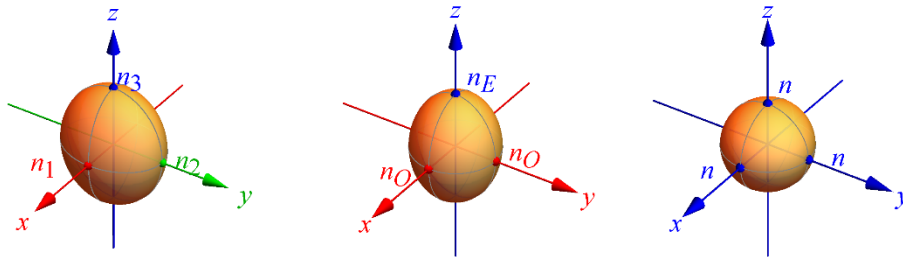


Figure 2.25 The index ellipsoid of (left) biaxial, (middle) positive uniaxial, and (right) isotropic materials. Their principal axes are aligned with the coordinate axes with $(x, y, z) = (D_x, D_y, D_z) / \sqrt{2u}$.

Consider a ray normally incident onto a uniaxial crystal in Figure 2.26 which has the index ellipsoid rotated from the z axis by α . At normal incidence, the refracted o - and e -rays have the same $\mathbf{k} = (0, 0, 1)$. The \mathbf{D} vectors and their corresponding refractive indices can be calculated geometrically using the index ellipsoid.

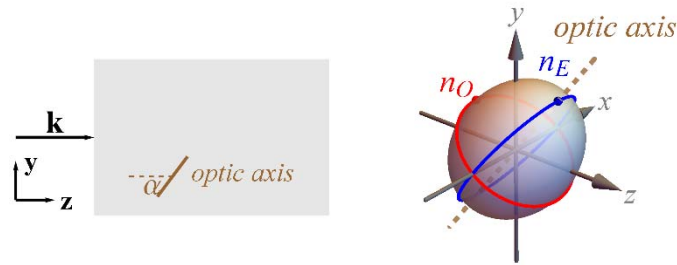


Figure 2.26 (Left) A ray normally incident to a block of uniaxial material. (Right) The index ellipsoid in the system coordinates where the optic axis is shown rotated by α from the z axis in the y - z plane. The blue ellipse goes through the optic axis. The red circle is perpendicular to the optics axis.

The eigenmodes in the uniaxial material follow from Maxwell's equations,

$$\mathbf{k} \times \mathbf{H} = -\omega \mathbf{D} \quad \text{and} \quad \mathbf{k} \times \mathbf{E} = \omega \mu_o \mathbf{H} \quad (2.36)$$

where ω is the light frequency in radians per second. Therefore,

$$\mathbf{k} \times (\mathbf{k} \times \mathbf{E}) = -\omega^2 \mu_o \mathbf{D}. \quad (2.37)$$

With equation (2.32),

$$-\frac{\mathbf{k}}{k} \times \left(\frac{\mathbf{k}}{k} \times \boldsymbol{\epsilon}^{-1} \mathbf{D} \right) = \frac{1}{n^2} \mathbf{D}, \quad (2.38)$$

where $k = n\omega/c$ and $k = |\mathbf{k}|$. This reveals that the projection of $\boldsymbol{\epsilon}^{-1} \mathbf{D}$ onto a plane perpendicular to \mathbf{k} is the \mathbf{D} field direction of the e -mode. Within the index ellipsoid, the surface orthogonal to \mathbf{k} including the origin is the index ellipse shown in Figure 2.27. For the example in Figure 2.26, the index ellipse is the intersection of the x - y plane with the crystal's index ellipsoid. The \mathbf{D} fields of the two eigenmodes are along the major and minor axes of the index ellipse. The lengths of these two axes correspond to the eigenmode

refractive indices. For the e -mode, \mathbf{D}_e is in the plane of the optic axis and orthogonal to \mathbf{k} , as shown in Figure 2.28. And \mathbf{D}_o for the o -mode is in the plane orthogonal to \mathbf{D}_e and \mathbf{k} .

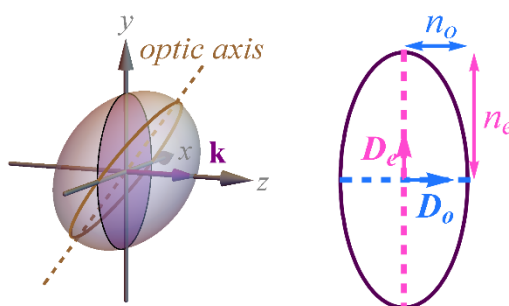


Figure 2.27 (Left) For a ray with propagation vector \mathbf{k} (purple) propagating through a negative uniaxial crystal, the ray index ellipse (light purple disk in the y - z plane) is the intersection of the plane normal to \mathbf{k} and the optical indicatrix. (Right) The minor and major axes of the index ellipse correspond to the \mathbf{D} field directions of the o - and e -modes, and the lengths of these two axes are the refractive indices.

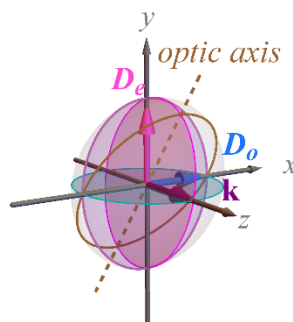


Figure 2.28 The index ellipse (light purple disk) in the x - y plane is normal to \mathbf{k} (purple arrow). \mathbf{D}_e (pink arrow) is on the pink plane in the y - z plane containing both the optic axis (dashed brown line) and the \mathbf{k} vector. \mathbf{D}_o (blue arrow) is on the blue plane in the x - z plane orthogonal to the pink \mathbf{D}_e plane. The three planes are orthogonal to each other, and both \mathbf{D}_o and \mathbf{D}_e are lying on the purple index ellipse in the x - y plane. The brown ellipse is the great ellipse containing the optic axis.

A general uniaxial index ellipse for any possible \mathbf{k} always has at least one axis with length n_o , as shown in Figure 2.29, corresponding to the o -ray index n_o . For a positive uniaxial material, the length of the major axis is the e -mode index n_e . The equation for n_e is obtained from Figure 2.30 by projecting the index ellipsoid and the index ellipse onto a 2D plane:

$$\frac{1}{n_e(\theta)^2} = \frac{\cos^2 \theta}{n_O^2} + \frac{\sin^2 \theta}{n_E^2} \quad (2.39)$$

where θ is the angle between \mathbf{k} and the optic axis. n_e becomes n_O in the limit when \mathbf{k} is along the optic axis, and n_e is n_E when \mathbf{k} lies in the plane orthogonal to the optic axis.

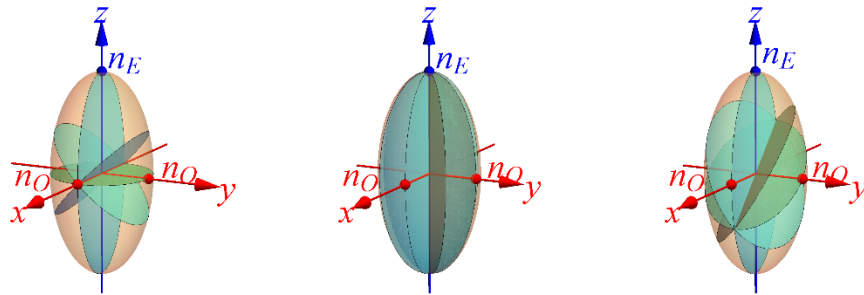


Figure 2.29 Several possible index ellipses (blue) in a positive uniaxial index ellipsoid (yellow) are shown. (Left) The index ellipses shown contain the x axis. (Middle) The index ellipses shown contain the z axis. (Right) The index ellipses shown contain an axis 45° from the x axis in the x - z plane.

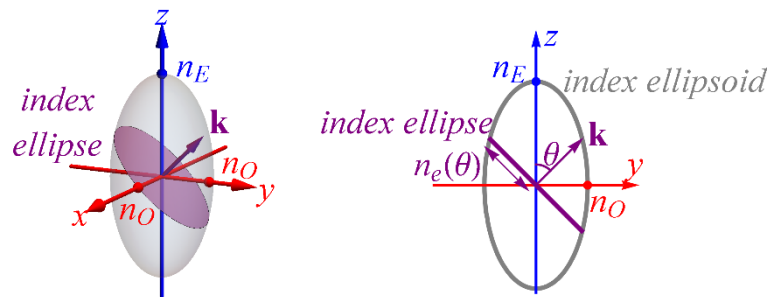


Figure 2.30 (Left) A ray propagating in the y - z plane has an index ellipse (purple disk) lying in a plane orthogonal to \mathbf{k} and containing the x axis. \mathbf{k} lies at an angle θ from the optic axis along the z axis. (Right) The projected length of the index ellipse is the magnitude of $n_e(\theta)$.

The direction of energy \mathbf{S} and its corresponding \mathbf{E} field are calculated using another ellipsoid derived from equation (2.37) which reduces to

$$\mathbf{k} \times (\mathbf{k} \times \mathbf{E}) + \mu \varepsilon \omega^2 \mathbf{E} = \mathbf{0}$$

$$\begin{pmatrix} n_1^2 k_0^2 - k_y^2 - k_z^2 & k_x k_y & k_x k_z \\ k_y k_x & n_2^2 k_0^2 - k_x^2 - k_z^2 & k_y k_z \\ k_z k_x & k_z k_y & n_3^2 k_0^2 - k_x^2 - k_y^2 \end{pmatrix} \begin{pmatrix} E_x \\ E_y \\ E_z \end{pmatrix} = \begin{pmatrix} 0 \\ 0 \\ 0 \end{pmatrix} \quad (2.40)$$

where $\mathbf{k} = \{k_x, k_y, k_z\}$, $k_0 = \omega/c$ and ω is the angular frequency. For a nontrivial solution of \mathbf{E} , the matrix determinant in equation (2.40) must be zero, which results in the dispersion relation and defines an ellipsoid called the K -surface, also called the normal surface^{78,104}.

For a uniaxial material, this is a function of k_0 :

$$\left(\frac{k_x^2/k_0^2}{n_O^2} + \frac{k_y^2/k_0^2}{n_O^2} + \frac{k_z^2/k_0^2}{n_O^2} - 1 \right) \left(\frac{k_x^2/k_0^2}{n_E^2} + \frac{k_y^2/k_0^2}{n_E^2} + \frac{k_z^2/k_0^2}{n_O^2} - 1 \right) = 0 \quad (2.41)$$

The left part of the equation is the solution for the o -mode with a spherical K -surface, while the right part is the solution for the e -mode with an ellipsoid K -surface. Both of these K -surfaces are plotted in their principal axes $\{k_x/k_0, k_y/k_0, k_z/k_0\}$ in Figure 2.31.

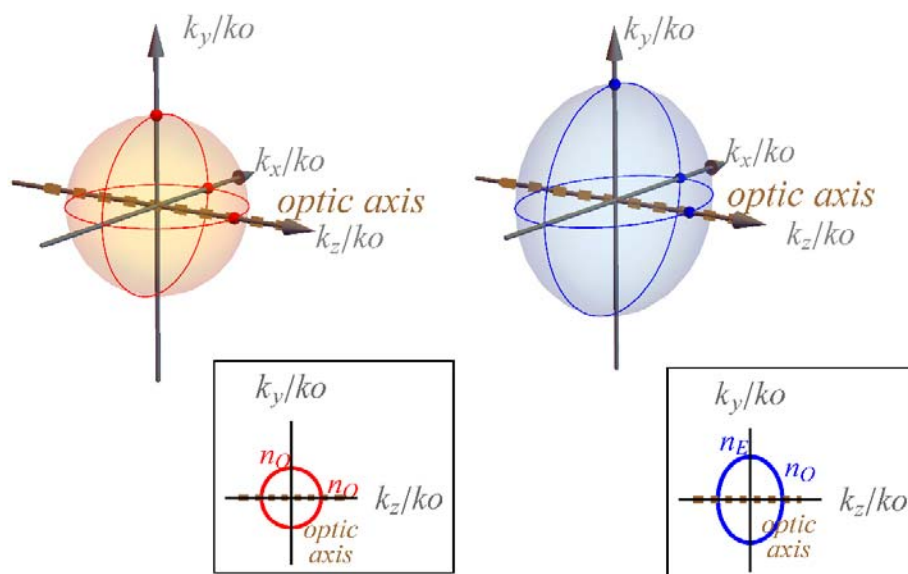


Figure 2.31 The K -surfaces and their cross sections for the o -mode (red, sphere) and the e -mode (blue, ellipsoid). The optic axis (dashed brown line) lies on the k_z/k_0 axis.

For the example shown in Figure 2.26, the K -surfaces are rotated by α , so Figure 2.31 becomes Figure 2.32. The Poynting vector \mathbf{S} is normal to the k -surface at the intersection of \mathbf{k} . The ordinary \mathbf{k}_o is always in the same direction as \mathbf{S}_o ; the ordinary wavefront is spherical just like an isotropic wavefront. On the other hand, the extraordinary \mathbf{k}_e is not parallel with \mathbf{S}_e , unless \mathbf{k}_e is along the optic axis or orthogonal to it. As the energy follows \mathbf{S}_e , the constant phase fronts along the \mathbf{D}_e field which are perpendicular to \mathbf{k}_e are skewed from \mathbf{S}_e , and the \mathbf{E}_e field orthogonal to \mathbf{S}_e lies tangent to the k -surface, as shown in Figure 2.33.

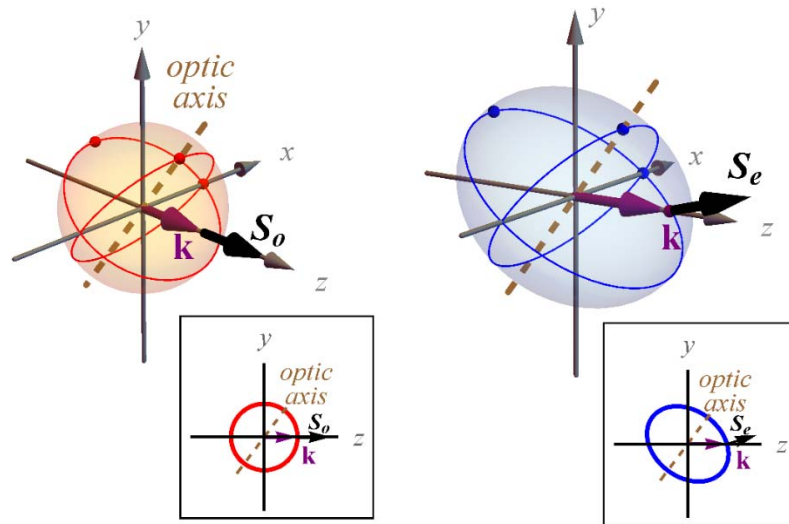


Figure 2.32 The K -surfaces are oriented for the example in Figure 2.26, where the optic axis is rotated by α from the z axis. The Poynting vectors are normal to the k -surface.

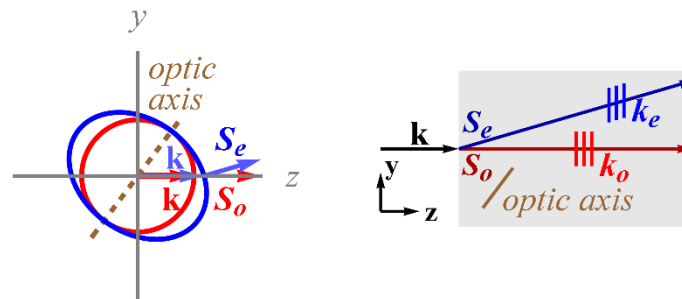


Figure 2.33 (Left) The Poynting vectors are normal to the K -surface in 2D. (Right) The incident energy divides into S_e and S_o direction. Their wavefronts D , shown as the three parallel lines, are orthogonal to k and skewed from S .

When a ray refracts through a birefringent interface, the refraction direction is fixed by the phase matching condition across the boundary for both eigenstates. The ordinary k_o is calculated as in an isotropic medium. The extraordinary k_e still obeys Snell's law with consideration for its varying refractive index as a function of direction:

$$\begin{aligned} n_{inc} \sin \theta_{inc} &= n_o \sin \theta_o \\ n_{inc} \sin \theta_{inc} &= n_e(\theta_a + \theta_e) \sin \theta_e \end{aligned} \quad (2.42)$$

where θ_a is the angle between the surface normal and the optic axis, θ_e is the refraction angle, and n_e is a function of θ_a and θ_e . Equation (2.39) and (2.42) must be solved simultaneously for the e -mode index and refraction angle. For the normal incidence example, the incident and exiting K -surfaces are shown in Figure 2.34 where $\theta_{inc} = \theta_o = \theta_e = 0$.

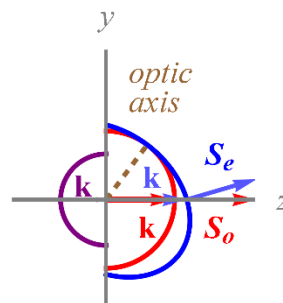


Figure 2.34 The K -surface for refraction from an isotropic material to a uniaxial material at normal incidence.

To ray trace using this geometrical method requires the crystal's principal indices, the principal axis orientations, and the incident \mathbf{k} direction. The ray trace procedure is as follows:

- (1) Calculate the refractive indices of the two eigenstates, and their propagation directions using equation (2.39) and (2.42).
- (2) Use the index ellipsoid to determine \mathbf{D} , from which \mathbf{E} is calculated.
- (3) Use the K -surfaces to determine \mathbf{S} .

The refractive index of the extraordinary mode in equation (2.39) is related to the phase velocity: $v_{p,e} = c/n_e$. The surface of equal phase, the S -surface, originates from a point source and expands at the speed of v_p along \mathbf{k} . So the ordinary wave surface is a sphere

while the extraordinary wave surface is proportional to $1/n_e$. The energy of the light flows along \mathbf{S} at ray velocity $v_r = v_p/\cos \beta$, where β is the angle between \mathbf{k} and \mathbf{S} ^{9,105,106}. Figure 2.35 shows the S -surfaces in the principal plane for positive and negative uniaxial materials. Consider a negative uniaxial material with \mathbf{k} is along the optic axis; then $v_{p,o} = v_{p,e}$. At other propagation direction, $n_e < n_o$, so $v_{p,o} < v_{p,e}$.

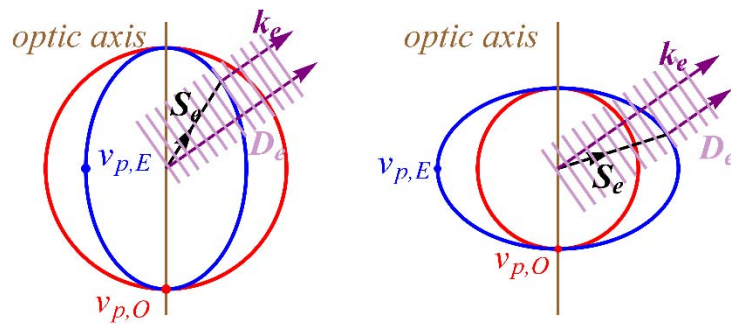


Figure 2.35 S -surface for positive (left) and negative (right) uniaxial material. Blue for e -mode, and red for o -mode. The optic axis (brown) is oriented vertically.

The K -surface and the S -surface of the e -mode are related to each other in Figure 2.36. Considering a \mathbf{k} vector originating from the origin, its intercept at the K -surface reveals the \mathbf{E} and \mathbf{S} directions to be the tangent and normal of the K -surface. For this \mathbf{S} direction originating from the origin, the intercept at the S -surface reveals the \mathbf{D} and \mathbf{k} directions to be the tangent and normal of the S -surface. The e -wavefront has the ellipsoidal shape of the S -surface, which expands along \mathbf{S} at the ray velocity.

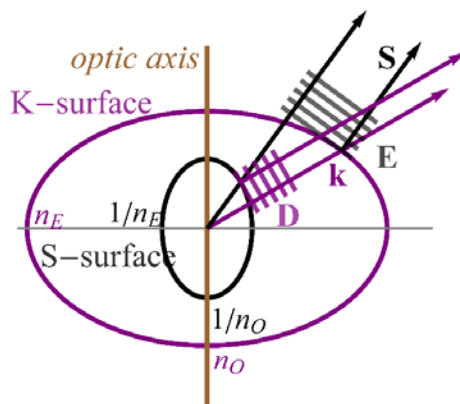


Figure 2.36 The *K*-surface and *S*-surface of the extraordinary mode in a positive uniaxial material.

2.7 Conclusions

The anisotropy of birefringent materials and optically active materials divides light waves into modes with mutually orthogonal polarizations. This ray doubling characteristic of anisotropic materials complicates the calculations of refracted and reflected electromagnetic waves at an uncoated anisotropic intercept in polarization ray tracing. Two algorithms were shown in this chapter to mathematically and geometrically calculate the ray parameters. The numerical algorithm is suitable for a computer ray trace, while the geometrical calculation provides intuition to understand the shape of the anisotropic wavefronts.

The polarized light interaction for an uncoated homogeneous anisotropic interface has similar properties to the refraction and reflection at an isotropic dielectric surface, except the eigen-polarizations propagate in different directions rather than in the same direction as with *s*- and *p*-polarizations. Also, the wavefront in an anisotropic material has a complex shape (orthogonal to \mathbf{k} but not orthogonal to \mathbf{S}) and different residual aberrations compared to a wavefront in an isotropic material. Further, the propagation within the

anisotropic material induces a phase difference between polarization states, retardance, which is commonly used in optical systems with anisotropic elements.

To study wavefront transmitted through anisotropic materials, a fan of rays should be traced. When tracing large grids of rays to accurately sample the multiple exiting wavefronts, accessing the ray properties along these ray paths through a specific surface or a series of surfaces is an important step in optical design. K incident rays refracting through N anisotropic intercepts result in $K \times 2^N$ exiting rays and $K \left(\sum_{n=1}^N 2^n \right)$ ray segments. These branches of ray segments can be organized by the cumulative mode label (introduced in Table 2.3) in a ray tree shown in Figure 2.37.

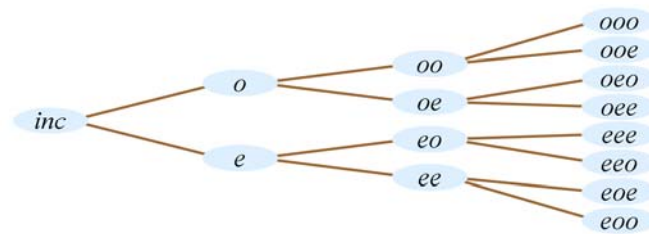


Figure 2.37 A ray tree for one incident ray refracting through three uniaxial interfaces, where the ordinary mode is o and the extraordinary mode is e .

This ray tree keeps track of the multiplicity of rays generated by anisotropic elements. The cumulative mode label identifies the individual polarized wavefront of a specific sequence of anisotropic energy splittings as the wavefront propagates through the series of optical surfaces. These mode labels accommodate the automation of ray doubling in a computer ray trace without imposing any assumptions, and assist in sorting the exiting rays for each polarized wavefront.

CHAPTER 3 POLARIZATION RAY TRACING P MATRICES FOR ANISOTROPIC RAY TRACING

3.1 Purposes of polarization ray tracing P matrix

The polarization ray tracing calculus is a method for performing polarization ray tracing in global 3D coordinates. The purpose of the polarization ray tracing matrix, \mathbf{P} , is to generalize the Jones matrix into three dimensions. This allows the calculation to avoid carrying the s - p local coordinate systems separately. Similar to the Jones matrix, the \mathbf{P} matrix describes the polarization change upon light-surface interaction, can be used to cascade the interactions through consecutive surfaces, and allow the calculation of polarization properties of each surface as well as a sequences of surfaces. Moreover, the \mathbf{P} matrix is defined directly in an xyz three dimensional coordinate system.

The \mathbf{P} matrix, which operates directly in 3D, is more preferable than the Jones matrix in ray tracing. Consider a ray normally incident on an uncoated isotropic interface reflects with Fresnel reflections $r_s = -r_p$ for the s - and p -polarizations. This opposite sign in the Fresnel coefficients means the reflected p -state has an extra π phase shift compared to the reflected s -state. However, when viewing the system in 3D, the s - and p -polarizations have the same interaction with the isotropic surface, as shown in Figure 3.1 because the two states are degenerate at normal incidence. Thus physically, their changes of electric field amplitude must be the same — the same amplitude change and the same phase change upon reflection. The extra π is a geometrical effect due to a local coordinate flip upon reflection. These local coordinate systems are defined by the s - p basis in the transverse plane of the incident and reflected rays, shown in Figure 3.1, where the basis vectors

$(\hat{s}, \hat{p}, \hat{k})$ and $(\hat{s}', \hat{p}', \hat{k}')$ follow the right-hand-rule. The Fresnel reflection coefficients are calculated relative to these basis coordinate systems. In perfect reflection, $r_s = -1$ and $r_p = 1$; in 3D, $\mathbf{E}_s = -\mathbf{E}_s'$ and $\mathbf{E}_p = \mathbf{E}_p'$. The Jones matrix for this reflection, $\begin{pmatrix} r_s & 0 \\ 0 & r_p \end{pmatrix} = \begin{pmatrix} -1 & 0 \\ 0 & 1 \end{pmatrix}$, does not clearly show the change of electric field in 3D without giving the pair of local bases.

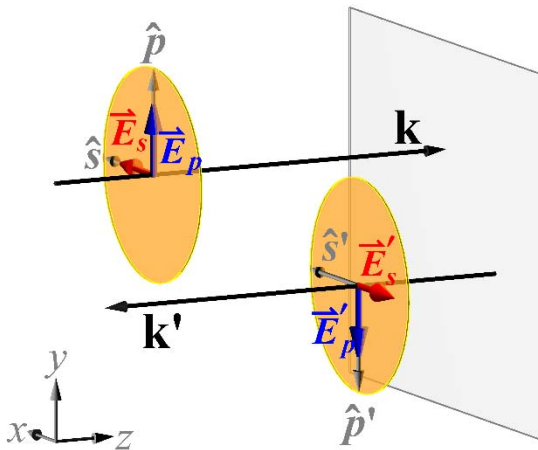


Figure 3.1 A ray is normally incident on a surface with $\mathbf{k} = (0, 0, 1)$ and reflects off the surface with $\mathbf{k}' = (0, 0, -1)$. The transverse plane (yellow) of the rays contains a pair of local basis (\hat{s}, \hat{p}) for the incident ray and (\hat{s}', \hat{p}') for the reflected ray. The s - and p -polarized incident electric fields $\bar{\mathbf{E}}_s$ and $\bar{\mathbf{E}}_p$ reflect to $\bar{\mathbf{E}}_s'$ and $\bar{\mathbf{E}}_p'$.

In this chapter, two formalisms of the \mathbf{P} matrix are presented. Their resultant \mathbf{P} matrices represent the change of \mathbf{E} field and ray direction. The first formalism is derived from the Jones matrix, which contains Fresnel coefficients defined in 2D local coordinate systems. Therefore it involves rotations from local to global coordinate system. The second formalism calculates the \mathbf{P} matrix directly from the 3D orthonormal basis, which is desired

for building the \mathbf{P} matrix using only the ray parameters (\mathbf{S} , \mathbf{E} , a , and OPL) calculated from the anisotropic algorithms shown in Section 2.4. This second formalism is the basis for calculating the \mathbf{P} matrix through anisotropic components to study the polarization aberrations of anisotropic elements, such as the angle dependence of crystal retarders and polarizers.

3.2 Calculation of the \mathbf{P} matrix from the Jones matrix

In the polarization ray tracing calculus, all electromagnetic fields are defined with 3×1 vectors. The polarization effects of an optical surface and the change of ray direction at an intercept are represented by the 3×3 \mathbf{P} matrix. A ray refracting through an isotropic interface, as shown in Figure 3.2, is represented by a single \mathbf{P} matrix. The exiting \mathbf{E}' after the interface is calculated as

$$\mathbf{E}' = \mathbf{P}\mathbf{E} \quad (3.1)$$

The \mathbf{P} matrix not only maps the electric field through an intercept, it also maps the incident propagation vector $\hat{\mathbf{k}}$ to the exiting propagation vector $\hat{\mathbf{k}}'$,²⁷

$$\hat{\mathbf{k}}' = \mathbf{P}\hat{\mathbf{k}} \quad (3.2)$$

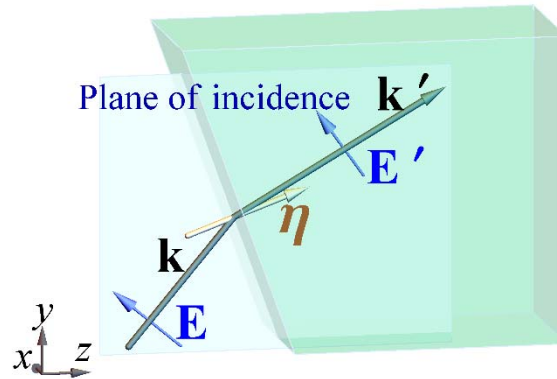


Figure 3.2 A ray with incident \mathbf{k} and electric field \mathbf{E} refracts through an optical interface with surface normal $\boldsymbol{\eta}$. The refracted ray propagates in \mathbf{k}' with electric field \mathbf{E}' . The plane of incidence contains \mathbf{k} , \mathbf{k}' and $\boldsymbol{\eta}$.

The 3×3 \mathbf{P} matrix can be calculated by transforming a 2×2 Jones matrix from its local coordinate systems to global coordinate systems. For an isotropic interface, the polarization change of the light is described by the Jones matrix with Fresnel coefficients^{**},

t_s and t_p for refraction, or r_s and r_p for reflection, as $\begin{pmatrix} t_s & 0 \\ 0 & t_p \end{pmatrix}$ or $\begin{pmatrix} r_s & 0 \\ 0 & r_p \end{pmatrix}$. These coefficients

are functions of incidence angle as shown in Figure 3.3. The isotropic interface couples s -polarized incident light to s -polarized exiting light with complex electric field amplitude change of t_s or r_s , p -polarized incident light to p -polarized exiting light with a complex

^{**} Fresnel equations for incident refractive index n_1 , transmitting refractive index n_2 , and incident

$$\text{angle } \theta: t_s = \frac{2n_1 \cos \theta}{n_1 \cos \theta + \sqrt{n_2^2 - n_1^2 \sin^2 \theta}}, t_p = \frac{2n_1 n_2 \cos \theta}{n_2^2 \cos \theta + n_1 \sqrt{n_2^2 - n_1^2 \sin^2 \theta}}, \text{ and}$$

$$r_s = \frac{n_1 \cos \theta - \sqrt{n_2^2 - n_1^2 \sin^2 \theta}}{n_1 \cos \theta + \sqrt{n_2^2 - n_1^2 \sin^2 \theta}}, r_p = \frac{n_2^2 \cos \theta - n_1 \sqrt{n_2^2 - n_1^2 \sin^2 \theta}}{n_2^2 \cos \theta + n_1 \sqrt{n_2^2 - n_1^2 \sin^2 \theta}}.$$

electric field amplitude change of t_p or r_p , and zero s -to- p or p -to- s coupling. In general,

the Jones matrix represents polarizing components as $\begin{pmatrix} J_{ss} & J_{ps} \\ J_{sp} & J_{pp} \end{pmatrix}$ which can have non-

zero J_{sp} and J_{ps} , coupling between s - and p -polarized light.

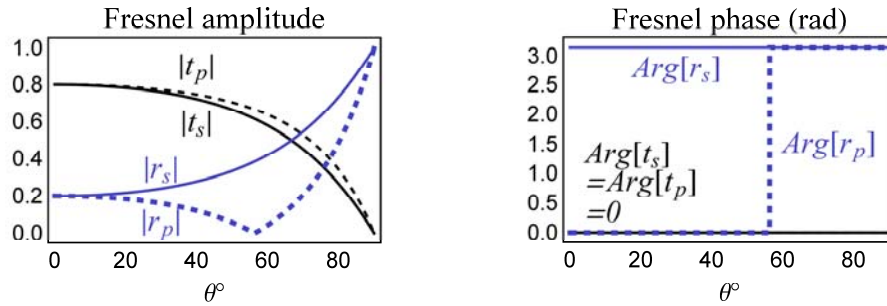


Figure 3.3 Fresnel coefficients, amplitude (left) and phase (right), for transmission and reflection at an air/glass interface. For external reflection from refractive index 1 to refractive index 1.5, the Brewster's angle is 56.31° . At normal incidence, the reflected s - and p -polarizations have a Fresnel π phase shift due to a coordinate flip during reflection.

In refraction or reflection, the incident and exiting local coordinate systems are pairs of three right-handed orthonormal basis vectors $(\hat{s}, \hat{p}, \hat{k})$ and $(\hat{s}', \hat{p}', \hat{k}')$,

$$\begin{aligned} \hat{s} &= (s_x, s_y, s_z) = \frac{\hat{\mathbf{k}} \times \hat{\boldsymbol{\eta}}}{|\hat{\mathbf{k}} \times \hat{\boldsymbol{\eta}}|}, & \hat{\mathbf{p}} &= (p_x, p_y, p_z) = \hat{\mathbf{k}} \times \hat{\mathbf{s}} \\ \hat{s}' &= (s'_x, s'_y, s'_z) = \frac{\hat{\mathbf{k}}' \times \hat{\boldsymbol{\eta}}}{|\hat{\mathbf{k}}' \times \hat{\boldsymbol{\eta}}|}, & \hat{\mathbf{p}}' &= (p'_x, p'_y, p'_z) = \hat{\mathbf{k}}' \times \hat{\mathbf{s}}' \end{aligned} \quad (3.3)$$

where $\hat{\boldsymbol{\eta}}$ is the surface normal of the interface, $\hat{\mathbf{k}} = (k_x, k_y, k_z)$ is the incident propagation direction and $\hat{\mathbf{k}}' = (k'_x, k'_y, k'_z)$ is the exiting propagation direction, as shown in Figure 3.4.

For an isotropic interface, $\hat{\mathbf{k}}$ and $\hat{\mathbf{p}}$ lie in the PoI, while $\hat{\mathbf{s}}$ is orthogonal to the PoI, and $\hat{\mathbf{s}}' = \hat{\mathbf{s}}$.

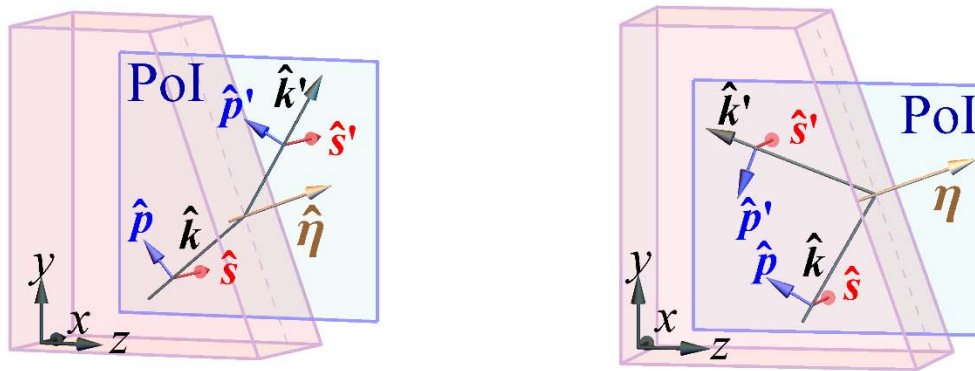


Figure 3.4 The incident and exiting s - p - k basis for refraction (left) and reflection (right) are shown. The plane of incidence (PoI) is the blue plane containing \mathbf{k} , \mathbf{p} , and $\boldsymbol{\eta}$.

The Jones matrix is transformed into the \mathbf{P} matrix by an orthonormal transformation^{††}. The \mathbf{P} matrix is calculated as

$$\mathbf{P} = \mathbf{O}_{\text{out}} \mathbf{J}_{3\text{D}} \mathbf{O}_{\text{in}}^{-1}, \quad (3.4)$$

where

$$\mathbf{O}_{\text{in}}^{-1} = \begin{pmatrix} s_x & p_x & k_x \\ s_y & p_y & k_y \\ s_z & p_z & k_z \end{pmatrix}^{-1} \quad (3.5)$$

^{††} An orthogonal transformation is a rotation from one coordinate system to another. It is performed by real

unitary rotation matrix $\mathbf{R} = \begin{pmatrix} a_x & b_x & c_x \\ a_y & b_y & c_y \\ a_z & b_z & c_z \end{pmatrix}$. \mathbf{R} rotates global $(\hat{\mathbf{x}}, \hat{\mathbf{y}}, \hat{\mathbf{z}})$ coordinate into $(\hat{\mathbf{a}}, \hat{\mathbf{b}}, \hat{\mathbf{c}})$. Similarly \mathbf{R}^{-1}

¹ rotates $(\hat{\mathbf{a}}, \hat{\mathbf{b}}, \hat{\mathbf{c}})$ back to $(\hat{\mathbf{x}}, \hat{\mathbf{y}}, \hat{\mathbf{z}})$.

operates on the incident \mathbf{E} in global Cartesian coordinate systems and calculates the $(\hat{\mathbf{s}}, \hat{\mathbf{p}}, \hat{\mathbf{k}})$ basis components for the incident light, $(E_s, E_p, 0)$ which is a projection of \mathbf{E} onto the s - p incident local coordinate systems. The 3×3 matrix

$$\mathbf{J}_{3\mathbf{D}} = \begin{pmatrix} J_{ss} & J_{ps} & 0 \\ J_{sp} & J_{pp} & 0 \\ 0 & 0 & 1 \end{pmatrix} \quad (3.6)$$

or,

$$\mathbf{J}_{3\mathbf{D}} = \begin{pmatrix} r_s & 0 & 0 \\ 0 & r_p & 0 \\ 0 & 0 & 1 \end{pmatrix} \quad \text{and} \quad \mathbf{J}_{3\mathbf{D}} = \begin{pmatrix} t_s & 0 & 0 \\ 0 & t_p & 0 \\ 0 & 0 & 1 \end{pmatrix} \quad (3.7)$$

for Fresnel refraction and reflection. Equations (3.6) and (3.7) are extended Jones matrix which describes amplitude and phase change to the s and p components. Then the matrix

$$\mathbf{O}_{\text{out}} = \begin{pmatrix} s'_x & p'_x & k'_x \\ s'_y & p'_y & k'_y \\ s'_z & p'_z & k'_z \end{pmatrix} \quad (3.8)$$

rotates the resultant field from the local $(\hat{\mathbf{s}}, \hat{\mathbf{p}}, \hat{\mathbf{k}}')$ coordinate system back to the global coordinate systems.

The polarization of a ray propagating through multiple interfaces is represented by multiplying the \mathbf{P} matrices in the order along the ray path as

$$\mathbf{P}_{\text{total}} = \mathbf{P}_N \cdot \mathbf{P}_{N-1} \cdots \mathbf{P}_n \cdots \mathbf{P}_2 \cdot \mathbf{P}_1 = \prod_{n=1}^N \mathbf{P}_{N-n+1} \quad (3.9)$$

where the ray interacts with surface 1 first and surface N last.

The \mathbf{P} matrix for a single isotropic interface with equation (3.7) performs the following:

$$\begin{aligned}\mathbf{P} \hat{\mathbf{E}}_s &= \mathbf{E}'_s = a_s \hat{\mathbf{s}}', \\ \mathbf{P} \hat{\mathbf{E}}_p &= \mathbf{E}'_p = a_p \hat{\mathbf{p}}', \text{ and} \\ \mathbf{P} \hat{\mathbf{k}} &= \hat{\mathbf{k}}',\end{aligned}\tag{3.10}$$

where a_s is r_s or t_s , and a_p is r_p or t_p . In general, the \mathbf{P} matrix representing interactions of multiple surfaces with non-aligned s - and p -polarizations or the \mathbf{P} matrix derived from equation (3.6) with non-zero s and p coupling performs the following:

$$\begin{aligned}\mathbf{P} \hat{\mathbf{E}}_s &= J_{ss} \hat{\mathbf{s}}' + J_{sp} \hat{\mathbf{p}}', \\ \mathbf{P} \hat{\mathbf{E}}_p &= J_{ps} \hat{\mathbf{s}}' + J_{pp} \hat{\mathbf{p}}', \text{ and} \\ \mathbf{P} \hat{\mathbf{k}} &= \hat{\mathbf{k}}' .\end{aligned}\tag{3.11}$$

Two example calculations of transforming a Jones matrix to a \mathbf{P} matrix are presented in the following: a ray reflects from a metal surface and a ray transmits through a half wave plate.

Consider a gold fold mirror shown in Figure 3.5. A converging beam reflected from the mirror is simulated as a grid of rays evenly spaced in angle. The mirror's surface normal is $(0, -1, -1)/\sqrt{2}$. Each ray in the grid has a different $\hat{\mathbf{k}}$, and only one of these rays at the edge of field (yellow highlight in Figure 3.5) is chosen to demonstrate the \mathbf{P} matrix calculation.

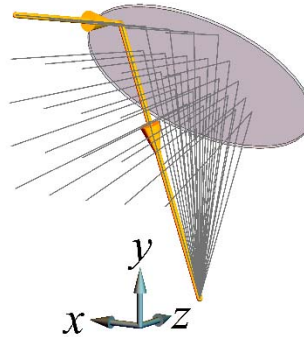


Figure 3.5 A converging grid of rays at 765nm reflects from a gold fold mirror with refractive index $0.718 + 4.749i$.

The selected incident ray with $\hat{\mathbf{k}} = (-0.195, -0.195, 0.961)$ reflects from the mirror with reflected $\hat{\mathbf{k}}' = (-0.195, -0.961, 0.195)$, so the incident and reflected angles are both 57.184° . With equation (3.3), the incident $\hat{\mathbf{s}} = (-0.973, 0.164, -0.164)$ and $\hat{\mathbf{p}} = (-0.126, -0.967, -0.221)$, and the exiting $\hat{\mathbf{s}}' = (-0.973, 0.164, -0.164)$ and $\hat{\mathbf{p}}' = (0.126, -0.221, -0.967)$. The Fresnel reflection coefficients r_s and r_p are $0.992e^{i2.918}$ and $0.975e^{-i0.751}$ respectively, as shown in Figure 3.6.

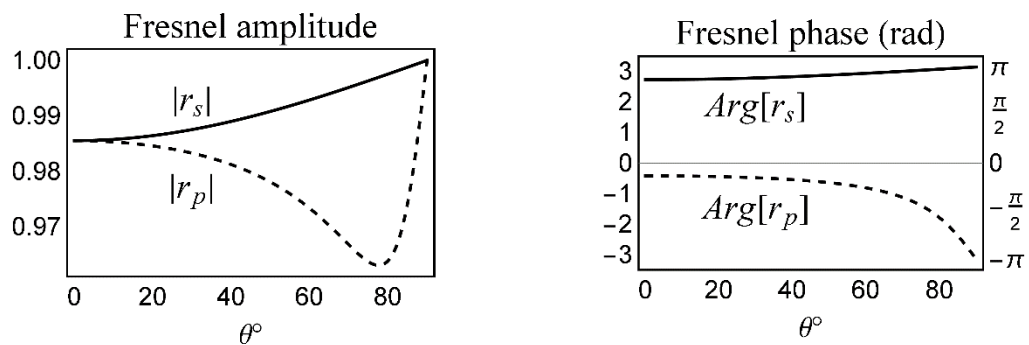


Figure 3.6 Fresnel coefficients, amplitude (left) and phase (right), for reflection at an air/gold interface. At normal incidence the s - and p -polarizations have a Fresnel π phase shift due to a coordinate flip during reflection.

With equation (3.4),

$$\mathbf{P} = \begin{pmatrix} -0.973 & 0.126 & -0.195 \\ 0.164 & -0.221 & -0.961 \\ -0.164 & -0.967 & 0.195 \end{pmatrix} \begin{pmatrix} 0.992e^{i2.918} & 0 & 0 \\ 0 & 0.975e^{-i0.751} & 0 \\ 0 & 0 & 1 \end{pmatrix} \begin{pmatrix} -0.973 & -0.126 & -0.195 \\ 0.164 & -0.967 & -0.195 \\ -0.164 & -0.221 & 0.961 \end{pmatrix}^{-1}$$

$$= \begin{pmatrix} -0.889 + 0.219i & 0.106 + 0.046i & -0.361 + 0.054i \\ 0.361 - 0.054i & 0.314 - 0.137i & -0.863 - 0.039i \\ -0.106 - 0.046i & 0.655 - 0.628i & 0.314 - 0.137i \end{pmatrix}.$$

Through the \mathbf{P} matrix, the electric field \mathbf{E} in the $(\hat{\mathbf{s}}, \hat{\mathbf{p}}, \hat{\mathbf{k}})$ basis is mapped to $(r_s \hat{\mathbf{s}}', r_p \hat{\mathbf{p}}', \hat{\mathbf{k}}')$.

Since both rotation matrices, \mathbf{O}_{in} and \mathbf{O}_{out} , are defined by right-handed orthonormal bases, two of the three exiting basis, $\hat{\mathbf{k}}'$ and $\hat{\mathbf{p}}'$, have a π phase change due to the changing local coordinate systems in reflection, where $\hat{\mathbf{k}}'$ is understood as reflection, and a π phase in $\hat{\mathbf{p}}'$ is added to $\text{Arg}[r_p]$. So, the physical phase shift upon reflection for s - and p -polarizations are

$$\phi_{rs} = \text{Arg}[r_s] \quad \text{and} \quad \phi_{rp} = \pi + \text{Arg}[r_p], \quad (3.12)$$

as shown in Figure 3.7. At normal incidence, the phase change of the degenerate s - and p -polarizations are both 2.727 radian.

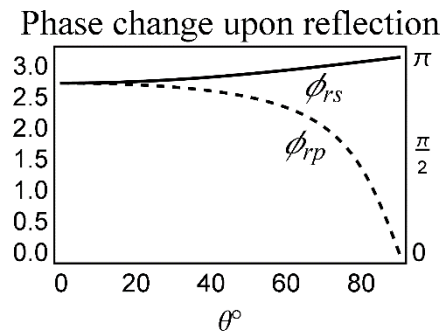


Figure 3.7 Phase change of electric field upon reflection at an air/gold interface. At normal incidence, the s - and p -polarizations are degenerate.

Consider a ray with $\hat{\mathbf{k}} = (0, \sin 10^\circ, \cos 10^\circ)$ that passes through a half waveplate which has its fast axis oriented α from the local x axis, surface normal $\hat{\mathbf{n}} = (0, \sin 10^\circ, \cos 10^\circ)$, and Jones matrix $\begin{pmatrix} \cos 2\alpha & \sin 2\alpha \\ \sin 2\alpha & -\cos 2\alpha \end{pmatrix}$, as shown in Figure 3.8. The finite thickness of the half wave plate is ignored in this example.

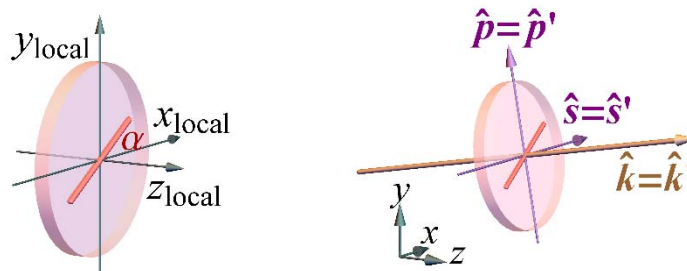


Figure 3.8 (Left) A half wave plate has its fast axis (pink line) oriented at α from the x_{local} axis. (Right) The plate is tilted 10° from the z axis. A normal incident ray (brown arrow) passes through the tilted waveplate in the global xyz coordinate systems.

For normal incidence, s - and p -polarizations are degenerate. $\hat{\mathbf{s}}$ is chosen to be $(1, 0, 0)$.

Then $\hat{\mathbf{p}} = (0, \cos 10^\circ, -\sin 10^\circ)$, calculated by equation (3.3). For this waveplate example,

$\hat{\mathbf{s}} = \hat{\mathbf{s}}'$, $\hat{\mathbf{p}} = \hat{\mathbf{p}}'$, and $\hat{\mathbf{k}} = \hat{\mathbf{k}}'$. By equation (3.4), the \mathbf{P} matrix representing this ray normally incident on the tilted waveplate is

$$\mathbf{P} = \begin{pmatrix} 1 & 0 & 0 \\ 0 & \cos 10^\circ & \sin 10^\circ \\ 0 & -\sin 10^\circ & \cos 10^\circ \end{pmatrix} \begin{pmatrix} \cos 2\alpha & \sin 2\alpha & 0 \\ \sin 2\alpha & -\cos 2\alpha & 0 \\ 0 & 0 & 1 \end{pmatrix} \begin{pmatrix} 1 & 0 & 0 \\ 0 & \cos 10^\circ & \sin 10^\circ \\ 0 & -\sin 10^\circ & \cos 10^\circ \end{pmatrix}^{-1}$$

$$= \begin{pmatrix} \cos 2\alpha & \cos 10^\circ \sin 2\alpha & -\sin 10^\circ \sin 2\alpha \\ \cos 10^\circ \sin 2\alpha & -\cos^2 10^\circ \cos 2\alpha + \sin^2 10^\circ & \cos^2 \alpha \sin 20^\circ \\ -\sin 10^\circ \sin 2\alpha & \cos^2 \alpha \sin 20^\circ & \cos^2 10^\circ - \cos 2\alpha \sin^2 10^\circ \end{pmatrix}.$$

The incident p -polarization $\begin{pmatrix} 0 \\ \cos 10^\circ \\ -\sin 10^\circ \end{pmatrix}$, originally oriented at $\pi/2 - \alpha$ from the fast axis, is

rotated to $\mathbf{P} \cdot \begin{pmatrix} 0 \\ \cos 10^\circ \\ -\sin 10^\circ \end{pmatrix} = \begin{pmatrix} \sin 2\alpha \\ -\cos 10^\circ \cos 2\alpha \\ \sin 10^\circ \cos 2\alpha \end{pmatrix}$, $\cos^{-1}(\sin 2\alpha)$ from the fast axis. The

incident s -polarization, originally oriented at α from the fast axis, is rotated to

$\mathbf{P} \cdot \begin{pmatrix} 1 \\ 0 \\ 0 \end{pmatrix} = \begin{pmatrix} \cos 2\alpha \\ \cos 10^\circ \sin 2\alpha \\ -\sin 10^\circ \sin 2\alpha \end{pmatrix}$, 2α from the fast axis.

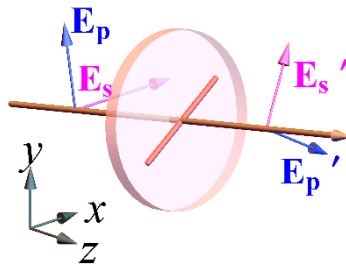


Figure 3.9 The incident electric field \mathbf{E}_s (magenta) and \mathbf{E}_p (blue) passes through a half wave plate shown in Figure 3.8 and rotates to \mathbf{E}_s' and \mathbf{E}_p' .

3.3 Calculations of the \mathbf{P} matrix from 3D polarization vectors

In this section, the \mathbf{P} matrix is derived for a pair of incident and exiting modes through an anisotropic intercept where ray doubling occurs. For example, part of the energy of an e -mode refracts to a *fast*-mode at a uniaxial/biaxial interface, or the p -polarized component couples to right circularly polarized light through an isotropic/optically-active interface. The electromagnetic fields of a pair of incident and exiting modes propagating through an isotropic interface and an anisotropic interface are depicted in Figure 3.10. $\hat{\mathbf{E}}_s \perp \hat{\mathbf{E}}_p \perp \hat{\mathbf{S}} = \hat{\mathbf{k}}$ within the isotropic medium, and $\hat{\mathbf{E}}_m \perp \hat{\mathbf{E}}_n \perp \hat{\mathbf{S}} \neq \hat{\mathbf{k}}$ within the anisotropic medium, where $\hat{\mathbf{E}}_m$ and $\hat{\mathbf{E}}_n$ are orthogonal electric fields in the transverse plane of $\hat{\mathbf{S}}$.

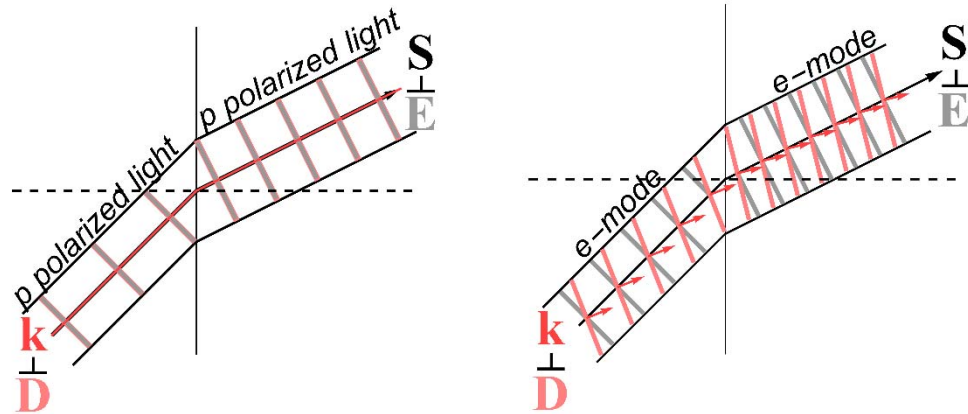


Figure 3.10 The incident and refracted \mathbf{E} (gray), \mathbf{D} (pink), \mathbf{k} (red) and \mathbf{S} (black) field orientations of an isotropic/isotropic (left) and a birefringent/birefringent (right) interface. Only p -polarization coupling to p -polarization is shown refracting through the isotropic interface. Only e -mode coupling to e -mode is shown refracting through the birefringent interface.

In an anisotropic ray trace, two \mathbf{P} matrices are needed to represent the two refracted or reflected modes at an anisotropic ray intercept because the two exiting rays take different paths. Since the incident and exiting eigenmodes are generally not aligned, one of the

incident eigenmodes can couple light into both exiting eigenmodes. The \mathbf{P} matrix maps the three incident orthonormal basis vectors $(\hat{\mathbf{E}}_{\mathbf{m}}, \hat{\mathbf{E}}_{\mathbf{n}}, \hat{\mathbf{S}})$ into three exiting vectors $(\mathbf{E}'_{\mathbf{m}}, \mathbf{E}'_{\mathbf{n}}, \hat{\mathbf{S}}')$ associated with one eigenstate in the exiting medium along $\hat{\mathbf{S}}'$. So, the conditions defining the two exiting \mathbf{P} matrices at an anisotropic ray intercept are

$$\begin{cases} \mathbf{P}_{\mathbf{v}} \hat{\mathbf{E}}_{\mathbf{m}} = \mathbf{E}'_{\mathbf{mv}} = a_{mv} \hat{\mathbf{E}}_{\mathbf{v}}, \\ \mathbf{P}_{\mathbf{v}} \hat{\mathbf{E}}_{\mathbf{n}} = \mathbf{E}'_{\mathbf{nv}} = a_{nv} \hat{\mathbf{E}}_{\mathbf{v}}, \\ \mathbf{P}_{\mathbf{v}} \hat{\mathbf{S}} = \hat{\mathbf{S}}'_{\mathbf{v}}, \end{cases} \quad \text{and} \quad \begin{cases} \mathbf{P}_{\mathbf{w}} \hat{\mathbf{E}}_{\mathbf{m}} = \mathbf{E}'_{\mathbf{mw}} = a_{mw} \hat{\mathbf{E}}_{\mathbf{w}}, \\ \mathbf{P}_{\mathbf{w}} \hat{\mathbf{E}}_{\mathbf{n}} = \mathbf{E}'_{\mathbf{nw}} = a_{nw} \hat{\mathbf{E}}_{\mathbf{w}}, \\ \mathbf{P}_{\mathbf{w}} \hat{\mathbf{S}} = \hat{\mathbf{S}}'_{\mathbf{w}}, \end{cases} \quad (3.13)$$

for refraction/reflection, where $(a_{mv}, a_{mw}, a_{nv}, a_{nw})$ are the complex amplitude coefficients associated with the \mathbf{E} field coupling between each pair of incident and exiting states. These coefficients are calculated in section 2.4. In general, the incident $\hat{\mathbf{E}}_{\mathbf{m}}$ couples to both $\mathbf{E}'_{\mathbf{mv}}$ and $\mathbf{E}'_{\mathbf{mw}}$, and $\hat{\mathbf{E}}_{\mathbf{n}}$ couples to both $\mathbf{E}'_{\mathbf{nv}}$ and $\mathbf{E}'_{\mathbf{nw}}$. These exiting \mathbf{E} fields $\mathbf{E}'_{\mathbf{mv}}$ and $\mathbf{E}'_{\mathbf{nv}}$ are in the transverse plane of $\hat{\mathbf{S}}'_{\mathbf{v}}$; $\mathbf{E}'_{\mathbf{mw}}$ and $\mathbf{E}'_{\mathbf{nw}}$ are in the transverse plane of $\hat{\mathbf{S}}'_{\mathbf{w}}$ in the exiting medium. The refracted/reflected exiting electric fields resulting from $\hat{\mathbf{E}}_{\mathbf{m}}$ and $\hat{\mathbf{E}}_{\mathbf{n}}$ at the ray intercept are

$$\mathbf{E}'_{\mathbf{m}}(\mathbf{r}, t) = \mathcal{R}e \left\{ E_{inc} \left[a_{mv} \hat{\mathbf{E}}_{\mathbf{v}} e^{i \frac{2\pi}{\lambda} n_{mv} \hat{\mathbf{k}}_{\mathbf{mv}} \cdot \mathbf{r}} + a_{mw} \hat{\mathbf{E}}_{\mathbf{w}} e^{i \frac{2\pi}{\lambda} n_{mw} \hat{\mathbf{k}}_{\mathbf{mw}} \cdot \mathbf{r}} \right] e^{-i\omega t} \right\}, \quad (3.14)$$

and

$$\mathbf{E}'_{\mathbf{n}}(\mathbf{r}, t) = \mathcal{R}e \left\{ E_{inc} \left[a_{nv} \hat{\mathbf{E}}_{\mathbf{v}} e^{i \frac{2\pi}{\lambda} n_{nv} \hat{\mathbf{k}}_{\mathbf{nv}} \cdot \mathbf{r}} + a_{nw} \hat{\mathbf{E}}_{\mathbf{w}} e^{i \frac{2\pi}{\lambda} n_{nw} \hat{\mathbf{k}}_{\mathbf{nw}} \cdot \mathbf{r}} \right] e^{-i\omega t} \right\}. \quad (3.15)$$

Consider the o - and e -modes with two different \hat{S}' emerging from an isotropic/uniaxial intercept: they each have their own \mathbf{P} matrix because $\hat{S}'_o \neq \hat{S}'_e$. In this case, (m, n, v, w) in equation (3.13) are (s, p, o, e) ; the detailed calculations of \mathbf{P}_o and \mathbf{P}_e are described in section 3.4.1. In general, $\hat{\mathbf{E}}_m$ can couple to both $\hat{\mathbf{E}}_v$ and $\hat{\mathbf{E}}_w$, and $(a_{mv}, a_{mw}, a_{nv}, a_{nw})$ are all non-zero. In some situations, the amplitude coefficients are set to zero for certain properties of the interface. For example, at an uncoated isotropic ray intercept, the coupling between s - and p -polarizations is zero; $(m, n, v, w) = (s, p, s', p')$ and $(a_{mw}, a_{nv}) = (a_{sp'}, a_{ps'}) = (0, 0)$. Also, if a ray is incident at a uniaxial/isotropic intercept polarized in only one eigenmode for a given \hat{S} , then $(m, n, v, w) = (e, e_\perp, s, p)$ and $(a_{nv}, a_{nw}) = (a_{e_\perp s}, a_{e_\perp p}) = (0, 0)$. This will be further explained in section 3.4.2. Since each exiting mode is in a particular eigenpolarization, the corresponding \mathbf{P} matrix of the exiting mode has the form of a polarizer.

By placing the three pairs of incident and exiting 3×1 vectors in matrix form, the \mathbf{P} matrix is calculated as

$$\begin{aligned}
 \mathbf{P} &= \begin{pmatrix} \mathbf{E}'_m & \mathbf{E}'_n & \hat{S}' \end{pmatrix} \cdot \begin{pmatrix} \hat{\mathbf{E}}_m & \hat{\mathbf{E}}_n & \hat{S} \end{pmatrix}^{-1} \\
 &= \begin{pmatrix} E'_{m,x} & E'_{n,x} & S'_x \\ E'_{m,y} & E'_{n,y} & S'_y \\ E'_{m,z} & E'_{n,z} & S'_z \end{pmatrix} \cdot \begin{pmatrix} E_{m,x} & E_{n,x} & S_x \\ E_{m,y} & E_{n,y} & S_y \\ E_{m,z} & E_{n,z} & S_z \end{pmatrix}^{-1} \\
 &= \begin{pmatrix} E'_{m,x} & E'_{n,x} & S'_x \\ E'_{m,y} & E'_{n,y} & S'_y \\ E'_{m,z} & E'_{n,z} & S'_z \end{pmatrix} \cdot \begin{pmatrix} E_{m,x} & E_{n,x} & S_x \\ E_{m,y} & E_{n,y} & S_y \\ E_{m,z} & E_{n,z} & S_z \end{pmatrix}^T,
 \end{aligned} \tag{3.16}$$

where $(\hat{\mathbf{E}}_m \ \hat{\mathbf{E}}_n \ \hat{\mathbf{S}})$ is a real unitary matrix, so its inverse equals its transpose. The amplitude coefficients for the interface are contained in $(\mathbf{E}'_m \ \mathbf{E}'_n \ \hat{\mathbf{S}}')$.

3.4 Calculating \mathbf{P} matrices for anisotropic interfaces

Since the \mathbf{P} matrix is defined for one pair of $\hat{\mathbf{S}}$ and $\hat{\mathbf{S}}'$, the multiple exiting modes from anisotropic interfaces need to be described by multiple \mathbf{P} matrices. The derivations of the \mathbf{P} matrices for the three cases of uncoated anisotropic interfaces: (1) isotropic/anisotropic, (2) anisotropic/isotropic, and (3) anisotropic/anisotropic interfaces in refraction and reflection are shown in the following sub-sections. In the derivations, the (m, n, v, w) states used in equation (3.13) for each of the cases are shown in Table 3.1. In an isotropic medium, s - and p -modes share the same \mathbf{S} , so the associated \mathbf{P} matrices can be reduced to one \mathbf{P} matrix (see sections 3.4.1 and 3.4.2).

Table 3.1 The polarization states for calculating the \mathbf{P} matrices for an uncoated interface. (m, n, v, w) are defined in equation (3.13). ' indicates exiting mode. The split eigenmodes in an anisotropic material are described by two \mathbf{P} matrices. However, the two \mathbf{P} matrices for s' and p' exiting states can be combined (\Rightarrow) to one \mathbf{P} matrix

Interface	Reflected $(m, n) \rightarrow v$ & $(m, n) \rightarrow w$	Refracted $(m, n) \rightarrow v$ & $(m, n) \rightarrow w$
Isotropic/ Isotropic	$(s, p) \rightarrow s'$ $(s, p) \rightarrow p'$ $\Rightarrow (s, p) \rightarrow (s', p')$	$(s, p) \rightarrow s'$ $(s, p) \rightarrow p'$ $\Rightarrow (s, p) \rightarrow (s', p')$
Isotropic/ Anisotropic	$(s, p) \rightarrow s'$ $(s, p) \rightarrow p'$ $\Rightarrow (s, p) \rightarrow (s', p')$	$(s, p) \rightarrow v$ $(s, p) \rightarrow w$
Anisotropic/ Isotropic	$(m, n) \rightarrow v$ $(m, n) \rightarrow w$	$(m, n) \rightarrow s'$ $(m, n) \rightarrow p'$ $\Rightarrow (m, n) \rightarrow (s', p')$
Anisotropic/ Anisotropic	$(m, n) \rightarrow v$ $(m, n) \rightarrow w$	$(m, n) \rightarrow v$ $(m, n) \rightarrow w$

3.4.1 Isotropic to anisotropic intercept

For an isotropic incident medium, the incident eigenstates are s - and p -polarizations,

$$\hat{\mathbf{E}}_s = \frac{\hat{\mathbf{S}} \times \hat{\boldsymbol{\eta}}}{|\hat{\mathbf{S}} \times \hat{\boldsymbol{\eta}}|} \quad \text{and} \quad \hat{\mathbf{E}}_p = \frac{\hat{\mathbf{S}} \times \hat{\mathbf{E}}_s}{|\hat{\mathbf{S}} \times \hat{\mathbf{E}}_s|}. \quad (3.17)$$

In this case, two reflected modes reflect back to the incident isotropic medium and two refracted modes refract into the birefringent medium. The two reflected s - and p -modes share the same $\hat{\mathbf{S}}'$, while the two refracted anisotropic modes, labeled with subscripts v and w , split into two directions. So, $(m, n, v, w) = (s, p, s', p')$ in reflection, and (s, p, v, w) for refraction. If the refracting medium is biaxial, the two refracted modes are *fast*- and *slow*-modes; $(m, n, v, w) = (s, p, \text{fast}, \text{slow})$. The refraction of this case is depicted in Figure 3.11.

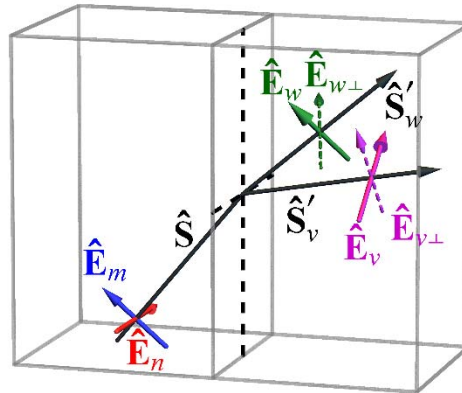


Figure 3.11 Mode coupling in refraction through an isotropic/anisotropic interface. The incident ray with orthogonal modes, labeled as n (red) and m (blue), splits into two exiting modes as v (pink) and w (green) in two directions. In biaxial and uniaxial materials, \mathbf{E}_v and \mathbf{E}_w are linearly polarized. In optically active materials, \mathbf{E}_v and \mathbf{E}_w are circularly polarized. Given a ray with a specific pair of \mathbf{k}'_v and \mathbf{S}'_v in an anisotropic material, the ray can only be polarized in \mathbf{E}_v , so the orthogonal state $\mathbf{E}_{v\perp}$ (dashed arrow) has zero amplitude.

The amplitude coefficients of coupling from each incident mode to each exiting mode are calculated in section 2.4. From equation (2.18), the transmission and reflection amplitude coefficients, t and r , of the exiting modes from each incident mode are

$$\begin{pmatrix} t_{sv} \\ t_{sw} \\ r_{ss'} \\ r_{sp'} \end{pmatrix} = \mathbf{F}^{-1} \cdot \begin{pmatrix} \mathbf{s}_1 \cdot \hat{\mathbf{E}}_s \\ \mathbf{s}_2 \cdot \hat{\mathbf{E}}_s \\ \mathbf{s}_1 \cdot \mathbf{H}_s \\ \mathbf{s}_2 \cdot \mathbf{H}_s \end{pmatrix} \quad \text{and} \quad \begin{pmatrix} t_{pv} \\ t_{pw} \\ r_{ps'} \\ r_{pp'} \end{pmatrix} = \mathbf{F}^{-1} \cdot \begin{pmatrix} \mathbf{s}_1 \cdot \hat{\mathbf{E}}_p \\ \mathbf{s}_2 \cdot \hat{\mathbf{E}}_p \\ \mathbf{s}_1 \cdot \mathbf{H}_p \\ \mathbf{s}_2 \cdot \mathbf{H}_p \end{pmatrix}. \quad (3.18)$$

With these amplitude coefficients and applying equation (3.13), the two reflected \mathbf{P} matrices for the s - and p -modes should satisfy:

$$\begin{cases} \mathbf{P}_{rs} \hat{\mathbf{E}}_s = r_{ss} \hat{\mathbf{E}}_{rs}, \\ \mathbf{P}_{rs} \hat{\mathbf{E}}_p = r_{ps} \hat{\mathbf{E}}_{rs}, \\ \mathbf{P}_{rs} \hat{\mathbf{S}} = \hat{\mathbf{S}}'_{rs}, \end{cases} \quad \text{and} \quad \begin{cases} \mathbf{P}_{rp} \hat{\mathbf{E}}_s = r_{sp} \hat{\mathbf{E}}_{rp}, \\ \mathbf{P}_{rp} \hat{\mathbf{E}}_p = r_{pp} \hat{\mathbf{E}}_{rp}, \\ \mathbf{P}_{rp} \hat{\mathbf{S}} = \hat{\mathbf{S}}'_{rp}. \end{cases} \quad (3.19)$$

With equation (3.16), the two \mathbf{P} matrices for reflection are

$$\begin{aligned} \mathbf{P}_{rs} &= \begin{pmatrix} r_{ss} \hat{\mathbf{E}}_{rs} & r_{ps} \hat{\mathbf{E}}_{rs} & \hat{\mathbf{S}}'_{rs} \end{pmatrix} \cdot \begin{pmatrix} \hat{\mathbf{E}}_s & \hat{\mathbf{E}}_p & \hat{\mathbf{S}} \end{pmatrix}^T \quad \text{and} \\ \mathbf{P}_{rp} &= \begin{pmatrix} r_{sp} \hat{\mathbf{E}}_{rp} & r_{pp} \hat{\mathbf{E}}_{rp} & \hat{\mathbf{S}}'_{rp} \end{pmatrix} \cdot \begin{pmatrix} \hat{\mathbf{E}}_s & \hat{\mathbf{E}}_p & \hat{\mathbf{S}} \end{pmatrix}^T. \end{aligned} \quad (3.20)$$

Since the two reflected modes share the same pair of $\hat{\mathbf{S}}'_{rs} = \hat{\mathbf{S}}'_{rp}$, and the couplings between s - and p -states are zero for an uncoated surface ($r_{sp}=r_{ps}=0$). Therefore \mathbf{P}_{rs} and \mathbf{P}_{rp} are combined to

$$\mathbf{P}_r = \begin{pmatrix} r_{ss} \hat{\mathbf{E}}_{rs} & r_{pp} \hat{\mathbf{E}}_{rp} & \hat{\mathbf{S}}'_r \end{pmatrix} \cdot \begin{pmatrix} \hat{\mathbf{E}}_s & \hat{\mathbf{E}}_p & \hat{\mathbf{S}} \end{pmatrix}^T. \quad (3.21)$$

On the other hand, the two refracted modes split into two directions with different $\hat{\mathbf{S}}'_t$, as shown in Figure 3.9. Therefore, the two refracted \mathbf{P} matrices, which cannot be combined, are needed to describe the two refracted modes. \mathbf{P}_{tv} and \mathbf{P}_{tw} satisfy

$$\begin{cases} \mathbf{P}_{\text{tv}} \hat{\mathbf{E}}_{\text{s}} = t_{\text{sv}} \hat{\mathbf{E}}_{\text{tv}}, \\ \mathbf{P}_{\text{tv}} \hat{\mathbf{E}}_{\text{p}} = t_{\text{pv}} \hat{\mathbf{E}}_{\text{tv}}, \\ \mathbf{P}_{\text{tv}} \hat{\mathbf{S}} = \hat{\mathbf{S}}'_{\text{tv}}, \end{cases} \text{ and } \begin{cases} \mathbf{P}_{\text{tw}} \hat{\mathbf{E}}_{\text{s}} = t_{\text{sw}} \hat{\mathbf{E}}_{\text{tw}}, \\ \mathbf{P}_{\text{tw}} \hat{\mathbf{E}}_{\text{p}} = t_{\text{pw}} \hat{\mathbf{E}}_{\text{tw}}, \\ \mathbf{P}_{\text{tw}} \hat{\mathbf{S}} = \hat{\mathbf{S}}'_{\text{tw}}, \end{cases} \quad (3.22)$$

respectively. So,

$$\begin{aligned} \mathbf{P}_{\text{tv}} &= (t_{\text{sv}} \hat{\mathbf{E}}_{\text{tv}} \quad t_{\text{pv}} \hat{\mathbf{E}}_{\text{tv}} \quad \hat{\mathbf{S}}'_{\text{v}}) \cdot (\hat{\mathbf{E}}_{\text{s}} \quad \hat{\mathbf{E}}_{\text{p}} \quad \hat{\mathbf{S}})^T \text{ and} \\ \mathbf{P}_{\text{tw}} &= (t_{\text{sw}} \hat{\mathbf{E}}_{\text{tw}} \quad t_{\text{pw}} \hat{\mathbf{E}}_{\text{tw}} \quad \hat{\mathbf{S}}'_{\text{w}}) \cdot (\hat{\mathbf{E}}_{\text{s}} \quad \hat{\mathbf{E}}_{\text{p}} \quad \hat{\mathbf{S}})^T. \end{aligned} \quad (3.23)$$

3.4.2 Anisotropic to isotropic intercept

A ray in a birefringent medium with a specified $\hat{\mathbf{k}}$ and $\hat{\mathbf{S}}$ incident on an interface is constrained to be in one of the two eigenmodes which is calculated for the previous ray intercept by equations (2.12) through (2.14). The electric field for this incident ray is $\hat{\mathbf{E}}_{\text{m}}$ with index n_m . To construct the \mathbf{P} matrix with equations (3.13) and (3.16), a pseudo electric field or absent mode $\hat{\mathbf{E}}_{\text{n}} = \hat{\mathbf{E}}_{\text{m}\perp}$ conveying no power and orthogonal to $\hat{\mathbf{E}}_{\text{m}}$ is calculated as:

$$\hat{\mathbf{E}}_{\text{n}} = \frac{\hat{\mathbf{S}} \times \hat{\mathbf{E}}_{\text{m}}}{|\hat{\mathbf{S}} \times \hat{\mathbf{E}}_{\text{m}}|}. \quad (3.24)$$

The absent mode has no power because the orthogonal polarization has refracted into another direction and is described by the other \mathbf{P} matrix. This state needs to be defined to properly setup the 3×3 matrices.

The exiting modes for $\hat{\mathbf{E}}_{\text{m}}$ are the s - and p -polarized transmitted states and the two bi-reflected rays with $\hat{\mathbf{E}}_{\text{v}}$ and $\hat{\mathbf{E}}_{\text{w}}$. The refraction is depicted in Figure 3.12.

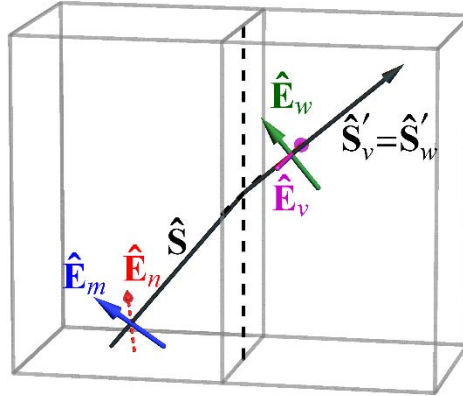


Figure 3.12 Mode coupling in refraction through an anisotropic/isotropic interface. The incident ray is polarized along \mathbf{E}_m (blue) and has a zero amplitude component \mathbf{E}_n (red, dashed arrow). The incident polarization couples to the s - and p -states in the isotropic medium which are \mathbf{E}_v (pink) and \mathbf{E}_w (green) and propagate in the same direction \mathbf{S}' .

Inside the incident anisotropic medium, only $\hat{\mathbf{E}}_m$ carries non-zero amplitude,

$$\begin{pmatrix} t_{ms} \\ t_{mp} \\ r_{mv} \\ r_{mw} \end{pmatrix} = \mathbf{F}^{-1} \cdot \begin{pmatrix} \mathbf{s}_1 \cdot \hat{\mathbf{E}}_1 \\ \mathbf{s}_2 \cdot \hat{\mathbf{E}}_1 \\ \mathbf{s}_1 \cdot \mathbf{H}_1 \\ \mathbf{s}_2 \cdot \mathbf{H}_1 \end{pmatrix}, \quad (3.25)$$

and the amplitude coefficients from $\hat{\mathbf{E}}_n$, (t_{ns} , t_{np} , r_{nv} , r_{nw}) are zeros. As depicted in Figure

3.12, the three pairs of conditions for each transmitted \mathbf{P} matrix are:

$$\left\{ \begin{array}{l} \mathbf{P}_{ts} \hat{\mathbf{E}}_m = t_{ms} \hat{\mathbf{E}}_{ts}, \\ \mathbf{P}_{ts} \hat{\mathbf{E}}_n = t_{ns} \hat{\mathbf{E}}_{ts} = \mathbf{0}, \\ \mathbf{P}_{ts} \hat{\mathbf{S}} = \hat{\mathbf{S}}'_{ts}, \end{array} \right. \text{ and } \left\{ \begin{array}{l} \mathbf{P}_{tp} \hat{\mathbf{E}}_m = t_{mp} \hat{\mathbf{E}}_{tp}, \\ \mathbf{P}_{tp} \hat{\mathbf{E}}_n = t_{np} \hat{\mathbf{E}}_{tp} = \mathbf{0}, \\ \mathbf{P}_{tp} \hat{\mathbf{S}} = \hat{\mathbf{S}}'_{tp}, \end{array} \right. \quad (3.26)$$

where $\mathbf{0}$ is a 3×1 zero vector. Since the transmitted medium is isotropic, $\hat{\mathbf{S}}'_{ts} = \hat{\mathbf{S}}'_{tp} = \hat{\mathbf{S}}$, and

the refracted \mathbf{P} matrix is

$$\mathbf{P}_t = (t_{ms}\hat{\mathbf{E}}_{ts} + t_{mp}\hat{\mathbf{E}}_{tp} \quad \mathbf{0} \quad \hat{\mathbf{S}}_t) \cdot (\hat{\mathbf{E}}_m \quad \hat{\mathbf{E}}_n \quad \hat{\mathbf{S}})^T. \quad (3.27)$$

The two reflected \mathbf{P} matrices for the two rays reflecting back to the anisotropic medium are

$$\begin{aligned} \mathbf{P}_{rv} &= (r_{mv}\hat{\mathbf{E}}_{rv} \quad \mathbf{0} \quad \hat{\mathbf{S}}'_{rv}) \cdot (\hat{\mathbf{E}}_m \quad \hat{\mathbf{E}}_n \quad \hat{\mathbf{S}})^T \text{ and} \\ \mathbf{P}_{rw} &= (r_{mw}\hat{\mathbf{E}}_{rw} \quad \mathbf{0} \quad \hat{\mathbf{S}}'_{rw}) \cdot (\hat{\mathbf{E}}_m \quad \hat{\mathbf{E}}_n \quad \hat{\mathbf{S}})^T. \end{aligned} \quad (3.28)$$

The calculation shown in this section is for one incident mode only. In general each incident mode has its own associated calculations of \mathbf{P} matrices for transmission and reflection.

3.4.3 Anisotropic to anisotropic intercept

Similar to the last case, $\hat{\mathbf{E}}_m$ is the incident state along $\hat{\mathbf{S}}$, and $\hat{\mathbf{E}}_n = \hat{\mathbf{E}}_{m\perp}$ is an absent mode with zero energy constructed orthogonal to $\hat{\mathbf{E}}_m$. The four exiting modes all propagate in different directions. The refraction is depicted in Figure 3.13.

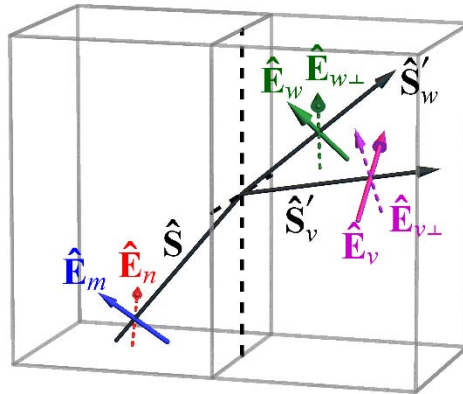


Figure 3.13 Mode coupling in refraction through an anisotropic/anisotropic interface. The incident ray propagating in \mathbf{S} is polarized along \mathbf{E}_m (blue) and has a zero amplitude component \mathbf{E}_n (red, dashed arrow). It splits into two exiting modes as v (green) and w (pink) in two directions. Their orthogonal states $\mathbf{E}_{v\perp}$ and $\mathbf{E}_{w\perp}$ (dashed arrows) both have zero amplitude.

The amplitude coefficients associated with $\hat{\mathbf{E}}_{\mathbf{m}}$ are calculated by (2.18), and the amplitude coefficients associated with $\hat{\mathbf{E}}_{\mathbf{n}}$ are zeros. The \mathbf{P} matrices for the two transmitted rays are:

$$\begin{aligned} \mathbf{P}_{\mathbf{tv}} &= (t_{mv} \hat{\mathbf{E}}_{\mathbf{tv}} \mathbf{0} \hat{\mathbf{S}}'_{\mathbf{tv}}) \cdot (\hat{\mathbf{E}}_{\mathbf{m}} \hat{\mathbf{E}}_{\mathbf{n}} \hat{\mathbf{S}})^T \text{ and} \\ \mathbf{P}_{\mathbf{tw}} &= (t_{mw} \hat{\mathbf{E}}_{\mathbf{tw}} \mathbf{0} \hat{\mathbf{S}}'_{\mathbf{tw}}) \cdot (\hat{\mathbf{E}}_{\mathbf{m}} \hat{\mathbf{E}}_{\mathbf{n}} \hat{\mathbf{S}})^T . \end{aligned} \quad (3.29)$$

The \mathbf{P} matrices for the two reflected rays are:

$$\begin{aligned} \mathbf{P}_{\mathbf{rv}} &= (r_{rv} \hat{\mathbf{E}}_{\mathbf{rv}} \mathbf{0} \hat{\mathbf{S}}'_{\mathbf{rv}}) \cdot (\hat{\mathbf{E}}_{\mathbf{m}} \hat{\mathbf{E}}_{\mathbf{n}} \hat{\mathbf{S}})^T \text{ and} \\ \mathbf{P}_{\mathbf{rw}} &= (r_{rw} \hat{\mathbf{E}}_{\mathbf{rw}} \mathbf{0} \hat{\mathbf{S}}'_{\mathbf{rw}}) \cdot (\hat{\mathbf{E}}_{\mathbf{m}} \hat{\mathbf{E}}_{\mathbf{n}} \hat{\mathbf{S}})^T . \end{aligned} \quad (3.30)$$

3.4.4 Example

Consider the ray doublings shown in Figure 3.14. The o - i and e - i couplings at the second surface are described by two \mathbf{P} matrices.

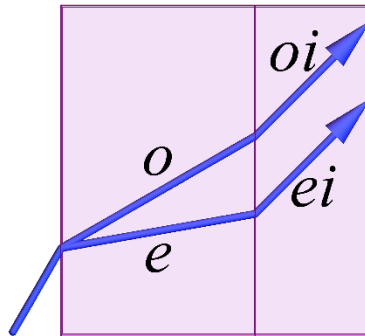


Figure 3.14 An incident ray refracts through two anisotropic interfaces to two branches of rays. A ray starts from an isotropic medium, splits into o - and e -modes, and refracts into oi - and ei -modes.

Following the one ray path from o to oi , the Poynting vector changes from $\hat{\mathbf{S}}_o$ to $\hat{\mathbf{S}}_i$, the o_\perp -mode (orthogonal states of o -mode) along $\hat{\mathbf{S}}_o$ has zero energy, so the coupling from o_\perp to $o_\perp-i$ is zero. Then applying equation (3.26) as shown in section 3.4.2,

$$\begin{cases} \mathbf{P}_{oi} \hat{\mathbf{E}}_o = t_{os} \hat{\mathbf{E}}_s + t_{op} \hat{\mathbf{E}}_p, \\ \mathbf{P}_{oi} \hat{\mathbf{E}}_{o\perp} = \mathbf{0}, \text{ and} \\ \mathbf{P}_{oi} \hat{\mathbf{S}}_o = \hat{\mathbf{S}}_i. \end{cases} \quad (3.31)$$

Then,

$$\mathbf{P}_{oi} = \begin{pmatrix} t_{os} \hat{\mathbf{E}}_s + t_{op} \hat{\mathbf{E}}_p & \mathbf{0} & \hat{\mathbf{S}}_i \end{pmatrix} \cdot \begin{pmatrix} \hat{\mathbf{E}}_o & \hat{\mathbf{E}}_{o\perp} & \hat{\mathbf{S}} \end{pmatrix}^T. \quad (3.32)$$

Similarly,

$$\mathbf{P}_{ei} = \begin{pmatrix} t_{es} \hat{\mathbf{E}}_s + t_{ep} \hat{\mathbf{E}}_p & \mathbf{0} & \hat{\mathbf{S}}_i \end{pmatrix} \cdot \begin{pmatrix} \hat{\mathbf{E}}_e & \hat{\mathbf{E}}_{e\perp} & \hat{\mathbf{S}} \end{pmatrix}^T. \quad (3.33)$$

3.5 Incorporating optical path length into \mathbf{P} matrices

Many optical components utilize anisotropic materials to induce a desired retardance. This important property can be incorporated into the \mathbf{P} matrix. The goal of incorporating the OPL into the \mathbf{P} matrix is to include the phase change of a ray segment in the amplitude of the two \mathbf{E} field components. The definition of the \mathbf{P} matrix is adjusted to map the orthogonal vectors $(\hat{\mathbf{E}}_m, \hat{\mathbf{E}}_n, \hat{\mathbf{S}})$ to $\left(a_m e^{i \frac{2\pi}{\lambda} OPL} \hat{\mathbf{E}}'_m, a_n e^{i \frac{2\pi}{\lambda} OPL} \hat{\mathbf{E}}'_n, \hat{\mathbf{S}}' \right)$, where the OPL of an eigenmode propagating in anisotropic material is defined in equation (2.17). In some applications, such as Michelson interferometer, optical coherence tomography (OCT), and pulse measurement, the cumulative OPL is desired for accurate simulation, and

the absolute *OPL* should be kept separately from the \mathbf{P} matrix. In other applications, such as utilizing retarders to generate elliptically polarized light, only the relative phase (wrap around 2π) is under consideration, and the *OPL* can be comprised in the \mathbf{P} matrix. This section will show two algorithms to include the *OPL* into the \mathbf{P} matrix. Depending on the purpose of the analysis, one method might be better than the other, but they produce the same overall \mathbf{P} matrix. These algorithms will be used in Chapter 4 to incorporate *OPL* to the \mathbf{P} matrix representing the property of a waveplate.

In the first algorithm, the \mathbf{P} matrix of the light-surface interaction and the \mathbf{P} matrix related to the propagation are considered as two separate polarization changes happened sequentially along a ray path. At a ray intercept, $\mathbf{P}_{\text{interface}}$ maps $(\hat{\mathbf{E}}_{\mathbf{m}}, \hat{\mathbf{E}}_{\mathbf{n}}, \hat{\mathbf{S}})$ to $(a_m \hat{\mathbf{E}}'_{\mathbf{m}}, a_n \hat{\mathbf{E}}'_{\mathbf{n}}, \hat{\mathbf{S}}')$. With equation (3.16),

$$\mathbf{P}_{\text{interface}} = (a_m \hat{\mathbf{E}}'_{\mathbf{m}} \quad a_n \hat{\mathbf{E}}'_{\mathbf{n}} \quad \hat{\mathbf{S}}') (\hat{\mathbf{E}}_{\mathbf{m}} \quad \hat{\mathbf{E}}_{\mathbf{n}} \quad \hat{\mathbf{S}})^T. \quad (3.34)$$

As this mode propagates, the absolute phase of the mode increases through the material. This is represented by another \mathbf{P} matrix, $\mathbf{P}_{\text{segment}}$ which maps $(\hat{\mathbf{E}}'_{\mathbf{m}}, \hat{\mathbf{E}}'_{\mathbf{n}}, \hat{\mathbf{S}}')$ to

$$\left(e^{i \frac{2\pi}{\lambda} OPL} \hat{\mathbf{E}}'_{\mathbf{m}}, e^{i \frac{2\pi}{\lambda} OPL} \hat{\mathbf{E}}'_{\mathbf{n}}, \hat{\mathbf{S}}' \right);$$

$$\mathbf{P}_{\text{segment}} = \left(e^{i \frac{2\pi}{\lambda} OPL} \hat{\mathbf{E}}'_{\mathbf{m}} \quad e^{i \frac{2\pi}{\lambda} OPL} \hat{\mathbf{E}}'_{\mathbf{n}} \quad \hat{\mathbf{S}}' \right) (\hat{\mathbf{E}}'_{\mathbf{m}} \quad \hat{\mathbf{E}}'_{\mathbf{n}} \quad \hat{\mathbf{S}}')^T. \quad (3.35).$$

Then total \mathbf{P} matrix before the next ray intercept is:

$$\begin{aligned}
& \mathbf{P}_{\text{segment}} \cdot \mathbf{P}_{\text{interface}} \\
&= \begin{pmatrix} e^{i\frac{2\pi}{\lambda}OPL} \hat{\mathbf{E}}'_m & e^{i\frac{2\pi}{\lambda}OPL} \hat{\mathbf{E}}'_n & \hat{\mathbf{S}}' \end{pmatrix} (\hat{\mathbf{E}}'_m \ \hat{\mathbf{E}}'_n \ \hat{\mathbf{S}}')^T (a_m \hat{\mathbf{E}}'_m \ a_n \hat{\mathbf{E}}'_n \ \hat{\mathbf{S}}') (\hat{\mathbf{E}}_m \ \hat{\mathbf{E}}_n \ \hat{\mathbf{S}})^T \quad (3.36) \\
&= \begin{pmatrix} a_m e^{i\frac{2\pi}{\lambda}OPL} \hat{\mathbf{E}}'_m & a_n e^{i\frac{2\pi}{\lambda}OPL} \hat{\mathbf{E}}'_n & \hat{\mathbf{S}}' \end{pmatrix} (\hat{\mathbf{E}}'_m \ \hat{\mathbf{E}}'_n \ \hat{\mathbf{S}}')^T,
\end{aligned}$$

where $\hat{\mathbf{E}}_m \cdot \hat{\mathbf{E}}_n = 0$, $\hat{\mathbf{S}}' \cdot \hat{\mathbf{E}}'_m = 0$ and $\hat{\mathbf{S}}' \cdot \hat{\mathbf{E}}'_n = 0$. So, it maps $(\hat{\mathbf{E}}_m, \hat{\mathbf{E}}_n, \hat{\mathbf{S}})$ to

$$\begin{pmatrix} a_m e^{i\frac{2\pi}{\lambda}OPL} \hat{\mathbf{E}}'_m, a_n e^{i\frac{2\pi}{\lambda}OPL} \hat{\mathbf{E}}'_n, \hat{\mathbf{S}}' \end{pmatrix}.$$

When the ray propagation and the surface interaction to be combined into one \mathbf{P} matrix are not in sequence, as shown in the example in section 4.3, the mapping of the Poynting vectors $(\hat{\mathbf{S}} \rightarrow \hat{\mathbf{S}}')$ needs to be completely removed from $\mathbf{P}_{\text{interface}}$ before incorporating $e^{i\frac{2\pi}{\lambda}OPL}$. By removing $(\hat{\mathbf{S}} \rightarrow \hat{\mathbf{S}}')$, the operations affect only the \mathbf{E} field component. After that, the original mapping of \mathbf{S} is added back into the final \mathbf{P} matrix. The step by step procedures are:

(1) The mapping of $(\hat{\mathbf{S}} \rightarrow \hat{\mathbf{S}}')$ is represented by the 3×3 matrix \mathbf{S}_D (\mathbf{S} dyad) which is the outer product of $\hat{\mathbf{S}}$ and $\hat{\mathbf{S}}'$,

$$\mathbf{S}_D = \hat{\mathbf{S}}' \cdot \hat{\mathbf{S}}^T. \quad (3.37)$$

\mathbf{S}_D maps $(\hat{\mathbf{E}}_m, \hat{\mathbf{E}}_n, \hat{\mathbf{S}})$ to $(\mathbf{0}, \mathbf{0}, \hat{\mathbf{S}}')$, and all other vectors orthogonal to $\hat{\mathbf{S}}$ into $\mathbf{0}$.

(2) The mapping of the Poynting vector is removed from $\mathbf{P}_{\text{interface}}$ by subtracting \mathbf{S}_D .

$$\check{\mathbf{P}} = \mathbf{P}_{\text{interface}} - \mathbf{S}_D \quad (3.38)$$

which maps $(\hat{\mathbf{E}}_{\mathbf{m}}, \hat{\mathbf{E}}_{\mathbf{n}}, \hat{\mathbf{S}})$ to $(a_m \hat{\mathbf{E}}'_{\mathbf{m}}, a_n \hat{\mathbf{E}}'_{\mathbf{n}}, \mathbf{0})$. So $\check{\mathbf{P}} \cdot \mathbf{S} = \mathbf{0}$.

(3) By multiplying $e^{i\frac{2\pi}{\lambda}OPL}$ to $\check{\mathbf{P}}$,

$$\bar{\mathbf{P}} = \check{\mathbf{P}} e^{i\frac{2\pi}{\lambda}OPL} \quad (3.39)$$

which maps $(\hat{\mathbf{E}}_{\mathbf{m}}, \hat{\mathbf{E}}_{\mathbf{n}}, \hat{\mathbf{S}})$ to $\left(a_m e^{i\frac{2\pi}{\lambda}OPL} \hat{\mathbf{E}}'_{\mathbf{m}}, a_n e^{i\frac{2\pi}{\lambda}OPL} \hat{\mathbf{E}}'_{\mathbf{n}}, \mathbf{0} \right)$.

(4) Then, by adding $\mathbf{S}_{\mathbf{D}}$ back into the \mathbf{P} matrix, the mapping of $\hat{\mathbf{S}}$ is restored. So,

$$\bar{\bar{\mathbf{P}}} = \bar{\mathbf{P}} + \mathbf{S}_{\mathbf{D}} \quad (3.40)$$

maps $(\hat{\mathbf{E}}_{\mathbf{m}}, \hat{\mathbf{E}}_{\mathbf{n}}, \hat{\mathbf{S}})$ to $\left(a_m e^{i\frac{2\pi}{\lambda}OPL} \hat{\mathbf{E}}'_{\mathbf{m}}, a_n e^{i\frac{2\pi}{\lambda}OPL} \hat{\mathbf{E}}'_{\mathbf{n}}, \hat{\mathbf{S}}' \right)$.

Finally, the overall \mathbf{P} matrix with both surface interactions and propagation effects is

$$\bar{\bar{\mathbf{P}}} = (\mathbf{P}_{\text{interface}} - \mathbf{S}_{\mathbf{D}}) e^{i\frac{2\pi}{\lambda}OPL} + \mathbf{S}_{\mathbf{D}}, \quad (3.41)$$

which keeps the mapping of $\hat{\mathbf{S}}$ unchanged and incorporates the *OPL* effect to the electric fields.

Many intermediate \mathbf{P} matrices are used in the steps to incorporate *OPL* into the overall \mathbf{P} matrix. These intermediate \mathbf{P} matrices are summarized in Table 3.2.

Table 3.2 Summary of the intermediate \mathbf{P} matrices for incorporating OPL .

$\mathbf{P}_{\text{interface}}$	$(\hat{\mathbf{E}}_{\mathbf{m}}, \hat{\mathbf{E}}_{\mathbf{n}}, \hat{\mathbf{S}}) \rightarrow (a_m \hat{\mathbf{E}}'_{\mathbf{m}}, a_n \hat{\mathbf{E}}'_{\mathbf{n}}, \hat{\mathbf{S}}')$
$\mathbf{P}_{\text{segment}}$	$(\hat{\mathbf{E}}_{\mathbf{m}}, \hat{\mathbf{E}}_{\mathbf{n}}, \hat{\mathbf{S}}) \rightarrow \left(e^{i\frac{2\pi}{\lambda}OPL} \hat{\mathbf{E}}_{\mathbf{m}}, e^{i\frac{2\pi}{\lambda}OPL} \hat{\mathbf{E}}_{\mathbf{n}}, \hat{\mathbf{S}} \right)$
$\check{\mathbf{P}}$	$(\hat{\mathbf{E}}_{\mathbf{m}}, \hat{\mathbf{E}}_{\mathbf{n}}, \hat{\mathbf{S}}) \rightarrow (a_m \hat{\mathbf{E}}'_{\mathbf{m}}, a_n \hat{\mathbf{E}}'_{\mathbf{n}}, \mathbf{0})$
$\bar{\mathbf{P}}$	$(\hat{\mathbf{E}}_{\mathbf{m}}, \hat{\mathbf{E}}_{\mathbf{n}}, \hat{\mathbf{S}}) \rightarrow \left(a_m e^{i\frac{2\pi}{\lambda}OPL} \hat{\mathbf{E}}'_{\mathbf{m}}, a_n e^{i\frac{2\pi}{\lambda}OPL} \hat{\mathbf{E}}'_{\mathbf{n}}, \mathbf{0} \right)$
$\overline{\mathbf{P}}$	$(\hat{\mathbf{E}}_{\mathbf{m}}, \hat{\mathbf{E}}_{\mathbf{n}}, \hat{\mathbf{S}}) \rightarrow \left(a_m e^{i\frac{2\pi}{\lambda}OPL} \hat{\mathbf{E}}'_{\mathbf{m}}, a_n e^{i\frac{2\pi}{\lambda}OPL} \hat{\mathbf{E}}'_{\mathbf{n}}, \hat{\mathbf{S}}' \right)$

The phase of all the light components exiting an optical system, usually in the exit pupil, is necessary for image formation and optical transfer function calculations. These pupil functions, the wavefront aberration function or the Jones pupil, are inputs of Fourier transform algorithms, which only need the input complex numbers modulo 2π . This phase contribution is contained in the $\mathbf{P}_{\text{segment}}$ matrices, which are modulo 2π . Separately in optical design it is also important to be able to describe the exiting wavefront's peak-to-valley wavefront aberration, and show phase maps which are unwrapped. These are calculated from the separate calculation of optical path length, equation (2.17). The absolute optical path length is also needed in other calculations such as determining where the white light fringe will occur in Michelson interferometers, Fourier transform spectrometers, and optical coherence tomography, where the differences in optical path lengths between wavelengths are required

3.6 Conclusions

The definition of three-dimensional polarization ray tracing matrices has been extended to incorporate anisotropic ray tracing. The algorithms handle ray doublings and calculate the

P matrices for each exiting ray at various types of anisotropic interfaces. Each of these **P** matrices represents polarization coupling between eigenmodes in the incident and exiting materials. The **P_{segment}** matrix is introduced to incorporate optical phase change due to ray propagation.

The calculations of the **P** matrix shown in this chapter provide the basis to perform systematic ray tracing through anisotropic interfaces, and have been programmed in Polaris-M (a polarization ray tracing program mentioned in section 1.7) to efficiently model the polarization performance of anisotropic optical components. The polarization properties (retardance and diattenuation) along a ray path are contained in the **P** matrix and can be extracted for a specific ray intercept, for a combination of ray intercepts, through a series of ray segment, or for a specific eigenmode. A numerical example of calculating the **P** matrix for a biaxial plane parallel plate will be presented in Chapter 4. These methods can be applied to analyze complex retarders with multiple anisotropic waveplates cemented together. Further analysis of the **P** matrices for their polarization properties (retardance and diattenuation) will also be shown in Chapter 4.

This dissertation only shows the ray parameter calculations for uncoated anisotropic interfaces in Chapter 2 for simplicity. However, the method to build the **P** matrix shown in this chapter can also apply to build the **P** matrix for other optical interfaces with other ray tracing algorithms which split the incident ray in multiple directions with different polarizations, such as surfaces with anisotropic thin films, isotropic and anisotropic gratings, stress birefringent materials, and so on. Assumptions can be made to

simplify the complexity of ray doubling. An example assuming small spatial ray splitting in stress induced birefringent materials will be explained in detail in Chapter 8.

CHAPTER 4 RAY TRACING A BIAXIAL PLATES WITH THE **P** MATRIX, AND THE CALCULATION OF DIATTENUATION AND RETARDANCE

4.1 Demonstrating the anisotropic ray trace with the **P** matrix

In this chapter, ray tracing through an example anisotropic waveplate is numerically demonstrated by algorithms shown in section 2.4. An off-axis collimated wavefront propagates through one biaxial waveplate and results in two partially overlapping exiting wavefronts. The polarizations of these two overlapping wavefronts, represented by two **P** matrices, need to be combined to represent the total effects of the waveplate. The details of combining these two **P** matrices involve the incorporation of their *OPLs* and the calculation of their optical path difference (*OPD*), which will be shown numerically in this chapter.

The polarizations of a ray path, as described by the **P** matrix, has a diattenuation and a retardance. The calculation of these polarization parameters from the **P** matrix will be demonstrated in section 4.4 and section 4.5. The diattenuation of the **P** matrix related to the maximum and minimum transmissions of an intercept or a series of intercepts is calculated through singular value decomposition^{25,27,107}. The retardance of the ray path can be separated into two parts: physical retardance and geometrical transformation²⁸. A geometrical transformation matrix, **Q**, for an anisotropic intercept will be introduced to describe the geometrical transformation. The retardance of multiple overlapping wavefronts is not simply phase delay between two polarized wavefronts, but is defined between two eigen-polarizations calculated from the combined **P** matrix for all the modes.

4.2 Ray tracing an off-axis beam through a biaxial waveplate with P matrix

Consider a 0.5mm thick plate made of KTP (Potassium titanyl phosphate, KTiOPO_4) with principal refractive indices $(n_F, n_M, n_S) = (1.786, 1.797, 1.902)$ whose principal axes are oriented along the (x, y, z) axes, as shown in Figure 4.1. A 500 nm incident ray propagates from air onto the biaxial plate at an angle. It splits into two transmissive modes, *fast* and *slow*, at the isotropic/anisotropic interface. The two modes reach the anisotropic/isotropic interface at two different directions with different optical path lengths. Then they refract out from the plate and propagate in the same direction again, but slightly separated. The crystal axes in this example is aligned with the Cartesian axes, (x, y, z) , which allow the refraction of any incident ray in the y - z plane to occur in the PoI.

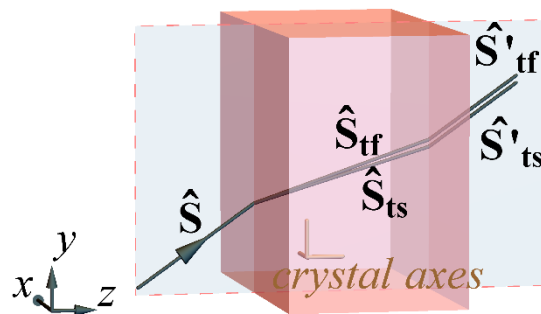


Figure 4.1 A ray propagates with $\hat{\mathbf{k}} = \hat{\mathbf{S}}$ from air into a KTP biaxial crystal (in pink). The entrance surface and the exit surface have the same surface normal $\hat{\boldsymbol{\eta}} = (0, 0, 1)$. The KTP crystal splits the ray in two at the exit surface with direction $\hat{\mathbf{S}}'_{\text{tf}}$ and $\hat{\mathbf{S}}'_{\text{ts}}$ which are parallel in air. The plane that contains the PoI and the doubled rays is highlighted in gray.

All ray parameters are calculated following the procedure in section 2.4. In air, the

light propagation direction is $\mathbf{k}_{\text{in}} = \begin{pmatrix} 0 \\ \sin \theta \\ \cos \theta \end{pmatrix} = \begin{pmatrix} 0 \\ \sin 35^\circ \\ \cos 35^\circ \end{pmatrix}$ and the Poynting vector is

$$\mathbf{S}_{\text{in}} = \begin{pmatrix} 0 \\ \sin \theta \\ \cos \theta \end{pmatrix} = \begin{pmatrix} 0 \\ \sin 35^\circ \\ \cos 35^\circ \end{pmatrix}. \text{ The interface has } \boldsymbol{\eta} = \begin{pmatrix} 0 \\ 0 \\ 1 \end{pmatrix}, \boldsymbol{\varepsilon} = \begin{pmatrix} 1 & 0 & 0 \\ 0 & 1 & 0 \\ 0 & 0 & 1 \end{pmatrix}, \boldsymbol{\varepsilon}' = \begin{pmatrix} n_F^2 & 0 & 0 \\ 0 & n_M^2 & 0 \\ 0 & 0 & n_S^2 \end{pmatrix}$$

$$\text{and } \mathbf{G} = \mathbf{G}' = \begin{pmatrix} 0 & 0 & 0 \\ 0 & 0 & 0 \\ 0 & 0 & 0 \end{pmatrix}.$$

From equations (2.11) and (2.13), the resultant propagation parameters are:

$$\hat{\mathbf{k}} = \frac{1}{n'} \begin{pmatrix} 0 \\ \sin \theta \\ \pm \sqrt{n'^2 - \sin^2 \theta} \end{pmatrix} \text{ and } \mathbf{K} = \frac{1}{n} \begin{pmatrix} 0 & \mp \sqrt{n'^2 - \sin^2 \theta} & \sin \theta \\ \pm \sqrt{n'^2 - \sin^2 \theta} & 0 & 0 \\ -\sin \theta & 0 & 0 \end{pmatrix}$$

for both transmission and reflection. In transmission, based on equation (2.12),

$$\begin{pmatrix} n_F^2 - n'^2 & 0 & 0 \\ 0 & \sin^2 \theta + n_M^2 - n'^2 & \sin \theta \sqrt{n'^2 - \sin^2 \theta} \\ \sin \theta \sqrt{n'^2 - \sin^2 \theta} & n_S^2 - \sin^2 \theta & 0 \end{pmatrix} \mathbf{E}_t = 0.$$

Based on equation (2.14), for non-zero \mathbf{E}_t , the determinant of the matrix is zero,

$$\frac{1}{2} (n_F^2 - n'^2) [n_M^2 + n_S^2 (-1 - 2n_M^2 + 2n'^2) + (n_S^2 - n_M^2) \cos 2\theta] = 0.$$

With $n' > 0$, $n' = n_F$ or $n' = \sqrt{n_M^2 + \left(1 - \frac{n_M^2}{n_S^2}\right) \sin^2 \theta}$, then $n_f = 1.786$ and $n_s = 1.807$. From

equation (2.12), the transmission *fast*-mode satisfies

$$\begin{pmatrix} n_F^2 - n_f^2 & 0 & 0 \\ 0 & \sin^2 \theta - n_f^2 + n_M^2 & \sin \theta \sqrt{n_f^2 - \sin^2 \theta} \\ 0 & \sin \theta \sqrt{n_f^2 - \sin^2 \theta} & n_S^2 - \sin^2 \theta \end{pmatrix} \mathbf{E}_{\text{tf}} = 0$$

$$\begin{pmatrix} 0 & 0 & 0 \\ 0 & 0.371 & 0.970 \\ 0 & 0.970 & 3.289 \end{pmatrix} \mathbf{E}_{\text{tf}} = 0.$$

By singular value decomposition, the matrix is further expressed as

$$\begin{pmatrix} 0 & 0 & 0 \\ 0 & 0.371 & 0.970 \\ 0 & 0.970 & 3.289 \end{pmatrix} = \begin{pmatrix} 0 & 0 & 1 \\ -0.289 & -0.957 & 0 \\ -0.957 & 0.289 & 0 \end{pmatrix} \begin{pmatrix} 3.582 & 0 & 0 \\ 0 & 0.078 & 0 \\ 0 & 0 & 0 \end{pmatrix} \begin{pmatrix} 0 & 0 & 1 \\ -0.289 & -0.957 & 0 \\ -0.957 & 0.289 & 0 \end{pmatrix}^\dagger.$$

The exiting state corresponds to the singular value of zero with electric field, $\mathbf{E}_{\text{tf}} = \begin{pmatrix} 1 \\ 0 \\ 0 \end{pmatrix}$.

From equations (2.15) and (2.16), the \mathbf{H} and \mathbf{S} fields are

$$\mathbf{H}_{\text{tf}} = (n_f \mathbf{K}_{\text{tf}} + i \mathbf{G}') \hat{\mathbf{E}}_{\text{tf}} = \begin{pmatrix} 0 & -1.691 & 0.574 \\ 1.691 & 0 & 0 \\ -0.574 & 0 & 0 \end{pmatrix} \begin{pmatrix} 1 \\ 0 \\ 0 \end{pmatrix} = \begin{pmatrix} 0 \\ 1.691 \\ -0.574 \end{pmatrix}, \text{ and}$$

$$\hat{\mathbf{S}}_{\text{tf}} = \frac{\mathcal{R}e[\hat{\mathbf{E}}_{\text{tf}} \times \hat{\mathbf{H}}_{\text{tf}}^*]}{|\mathcal{R}e[\hat{\mathbf{E}}_{\text{tf}} \times \hat{\mathbf{H}}_{\text{tf}}^*]|} = \begin{pmatrix} 0 \\ 0.321 \\ 0.947 \end{pmatrix}.$$

The transmission *slow*-mode satisfies

$$\begin{pmatrix} n_F^2 - n_s^2 & 0 & 0 \\ 0 & \sin^2 \theta + n_M^2 - n_s^2 & \sin \theta \sqrt{n_s^2 - \sin^2 \theta} \\ 0 & \sin \theta \sqrt{n_s^2 - \sin^2 \theta} & n_s^2 - \sin^2 \theta \end{pmatrix} \mathbf{E}_{\text{ts}} = 0$$

$$\begin{pmatrix} -0.077 & 0 & 0 \\ 0 & 0.294 & 0.983 \\ 0 & 0.983 & 3.289 \end{pmatrix} \mathbf{E}_{\text{ts}} = 0.$$

By singular value decomposition,

$$\begin{pmatrix} -0.077 & 0 & 0 \\ 0 & 0.294 & 0.983 \\ 0 & 0.983 & 3.289 \end{pmatrix} = \begin{pmatrix} 0 & -1 & 0 \\ -0.286 & 0 & -0.958 \\ -0.958 & 0 & 0.286 \end{pmatrix} \begin{pmatrix} 3.583 & 0 & 0 \\ 0 & 0.077 & 0 \\ 0 & 0 & 0 \end{pmatrix} \begin{pmatrix} 0 & 1 & 0 \\ -0.286 & 0 & -0.958 \\ -0.958 & 0 & 0.286 \end{pmatrix}^\dagger.$$

The exiting state corresponds to the singular value of zero with electric field

$$\mathbf{E}_{\text{ts}} = \begin{pmatrix} 0 \\ -0.958 \\ 0.286 \end{pmatrix}. \text{ The } \mathbf{H} \text{ and } \mathbf{S} \text{ fields are}$$

$$\mathbf{H}_{\text{ts}} = (n_s \mathbf{K}_{\text{ts}} + i\mathbf{G}) \hat{\mathbf{E}}_{\text{ts}} = \begin{pmatrix} 0 & -1.714 & 0.574 \\ 1.714 & 0 & 0 \\ -0.574 & 0 & 0 \end{pmatrix} \begin{pmatrix} 0 \\ -0.958 \\ 0.286 \end{pmatrix} = \begin{pmatrix} 1.806 \\ 0 \\ 0 \end{pmatrix}, \text{ and}$$

$$\hat{\mathbf{S}}_{\text{tf}} = \frac{\mathcal{R}e \left[\hat{\mathbf{E}}_{\text{tf}} \times \hat{\mathbf{H}}_{\text{tf}}^* \right]}{\left| \mathcal{R}e \left[\hat{\mathbf{E}}_{\text{tf}} \times \hat{\mathbf{H}}_{\text{tf}}^* \right] \right|} = \begin{pmatrix} 0 \\ 0.321 \\ 0.947 \end{pmatrix}.$$

In reflection, $n_r=1$, with equation (2.12),

$$\begin{pmatrix} 1-n_r^2 & 0 & 0 \\ 0 & 1-n_r^2+\sin^2\theta & -\sin\theta\sqrt{n_r^2-\sin^2\theta} \\ 0 & -\sin\theta\sqrt{n_r^2-\sin^2\theta} & \cos^2\theta \end{pmatrix} \mathbf{E}_r = 0$$

$$\begin{pmatrix} 0 & 0 & 0 \\ 0 & 0.329 & -0.470 \\ 0 & -0.470 & 0.671 \end{pmatrix} \mathbf{E}_r = 0.$$

By singular value decomposition,

$$\begin{pmatrix} 0 & 0 & 0 \\ 0 & 0.329 & -0.470 \\ 0 & -0.470 & 0.671 \end{pmatrix} = \begin{pmatrix} 0 & 0 & 1 \\ -0.574 & 0.819 & 0 \\ 0.819 & 0.574 & 0 \end{pmatrix} \begin{pmatrix} 1 & 0 & 0 \\ 0 & 0 & 0 \\ 0 & 0 & 0 \end{pmatrix} \begin{pmatrix} 0 & 0 & 1 \\ -0.574 & 0.819 & 0 \\ 0.819 & 0.574 & 0 \end{pmatrix}^\dagger.$$

The exiting states correspond to the singular value of zero are $\mathbf{E}_{ts} = \begin{pmatrix} 1 \\ 0 \\ 0 \end{pmatrix}$ and

$$\mathbf{E}_{rp} = \begin{pmatrix} 0 \\ 0.819 \\ 0.574 \end{pmatrix}. \text{ Their } \mathbf{H} \text{ and } \mathbf{S} \text{ fields are}$$

$$\mathbf{H}_{rs} = (n_r \mathbf{K}_r + i \mathbf{G}) \hat{\mathbf{E}}_{rs} = \begin{pmatrix} 0 & 0.819 & 0.574 \\ -0.819 & 0 & 0 \\ -0.574 & 0 & 0 \end{pmatrix} \begin{pmatrix} 1 \\ 0 \\ 0 \end{pmatrix} = \begin{pmatrix} 0 \\ -0.819 \\ -0.574 \end{pmatrix},$$

$$\mathbf{H}_{rp} = (n_r \mathbf{K}_r + i \mathbf{G}) \hat{\mathbf{E}}_{rp} = \begin{pmatrix} 0 & 0.819 & 0.574 \\ -0.819 & 0 & 0 \\ -0.574 & 0 & 0 \end{pmatrix} \begin{pmatrix} 0 \\ 0.819 \\ 0.574 \end{pmatrix} = \begin{pmatrix} 1 \\ 0 \\ 0 \end{pmatrix}, \text{ and}$$

$$\hat{\mathbf{S}}_r = \frac{\mathcal{R}e[\hat{\mathbf{E}}_r \times \hat{\mathbf{H}}_r^*]}{|\mathcal{R}e[\hat{\mathbf{E}}_r \times \hat{\mathbf{H}}_r^*]|} = \begin{pmatrix} 0 \\ 0.574 \\ -0.819 \end{pmatrix}.$$

The electromagnetic field vectors at the air/KTP interface is summarized in Table 4.1.

Table 4.1 Ray parameters at the entrance surface (external reflection/refraction).

	Polarization	$\hat{\mathbf{k}}$	$\hat{\mathbf{s}}$	$\hat{\mathbf{E}}$	\mathbf{H}
Refracted	<i>fast</i>	$\begin{pmatrix} 0 \\ 0.321 \\ 0.947 \end{pmatrix}$	$\begin{pmatrix} 0 \\ 0.321 \\ 0.947 \end{pmatrix}$	$\begin{pmatrix} 1 \\ 0 \\ 0 \end{pmatrix}$	$\begin{pmatrix} 0 \\ 1.691 \\ -0.574 \end{pmatrix}$
	<i>slow</i>	$\begin{pmatrix} 0 \\ 0.317 \\ 0.948 \end{pmatrix}$	$\begin{pmatrix} 0 \\ 0.286 \\ 0.958 \end{pmatrix}$	$\begin{pmatrix} 0 \\ -0.958 \\ 0.286 \end{pmatrix}$	$\begin{pmatrix} 1.806 \\ 0 \\ 0 \end{pmatrix}$
Reflected	<i>s</i>	$\begin{pmatrix} 0 \\ 0.574 \\ -0.819 \end{pmatrix}$	$\begin{pmatrix} 0 \\ 0.574 \\ -0.819 \end{pmatrix}$	$\begin{pmatrix} 1 \\ 0 \\ 0 \end{pmatrix}$	$\begin{pmatrix} 0 \\ -0.819 \\ -0.574 \end{pmatrix}$
	<i>p</i>	$\begin{pmatrix} 0 \\ 0.574 \\ -0.819 \end{pmatrix}$	$\begin{pmatrix} 0 \\ 0.574 \\ -0.819 \end{pmatrix}$	$\begin{pmatrix} 0 \\ 0.819 \\ 0.574 \end{pmatrix}$	$\begin{pmatrix} 1 \\ 0 \\ 0 \end{pmatrix}$

Now the amplitude coefficients are calculated with the \mathbf{F} matrix. From equation (2.18),

$$\hat{\mathbf{s}}_1 = \hat{\mathbf{k}}_{\text{in}} \times \hat{\boldsymbol{\eta}} = \begin{pmatrix} 0 \\ \sin 35^\circ \\ 0 \end{pmatrix}, \quad \hat{\mathbf{s}}_2 = \hat{\boldsymbol{\eta}} \times \hat{\mathbf{s}}_1 = \begin{pmatrix} 0 \\ \sin 35^\circ \\ 0 \end{pmatrix},$$

$$\mathbf{F} = \begin{pmatrix} \mathbf{s}_1 \cdot \hat{\mathbf{E}}_{\text{tf}} & \mathbf{s}_1 \cdot \hat{\mathbf{E}}_{\text{ts}} & -\mathbf{s}_1 \cdot \hat{\mathbf{E}}_{\text{rs}} & -\mathbf{s}_1 \cdot \hat{\mathbf{E}}_{\text{rp}} \\ \mathbf{s}_2 \cdot \hat{\mathbf{E}}_{\text{tf}} & \mathbf{s}_2 \cdot \hat{\mathbf{E}}_{\text{ts}} & -\mathbf{s}_2 \cdot \hat{\mathbf{E}}_{\text{rs}} & -\mathbf{s}_2 \cdot \hat{\mathbf{E}}_{\text{rp}} \\ \mathbf{s}_1 \cdot \vec{\mathbf{H}}_{\text{tf}} & \mathbf{s}_1 \cdot \vec{\mathbf{H}}_{\text{ts}} & -\mathbf{s}_1 \cdot \vec{\mathbf{H}}_{\text{rs}} & -\mathbf{s}_1 \cdot \vec{\mathbf{H}}_{\text{rp}} \\ \mathbf{s}_2 \cdot \vec{\mathbf{H}}_{\text{tf}} & \mathbf{s}_2 \cdot \vec{\mathbf{H}}_{\text{ts}} & -\mathbf{s}_2 \cdot \vec{\mathbf{H}}_{\text{rs}} & -\mathbf{s}_2 \cdot \vec{\mathbf{H}}_{\text{rp}} \end{pmatrix} = \begin{pmatrix} 0.574 & 0 & -0.574 & 0 \\ 0 & -0.550 & 0 & -0.470 \\ 0 & 1.036 & 0 & -0.574 \\ 0.970 & 0 & 0.470 & 0 \end{pmatrix}, \text{ and}$$

$$\mathbf{F}^{-1} = \begin{pmatrix} 0.569 & 0 & 0 & 0.695 \\ 0 & -0.715 & 0.586 & 0 \\ -1.174 & 0 & 0 & 0.695 \\ 0 & -1.292 & -0.685 & 0 \end{pmatrix}.$$

With *s*-polarized incident light,

$$\hat{\mathbf{E}}_{\text{inc},s} = \frac{\hat{\mathbf{k}}_{\text{in}} \times \hat{\boldsymbol{\eta}}}{\|\hat{\mathbf{k}}_{\text{in}} \times \hat{\boldsymbol{\eta}}\|} = \begin{pmatrix} 1 \\ 0 \\ 0 \end{pmatrix}, \quad \mathbf{H}_{\text{inc},s} = (n\mathbf{K}_{\text{in}} + i\mathbf{G})\hat{\mathbf{E}}_{\text{inc},s} = \begin{pmatrix} 0 \\ \cos 35^\circ \\ -\sin 35^\circ \end{pmatrix},$$

$$\mathbf{C}_s = \begin{pmatrix} \mathbf{s}_1 \cdot \hat{\mathbf{E}}_{\text{inc},s} \\ \mathbf{s}_2 \cdot \hat{\mathbf{E}}_{\text{inc},s} \\ \mathbf{s}_1 \cdot \bar{\mathbf{H}}_{\text{inc},s} \\ \mathbf{s}_2 \cdot \bar{\mathbf{H}}_{\text{inc},s} \end{pmatrix} = \begin{pmatrix} \sin 35^\circ \\ 0 \\ 0 \\ \cos 35^\circ \sin 35^\circ \end{pmatrix} \text{ and}$$

$$\mathbf{A}_s = \mathbf{F}^{-1} \cdot \mathbf{C}_s = \begin{pmatrix} 0.569 & 0 & 0 & 0.695 \\ 0 & -0.715 & 0.586 & 0 \\ -1.174 & 0 & 0 & 0.695 \\ 0 & -1.292 & -0.685 & 0 \end{pmatrix} \begin{pmatrix} \sin 35^\circ \\ 0 \\ 0 \\ \cos 35^\circ \sin 35^\circ \end{pmatrix} = \begin{pmatrix} 0.653 \\ 0 \\ -0.347 \\ 0 \end{pmatrix} = \begin{pmatrix} a_{s \rightarrow tf} \\ a_{s \rightarrow ts} \\ a_{s \rightarrow rs} \\ a_{s \rightarrow rp} \end{pmatrix}.$$

With p -polarized incident light,

$$\hat{\mathbf{E}}_{\text{inc},p} = \frac{\hat{\mathbf{k}}_{\text{in}} \times \hat{\mathbf{E}}_{\text{inc},s}}{\|\hat{\mathbf{k}}_{\text{in}} \times \hat{\mathbf{E}}_{\text{inc},s}\|} = \begin{pmatrix} 0 \\ \cos 35^\circ \\ -\sin 35^\circ \end{pmatrix}, \quad \mathbf{H}_{\text{inc},p} = (n\mathbf{K}_{\text{in}} + i\mathbf{G})\hat{\mathbf{E}}_{\text{inc},p} = \begin{pmatrix} -1 \\ 0 \\ 0 \end{pmatrix},$$

$$\mathbf{C}_p = \begin{pmatrix} \mathbf{s}_1 \cdot \hat{\mathbf{E}}_{\text{inc},p} \\ \mathbf{s}_2 \cdot \hat{\mathbf{E}}_{\text{inc},p} \\ \mathbf{s}_1 \cdot \bar{\mathbf{H}}_{\text{inc},p} \\ \mathbf{s}_2 \cdot \bar{\mathbf{H}}_{\text{inc},p} \end{pmatrix} = \begin{pmatrix} 0 \\ 0.470 \\ -0.574 \\ 0 \end{pmatrix}, \text{ and}$$

$$\mathbf{A}_p = \mathbf{F}^{-1} \cdot \mathbf{C}_p = \begin{pmatrix} 0.569 & 0 & 0 & 0.695 \\ 0 & -0.715 & 0.586 & 0 \\ -1.174 & 0 & 0 & 0.695 \\ 0 & -1.292 & -0.685 & 0 \end{pmatrix} \begin{pmatrix} 0 \\ 0.470 \\ -0.574 \\ 0 \end{pmatrix} = \begin{pmatrix} 0 \\ -0.672 \\ 0 \\ -0.214 \end{pmatrix} = \begin{pmatrix} a_{p \rightarrow tf} \\ a_{p \rightarrow ts} \\ a_{p \rightarrow rs} \\ a_{p \rightarrow rp} \end{pmatrix}.$$

In summary, the amplitude coefficients at the entrance surface are

$$\begin{pmatrix} a_{s \rightarrow tf} \\ a_{s \rightarrow ts} \\ a_{s \rightarrow rs} \\ a_{s \rightarrow rp} \end{pmatrix} = \begin{pmatrix} 0.653 \\ 0 \\ -0.347 \\ 0 \end{pmatrix} \text{ and } \begin{pmatrix} a_{p \rightarrow tf} \\ a_{p \rightarrow ts} \\ a_{p \rightarrow rs} \\ a_{p \rightarrow rp} \end{pmatrix} = \begin{pmatrix} 0 \\ -0.672 \\ 0 \\ -0.214 \end{pmatrix}.$$

Then the \mathbf{P} matrices of the first two refracted rays are:

$$\begin{aligned} \mathbf{P}_{tf} &= \begin{pmatrix} a_{s \rightarrow tf} E_{tf,x} & a_{p \rightarrow tf} E_{tf,x} & S_{tf,x} \\ a_{s \rightarrow tf} E_{tf,y} & a_{p \rightarrow tf} E_{tf,y} & S_{tf,y} \\ a_{s \rightarrow tf} E_{tf,z} & a_{p \rightarrow tf} E_{tf,z} & S_{tf,z} \end{pmatrix} \begin{pmatrix} E_{inc,s,x} & E_{inc,p,x} & S_{inc,x} \\ E_{inc,s,y} & E_{inc,p,y} & S_{inc,y} \\ E_{inc,s,z} & E_{inc,p,z} & S_{inc,z} \end{pmatrix}^T \\ &= \begin{pmatrix} 0.653 & 0 & 0 \\ 0 & 0 & 0.321 \\ 0 & 0 & 0.947 \end{pmatrix} \begin{pmatrix} 1 & 0 & 0 \\ 0 & \cos 35^\circ & \sin 35^\circ \\ 0 & -\sin 35^\circ & \cos 35^\circ \end{pmatrix}^T = \begin{pmatrix} 0.653 & 0 & 0 \\ 0 & 0.184 & 0.263 \\ 0 & 0.543 & 0.776 \end{pmatrix}, \text{ and} \end{aligned}$$

$$\begin{aligned} \mathbf{P}_{ts} &= \begin{pmatrix} a_{s \rightarrow ts} E_{ts,x} & a_{p \rightarrow ts} E_{ts,x} & S_{ts,x} \\ a_{s \rightarrow ts} E_{ts,y} & a_{p \rightarrow ts} E_{ts,y} & S_{ts,y} \\ a_{s \rightarrow ts} E_{ts,z} & a_{p \rightarrow ts} E_{ts,z} & S_{ts,z} \end{pmatrix} \begin{pmatrix} E_{inc,s,x} & E_{inc,p,x} & S_{inc,x} \\ E_{inc,s,y} & E_{inc,p,y} & S_{inc,y} \\ E_{inc,s,z} & E_{inc,p,z} & S_{inc,z} \end{pmatrix}^T \\ &= \begin{pmatrix} 0 & 0 & 0 \\ 0 & 0.644 & 0.286 \\ 0 & -0.192 & 0.958 \end{pmatrix} \begin{pmatrix} 1 & 0 & 0 \\ 0 & \cos 35^\circ & \sin 35^\circ \\ 0 & -\sin 35^\circ & \cos 35^\circ \end{pmatrix}^T = \begin{pmatrix} 0 & 0 & 0 \\ 0 & 0.692 & -0.135 \\ 0 & 0.392 & 0.895 \end{pmatrix}. \end{aligned}$$

Following the same procedure of tracing the *fast* and *slow*-modes to the exit surface, the ray tracing parameters at the KTP/air interface are calculated and are summarized in Table 4.2.

Table 4.2 Ray parameters at the exit surface (internal reflection/refraction)

Polarization	$\hat{\mathbf{k}}$	$\hat{\mathbf{S}}$	$\hat{\mathbf{E}}$	\mathbf{H}	a
<i>fast-s</i>	$\begin{pmatrix} 0 \\ \sin 35^\circ \\ \cos 35^\circ \end{pmatrix}$	$\begin{pmatrix} 0 \\ \sin 35^\circ \\ \cos 35^\circ \end{pmatrix}$	$\begin{pmatrix} 1 \\ 0 \\ 0 \end{pmatrix}$	$\begin{pmatrix} 0 \\ 0.819 \\ -0.574 \end{pmatrix}$	1.347

<i>fast-p</i>	$\begin{pmatrix} 0 \\ \sin 35^\circ \\ \cos 35^\circ \end{pmatrix}$	$\begin{pmatrix} 0 \\ \sin 35^\circ \\ \cos 35^\circ \end{pmatrix}$	$\begin{pmatrix} 0 \\ 0.819 \\ -0.574 \end{pmatrix}$	$\begin{pmatrix} -1 \\ 0 \\ 0 \end{pmatrix}$	0
<i>slow-s</i>	$\begin{pmatrix} 0 \\ \sin 35^\circ \\ \cos 35^\circ \end{pmatrix}$	$\begin{pmatrix} 0 \\ \sin 35^\circ \\ \cos 35^\circ \end{pmatrix}$	$\begin{pmatrix} 1 \\ 0 \\ 0 \end{pmatrix}$	$\begin{pmatrix} 0 \\ 0.819 \\ -0.574 \end{pmatrix}$	0
<i>slow-p</i>	$\begin{pmatrix} 0 \\ \sin 35^\circ \\ \cos 35^\circ \end{pmatrix}$	$\begin{pmatrix} 0 \\ \sin 35^\circ \\ \cos 35^\circ \end{pmatrix}$	$\begin{pmatrix} 0 \\ -0.819 \\ 0.574 \end{pmatrix}$	$\begin{pmatrix} 1 \\ 0 \\ 0 \end{pmatrix}$	1.420

The exiting $\hat{\mathbf{S}}'_{\text{tf}}$ and $\hat{\mathbf{S}}'_{\text{ts}}$ are equal to the incident $\hat{\mathbf{S}}$, since the birefringent plate is a plane parallel plate. The transmitted matrices at the exit interface for the two modes are

$$\mathbf{P}'_{\text{tf}} = \begin{pmatrix} 1.347 & 0 & 0 \\ 0 & 0.184 & 0.543 \\ 0 & 0.263 & 0.776 \end{pmatrix} \quad \text{and} \quad \mathbf{P}'_{\text{ts}} = \begin{pmatrix} 0 & 0 & 0 \\ 0 & 1.279 & 0.217 \\ 0 & -0.546 & 1.018 \end{pmatrix}.$$

The final ray parameters for each of the polarized rays are the *OPLs*. The two rays propagate from the entrance surface to the exit surface at two different angles, and therefore accumulate different *OPLs*. In our example, the *f*-mode propagates 0.527981 mm along $\hat{\mathbf{S}}_{\text{tf}}$ while *s*-mode propagates 0.521849 mm along $\hat{\mathbf{S}}_{\text{ts}}$. By equation (2.17), OPL_{tf} is 0.942760 mm and OPL_{ts} is 0.942464 mm inside the biaxial plate.

This example is set up to have the *s*-polarization refracts entirely to *fast*-mode and the *p*-polarization refracts entirely to *slow*-mode. The polarizations of the two ray paths are depicted in Figure 4.2.

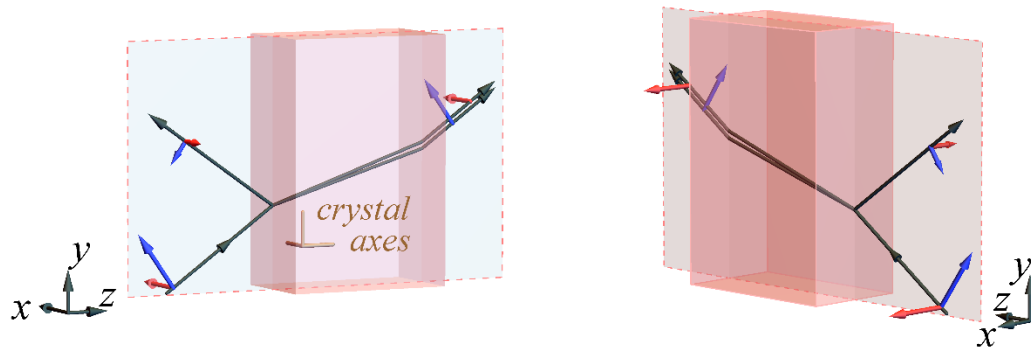


Figure 4.2 The polarizations of the two ray paths are shown from two different perspectives. The s - and p -polarized components are shown as red and blue arrows, respectively. Part of the ray reflects with a π phase shift on both s - and p -polarizations. The refracted light splits into two modes where the s -polarization couples to *fast*-mode, and p -polarization couples to refracted *slow*-mode in this configuration. With two different propagation directions, the two modes exit the plate with a phase delay between them.

4.3 Calculation of total \mathbf{P} matrices with propagation effects

The OPD along the ray paths of the two modes is the cause of retardance in the exiting beam. The one incident ray shown in Figure 4.3 (a) can represent the propagation of a collimated plane wave through the waveplate, and the two exiting rays (*fast* and *slow*-modes) represent the two partially overlapping exiting plane waves. All rays of the *fast*-mode have the same cumulative \mathbf{P}_{tr} matrix and all rays of the *slow*-mode have the same cumulative \mathbf{P}_{ts} matrix. In the region where the exiting wavefronts overlap, the \mathbf{P} matrices of the two modes with the same incident and exiting $\hat{\mathbf{S}}$ can be combined.

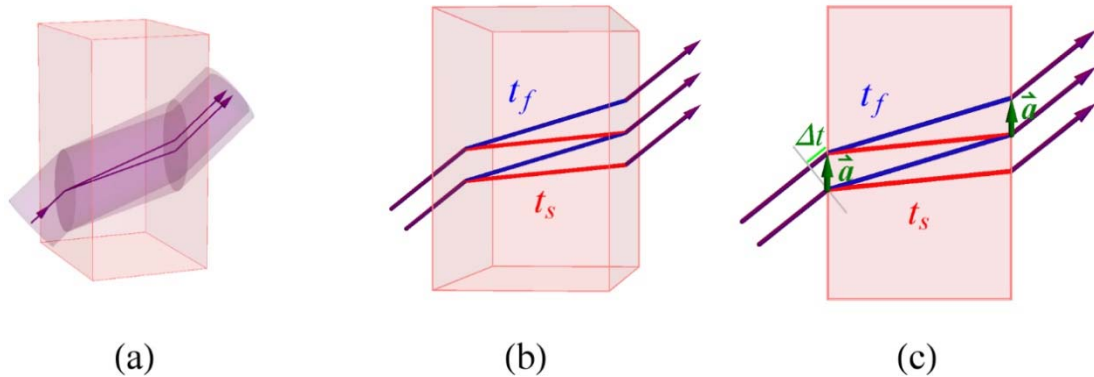


Figure 4.3 (a) A collimated wavefront refracts through a birefringent plate. Two partially overlapping collimated beams exit the plate in the same direction. (b) Two rays of the incident wavefront are traced through the plate, where the s -mode (red) from the upper incident ray overlaps with the f -mode (blue) from the lower incident ray. (c) The resultant split rays have a displacement of \vec{a} between the two exiting modes, which contributes to the OPL difference between the two modes outside of the waveplate.

For the rays in the partially overlapping region, as shown in Figure 4.3 (b), due to the shear between the two exiting beams, two different modes from two separated incident rays exit as one ray at the exit surface. Technically, two rays will be traced which exit superposed to explicitly show the OPD contribution due to the shear. However, since the waveplate induces the same effect on these two incident rays, the ray tracing results from tracing one of the incident ray provide sufficient information to analyze the overall effect of the waveplate.

The separation between the two incident rays depends on the thickness of the plate such that the rays are closer together with thinner plates. As illustrated in Figure 4.3 (c), there is an optical path Δt outside of the waveplate that needs to be accounted for in addition to the OPL within the birefringent plate, where

$$\Delta t = \vec{a} \cdot \hat{\mathbf{S}}. \quad (4.1)$$

In our example, $\Delta t = (0, 0.02018 \text{ mm}, 0) \cdot (0, \sin 35^\circ, \cos 35^\circ) = 11.5756 \text{ } \mu\text{m}$.

In the following discussion, the cumulative \mathbf{P} matrices are constructed to represent the propagation of rays that interacts with the entrance surface, travels through the birefringent material, and passes the exit surface. The various intermediate \mathbf{P} matrices are shown in Figure 4.4.

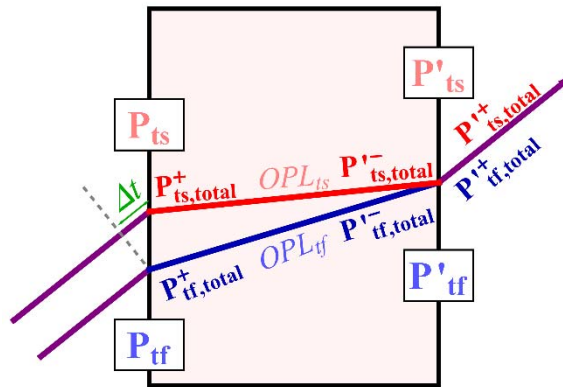


Figure 4.4 \mathbf{P} matrices of individual ray intercepts, cumulative \mathbf{P} matrices, and $OPLs$ of the split ray paths for the two modes are represented in the figure. The refraction \mathbf{P} matrices at the entrance surface are \mathbf{P}_{tf} and \mathbf{P}_{ts} , shown in boxes. The refraction \mathbf{P} matrices for the exit surface are \mathbf{P}'_{tf} and \mathbf{P}'_{ts} , shown in boxes at the exit interface. The cumulative \mathbf{P} matrices with the $OPLs$ right after the entrance are $\mathbf{P}^+_{tf,total}$ and $\mathbf{P}^+_{ts,total}$, respectively. The cumulative \mathbf{P} matrices right before the exit surface with the corresponding $OPLs$ are $\mathbf{P}^-_{tf,total}$ and $\mathbf{P}^-_{ts,total}$, respectively. Finally the cumulative \mathbf{P} matrices after the exit surface are $\mathbf{P}'^+_{tf,total}$ and $\mathbf{P}'^+_{ts,total}$.

The two ray paths shown in Figure 4.4 start to have different $OPLs$ after they propagate passed the gray dashed line shown at the incident interface. The *slow*-mode experiences extra optical phase due to Δt , which is the propagation difference between the rays in the incident space. Then, at the entrance surface, the *fast*- and *slow*-modes

experience the polarization change due to refraction. The cumulative \mathbf{P} matrices for the two modes after the entrance surface are:

$$\mathbf{P}_{\text{tf},\text{total}}^+ = \mathbf{P}_{\text{tf}} = \begin{pmatrix} 0.653 & 0 & 0 \\ 0 & 0.184 & 0.263 \\ 0 & 0.543 & 0.776 \end{pmatrix} \text{ and}$$

$$\mathbf{P}_{\text{ts},\text{total}}^+ = (\mathbf{P}_{\text{ts}} - \mathbf{S}_{\text{Ds}}) e^{i\frac{2\pi}{\lambda}\Delta t} + \mathbf{S}_{\text{Ds}} = \begin{pmatrix} 0 & 0 & 0 \\ 0 & 0.471 + 0.429i & 0.02 - 0.30i \\ 0 & 0.458 - 0.128i & 0.849 + 0.09i \end{pmatrix},$$

where $\mathbf{S}_{\text{D2}} = \begin{pmatrix} 0 & 0 & 0 \\ 0 & 0.164 & 0.235 \\ 0 & 0.550 & 0.785 \end{pmatrix}$ maps $\hat{\mathbf{S}}$ to $\hat{\mathbf{S}}_{\text{ts}}$. The two modes experience different *OPLs*

propagating through the birefringent material due to different path lengths and refractive indices. The cumulative \mathbf{P} matrices right before the exit surface inside the waveplate are calculated as $\overline{\mathbf{P}}$ in equation (3.41),

$$\mathbf{P}'_{\text{tf},\text{total}} = (\mathbf{P}_{\text{tf},\text{total}}^+ - \mathbf{S}_{\text{Df}}) e^{i\frac{2\pi}{\lambda}OPL_{\text{tf}}} + \mathbf{S}_{\text{Df}} = (\mathbf{P}_{\text{tf}} - \mathbf{S}_{\text{Df}}) e^{i\frac{2\pi}{\lambda}OPL_{\text{tf}}} + \mathbf{S}_{\text{Df}}$$

$$= \begin{pmatrix} -0.648 - 0.080i & 0 & 0 \\ 0 & 0.184 & 0.263 \\ 0 & 0.543 & 0.776 \end{pmatrix}, \text{ and}$$

$$\mathbf{P}'_{\text{ts},\text{total}} = (\mathbf{P}_{\text{ts},\text{total}}^+ - \mathbf{S}_{\text{Ds}}) e^{i\frac{2\pi}{\lambda}OPL_{\text{ts}}} + \mathbf{S}_{\text{Ds}} = (\mathbf{P}_{\text{ts}} - \mathbf{S}_{\text{Ds}}) e^{i\frac{2\pi}{\lambda}(OPL_{\text{ts}} + \Delta t)} + \mathbf{S}_{\text{Ds}}$$

$$= \begin{pmatrix} 0 & 0 & 0 \\ 0 & 0.627 + 0.253i & -0.090 - 0.177i \\ 0 & 0.411 - 0.076i & 0.882 + 0.053i \end{pmatrix},$$

where $\mathbf{S}_{\text{tf}} = \begin{pmatrix} 0 & 0 & 0 \\ 0 & 0.184 & 0.263 \\ 0 & 0.543 & 0.776 \end{pmatrix}$ maps $\hat{\mathbf{S}}$ to $\hat{\mathbf{S}}_{\text{tf}}$. Finally, the two modes exit the birefringent

plate parallel to the incident rays with $\hat{\mathbf{S}}_{\text{t}}$. The cumulative \mathbf{P} matrices right after the exit surface are

$$\begin{aligned} \mathbf{P}_{\text{tf,total}}^{'+} &= \mathbf{P}'_{\text{tf}} \cdot \mathbf{P}_{\text{tf,total}}'^{-} = (\mathbf{P}'_{\text{tf}} \cdot \mathbf{P}_{\text{tf}} - \mathbf{S}'_{\mathbf{D}}) e^{i \frac{2\pi}{\lambda} \text{OPL}_{\text{tf}}} + \mathbf{S}'_{\mathbf{D}} \\ &= \begin{pmatrix} -0.873 - 0.108i & 0 & 0 \\ 0 & 0.329 & 0.470 \\ 0 & 0.470 & 0.671 \end{pmatrix}, \text{ and} \end{aligned}$$

$$\begin{aligned} \mathbf{P}_{\text{ts,total}}^{'+} &= \mathbf{P}'_{\text{ts}} \cdot \mathbf{P}_{\text{ts,total}}'^{-} = (\mathbf{P}'_{\text{ts}} \cdot \mathbf{P}_{\text{ts}} - \mathbf{S}'_{\mathbf{D}}) e^{i \frac{2\pi}{\lambda} (\text{OPL}_{\text{ts}} + \Delta t)} + \mathbf{S}'_{\mathbf{D}} \\ &= \begin{pmatrix} 0 & 0 & 0 \\ 0 & 0.891 + 0.307i & 0.076 - 0.215i \\ 0 & 0.076 - 0.215i & 0.946 + 0.151i \end{pmatrix}, \end{aligned}$$

where $\mathbf{S}'_{\mathbf{D}} = \begin{pmatrix} 0 & 0 & 0 \\ 0 & \sin^2 35^\circ & \cos 35^\circ \sin 35^\circ \\ 0 & \cos 35^\circ \sin 35^\circ & \cos^2 35^\circ \end{pmatrix}$ is the outer product of $\hat{\mathbf{S}}$ with itself

because $\hat{\mathbf{S}}' = \hat{\mathbf{S}}_{\text{t}}$, and $\mathbf{P}'_{\text{t}} \cdot \mathbf{S}_{\mathbf{D}} = \mathbf{S}'_{\mathbf{D}}$.

After the waveplate, the two modes from the two incident rays in Figure 4.3 (a) propagate on top of each other, so their \mathbf{P} matrices can be combined to describe the polarization of the resultant beam. \mathbf{P} matrices can only be combined if they contain the same $\mathbf{S}_{\mathbf{D}}$; they must have the same incident and exiting \mathbf{S} as is the case in this example, and the combined \mathbf{P} matrix of the overlapping rays is:

$$\begin{aligned}
\mathbf{P}_{\text{overlap}} &= (\mathbf{P}'_{\text{tf,total}} - \mathbf{S}'_{\mathbf{D}}) + (\mathbf{P}'_{\text{ts,total}} - \mathbf{S}'_{\mathbf{D}}) + \mathbf{S}'_{\mathbf{D}} \\
&= (\mathbf{P}'_{\text{tf}} \cdot \mathbf{P}_{\text{tf}} - \mathbf{S}'_{\mathbf{D}}) e^{i \frac{2\pi}{\lambda} \text{OPL}_{\text{tf}}} + (\mathbf{P}'_{\text{ts}} \cdot \mathbf{P}_{\text{ts}} - \mathbf{S}'_{\mathbf{D}}) e^{i \frac{2\pi}{\lambda} (\text{OPL}_{\text{ts}} + \Delta t)} + \mathbf{S}'_{\mathbf{D}} \quad (4.2) \\
&= \begin{pmatrix} -0.873 - 0.108i & 0 & 0 \\ 0 & 0.891 + 0.307i & 0.076 - 0.215i \\ 0 & 0.076 - 0.215i & 0.946 + 0.151i \end{pmatrix}.
\end{aligned}$$

If the \mathbf{P} matrices do not have the same $\mathbf{S}_{\mathbf{D}}$, they cannot be combined. In that case, the electric fields are combined instead. Combining \mathbf{P} matrices has the advantage of describing the output polarization for any incident polarization. Further details about combining modes are provided in Chapter 5.

4.4 Calculation of diattenuation

Diattenuation D describes the polarization dependent reflection or transmission. It is a function of maximum I_{max} and the minimum I_{min} intensity over all polarization states,

$$D = \frac{I_{\text{max}} - I_{\text{min}}}{I_{\text{max}} + I_{\text{min}}}. \quad (4.3)$$

The \mathbf{P} matrix of one mode at an anisotropic ray intercept has a form of a polarizer, with diattenuation 1. But when two \mathbf{P} matrices for a ray path are combined, the diattenuation depends on the brightness of the two modes. The diattenuation for a ray path associated with a \mathbf{P} matrix is calculated from the singular values corresponding to the maximum and minimum intensities²⁷. The singular value decomposition of $\mathbf{P}_{\text{overlap}}$ for the biaxial waveplate in the preceding example is:

$$\mathbf{U} \cdot \mathbf{D} \cdot \mathbf{V}^\dagger = \begin{pmatrix} 0 & 0 & e^{-i3.019} \\ 0.574 & 0.819e^{i0.500} & 0 \\ 0.819 & -0.574e^{i0.500} & 0 \end{pmatrix} \cdot \begin{pmatrix} 1 & 0 & 0 \\ 0 & 0.964 & 0 \\ 0 & 0 & 0.879 \end{pmatrix} \cdot \begin{pmatrix} 0 & 0 & 1 \\ 0.574 & 0.819 & 0 \\ 0.819 & -0.574 & 0 \end{pmatrix}^\dagger.$$

The \mathbf{P} matrix performs a mapping of incident states, $(\hat{\mathbf{E}}_m, \hat{\mathbf{E}}_n, \hat{\mathbf{S}})$, to exiting states, $(a_m \hat{\mathbf{E}}'_m, a_n \hat{\mathbf{E}}'_n, \hat{\mathbf{S}}')$, the columns of \mathbf{U} correspond to $(\hat{\mathbf{S}}', \hat{\mathbf{E}}'_m e^{i\phi_m}, \hat{\mathbf{E}}'_n e^{i\phi_n})$, the columns of \mathbf{V} corresponds to $(\hat{\mathbf{S}}, \hat{\mathbf{E}}_m, \hat{\mathbf{E}}_n)$, and the diagonal elements of \mathbf{D} are the singular values $(1, a_m, a_n)$. The singular value 1 corresponds to the mapping of incident to exiting \mathbf{S} vectors, $\hat{\mathbf{S}}=(0, \sin 35^\circ, \cos 35^\circ)=(0, 0.574, 0.819)$. The singular value of 0.964 is the amplitude coefficients associated with state $\mathbf{E}_p=(0, 0.819, -0.574)$ mapping to $0.964e^{i0.500}\mathbf{E}_p$. The singular value of 0.879 is the amplitude coefficients associated with $\mathbf{E}_s=(1, 0, 0)$ mapping to $0.879e^{-i3.019}\mathbf{E}_s$. Therefore the cumulative diattenuation is $\frac{0.964^2 - 0.879^2}{0.964^2 + 0.879^2} = 0.0816$ with the maximum transmission axis along \mathbf{E}_p .

4.5 Calculation of retardance and geometrical rotation

Retardance δ is the phase difference between the eigenpolarizations of a system,

$$\delta = \phi_1 - \phi_2, \quad (4.4)$$

where ϕ_1 and ϕ_2 are the phase change of the eigenstates. The eigenstate with the smaller phase change is the fast axis. The retardance of a \mathbf{P} matrix divides into physical retardance and the geometrical transformation¹⁰⁸.

Physical retardance is the phase change due to propagation in medium, characterized by OPL defined in equation (2.17). It provides the phase difference between eigenpolarizations through birefringent material. For example, Figure 4.5 (a) shows a linearly polarized light passing through a birefringent waveplate which becomes elliptically polarized. Also, physical retardance includes the phase change due to surface

interactions, such as metallic reflection where a linearly polarized light physically reflects to elliptically polarized light, as shown in Figure 4.5 (b).

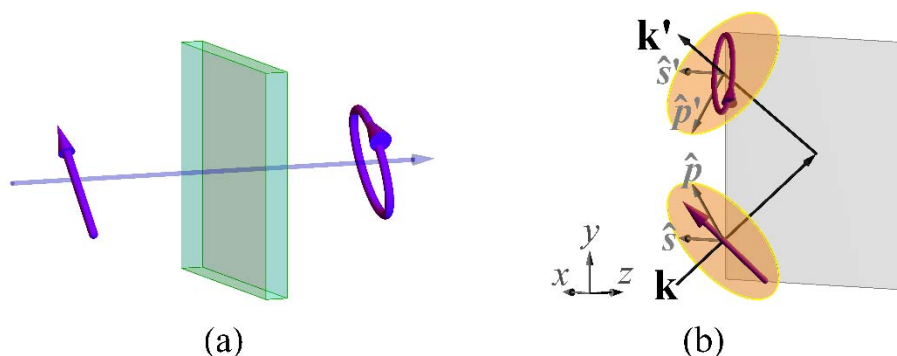


Figure 4.5 Physical retardance: (a) Linearly polarized light passes through a waveplate and becomes elliptically polarized. (b) Linearly polarized light reflect from a metal surface and becomes elliptically polarized.

Geometrical transformation is retardance induced by the geometry of a ray path. It can result in polarization rotation and/or inversion. A polarization rotation appears as a circular retardance, while a polarization inversion appears as half wave of retardance. The polarization of a solid corner cube shown in Figure 4.6 demonstrate polarization rotation after three reflections. All three reflections are set to be perfect total internally reflection at the critical angle where $r_s=1$ and $r_p=1$. Therefore the resultant circular retardance of the reflected light is solely induced by the geometry of the ray paths. The polarization rotations around the exit surface are 0° , 120° and 240° .

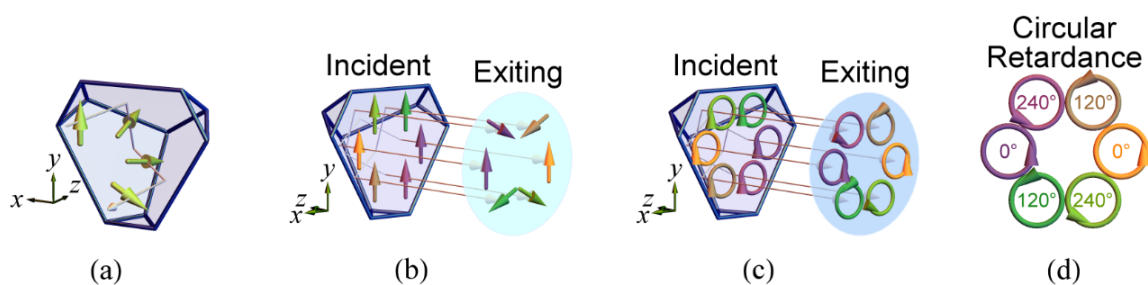


Figure 4.6 (a) Linear polarization, represented by green arrows, rotates 120° after three total internal reflections within a solid corner cube. (b) Six incident rays incident at different regions of the entrance surface follow different paths within the corner cube, and the corresponding exiting states have a different amount of polarization rotations. (c) Circular retardance induced by the corner cube alters the absolute phase of circular incident light. The amount of circular retardance depends on the ray path inside the corner cube. (d) The rotation associated with the induced circular retardance are 0° , 120° , 240° , 360° and so on around the exit surface.

Another example with geometrical transformation is seen in the dove prism. Figure 4.7 shows a dove prism with non-polarizing reflection. When a dove prism rotates about the direction of the incident light, the exiting x -polarization rotates twice as much as the prism. Since the internal reflection is beyond critical angle, the incident y -polarization has an inversion, as shown in Figure 4.8. The dove prism induces half wave of retardance with a fast axis lying along the bottom surface of the prism.

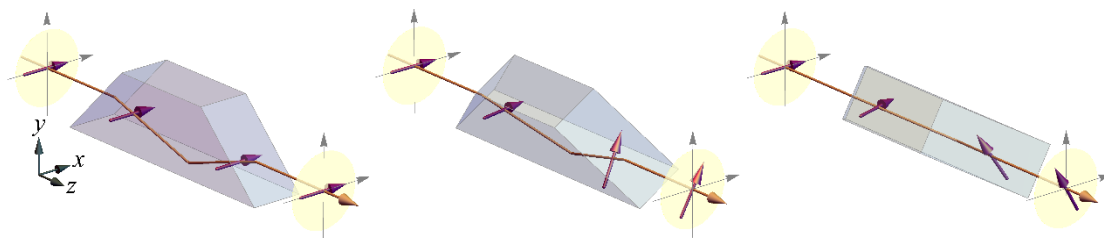


Figure 4.7 Horizontally polarized light propagates through a dove prism which rotates about the incident direction by 0° , 30° and 60° . Then the resultant polarization rotates 0° , 60° and 120° about the exiting direction.

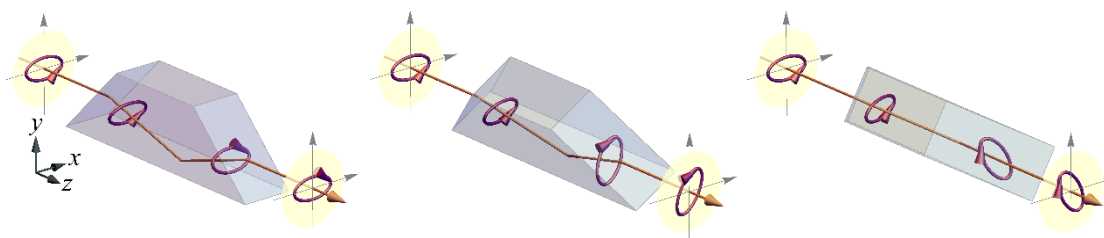


Figure 4.8 Elliptically polarized light propagates through a dove prism which is rotated about the incident direction by 0° , 30° and 60° . The major axis of the resultant polarization ellipse rotates by 0° , 60° and 120° with a change of helicity.

4.5.1 Geometrical transformation \mathbf{Q} matrix

\mathbf{P} matrix contains both the physical and the geometrical polarization change of a ray path. Therefore, the retardance calculated from the \mathbf{P} matrix contains both physical retardance and geometrical transformation. The geometrical transformation of a ray path can be represented by geometrical transformation \mathbf{Q} matrix which is a non-polarizing \mathbf{P} matrix. The calculation of the \mathbf{Q} matrix assumes all surfaces are non-polarizing such that the magnitude of the Fresnel coefficient is always 1. To the \mathbf{Q} matrix contains only the geometrical transformation. For an isotropic interface, the refraction and reflection \mathbf{Q} matrices are

$$\mathbf{Q} = \mathbf{O}_{\text{out}} \mathbf{I}_{3\mathbf{D}} \mathbf{O}_{\text{in}}^{-1} \quad (4.5)$$

with

$$\mathbf{I}_{3\mathbf{D}} = \begin{pmatrix} 1 & 0 & 0 \\ 0 & 1 & 0 \\ 0 & 0 & 0 \end{pmatrix} \quad \text{and} \quad \mathbf{I}_{3\mathbf{D}} = \begin{pmatrix} 1 & 0 & 0 \\ 0 & -1 & 0 \\ 0 & 0 & 0 \end{pmatrix}, \quad (4.6)$$

respectively, where \mathbf{O}_{in} and \mathbf{O}_{out} are defined in equations (3.5) and (3.8). These \mathbf{Q} matrices maps the incident $(\hat{\mathbf{s}}, \hat{\mathbf{p}}, \hat{\mathbf{k}})$ coordinate system to the exiting $(\hat{\mathbf{s}}', \hat{\mathbf{p}}', \hat{\mathbf{k}}')$ and exiting $(\hat{\mathbf{s}}', -\hat{\mathbf{p}}', \hat{\mathbf{k}}')$ for refraction and reflection, respectively. The negative sign in reflection means a right-handed orthonormal basis becomes left-handed after reflection.

In order to adapt this to an anisotropic interface, the definition of the $(\hat{\mathbf{s}}, \hat{\mathbf{p}}, \hat{\mathbf{k}})$ basis is adjusted to $(\hat{\mathbf{s}}, \hat{\mathbf{p}}, \hat{\mathbf{S}})$ because the energy of the ray follows $\hat{\mathbf{S}}$ which is not equal to $\hat{\mathbf{k}}$. And the definition of $\hat{\mathbf{s}}$ and $\hat{\mathbf{p}}$ are also adjusted to stay in the transverse plane of $\hat{\mathbf{S}}$,

$$\hat{\mathbf{s}} = \begin{pmatrix} s_x \\ s_y \\ s_z \end{pmatrix} = \frac{\hat{\mathbf{S}} \times \hat{\boldsymbol{\eta}}}{|\hat{\mathbf{S}} \times \hat{\boldsymbol{\eta}}|}, \quad \hat{\mathbf{p}} = \begin{pmatrix} p_x \\ p_y \\ p_z \end{pmatrix} = \frac{\hat{\mathbf{S}} \times \hat{\mathbf{s}}}{|\hat{\mathbf{S}} \times \hat{\mathbf{s}}|}, \quad \hat{\mathbf{S}} = \begin{pmatrix} S_x \\ S_y \\ S_z \end{pmatrix} \quad (4.7)$$

for incident basis, and

$$\hat{\mathbf{s}}' = \begin{pmatrix} s'_x \\ s'_y \\ s'_z \end{pmatrix} = \frac{\hat{\mathbf{S}}' \times \hat{\boldsymbol{\eta}}}{|\hat{\mathbf{S}}' \times \hat{\boldsymbol{\eta}}|}, \quad \hat{\mathbf{p}}' = \begin{pmatrix} p'_x \\ p'_y \\ p'_z \end{pmatrix} = \frac{\hat{\mathbf{S}}' \times \hat{\mathbf{s}}'}{|\hat{\mathbf{S}}' \times \hat{\mathbf{s}}'|}, \quad \hat{\mathbf{S}}' = \begin{pmatrix} S'_x \\ S'_y \\ S'_z \end{pmatrix} \quad (4.8)$$

for exiting basis. $(\hat{\mathbf{s}}, \hat{\mathbf{p}}, \hat{\mathbf{S}})$ and $(\hat{\mathbf{s}}', \hat{\mathbf{p}}', \hat{\mathbf{S}}')$ are the orthonormal bases before and after a ray intercept. The refracted and reflected $\hat{\mathbf{S}}'$ do not need to be in the PoI and $\hat{\mathbf{s}} \neq \hat{\mathbf{s}}'$. The \mathbf{O}_{in} and \mathbf{O}_{out} in equation (4.5) becomes

$$\mathbf{O}_{\text{in}} = \begin{pmatrix} s_x & p_x & S_x \\ s_y & p_y & S_y \\ s_z & p_z & S_z \end{pmatrix} \quad \text{and} \quad \mathbf{O}_{\text{out}} = \begin{pmatrix} s'_x & p'_x & S'_x \\ s'_y & p'_y & S'_y \\ s'_z & p'_z & S'_z \end{pmatrix}. \quad (4.9)$$

The geometrical transformation can be observed when skew rays spiral through the edges of a series of lenses. This is similar to a ray propagating through three arbitrarily oriented prisms, as shown in Figure 4.9. For simplicity, the prisms are made of isotropic glass with index 1.515. The incident and exiting propagation directions of the ray path are the same, and the slight spiral of the ray path induces rotation in the plane of polarization.

The \mathbf{P} and \mathbf{Q} matrices of the ray shown in Figure 4.9 are $\begin{pmatrix} 0.806 & -0.100 & 0 \\ 0.050 & 0.823 & 0 \\ 0 & 0 & 1 \end{pmatrix}$ and

$\begin{pmatrix} 0.996 & -0.092 & 0 \\ 0.092 & 0.996 & 0 \\ 0 & 0 & 1 \end{pmatrix}$. They both contain circular retardance that will be calculated in

section 4.5.2.

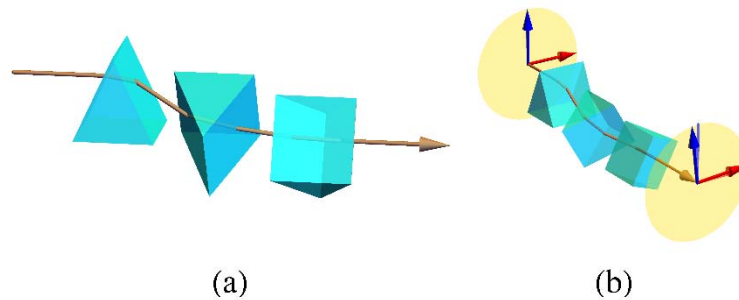


Figure 4.9 (a) A ray propagates through three prisms and exits in the same incident direction, $\mathbf{k}=(0, 0, 1)$. The surface normal of these six surfaces are $(0, -0.423, 0.906)$, $(0, 0.423, 0.906)$, $(0.366, 0.211, 0.906)$, $(-0.366, -0.211, 0.906)$, $(-0.380, 0.198, 0.903)$ and $(0.378, -0.201, 0.903)$. (b) Two orthogonal polarizations propagate through the three prisms and rotate slightly due to the geometry of the ray path.

The geometrical transformation of the \mathbf{P} matrix is undone by multiplication of \mathbf{Q}^{-1} . The

$\mathbf{Q}^{-1} \cdot \mathbf{P}$ of the example system of prisms is $\begin{pmatrix} 0.807 & -0.024 & 0 \\ -0.025 & 0.829 & 0 \\ 0 & 0 & 1 \end{pmatrix}$, which represents a

linear diattenuator. Therefore all 6 surface interactions induce zero physical retardance.

With the method described in section 4.4, $\mathbf{Q}^{-1} \cdot \mathbf{P}$ is a linear diattenuator with maximum/minimum amplitude transmission of $(0.845/0.792)$, and maximum transmission axis oriented at 123.12° from the x axis. The retardance calculation of \mathbf{P} and \mathbf{Q} matrices are presented in section 4.5.2.



4.5.2 Calculation of retardance

The retardance of a \mathbf{P} matrix is calculated by applying eigenanalysis on the unitary matrix of \mathbf{P} ^{25,28}. The polar decomposition of $\mathbf{P} = \mathbf{M}_R \mathbf{M}_D = \mathbf{M}_D \mathbf{M}_R$ which yields a unitary matrix \mathbf{M}_R and a Hermitian matrix \mathbf{M}_D . By singular value decomposition, $\mathbf{P} = \mathbf{U} \mathbf{D} \mathbf{V}^\dagger$, then $\mathbf{M}_R = \mathbf{U} \mathbf{V}^\dagger$ and $\mathbf{M}_D = \mathbf{D}$. Then the retardance of a 3×3 unitary matrix \mathbf{M}_R is calculated by eigenanalysis. The three eigenvalue and vector pairs of \mathbf{M}_R are: $(\lambda_1, \lambda_2, \lambda_3)$ and $(\mathbf{v}_1, \mathbf{v}_2, \mathbf{v}_3)$, respectively.

For \mathbf{P} , \mathbf{Q} , and $\mathbf{Q}^{-1} \cdot \mathbf{P}$ matrices, one of the eigenvalue of their \mathbf{M}_R will be $\lambda_1=1$ which corresponds to the ray direction $\mathbf{v}_1=\hat{\mathbf{S}}$. The argument of the other two eigenvalues λ_2 and λ_3 are the phase of the *fast*- and *slow*-eigenstates \mathbf{v}_2 and \mathbf{v}_3 , where $\arg(\lambda_2) < \arg(\lambda_3)$.

The eigenanalysis of \mathbf{M}_R of \mathbf{P} and \mathbf{Q} matrices of the three prisms example in Figure 4.9 is summarized in Table 4.3. The \mathbf{Q} matrix contains 10.546° circular retardance induced by the ray path geometry, which rotates linear polarization by 5.273° . As shown in the end of last section, the physical retardance calculated from $\mathbf{Q}^{-1} \cdot \mathbf{P}$ is zero because refraction through uncoated surface induces zero retardance. However, an uncoated surface does induce diattenuation. Since the fast axis associated with \mathbf{Q} and the maximum transmission axis associated with $\mathbf{Q}^{-1} \cdot \mathbf{P}$ are not aligned, the resultant \mathbf{M}_R of the \mathbf{P} matrix has elliptical eigenstates, as shown in Table 4.3, and the retardance of \mathbf{P} and \mathbf{Q} are slightly different.¹⁰⁹

Table 4.3 Eigenanalysis of \mathbf{M}_R of the \mathbf{P} and \mathbf{Q} matrices for the three prisms example in Figure 4.9.

	Eigenvalues	Eigenvectors	Retardance	Fast axis
Q	$e^{0.092i}$ $e^{-0.092i}$	$\left(\frac{1}{\sqrt{2}}\begin{pmatrix} -1 \\ i \\ 0 \end{pmatrix}, \frac{1}{\sqrt{2}}\begin{pmatrix} -1 \\ -i \\ 0 \end{pmatrix}\right)$	10.546°	$\frac{1}{\sqrt{2}}\begin{pmatrix} -1 \\ -i \\ 0 \end{pmatrix}$
				
P	$0.818e^{-3.056i}$ $0.818e^{-3.227i}$	$\left(\begin{pmatrix} -0.817 \\ 0.58e^{1.45i} \\ 0 \end{pmatrix}, \begin{pmatrix} -0.817 \\ -0.58e^{-1.7i} \\ 0 \end{pmatrix}\right)$	9.834°	$\begin{pmatrix} -0.817 \\ -0.58e^{-1.7i} \\ 0 \end{pmatrix}$
				

For the previous biaxial waveplate example with a collimated beam shown in Figure 4.1 and sections 4.2 and 4.3, the total geometrical transformation of the waveplate, $\mathbf{Q}_{\text{overlap}} = \mathbf{Q}_t' \cdot \mathbf{Q}_t$, is an identity matrix because the two surfaces create a plane parallel plate. So $\mathbf{Q}_{\text{overlap}}^{-1} \cdot \mathbf{P}_{\text{overlap}} = \mathbf{P}_{\text{overlap}}$, and its eigenvectors and eigenvalues are

$$\begin{aligned} \mathbf{v}_1 &= (1, 0, 0) & \lambda_1 &= e^{-3.01865i} \\ \mathbf{v}_2 &= (0, 0.819, -0.574) & \text{and} & \lambda_2 = e^{0.500467i} \\ \mathbf{v}_3 &= (0, 0.574, 0.819) & \lambda_3 &= 1 \end{aligned}$$

where \mathbf{v}_3 and λ_3 correspond to the mapping from the incident to exiting Poynting vectors. The retardance is $\arg(\lambda_2) - \arg(\lambda_1) = 3.519$ radians with a fast axis along \mathbf{v}_1 which is s-polarization along $(1, 0, 0)$.

4.6 Conclusions

A polarization ray tracing example of an off-axis ray propagating through a biaxial waveplate was performed and the associated \mathbf{P} matrices were calculated. The methods to accumulate polarization effects, including surface interactions and mode propagation, along a ray path into the \mathbf{P} matrices were demonstrated numerically. To represent the polarization in a region where the two polarized wavefronts overlap, the two associated \mathbf{P} matrices were combined to one \mathbf{P} matrix. The procedure shown in this chapter to combine the two \mathbf{P} matrices can be extended to combine multiple \mathbf{P} matrices, which is useful for analyzing retarder made of stack of anisotropic plates. More details about mode combination will be described in Chapter 5, which can be done by combining \mathbf{P} matrices or simply combining their corresponding electric fields spatially.

The calculations of diattenuation and retardance of the \mathbf{P} matrix were demonstrated numerically for the one biaxial plate example. The diattenuation of the \mathbf{P} matrix was calculated using singular value decomposition. The three dimensional nature of the \mathbf{P} matrix allows the definition of retardance to be separated into geometrical transformation and physical retardance. The geometrical transformation is represented by the geometrical transformation \mathbf{Q} matrix whose definition is generalized for an anisotropic intercept. Then the physical retardance is calculated from $\mathbf{Q}^{-1} \cdot \mathbf{P}$ using eigenanalysis.

CHAPTER 5 COMBINATION OF POLARIZED WAVEFRONTS

5.1 Introduction

Many optical systems divide a light beam into two or more partial waves, operates on each of these beams separately, and interfere them at an output plane. Such systems divide beams with components such as beam splitters and multiple element birefringent components, for example achromatic retarders, Lyot filters, optical isolators, and crystal polarizers. These birefringent components generate multiple wavefronts due to double refraction. The exiting wavefronts can completely or partially overlap in the case of a retarder, or split and not overlap in the case of beam splitters. When these wavefronts do overlap at an output plane, the resultant wavefront is the interference between the polarized beams. The output plane could be a detector such as a CCD, an exit pupil, a screen for viewing interferograms^{110,111,112,113}, a hologram to record an interference pattern^{114,115}, or a surface to be illuminated.

Algorithms for calculating each multiple wavefronts from the sequence of each eigenmodes generated from ray doubling were calculated in Chapter 2. The polarizations of each path can be characterized by its \mathbf{P} matrices; associated algorithms were described in Chapter 3 and Chapter 4 for polarization ray tracing. This chapter provides some general methods to combine these completely or partially overlapping wavefronts. In general, the \mathbf{E} fields of overlapping rays add, but their associated \mathbf{P} matrices do not, because each \mathbf{P} matrix operates on different incident \mathbf{E} , and \mathbf{P} is constrained by a unique pair of incident and exiting Poynting vectors \mathbf{S} . This chapter includes the following example: a special case

of co-propagating wavefronts whose incident and exiting beams are co-propagating, and their \mathbf{P} matrices can be combined.

Wavefront combination procedures have two subtle issues. (1) The exiting rays of each polarized wavefront calculated from ray tracing are not on the same exiting grid. This is addressed by either interpolating the partial waves as continuous functions, or by resampling each partial wave onto the same grid for each mode prior to the combination. (2) When the rays are converging or diverging close to focus, caustics form, the wavefront folds over on itself, and the *OPL* becomes multivalued at parts of the wavefront^{116,117}. To avoid this complication, it is best if the wavefront resampling is performed at the exit pupil where the rays are spatially distributed in a well-spaced grid, or at least in regions where caustics can be avoided.

5.2 Wavefronts and ray grids

The optical ray trace commonly starts by tracing a grid of rays emerging from a light source. This grid of rays is usually evenly distributed over the incident wavefront, as shown in Figure 5.1.

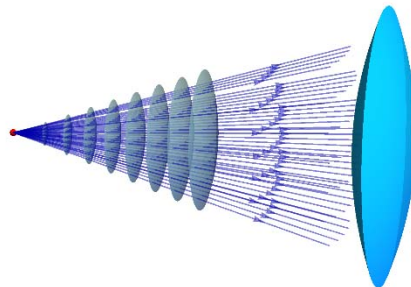


Figure 5.1 The point source on the left emits spherical wavefronts (gray surfaces) which are represented by a grid of rays (blue arrows) propagating towards the lens (light blue).

When these rays propagate, encounter birefringent components, and split into multiple wavefronts, they eventually reach an image plane or exit surface where the interference of the wavefronts may need to be evaluated. Depending on the system, the interfering wavefronts could be as simple as two overlapping collimated wavefronts exiting a retarder as shown in Chapter 4, or as complicated as hundreds of partially overlapping converging or diverging wavefronts from systems such as Lyot filters and Fabry Perot interferometers. These resultant rays at the output surface are most likely not evenly spaced due to aberration differences between modes. In Figure 5.2, an incident wavefront sampled by a grid of rays, converges through a birefringent material and exits as two grids of rays representing the two polarized exiting wavefronts. These two sets of rays are traced separately after splitting, and the effect of the birefringent plate is contained in the combination of these two wavefronts. Therefore, accurate analysis needs to encompass both ray grids where the wavefronts overlap.

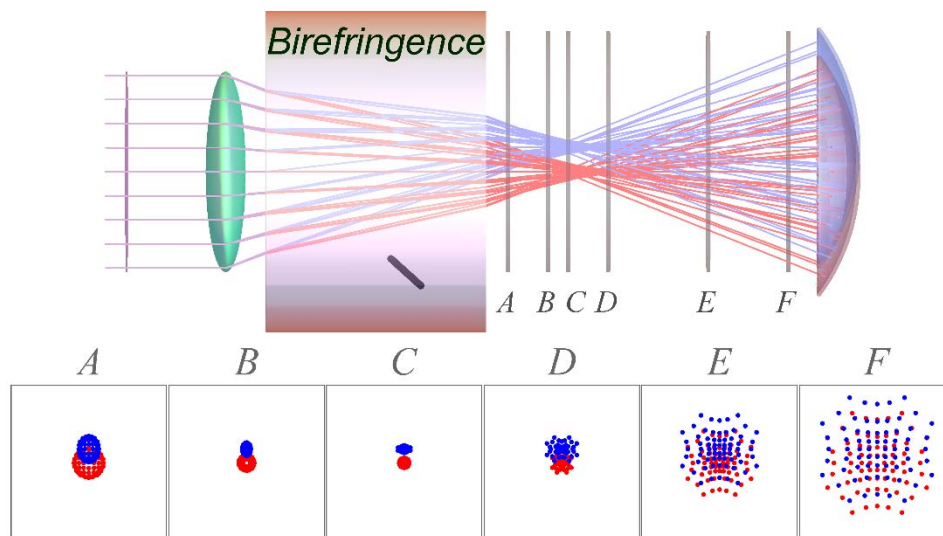


Figure 5.2 A collimated wavefront passes through a lens and converges through a birefringent plate. The optic axis (black line) of the birefringent plate lies in the plane of the page. Two aberrated wavefronts (red and blue) exit the birefringent plate and pass a series of planes labeled from *A* to *F*. The ray positions from the two modes overlap on those planes are spaced differently.

There are two broad classes of optical systems: imaging and non-imaging. Illumination systems which shine light onto a surface is a common example of a non-imaging system. They are usually used to provide uniform illumination on objects, such as illuminating a hologram with a spherical wavefront or illuminating a screen with a polarized wavefront using a liquid crystal projector^{118,119}. On the other hand, imaging systems are usually designed to take a spherical wavefront from a light source and image it through a series of optical components into another spherical wavefront centered at an image plane. Due to aberrations, the output wavefronts will deviate from the ideal spherical shape. As the aberrated wavefront approaches to its focus, it tends to have a complex electric field distribution. Figure 5.3 shows light focusing through a glass and forms a region of caustic (a nephroid-shaped bright area) where the wavefront folds over on itself

and neighboring rays intersect. These types of area will be avoided when combining wavefronts.

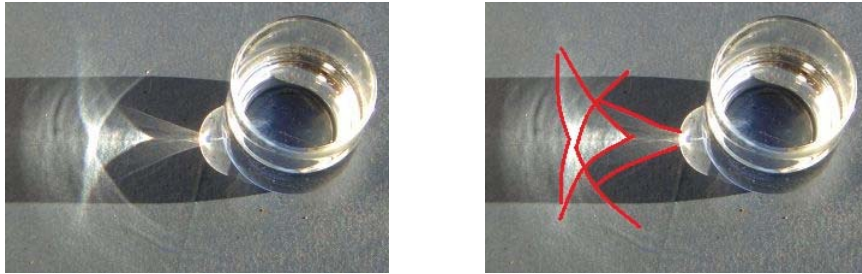


Figure 5.3 (Left) Illumination pattern created from a light focusing through a glass of water. The wavefront contains many bright lines which are the caustics. (Right) The caustics are highlighted in red.

Instead, the wavefronts will be combined at the exit pupil of the imaging system, where the ray grid are relatively well-spaced. For example, for a beam with spherical aberration, the region containing the caustic would be avoided. Then the electric field at the image plane will be evaluated by diffraction theory from the exit pupil, which was described in details in section 1.6.

5.3 Co-propagating wavefront combination

The simplest beam combining configuration occurs when combining two collimated wavefronts propagating in the same direction. Many retarders, polarizers and other anisotropic devices consist of planar surfaces, so it is a common occurrence that a collimated incident beam yields co-propagating collimated exiting beams. In general, \mathbf{P} matrices do not combine, but in the case of co-propagating wavefronts, as shown in Figure 5.4, they can be combined.

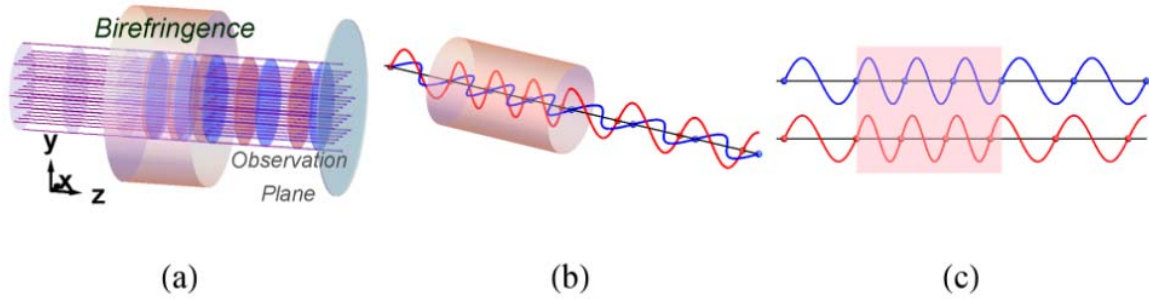


Figure 5.4 (a) A normal incident collimated beam with a planar wavefront (purple) incident onto a birefringent plate. The disks in the plot indicate the start of each period of the oscillating electric fields. The incident beam splits into two wavefronts (red and blue) with a phase delay between them and reaches an observation plane. (b) Electric fields of the two orthogonal eigenstates for a ray passing through the plate. Red for y -polarized and blue for x -polarized. (c) Both electric field oscillations are plotted in one plane to show that the x -polarized mode goes through 3 periods while the y -polarized mode goes through 3.25 periods traversing the plate.

Consider a collimated beam normally incident onto a birefringent plate, as shown in Figure 5.4. Two collimated and completely overlapping beams are generated. They are considered as two separate wavefronts in a sense that the birefringent plate delayed the phase of one mode's wavefront relative to the other mode. The orthogonally polarized eigenstates of the plate are x - and y -polarized light. The ray tracing parameters calculated using the ray tracing algorithm in Chapter 2 and Chapter 3 produces two \mathbf{P} matrices for the

two wavefronts, $\mathbf{P}_1 = \begin{pmatrix} t_1 & 0 & 0 \\ 0 & 0 & 0 \\ 0 & 0 & 1 \end{pmatrix}$ and $\mathbf{P}_2 = \begin{pmatrix} 0 & 0 & 0 \\ 0 & t_2 & 0 \\ 0 & 0 & 1 \end{pmatrix}$ where t_1 and t_2 are amplitude

transmittances. These two wavefronts are the o - and e -modes for uniaxial material, or *fast*- and *slow*-modes for biaxial material. Although these two \mathbf{P} matrices represent two different modes, they both perform the same transformation for the \mathbf{S} ;

$$\begin{aligned} \mathbf{S}' &= \mathbf{P}_1 \cdot \mathbf{S} \quad \text{and} \\ \mathbf{S}' &= \mathbf{P}_2 \cdot \mathbf{S}. \end{aligned} \tag{5.1}$$

As shown in section 3.5, \mathbf{P}_1 and \mathbf{P}_2 have the same $\mathbf{S}_D = \begin{pmatrix} 0 & 0 & 0 \\ 0 & 0 & 0 \\ 0 & 0 & 1 \end{pmatrix}$ which was defined in

equation (3.37). By subtracting \mathbf{S}_D from \mathbf{P} , as shown in equation (3.38), the resultant

$\tilde{\mathbf{P}} = \mathbf{P} - \mathbf{S}_D$ contains the electric field transformation, but not the \mathbf{S} transformation, so the

OPL accumulated from each mode can be coherently incorporated into these electric field

transformations to $\bar{\mathbf{P}} = \tilde{\mathbf{P}} e^{i\frac{2\pi}{\lambda}OPL} = (\mathbf{P} - \mathbf{S}_D) e^{i\frac{2\pi}{\lambda}OPL}$, as shown in equation (3.39). For an

incident \mathbf{E} , the combined exiting \mathbf{E} of two overlapping beams is

$$\begin{aligned} \mathbf{E} &= \bar{\mathbf{P}}_1 \cdot \mathbf{E}_i + \bar{\mathbf{P}}_2 \cdot \mathbf{E}_i \\ &= (\bar{\mathbf{P}}_1 + \bar{\mathbf{P}}_2) \cdot \mathbf{E}_i \\ &= \bar{\mathbf{P}}_{\text{combine}} \cdot \mathbf{E}_i, \end{aligned} \quad (5.2)$$

so the \mathbf{P} matrices can be combined. The combination is done by adding the $\bar{\mathbf{P}}$ matrices of each modes and also one of \mathbf{S}_D , so $\mathbf{P}_{\text{combine}} \cdot \mathbf{S} = \mathbf{S}'$. The combined \mathbf{P} matrix is

$$\begin{aligned} \mathbf{P}_{\text{combine}} &= (\mathbf{P}_1 - \mathbf{S}_D) e^{i\frac{2\pi}{\lambda}OPL_1} + (\mathbf{P}_2 - \mathbf{S}_D) e^{i\frac{2\pi}{\lambda}OPL_2} + \mathbf{S}_D \\ &= \left(\tilde{\mathbf{P}}_1 e^{i\frac{2\pi}{\lambda}OPL_1} + \tilde{\mathbf{P}}_2 e^{i\frac{2\pi}{\lambda}OPL_2} \right) + \mathbf{S}_D \\ &= (\bar{\mathbf{P}}_1 + \bar{\mathbf{P}}_2) + \mathbf{S}_D, \end{aligned} \quad (5.3)$$

as shown in equation (3.41).

For the example in Figure 5.4, the waveplate induces $OPL_1=3\lambda$ and $OPL_2=3.25\lambda$, and assume t_1 and t_2 are both 1. The combined \mathbf{P} matrix is

$$\begin{aligned}
\mathbf{P}_{\text{combine}} &= \begin{pmatrix} 1 & 0 & 0 \\ 0 & 0 & 0 \\ 0 & 0 & 0 \end{pmatrix} e^{i6\pi} + \begin{pmatrix} 0 & 0 & 0 \\ 0 & 1 & 0 \\ 0 & 0 & 0 \end{pmatrix} e^{i6.5\pi} + \begin{pmatrix} 0 & 0 & 0 \\ 0 & 0 & 0 \\ 0 & 0 & 1 \end{pmatrix} \\
&= \begin{pmatrix} e^{i6\pi} & 0 & 0 \\ 0 & e^{i6.5\pi} & 0 \\ 0 & 0 & 1 \end{pmatrix} = \begin{pmatrix} 1 & 0 & 0 \\ 0 & i & 0 \\ 0 & 0 & 1 \end{pmatrix}
\end{aligned}$$

which describes a linear quarter wave retarder as expected, and conveys information of the relative phase induced between the two wavefronts. In general, the combined \mathbf{P} for M co-propagating overlapped wavefronts is

$$\begin{aligned}
\mathbf{P}_{\text{combine}} &= \left(\sum_m^M (\mathbf{P}_m - \mathbf{S}_D) e^{i\frac{2\pi}{\lambda} OPL_m} \right) + \mathbf{S}_D \\
&= \left(\sum_m^M \tilde{\mathbf{P}}_m e^{i\frac{2\pi}{\lambda} OPL_m} \right) + \mathbf{S}_D \\
&= \left(\sum_m^M \bar{\mathbf{P}}_m \right) + \mathbf{S}_D.
\end{aligned} \tag{5.4}$$

Consider a 45° polarized incident beam in equation (5.3),

$$\begin{aligned}
\mathbf{E}' &= \mathbf{P}_{\text{combine}} \cdot \mathbf{E} \\
&= \begin{pmatrix} e^{i\frac{2\pi}{\lambda} OPL_1} & 0 & 0 \\ 0 & e^{i\frac{2\pi}{\lambda} OPL_2} & 0 \\ 0 & 0 & 1 \end{pmatrix} \begin{pmatrix} 1 \\ 1 \\ 0 \end{pmatrix} = \begin{pmatrix} e^{i\frac{2\pi}{\lambda} OPL_1} \\ e^{i\frac{2\pi}{\lambda} OPL_2} \\ 0 \end{pmatrix} \\
&= e^{i\frac{2\pi}{\lambda} OPL_1} \begin{pmatrix} 1 \\ e^{i\frac{2\pi}{\lambda} (OPL_2 - OPL_1)} \\ 0 \end{pmatrix} = e^{i\frac{2\pi}{\lambda} OPL_1} \begin{pmatrix} 1 \\ e^{i\frac{2\pi}{\lambda} \Delta OPL} \\ 0 \end{pmatrix}.
\end{aligned}$$

The resultant polarizations after the waveplate are a function of ΔOPL as shown in Figure 5.5.

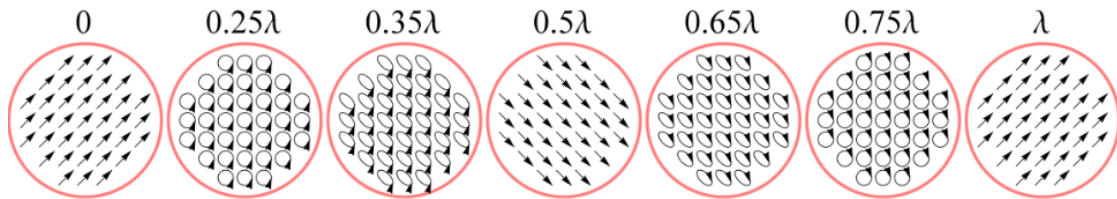


Figure 5.5 The resultant polarization states as a function of ΔOPL .

5.4 Sheared co-propagating wavefront combination

The method of combining \mathbf{P} matrices in the previous section applies to systems of multiple birefringent plates or wedges. The wavefronts exiting these systems do not always perfectly overlap. The difference between two wavefronts is referred to as their shear. They may be laterally sheared, where one is translated relative to the other, as in the case of lateral shear interferometers¹²⁰. They may be rotationally sheared, where one is rotated. Figure 4.3 shows partially overlapping wavefronts propagating in the same direction with a lateral shear. The \mathbf{P} matrices are combined where the beams overlap. As shown in section 4.3, extra adjustment Δt defined in equation (4.1) is made to the OPL for off-axis beams, so the resultant retardance is $\frac{2\pi}{\lambda} [(OPL_s + \Delta t) - OPL_f]$. Consider an evenly spaced incident grid of rays propagating through the birefringent plate at an angle, as shown in Figure 5.6. It results in two sets of exiting ray grids representing the two wavefronts. Depending on the system, the exiting rays may be analyzed on plane A , orthogonal to the ray direction, plane B which is parallel to the plate, or some other surface.

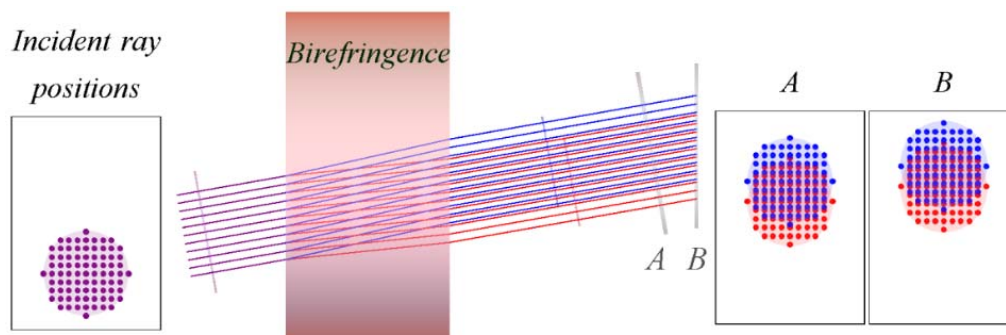


Figure 5.6 One off-axis collimated ray grid propagates through a birefringent plate splits into two collimated wavefronts. They partially overlap each other on plane *A* and plane *B*.

The ray locations of these two exiting modes do not coincide. The individual wavefront can be interpolated onto the same grid before combining the \mathbf{P} matrices or combining the \mathbf{E} fields. The given incident sample rays should be dense enough to resolve the structure of the beams and their boundaries. Although these rays are individual points on an exit plane (for example, the exit pupil), in this case they represent a smooth and predictable wavefront. Further considerations of interpolating wavefronts are given in section 5.6. The two ray sets in Figure 5.6 are assumed to have uniform \mathbf{E} field across the exit plane. One exiting ray set is horizontally polarized and the other ray set is vertically polarized, as shown in Figure 5.7. The result of combining these two modes gives an overlapping area of interference surrounded by two crescents with the polarization of the two individual modes.

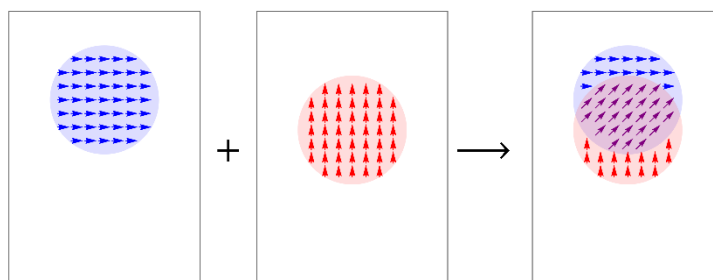


Figure 5.7 The two resultant wavefronts are horizontally (blue) and vertically (red) polarized. The overlapping area of the two orthogonal modes is 45° polarized.

The polarization of the overlapping area depends on the relative phase between the two modes. Figure 5.8 shows the various polarization ellipse patterns for different relative phases.

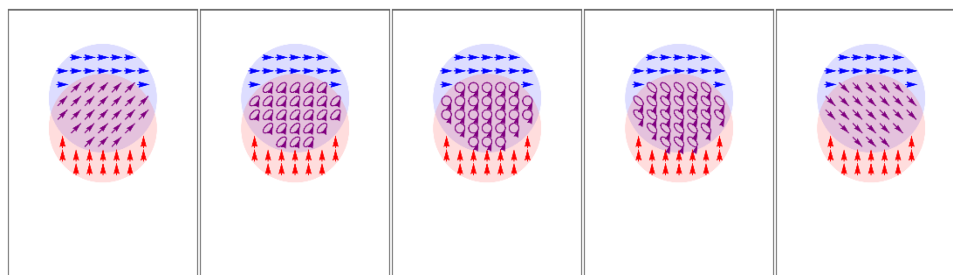


Figure 5.8 Two individual wavefronts, one horizontally and one vertically polarized, are laterally sheared by the waveplate. They partially overlap each other. The polarization of the overlapping region depends on the phase difference of the individual wavefront. Showing from left to right, the relative phases are (0, 0.15, 0.25, 0.35, 0.5) waves.

In general, ray doubling occurs each time a beam enters an anisotropic medium. An optical system containing N anisotropic interfaces can have 2^N separate exiting modes in transmission for one incident ray. To combine cumulative \mathbf{P} matrices of multiple off-axis modes from a system that consists of N plane parallel anisotropic plates, equations (4.2) and (5.4) become equation (5.5). Instead of 2 exiting modes, 2^N modes are combined within the beam overlapping region as

$$\begin{aligned}
\mathbf{P}_{\text{overlap}} &= \left(\sum_{m=1}^M \bar{\mathbf{P}}_{\text{tm,total}} \right) + \mathbf{S}'_{\mathbf{D}} \\
&= \sum_{m=1}^M \left(\bar{\mathbf{P}}_{\text{tm,total}} e^{i \frac{2\pi}{\lambda} (OPL_{tm} + \Delta t_m)} \right) + \mathbf{S}'_{\mathbf{D}} \\
&= \sum_{m=1}^M \left[\left(\mathbf{P}_{\text{tm,total}} - \mathbf{S}'_{\mathbf{D}} \right) e^{i \frac{2\pi}{\lambda} (OPL_{tm} + \Delta t_m)} \right] + \mathbf{S}'_{\mathbf{D}} \\
&= \left\{ \sum_{m=1}^M \left[\left(\prod_{n=1}^N \mathbf{P}_{\text{tm}, N-n+1} \right) - \mathbf{S}'_{\mathbf{D}} \right] e^{i \frac{2\pi}{\lambda} (OPL_{tm} + \Delta t_m)} \right\} + \mathbf{S}'_{\mathbf{D}},
\end{aligned} \tag{5.5}$$

where $M=2^N$, $\mathbf{P}_{\text{tm,total}} = \prod_{n=1}^N \mathbf{P}_{\text{tm}, N-n+1}$ is the cumulative \mathbf{P} matrix for the effects from all

of the interfaces, $\Delta t_m = \bar{\mathbf{a}}_{\mathbf{m}} \cdot \hat{\mathbf{S}} = (\bar{\mathbf{r}}_1 - \bar{\mathbf{r}}_{\mathbf{m}}) \cdot \hat{\mathbf{S}}$ and $\bar{\mathbf{r}}_{\mathbf{m}}$ is the ray intercept of mode m at the last surface of the anisotropic plate assembly.

5.5 Non co-propagating wavefront combination

This section describes combining the \mathbf{E} fields of sets of spatially overlapping ray grids propagating in different directions. The \mathbf{P} matrices with different $\mathbf{S}_{\mathbf{D}}$ cannot be combined with the method shown in sections 5.3 and section 5.4, but their \mathbf{E} fields can be added. When M modes are traced to the same spot spatially, the electric fields can be combined coherently as

$$\mathbf{E}_{\text{total}} = \sum_{m=1}^M \mathbf{E}_{\mathbf{m}} e^{i \frac{2\pi}{\lambda} OPL_m}. \tag{5.6}$$

A simple example of merging two grids of polarized rays with a polarizing beam splitter (PBS) to the same plane is shown in Figure 5.9.

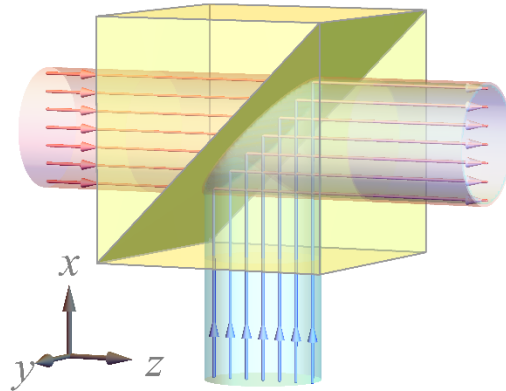


Figure 5.9 Two collimated wavefronts (red and blue) exiting a PBS into the same direction.

Since the two grids of rays are coming from different directions, instead of combining their

\mathbf{P} matrices, the resultant \mathbf{E} fields are combined. The x -polarized light with $\mathbf{P}_1 = \begin{pmatrix} 1 & 0 & 0 \\ 0 & 0 & 0 \\ 0 & 0 & 1 \end{pmatrix}$

exits the PBS as $\mathbf{E}_1 = (1, 0, 0)$. The y -polarized light with $\mathbf{P}_2 = \begin{pmatrix} 0 & 0 & 0 \\ 0 & 1 & 0 \\ 1 & 0 & 0 \end{pmatrix}$ reflects into $\mathbf{E}_2 =$

$(0, 1, 0)$. These two grids are shown coinciding with each other, but in general they do not share the same ray coordinate. The method to combine two overlapping beams with misaligned ray grids will be explained in section 5.6.

The exiting polarization depends on the optical path difference ΔOPL between the two beams,

$$\mathbf{E}_{\text{total}} = \mathbf{E}_1 e^{i\frac{2\pi}{\lambda}OPL_1} + \mathbf{E}_2 e^{i\frac{2\pi}{\lambda}OPL_2} = \begin{pmatrix} 1 \\ e^{i\frac{2\pi}{\lambda}(OPL_2 - OPL_1)} \\ 0 \end{pmatrix} e^{i\frac{2\pi}{\lambda}OPL_1} = \begin{pmatrix} 1 \\ e^{i\frac{2\pi}{\lambda}\Delta OPL} \\ 0 \end{pmatrix} e^{i\phi}. \quad (5.7)$$

If the two beams are perfectly collimated with no deviation, and the ray grids for the two wavefronts overlap each other perfectly, the resultant \mathbf{E} will have a constant ΔOPL across the resultant beam and produce a uniformly polarized beam, as shown in Figure 5.5. If the ΔOPL are spatially varying, the resultant polarization ellipses will also be spatially varying across the beam, as shown in Figure 5.10.

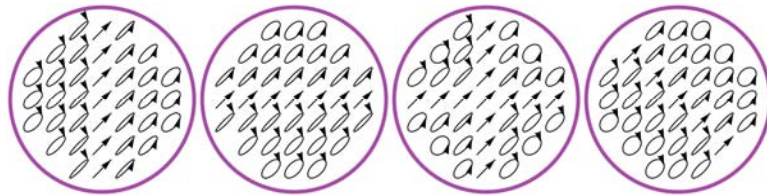


Figure 5.10 Resultant polarization states with spatially varying ΔOPL across the beam.

5.6 Combining irregular ray grids

In general the exiting ray locations corresponding to multiple wavefronts do not coincide. When a spherical wave propagates through a retarder, the two sets of rays for the two split modes are sheared with respect to each other. The two modes have different spacing between rays, as shown in Figure 5.2 *F*. Although the rays do not overlap exactly on top of each other, their wavefronts do substantially overlap, so they need to be combined to reveal their overall effect. This section describes the procedures to reconstruct and combine the wavefronts of these misaligned ray grids. These procedures involve interpolating data, and an example interpolation algorithm is also provided.

5.6.1 General steps to combine misaligned ray data

To combine \mathbf{E} field functions by vector addition, the discrete ray data for the \mathbf{E} fields needs to be interpolated into continuous functions. The discrete set of \mathbf{E} fields calculated for each wavefront from the ray trace is spatially distributed over a surface. The discrete \mathbf{E} field on

the irregular ray grid can be reconstructed into continuous function by interpolation. Interpolation is a method to estimate intermediate values between known data, so resampling can be done on the interpolated function. There are many algorithms to interpolate data, such as bilinear interpolation, spline interpolation, Kriging interpolation and many others^{121,122,123,124,125}. Those values estimated by interpolation contain interpolation errors. However, with sufficient sample points, and smooth input ray data, these errors can be minimized. By interpolating the ray data of the ray grids, and resampling the interpolated functions to a common ray grid, the resultant resampled \mathbf{E} fields can be added to simulate interfering multiple beams of light. Since the \mathbf{E} field is summed on a mode by mode basis, the ray trace data is first grouped into individual modes. Then the \mathbf{E} field, as shown in equation (5.8) with seven components (three orthogonal components of the complex \mathbf{E} field and an OPL), for each mode is interpolated using the discrete ray data and yields a continuous function. The resultant functions of \mathbf{E} of each mode are added to represent the combined \mathbf{E} field. The steps of constructing the overall \mathbf{E} field are summarized in Table 5.1.

$$\mathbf{E} = \begin{pmatrix} \mathcal{R}e[E_x] + i\mathcal{I}m[E_x] \\ \mathcal{R}e[E_y] + i\mathcal{I}m[E_y] \\ \mathcal{R}e[E_z] + i\mathcal{I}m[E_z] \end{pmatrix} e^{i\frac{2\pi}{\lambda}OPL} = \begin{pmatrix} |E_x| e^{i\phi_x} \\ |E_y| e^{i\phi_y} \\ |E_z| e^{i\phi_z} \end{pmatrix} e^{i\frac{2\pi}{\lambda}OPL} \quad (5.8)$$

Table 5.1 Steps to reconstruct wavefront from wavefront combination

Steps	Operation	Output
1	Group exiting ray trace data by mode	Grids of ray data
2	Calculate exiting \mathbf{E} for the grids of ray	Grids of \mathbf{E}
3	Interpolate each grid of \mathbf{E}	\mathbf{E} functions for each mode
4	Resample \mathbf{E} from each \mathbf{E} function onto a common grid	Grids of resampled \mathbf{E}
5	Add the resampled grids of \mathbf{E}	Final grid of \mathbf{E}

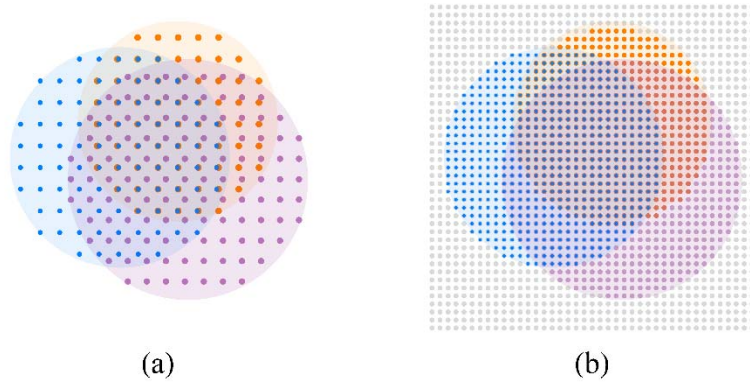


Figure 5.11 Three grids of rays corresponding to three modes reach a 2D plane. (a) The location of the rays are shown as dots. (b) The ray data are resampled in a regular grid with zeros values (gray dots) outside the region of the three beams.

An example of three overlapping grids of rays whose ray positions are unequally spaced and do not coincide is shown in Figure 5.11(a). A rectangular grid is preferred, so the matrix data structures and operations can be used. Therefore the region without data should be padded with zeros. In Figure 5.11 (b), the three ray grids have been resampled using interpolation onto a new grid with zeros around the data. This new grid is evenly spaced which is useful for further analysis using diffraction theory. For M individual modes, the resultant \mathbf{E} field is calculated by adding M interpolated \mathbf{E} fields as

$$\mathbf{E}(x, y) = \sum_m^M e^{i \frac{2\pi}{\lambda} OPL_m(x, y)} \begin{pmatrix} E_{x,m}(x, y) \\ E_{y,m}(x, y) \\ E_{z,m}(x, y) \end{pmatrix} \quad (5.9)$$

where (x, y) is the coordinate system at the surface of mode combination.

5.6.2 Inverse-distance weighted interpolation

This section describes the inverse-distance weighted interpolation algorithm¹²⁶ used in this dissertation to generate intermediate values within sample data. This weighted interpolation method uses the weighted averages of data from nearby points¹²⁷. This interpolation method is versatile and fairly accurate for a dense grid of sample points with smooth values.

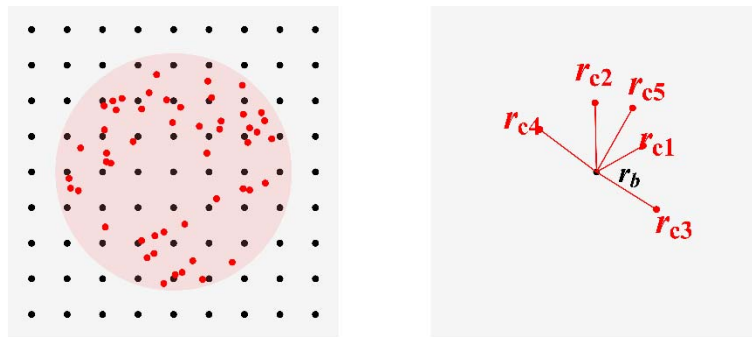


Figure 5.12 (Left) An unevenly spaced ray grid at locations $(\mathbf{r}_{E1}, \mathbf{r}_{E2}, \dots, \mathbf{r}_{Ea}, \dots, \mathbf{r}_{EA})$ are shown in red. The evenly spaced grid $(\mathbf{r}_1, \mathbf{r}_2, \dots, \mathbf{r}_b, \dots, \mathbf{r}_B)$ for resampling is shown in black. (Right) Interpolation involves weighting contributions from nearest neighbors. Five closest data location $(\mathbf{r}_{c1}, \mathbf{r}_{c2}, \mathbf{r}_{c3}, \mathbf{r}_{c4}, \mathbf{r}_{c5})$ to \mathbf{r}_b are shown.

Consider A samples of electric field $(\mathbf{E}_1, \mathbf{E}_2, \dots, \mathbf{E}_a, \dots, \mathbf{E}_A)$ at A irregularly spaced locations $(\mathbf{r}_{E1}, \mathbf{r}_{E2}, \dots, \mathbf{r}_{Ea}, \dots, \mathbf{r}_{EA})$, which will be resampled to a new evenly spaced grid at B locations $(\mathbf{r}_1, \mathbf{r}_2, \dots, \mathbf{r}_b, \dots, \mathbf{r}_B)$, as shown in Figure 5.12 (left). The Q closest data points from \mathbf{r}_b , as shown in Figure 5.12 (right), will be used to estimate the value at \mathbf{r}_b . At point \mathbf{r}_b , the Q closest electric field samples are $(\mathbf{E}_{c1}, \mathbf{E}_{c2}, \dots, \mathbf{E}_{cq}, \dots, \mathbf{E}_{cQ})$ at $(\mathbf{r}_{c1}, \mathbf{r}_{c2}, \dots, \mathbf{r}_{cq}, \dots, \mathbf{r}_{cQ})$. Q is chosen to produce a reasonable electric field estimation at intermediate locations. The distance of these Q data points from point \mathbf{r}_b are $(|\bar{r}_{c1}|, |\bar{r}_{c2}|, \dots, |\bar{r}_{cq}|, \dots, |\bar{r}_{cQ}|) = (|\mathbf{r}_{c1} - \mathbf{r}_b|, |\mathbf{r}_{c2} - \mathbf{r}_b|,$

... $|\mathbf{r}_{cq}-\mathbf{r}_b|$, ... $|\mathbf{r}_{cQ}-\mathbf{r}_b|$). Then, the interpolated value of the \mathbf{E} field at \mathbf{r}_b weighted by the Q data points is

$$\mathbf{E}_b = \sum_{q=1}^Q S_q \mathbf{E}_{cq}, \quad (5.10)$$

where

$$S_q = \frac{(|\bar{r}_{cq}| + \varepsilon)^{-p}}{\sum_{q=1}^Q [(|\bar{r}_{cq}| + \varepsilon)^{-p}]} \quad (5.11)$$

is a scaling factor based on distance $|\bar{r}_{cq}|$ and has a maximum of 1. $\varepsilon = 10^{-17}$ is a small number to avoid the situation of “divide by zero” in computer program, when $|\bar{r}_{cq}| = 0$. p is the inverse-distance weighting power which controls the region of influence of each of the data locations. As p increases, the region of influence decreases. When $p=0$, equation (5.11) simply averages the sampled values. As \mathbf{r}_{cq} is near \mathbf{r}_b , S_q emphasizes \mathbf{E}_{cq} . If \mathbf{r}_b is exactly on top of \mathbf{r}_{cq} , $|\bar{r}_{cq}| = 0$, then $S_q \approx 1$. When \mathbf{r}_b is far away from any one of the A data points, $S_q \rightarrow 0$. Abrupt magnitude changes at the edge of apertures can result in interpolation artifacts, and such artifacts can be minimized by using a small number of Q and limiting the area where sample can be accounted for in equation (5.10) during resampling.

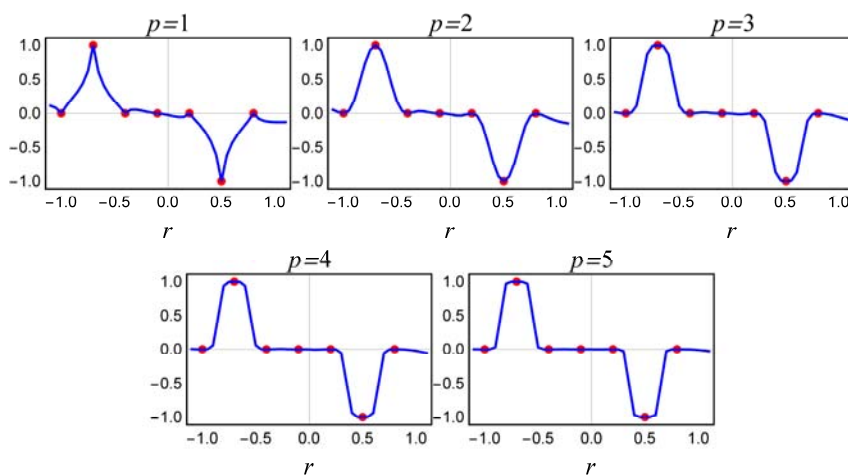


Figure 5.13 Seven data points (red) are interpolated using equation (5.10). The resultant interpolation functions are shown in blue for five different p .

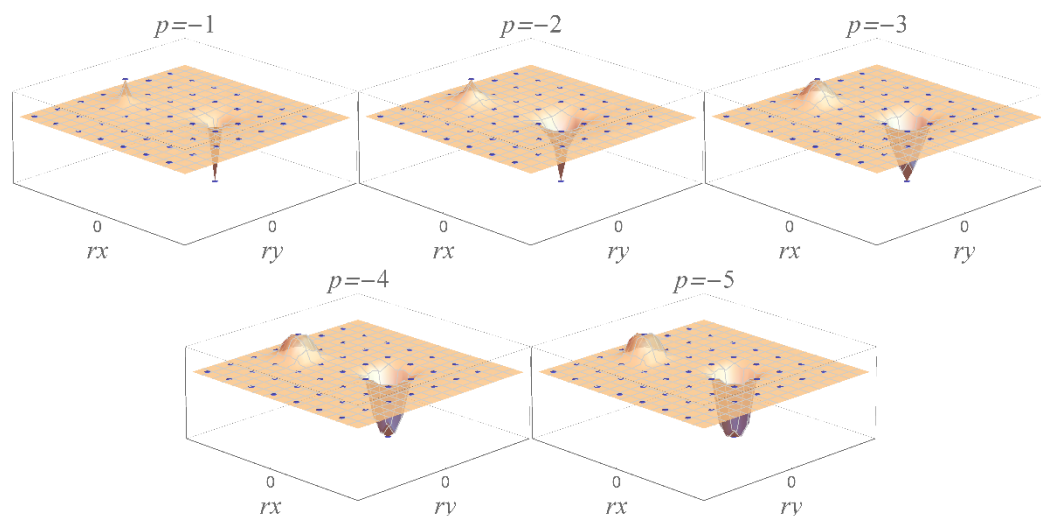


Figure 5.14 Two non-zero data point (blue) are interpolated using equation (5.10). The resultant 2D interpolated functions shown in orange for the different p reveal the influence function for the different p .

Two interpolation examples are shown in Figure 5.13 and Figure 5.14 for a set of 1D data and a set of 2D data. The interpolation algorithms produce a smooth function with $p=3$. Depending on the physical properties of the data, p should be chosen. For example, Kelway¹²⁸ and NOAA¹²⁹ uses $p=1.65$ and $p=2$ for interpolating rainfall. The ARMOS model¹³⁰ suggests p ranges from 4 to 8 for interpolating oil pressure heads.

Variations of the inverse-distance weighted interpolation algorithm can reduce the artifacts of the interpolation function, such as limiting the radius of the samples being used, or taking the slope of the samples into account¹³¹. Other interpolation algorithms, such as Kirging interpolation¹³² and thin plate spline¹³³ provide more sophisticated estimations and require more involved computer programming. These interpolation functions are usually built into programs, such as Mathematica and MATLAB.

5.7 Conclusions

The results of an anisotropic ray trace are grids of rays associated with multiple modes and multiple wavefronts. Each wavefront takes a different path and has its own amplitude, polarization, *OPL*, and aberration functions. When these wavefronts overlap, their combined effects are calculated from interfering their wavefronts. The optical analysis of interferometers and anisotropic optical elements requires combining these multiple wavefronts after the ray trace. This is done by: (1) sampling each wavefronts through polarization ray tracing, (2) fitting them to interpolating functions, one for each mode, and then (3a) add these functions of \mathbf{P} or \mathbf{E} to represent the interference at that plane, or (3b) resample \mathbf{P} or \mathbf{E} from their interpolation functions on an evenly spaced grid. Then, this recombined wavefront is used to calculate overall aberrations, point spread functions and other metrics.

It is preferred to combine the \mathbf{P} matrices rather than the \mathbf{E} fields from each mode when the beams are collimated. The advantages of combining \mathbf{P} matrices instead of \mathbf{E} fields are: (1) it preserves the polarization information along the ray path for any incident polarization, and (2) the calculations of diattenuation and retardance described in section

4.4 and section 4.5 still apply. However, when the \mathbf{S}_D of the modes being combined is not the same, the \mathbf{P} matrices cannot be combined, so the \mathbf{E} fields are combined instead.

The calculations of wavefront combination are usually done at the exit pupil of an imaging system or at the plane of illumination, where the \mathbf{P} matrices, \mathbf{E} fields and their *OPLs* sampled from ray tracing are located on a smooth and well-spaced exiting grid, and where caustics can be avoided. These sampled wavefront parameters are fitted and interpolated to wavefront functions. Interpolation over the pupil allows estimation of the associated values anywhere within the pupil using the ray trace data, and constructs new values at intermediate locations. Then the combining effect of each mode is calculated from the summation of these wavefront functions.

Assumptions are often made to reduce complex calculations, such as ignoring the small wavefront shear from a thin waveplate. However, for thick biaxial components or birefringent crystals which split an incident beam into different paths, and then redirects the beams to be combined to a plane of interest, care and caution are needed. When the calculation is done without assumptions, subtle effects of misalignments and fabrication defects in the system can be simulated and yield accurate results. Large amounts of ray tracing and interpolation may be required for wavefronts which are not smooth.

Detailed analysis of a crystal waveplate and a Glan-Type polarizer, using the ray tracing algorithms in Chapter 2 and Chapter 3 with the method of mode combination in this chapter, will be covered in Chapter 6 and Chapter 7. These simulations show the aberrations, undesired modes, and angle of incidence effects observed in laboratory measurements, which limit these high performance birefringent components.

CHAPTER 6 ABERRATIONS OF CRYSTAL RETARDERS

6.1 Introduction to crystal waveplates

A waveplate is a common type of retarder formed from a plane parallel plate of birefringent material. Its function is to introduce retardance between two orthogonal eigenmodes in the transmitted light. They are utilized to control polarized light, adjust ellipticity, rotate polarization, and even fine tune laser wavelengths when used inside laser cavities. They are widely used in polarimetry, medical imaging, microscopy, telecom, and laser cutting industry. Simple isotropic plane parallel plates cause a focus shift and spherical aberration on-axis, and add coma, and astigmatism off-axis, due to the variation of the OPL with angle¹³⁴. The aberrations of the retarder's ordinary wave are the same as for the isotropic plate. The aberrations of the extraordinary wave are more complicated because they include all the isotropic aberrations as well as additional aberrations arising from the variation of refractive index with direction. These aberrations and their effect on image formation will be calculated from polarization ray tracing.

Waveplates are characterized by the plate thickness t and the on-axis retardance δ at a reference wavelength λ_{ref} .

$$\delta = \frac{2\pi}{\lambda_{ref}} \Delta n t \quad (6.1)$$

where δ is the on-axis retardance in radians and, $\Delta n = |n_e - n_o|$ is the birefringence. The optical path difference of the two modes is $\Delta OPL = \Delta n t$. Common waveplates include quarter waveplates and half waveplates. A zero-order quarter waveplate with a thickness

of $\lambda_{ref}/(4\Delta n)$ is most commonly made of quartz or magnesium fluoride rather than calcite, because the smaller Δn translates into a more practical thickness. Calcite would require a thickness of less than $10\ \mu\text{m}$ to achieve $3\frac{1}{2}$ waves of retardance (a 3rd order waveplate) for $0.5\ \mu\text{m}$, which is impractically thin to manufacture. A $1\frac{1}{4}$ wave waveplate generates the same polarization changes on-axis at the λ_{ref} as a zero-order quarter waveplate, and is labeled as first order quarter waveplate. Similarly, a $2\frac{1}{4}$ wave waveplate is a second order quarter waveplate. The waveplates of different orders have the same effect on normal incident light at the λ_{ref} . The effects are different when the *OPL* is different, i.e. at other wavelengths or incident angles. A waveplate's retardance changes with incident angles and with changes in refractive index due to dispersion. It is common to stack multiple waveplates together with different dispersion properties in order to produce a nearly constant retardance over multiple wavelengths. Such a waveplate is called an achromatic waveplate^{46,135}.

Algorithms for ray paths through anisotropic elements were described in Chapter 4. These algorithms are applied in this chapter to study the aberrations of a waveplate. ΔOPL and the retardance are calculated for the on and off-axis incident rays. Consider a collimated beam passing through a uniaxial plate shown in Figure 6.1. The lateral shear between the two wavefronts is Δr and the two beams partially overlap after the plate. Depending on the incident angle, the incident polarization and the retardance of the plate, the two exiting states can combine to linear, circular, or elliptical polarization.

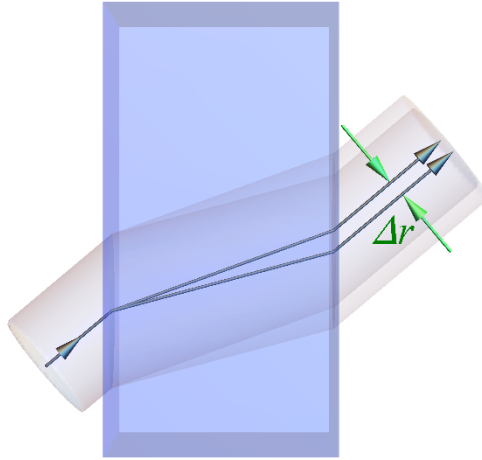


Figure 6.1 A ray of an incident beam refracts into a uniaxial plane parallel plate and splits into two rays in two directions. After these two rays refract out of the crystal, they both propagate in the same direction as the incident ray, but are displaced by Δr .

In the following discussion, the normalized incident propagation vector $\mathbf{k} = \{k_x, k_y, k_z\}$ is defined as

$$\hat{\mathbf{k}} = \left(\frac{\tan \theta_x}{\sqrt{\tan^2 \theta_x + \tan^2 \theta_y + 1}}, \frac{\tan \theta_y}{\sqrt{\tan^2 \theta_x + \tan^2 \theta_y + 1}}, \frac{1}{\sqrt{\tan^2 \theta_x + \tan^2 \theta_y + 1}} \right) \quad (6.2)$$

where $\tan \theta_x = k_x/k_z$, $\tan \theta_y = k_y/k_z$, and θ is the incident angle in air.

6.2 Angular behavior of a uniaxial A-plate

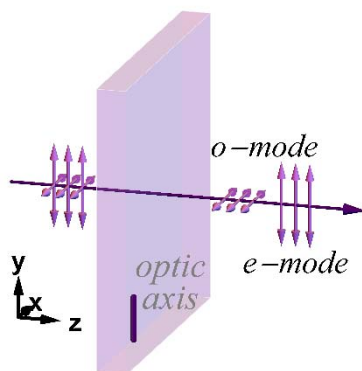


Figure 6.2 Negative uniaxial A-plate such as calcite with a y -oriented optic axis delaying the o -modes with respect to the e -mode.

An A-plate is a uniaxial waveplate whose optic axis lies on the plate surface, as shown in Figure 6.2. In this configuration, the maximum birefringence is obtained at normal incidence. Consider a zero-order quarter wave calcite A-plate with an optic axis along y axis. Ray splitting occurs for all off-axis rays. The index variation of the e -mode, n_e , for wavelength $0.5 \mu\text{m}$ is shown in Figure 6.3 (a) over a $\pm 40^\circ$ square field of view (FOV). $n_e(\theta_x, 0)$ is constant for light incident in the x - z plane, and decreases quadratically with respect to angle θ_y above and below that plane. All e -rays propagating in the x - z plane are linearly polarized along the optic axis, with the same index n_E . For e -rays in the y - z plane, the \mathbf{E} field inside the crystal rotates from the optic axis as they move off-axis, changing n_e towards n_o . The birefringence of the A-plate produces small lateral shear Δr , quadratic with angle and slightly larger along the x axis as plotted in Figure 6.3 (b), between the two parallel exiting modes. This shear is a function of Δn and increases with the plate's thickness.

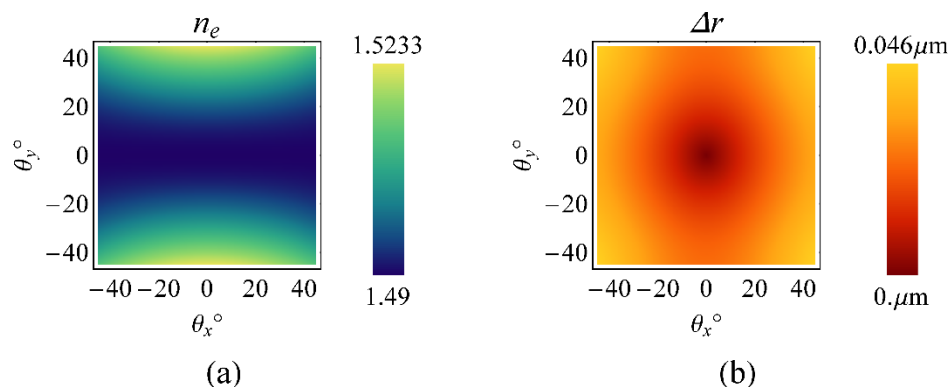


Figure 6.3 (a) n_e at wavelength $0.5 \mu\text{m}$ in a y -oriented calcite A-plate as a function of incident angle (θ_x, θ_y) in air. (b) The shear displacement Δr between the two exiting modes through the quarter wave calcite A-plate, measured transverse to the \mathbf{k} vector.

The retardance induced by a waveplate depends not only on Δn but also the physical ray paths of the two eigen-states. The ray paths of three rays at $0.5 \mu\text{m}$ with increasing angle of incidence in the y - z plane passing through a quarter wave A-plate with thickness 0.0007 mm are shown in Figure 6.4. The path length increases off-axis, but the birefringence reduces faster with angle, described in Figure 4.3 (c), yielding the net decrease in retardance (ΔOPL).

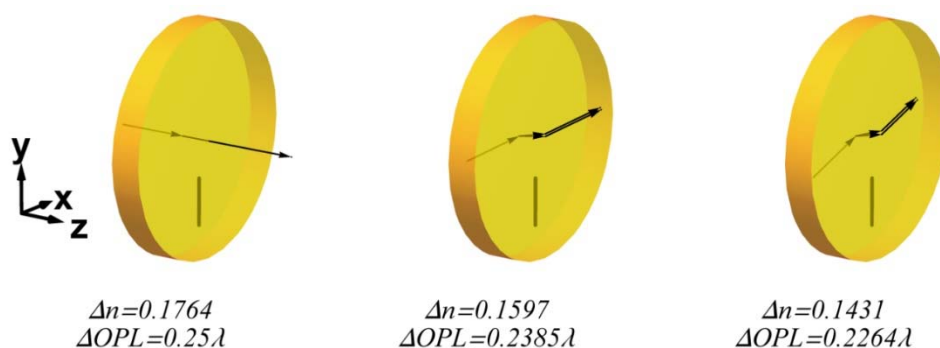


Figure 6.4 Three incident rays at $0.5 \mu\text{m}$ along the principal section with incident angles 0° , 30° , and 45° pass through a quarter wave A-plate, and experience different birefringence Δn and ΔOPL .

Due to the varying refractive index of the e -mode with angle, the angular behavior of the e -wavefront is very different than that of the o -wavefront. Consider a converging

beam focused through an A-plate. The wavefronts of the individual o - and e -modes take different paths, experience different refractive indices, and have different aberrations. Figure 6.5 shows the ray bundles and caustic formed near focus in both sagittal and tangential planes. The e -mode converges before the o -mode in the x - z plane, and after the o -mode in the y - z plane.

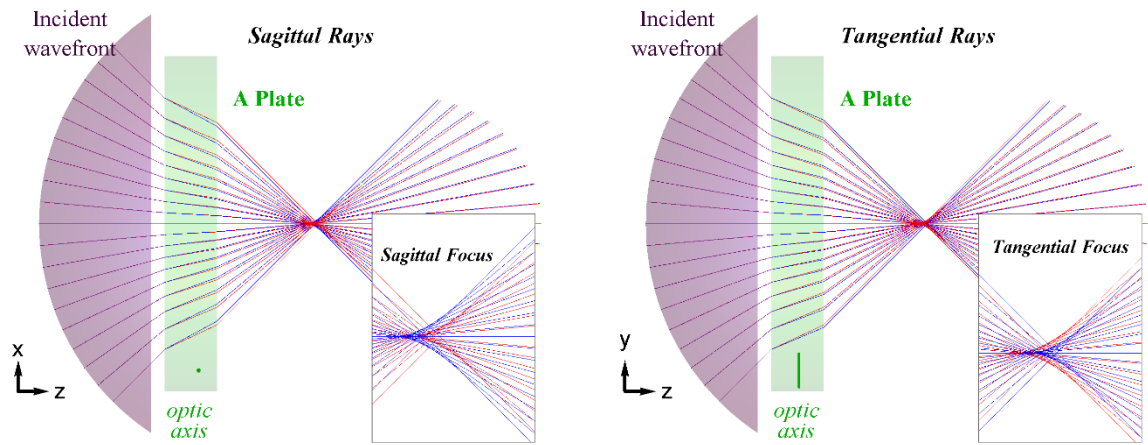


Figure 6.5 (Left) Sagittal and (right) tangential ray bundles ($\pm 45^\circ$) in the focal region are shown with o -rays in red and e -rays in blue. A thick waveplate is used to make the aberrations easily visible.

The OPL s of the two modes exiting the A-plate as a function of angle are calculated as in section 4.2 and are shown in Figure 6.6. The o -mode's OPL has circularly symmetric aberration about the z axis, comprising a focus shift and some spherical aberration. In contrast, the e -mode's OPL is symmetric about the optic axis (the y axis); the tangential e -rays have a larger OPL than the sagittal e -rays.

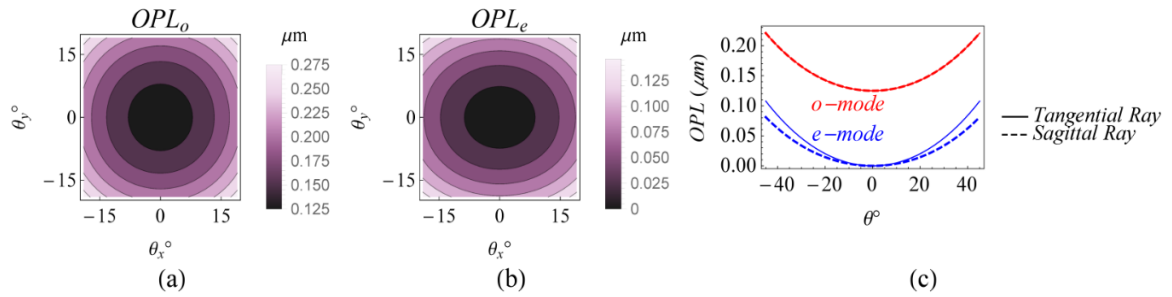


Figure 6.6 (a) and (b) show the OPL of the o - and e -wavefronts after the A-plate. (c) shows the OPL values in the tangential and sagittal planes.

The orientation of the exiting polarization states for the two modes plotted in three-dimensions viewed along the z axis are shown separately in Figure 6.7 (a). Moving away from the center of the pupil, the e -polarizations are slightly rotated from the y direction. Similarly, the o -polarizations are slightly rotated from the x direction. The OPL difference between the o - and e -rays is the retardance, as shown in Figure 6.7 (b), which is calculated as in section 4.5. The variation of retardance with angle is saddle shaped, increasing perpendicular to the optic axis (x - z plane) and decreasing along the y - z plane. The retardance magnitude in the retardance map is scaled as equation (6.1), linear with the plate thickness and Δn , and inversely with wavelength. Also, the shape of the retardance map is symmetric about the optic axis. If the optic axis lies orthogonal to the waveplate (C-plate configuration), the retardance map will become rotationally symmetric, zero retardance at normal incidence and increases quadratically with angle.

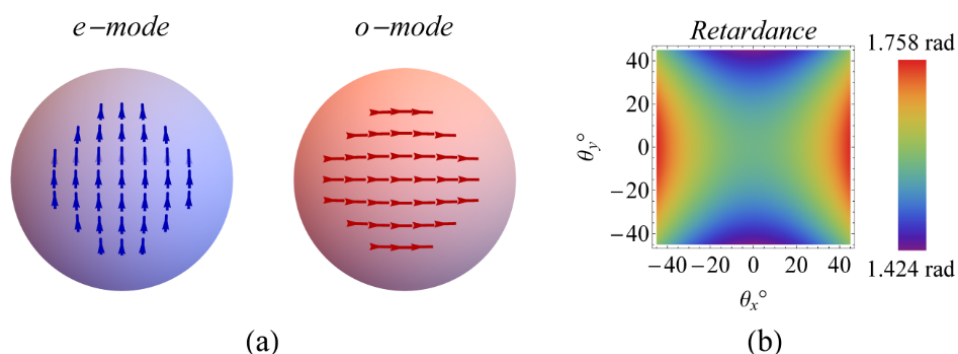


Figure 6.7 (a) *o*- and *e*-polarizations are shown on the exiting wavefronts in Figure 6.5 , thus the slight rotation. The arrow locations indicate phase. (b) Retardance magnitude through the quarter wave A-plate.

6.3 Polarization aberrations of a uniaxial A-plate

This section presents the methods of analyzing aberrations of crystal waveplates and their effects on image formation. The polarization aberrations of a quarter wave uniaxial calcite A-plate (Figure 6.8) for a beam with 0.5NA at $0.5\ \mu\text{m}$ are studied. Although the zero-order quarter waveplate is very thin and induces small aberrations, every uniaxial A-plate has similar polarization aberrations. Even the aberrations of this waveplate are arbitrary, the form and interpretation are similar to other waveplates.

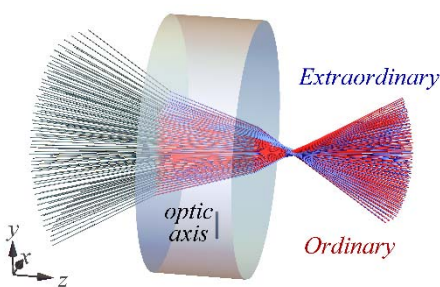


Figure 6.8 A beam with 0.5NA is simulated by a grid of rays which focuses through a quarter wave calcite A-plate with optic axis oriented along y . The incident ray grid splits into two ray grids, one for the ordinary mode (red), and one for the extraordinary mode (blue).

To evaluate the aberrated focus of the quarter wave A-plate, a converging ray bundle with 0.5NA is traced to the best RMS focus (Appendix A) of both modes. Using

the ray tracing results, the wavefronts are examined at the exit pupil, as described in section 1.6. The wavefront aberrations at the exit pupil of the two modes are shown in Figure 6.9. The o -wavefront is rotationally symmetric with spherical aberration, while the e -wavefront has astigmatism.

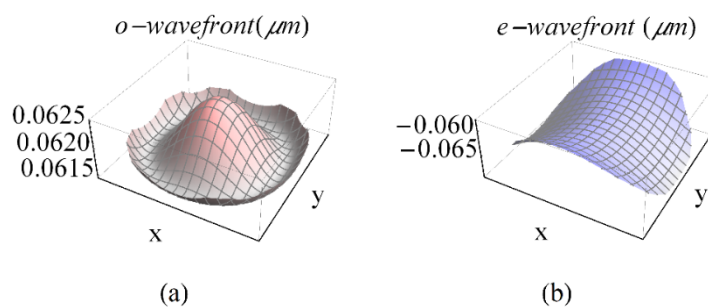


Figure 6.9 The o - and e -wavefronts at the exit pupil of the quarter wave calcite A-plate for 0.5 NA at $0.5 \mu\text{m}$.

Although the magnitude of the aberrations are small due to the example thin plate, they scale with the plate thickness t and birefringence Δn , and changes form with the optic axis orientation. For the example A-plate, the aberrations of both modes increase linearly with the plate thickness, as shown in Figure 6.10.

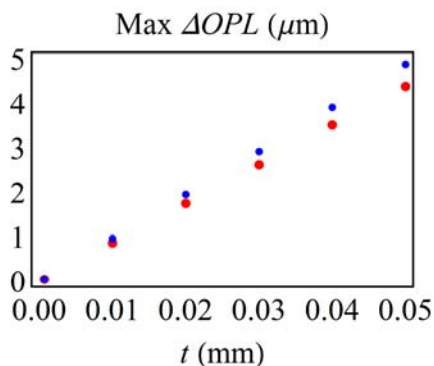


Figure 6.10 The maximum (red) o - and (blue) e - ΔOPL calculated from ray tracing at the exit pupil for six different plate thickness t

The \mathbf{P} matrices at the spherical exit pupil are shown in Figure 6.11. To examine the polarization aberrations, the \mathbf{P} matrices are extracted from the 3D representation and converted into a Jones pupil, as shown in Figure 6.12¹⁰⁸.

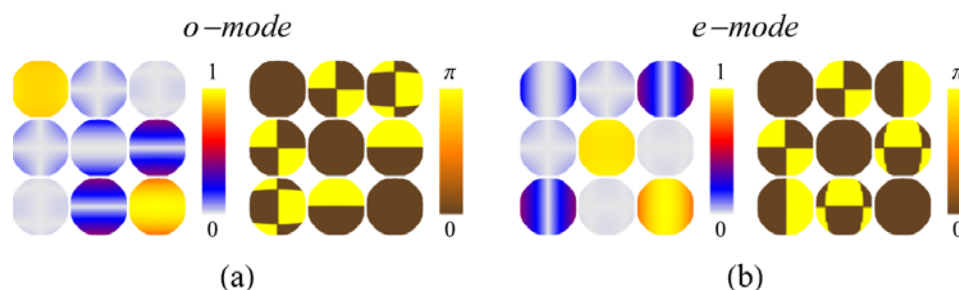


Figure 6.11 The \mathbf{P} matrices of the *o*- and *e*-wavefronts at the exit pupil. The magnitude (left 3x3 panels) and phase in radians (right 3x3 panels) of the (a) *e*-mode's and (b) *o*-mode's \mathbf{P} matrices.

The *o*-wavefront is an *x*-polarizer with aberrations; the *xx* component with the majority of the light has apodization, and its phase shows the spherical aberration. The *e*-wavefront is a *y*-polarizer with aberrations; the *yy* component has the most amplitude with apodization, and its phase shows astigmatism. The combined polarizations at the exit pupil are evaluated in the next section.

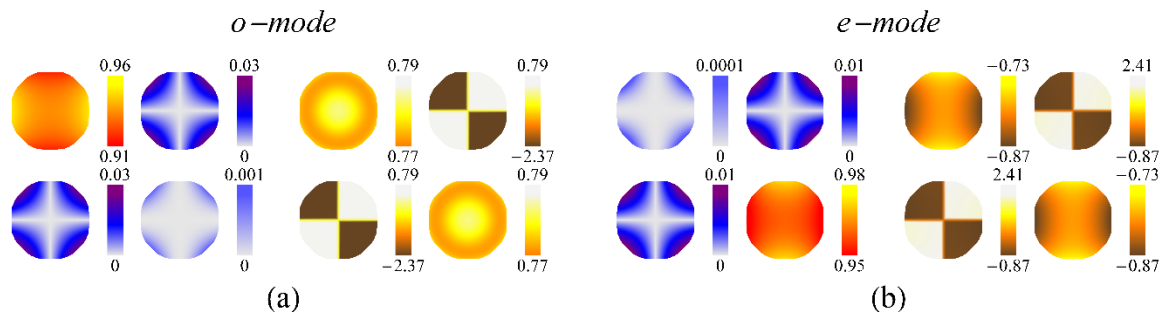


Figure 6.12 The Jones pupil of the *o*- and *e*-wavefronts at the exit pupil. The magnitude (left 2x2 panels) and phase in radians (right 2x2 panels) of the (a) *e*-mode's and (b) *o*-mode's Jones pupils.

Next, the form and polarization structure of these 0.5NA images are examined. The focus of the two modes is evaluated by the response matrix of the Jones pupil, which is the

amplitude response matrix (**ARM**) defined in equation (1.3), whose magnitude is plotted in Figure 6.13. With the small aberration of the thin quarter wave plate, the major polarization (ARM_{xx} of *o*-mode and ARM_{yy} of *e*-mode) forms an Airy disk. The cross coupling (ARM_{xy} and ARM_{yx}) forms a dark center and four islands. And, the orthogonal polarization (ARM_{yy} of *o*-mode and ARM_{xx} of *e*-mode) forms nine island leakage with extremely low amplitude.

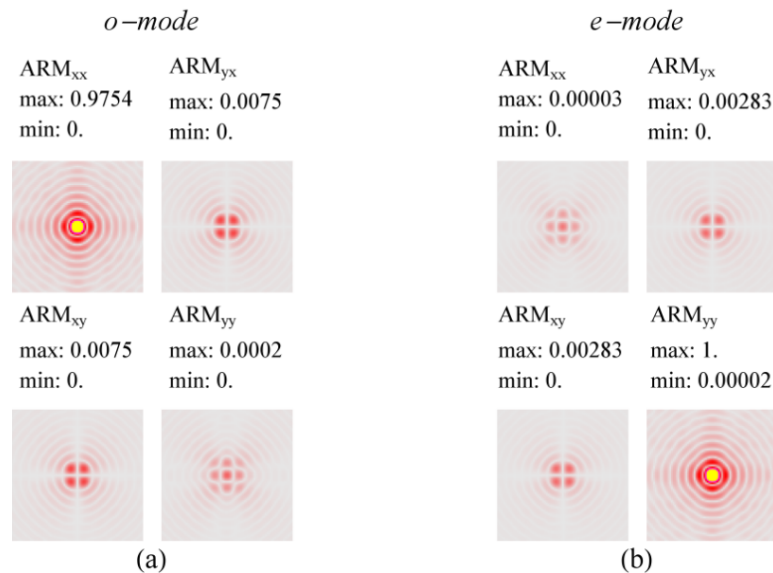


Figure 6.13 The amplitude of the 2×2 **ARMs** of the *o*- and *e*-wavefronts. Zero amplitude in gray, medium amplitude in red, and highest amplitude in yellow.

Since the magnitude of the aberration scales with the plate thickness, the effects of the aberration on the image are more visible with a thicker A-plate. Two more A-plates, 3rd order and 17th order half waveplate, are analyzed with the same procedures. As the thickness of the A-plate increases, the **ARM** of the ordinary focus stays about the same, while the structure of the extraordinary focus diffuses from the Airy disk due to aberrations, as shown in Figure 6.14. For the thicker plate, the *e*- ARM_{yy} has a higher energy in the *y*

direction than the x direction, which is formed from the astigmatism residual to the uniaxial plate.

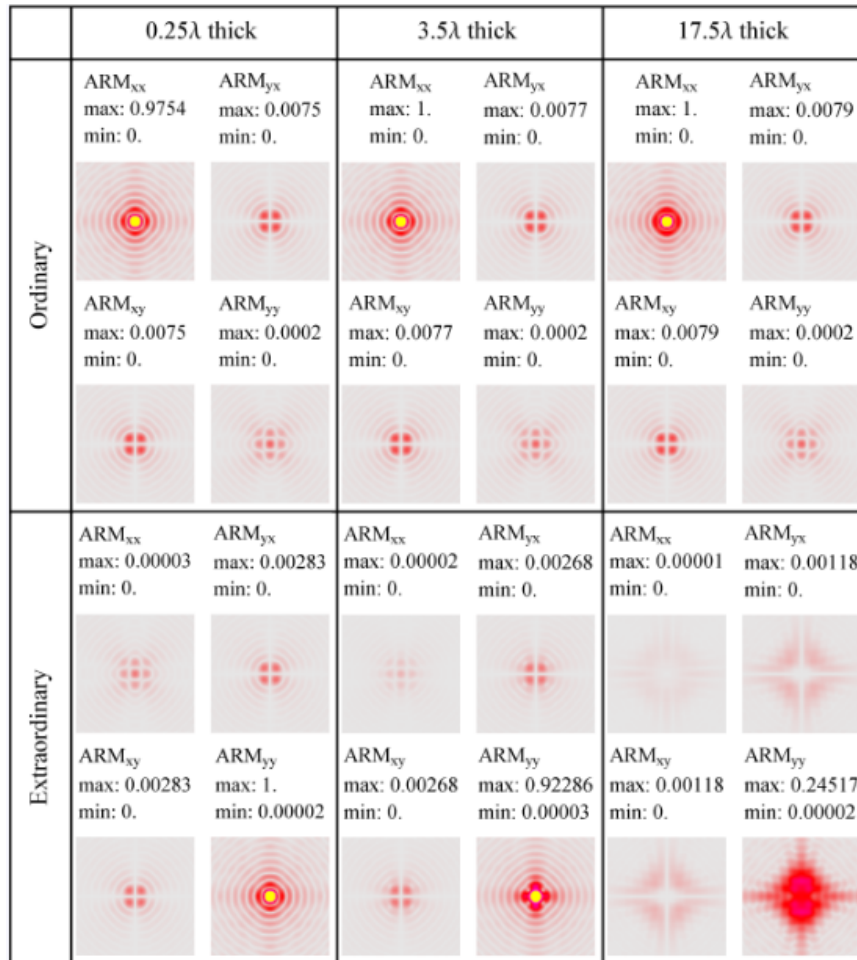


Figure 6.14 The **ARM** amplitude of the o - and e -wavefronts with 0.5NA for various A-plate thicknesses.

The overall **ARM** at the image is the sum of complex **ARM**_o and **ARM**_e. In the absence of

polarization aberration, the amplitude response matrices are $\begin{pmatrix} e^{i\pi/4} & 0 \\ 0 & e^{-i\pi/4} \end{pmatrix}$ and $\begin{pmatrix} 1 & 0 \\ 0 & -1 \end{pmatrix}$

modulated by the Airy disk patterns for the quarter and half waveplate, respectively. The thickness of the waveplate induces aberrations and increases the spatial extent of the yy

component of the overall **ARM**. The magnitudes of the overall **ARMs** are shown in Figure 6.15. The aberrations also increases the spatial extent of the xy and yz -leakages. These aberrations originate from the aberrated e -wavefront. The amplitude of the overall ARM_{yy} decreases and its spatial extent increases approximately quadratically with thickness, as shown in Figure 6.16.

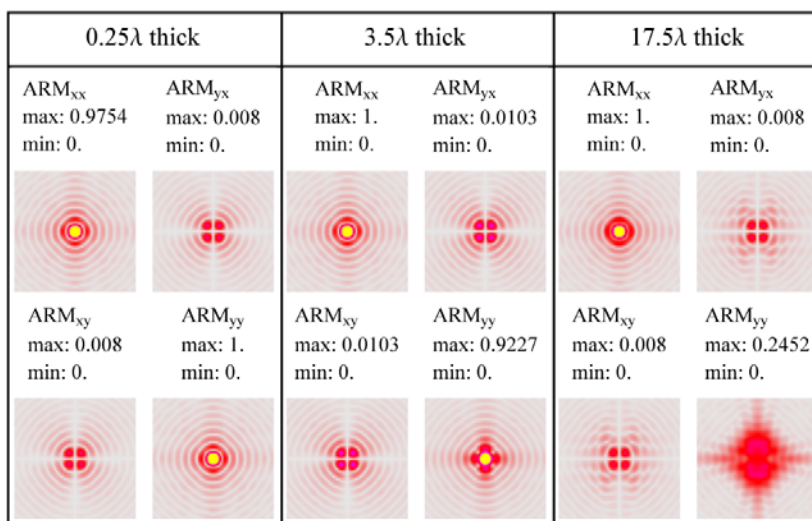


Figure 6.15 The amplitude of **ARM** of the combined o - and e -wavefronts with 0.5NA for various A-plate thicknesses.

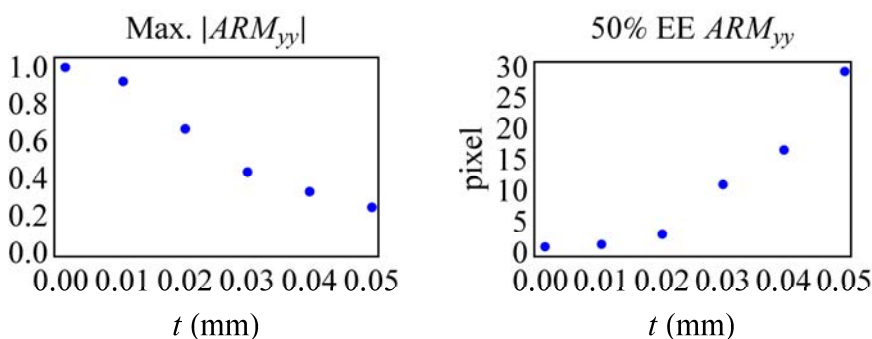


Figure 6.16 (Left) The maximum amplitude and (right) the 50% encircled energy (EE) for $ARM_{e,yy}$ calculated from ray tracing results at six different plate thickness t .

For the analysis of incoherent light, the **ARM** is converted to the 4×4 Mueller point spread matrix (**MPSM**) as described in section 1.6. The **MPSM** for the different plate

thicknesses are shown in Figure 6.17. The resulting **MPSMs** are consistent with the **ARMs**.

Without aberrations, the **MPSMs** are the Mueller matrices $\begin{pmatrix} 1 & 0 & 0 & 0 \\ 0 & 1 & 0 & 0 \\ 0 & 0 & 0 & -1 \\ 0 & 0 & 1 & 0 \end{pmatrix}$ and

$\begin{pmatrix} 1 & 0 & 0 & 0 \\ 0 & 1 & 0 & 0 \\ 0 & 0 & -1 & 0 \\ 0 & 0 & 0 & -1 \end{pmatrix}$ modulated by the Airy disk pattern for the quarter and half waveplates,

respectively. The aberrated **MPSM** for the thicker A-plates, as shown in Figure 6.17, contain large aberrations, produces polarization leakages and induces non-Airy disk image.

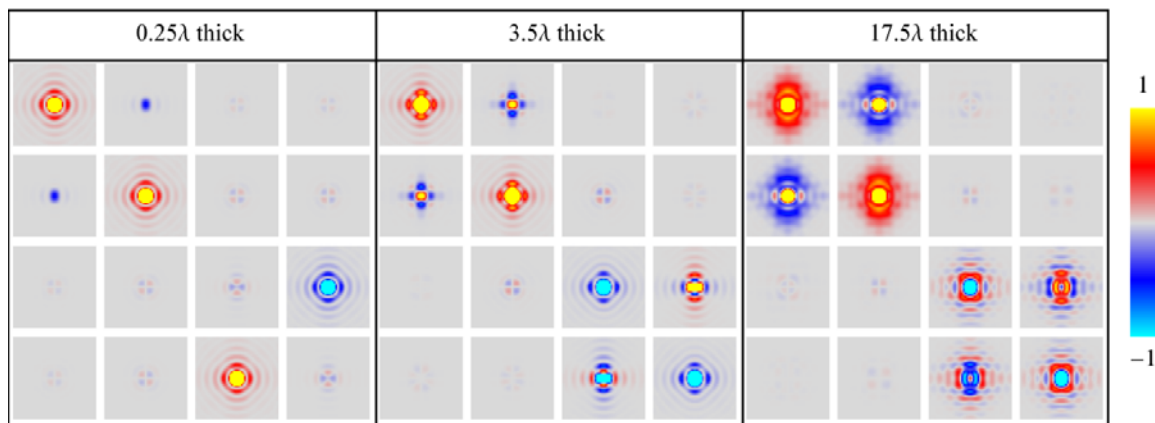


Figure 6.17 **MPSM** of the combined *o*- and *e*-wavefronts with 0.5NA for various A-plate thicknesses.

6.4 Polarization states exiting retarders

The combined polarizations of the two diverging wavefronts from the calcite A-waveplate, shown in Figure 6.18, are calculated in this section. A 45° linearly polarized wavefront propagates through the waveplate and becomes circularly polarized on-axis with polarization aberrations in the off-axis rays.

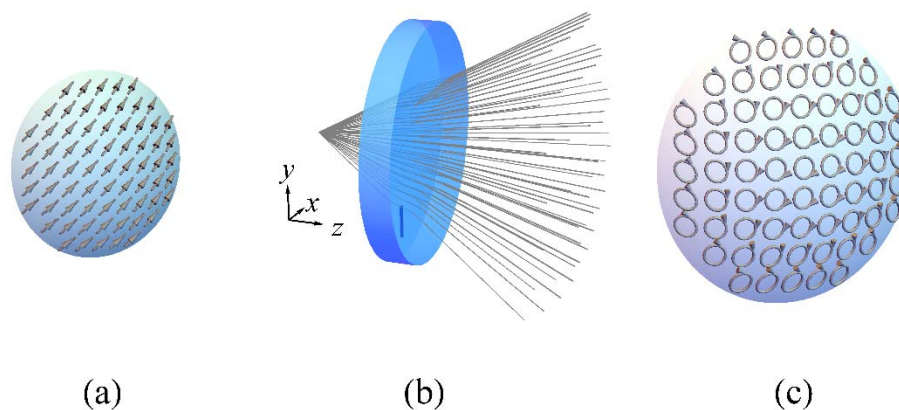


Figure 6.18 (a) A 45° linearly polarized wavefront is simulated for a circular grid of rays. (b) The circular grid of rays with $\pm 25^\circ$ incident angle propagate through a 1st order quarter waveplate whose optic axis is oriented along y . (c) The exiting wavefronts are circularly polarized with small aberrations. The locations of the arrows indicate the phase of each rays.

The resultant wavefronts are combined after the crystal plate. The shear between the o - and e -modes is very small since the quarter waveplate is thin. The ray locations of the exiting ray grids are shown in Figure 6.19.

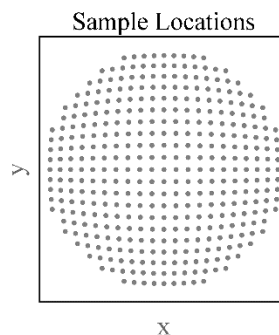


Figure 6.19 The grid locations on a spherical surface where the fields and $OPLs$ will be combined. The \mathbf{P}_o and \mathbf{P}_e of each exiting ray have been calculated. Multiplying the incident \mathbf{E} by \mathbf{P}_o and \mathbf{P}_e , two sets of exiting \mathbf{E} are obtained, \mathbf{E}_o and \mathbf{E}_e . To perform mode combination, the exiting \mathbf{E} field components of each mode are resampled onto the same grid, as described

by equation (5.8). The x , y and z components of \mathbf{E}_o and \mathbf{E}_e are shown in Figure 6.20. The overall magnitude of \mathbf{E}_o and \mathbf{E}_e depends on the incident \mathbf{E} .

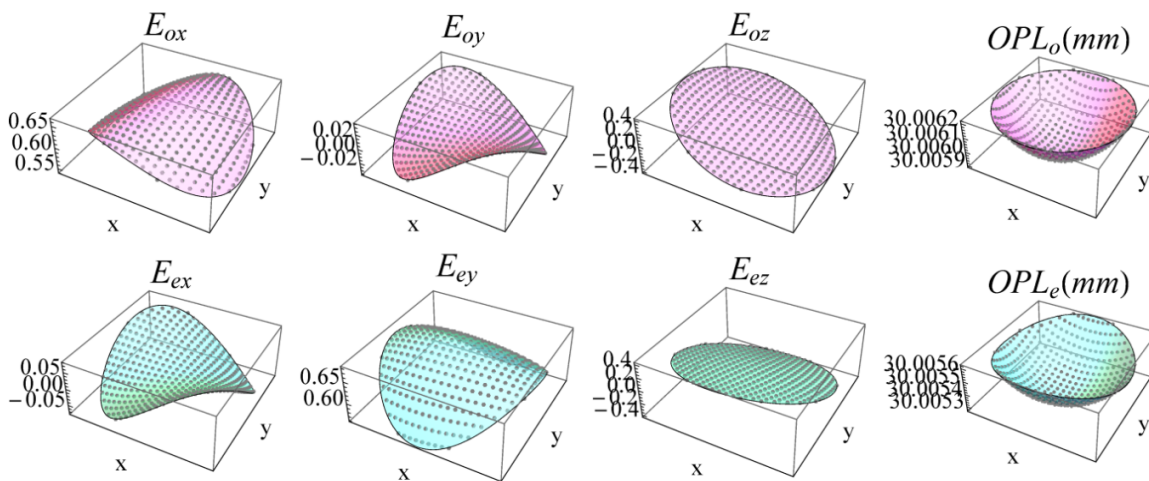


Figure 6.20 Fit functions for the \mathbf{E} field components and the OPL for the two exiting modes through the 1st order quarter waveplate. The dots are the discrete ray data, and the smooth surfaces are the fit.

Then the combined \mathbf{E} is calculated by equation (5.9) where m is o and e . The polarization aberration of \mathbf{E} is represented by a grid of polarization ellipses over the wavefront, shown in Figure 6.21 for $1\frac{1}{4}\lambda$, $2\frac{1}{4}\lambda$, and $5\frac{1}{4}\lambda$ A-plate. The diverging wavefront through the A-plate yields angularly varying retardance. This variation is symmetric about the y oriented optic axis. The exiting states stay circularly polarized along the 45° and 135° axes passing through the center of the field. As the angle of incidence increases, the exiting ellipse becomes less circular in the $\pm x$ and $\pm y$ regions due to the increasing off-axis contribution. This change of ellipticity increases approximately linearly with thickness and quadratically with the FOV. The orientations of the major axes are 45° in the $\pm x$ region and 135° in the $\pm y$ region of the field, and this variation is constant with thickness.

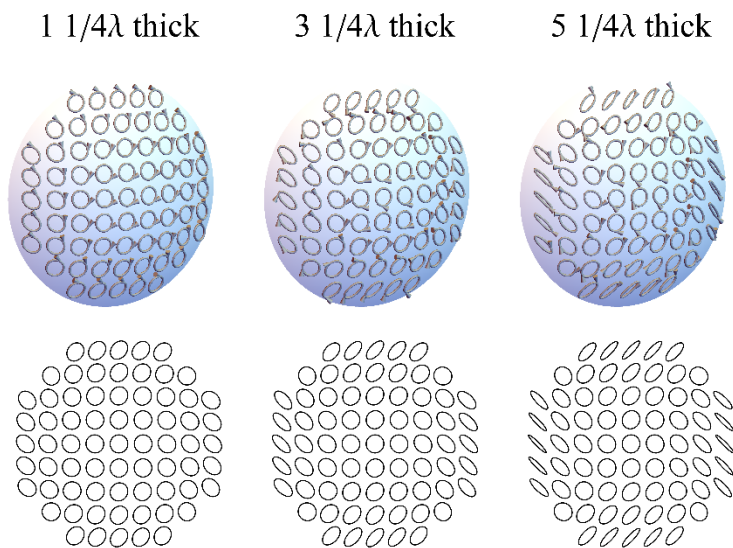


Figure 6.21 The polarization ellipses over $\pm 25^\circ$ after the $1\frac{1}{4}\lambda$, $3\frac{1}{4}\lambda$, and $5\frac{1}{4}\lambda$ waveplates.

As the plate gets thicker, polarization fringes (periodic modulations of polarization state) are observed, as shown in Figure 6.22 for a $50\frac{1}{4}\lambda$ A-plate.

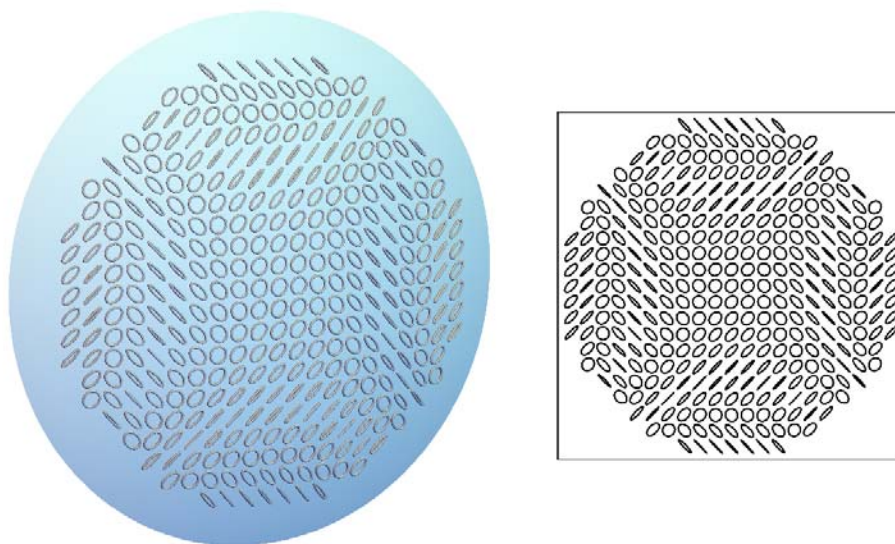


Figure 6.22 (Left) The polarization ellipse on the transverse plane of a wavefront with 15° NA after a $50\frac{1}{4}\lambda$ thick waveplate. (Right) The polarization ellipses plotted on a 2D plane.

6.5 Conclusions

The wavefront and polarization aberrations induced by an example crystal waveplate at the exit pupil and the image plane has been presented. The electric field distribution across the exit pupil was calculated using the polarization ray tracing algorithms of Chapter 2, Chapter 3, and Chapter 4. Then, the mode combination was applied as explained in Chapter 5. The polarization of a point source imaged at the image plane was calculated by diffraction theory described in section 1.6, and were presented as a pair of 2×2 **ARMs** for coherent imaging.

The uniaxial A-waveplate with various thickness were studied because its *o*-wavefront demonstrates isotropic aberrations while the *e*-wavefront demonstrates the more complex aberrations of extraordinary rays. The aberrations of each of these wavefronts were first calculated and analyzed individually. The *e*-wavefront has larger wavefront aberrations than the *o*-wavefront in the exit pupil and in the image plane. The combined wavefront at the exit pupil contains polarization aberrations that induce various polarization states across the pupil as a function of the plate thickness, material's birefringence, the NA of the beam, and the orientation of the optic axis.

The **MPSM** is calculated from the **ARM** with the same algorithm which converts Jones matrix into Mueller matrix. The image of an unpolarized or partially polarized point object is calculated by multiplying the system **MPSM** to the incident Stokes parameters. The Stokes images of a point source for seven different incident polarization states and for three different A-plates thicknesses are shown in Figure 6.23, Figure 6.24 and Figure 6.25.

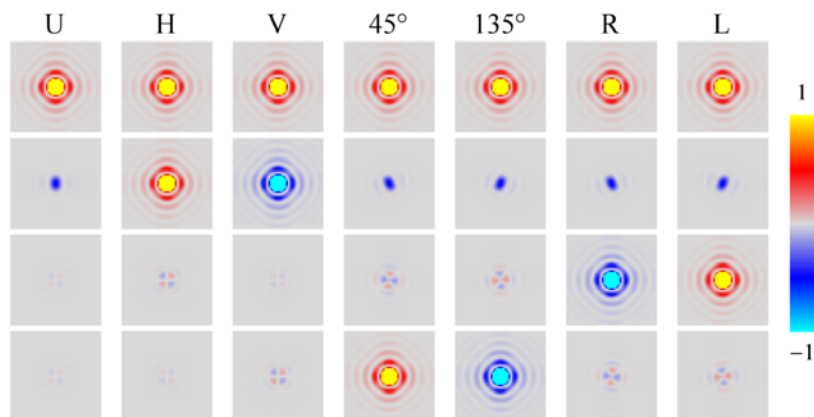


Figure 6.23 Exiting Stoke parameters for unpolarized, horizontally polarized, vertically polarized, 45° linearly polarized, 135° linearly polarized, right circularly polarized and left circularly polarized incident light for the quarter wave A-plate.

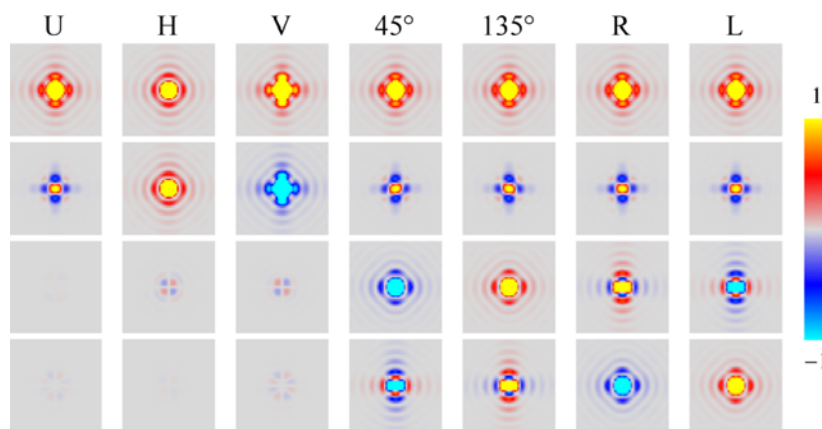


Figure 6.24 Exiting Stoke parameters for unpolarized, horizontally polarized, vertically polarized, 45° linearly polarized, 135° linearly polarized, right circularly polarized and left circularly polarized incident light for the 3.5 wave A-plate.

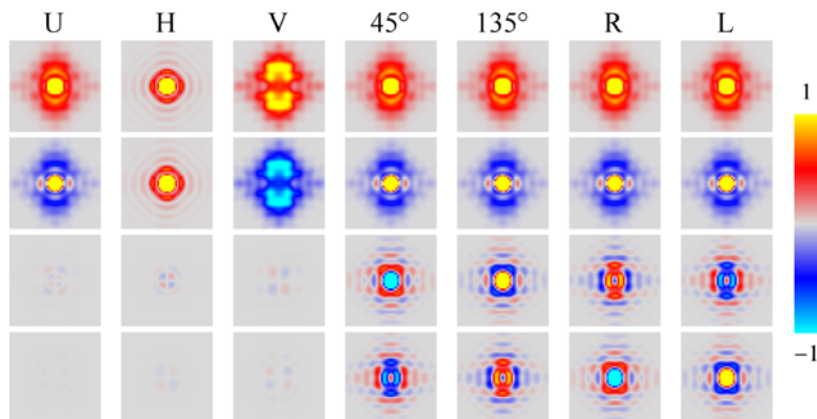


Figure 6.25 Exiting Stokes parameters for unpolarized, horizontally polarized, vertically polarized, 45° linearly polarized, 135° linearly polarized, right circularly polarized and left circularly polarized incident light for the 17.5 wave A-plate.

CHAPTER 7 ABERRATIONS IN THE GLAN-TAYLOR CRYSTAL POLARIZERS

7.1 Introduction to crystal polarizers

Crystal polarizers, polarizers fabricated from anisotropic materials which utilize double refraction to obtain a highly polarized exiting beams of light. The highest performing polarizers with the greatest extinction ratio are crystal polarizers, including the Glan-Taylor (Figure 7.1 right), Glan-Thompson, and the Nichol prism. These operate by totally internal reflecting (TIR) one eigenmode while transmitting most of the orthogonal mode. Since TIR reflects 100% of the incident mode, the degree of polarization of the transmitted beam can be very close to one, leading to exceptional extinction ratio and diattenuation. Polarization states can also be separated in angle by double refraction, such that two orthogonal polarization states exit in different directions, as with the Wollaston prism shown in Figure 7.1 (left). A comprehensive review of crystal polarizers is contained in references 136, 137, and 138 written by J. M. Bennett and H. E. Bennett in OSA Handbook of Optics.

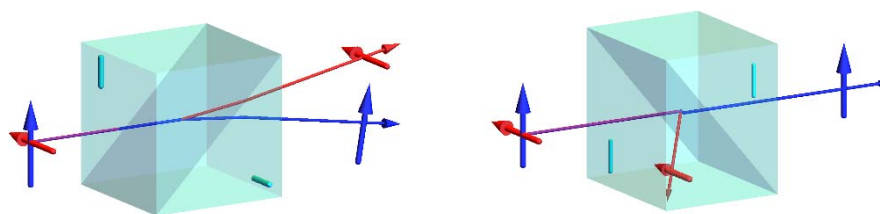


Figure 7.1 (Left) A Wollaston prism is made of two blocks of calcite which have orthogonal optic axes (light blue lines inside crystals). It directs two orthogonal modes into two directions, due to the different refractive index associated to each mode. (Right) A Glan-Taylor polarizer is also made of two blocks of calcite with the same optic axes orientation. It transmits the *e*-mode (blue arrows) while redirect the *o*-mode (red arrows) at the interface.

Crystal polarizers provide high performance in optical systems at a high cost: limited aperture and significant length. Total internal reflecting polarizers tend to be long

when compared to sheet and wire-grid polarizers which are particularly thin. Since the crystal surface needs to be included at a large angle for TIR with respect to the incident light, the ratio of the polarizer length to the aperture size is large, about 1 for Glan-Taylor polarizers and 3–5 for Glan Thompson polarizers. The common issues when incorporating this type of polarizers into imaging systems are small field of view (FOV), restricted étendue and vignetting.

The Glan-type crystal polarizers are commonly used in specialized applications, such as ellipsometry and polarimetry which require high performance, as well as laser systems where lengthy components are less of an issue for collimated beams. High power laser systems are another application for Glan-type polarizers, because their ability to handle much higher powers than sheet and wire grid polarizers is compelling. Such high power applications require highly transparent optical grade crystals, typically calcite and rutile, fabricated to tight specifications.

The ideal material for crystal polarizers should be highly transparent over a substantial spectral range, easy to polish to get high quality optical surfaces, and have a large birefringence. In practice, almost all crystal polarizers are fabricated from calcite which is a soft crystal, can be polished to very smooth surfaces and has a large birefringence over the 400nm to 1600nm wavelength range. Optical calcite is mined, and may have bubbles, inclusions, stria, and small refractive index inhomogeneities which often resemble curtains of weakly scattering inclusions. In contrast, quartz is another highly desirable birefringent material because it can be synthetically grown and is inexpensive. However, the birefringence of quartz is too small for effective Glan-Thompson and Glan-

Taylor polarizers; it is more useful for waveplate retarders. Rutile has high refractive index and is a strong birefringent crystal that can also be synthetically grown to manufacture polarizing cubes and coupling prisms^{139,140}. Many other minerals, such as sapphire and magnesium fluoride are also used to make prism and vacuum viewing ports for specific wavefront separation and combining purposes.

The complex behavior of the crystal polarizers should be considered when designing or using these polarizers. In most polarizers, the intended exiting polarization is the extraordinary mode; the refractive index of the extraordinary mode varies with angle which introduces astigmatism, apodization, and other aberrations into spherical wavefronts. Additionally, crystal polarizers have a small FOV and substantial chromatic aberration. At the edge of the FOV, the ordinary rays begin to leak through rapidly decreasing the degree of polarization of the transmitted light.

This chapter focuses on simulation results of these aberrations using the polarization ray tracing methods from the previous chapters, focusing on the polarization aberrations of Glan-Taylor crystal polarizers.

7.2 Polarization ray tracing of Glan-Taylor polarizer

A Glan-Taylor polarizer is an air-spaced crystal polarizer constructed from two right triangular pieces of calcite, as shown in Figure 7.2 (a). Its design was first described in 1948¹⁴¹. Light propagation in an example Glan-Taylor polarizer, shown in Figure 7.2 (b), is modeled in this chapter to study its wavefront and polarization aberrations. The optic axes of both calcite pieces are oriented vertically along the y axis. In the following

simulation, the hypotenuse is inclined at an angle $\theta_A=40^\circ$ with respect to the entrance and exit surfaces.

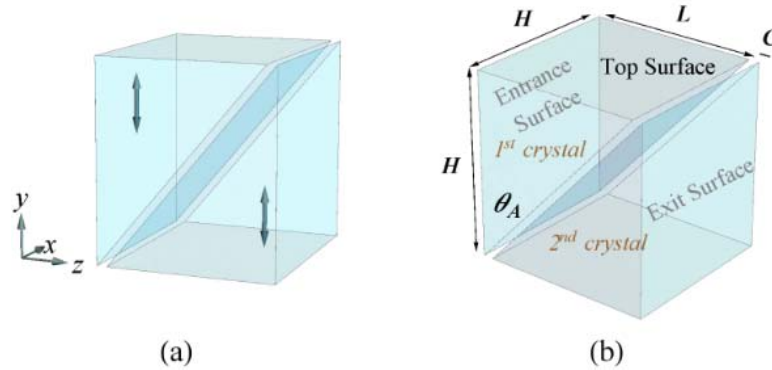


Figure 7.2 (a) Glan-Taylor polarizer consists of two calcite right-triangular pieces separated by an air gap with vertically oriented optic axes (black arrows inside the two blocks). (b) The geometry of the crystal polarizer is defined by θ_A , H , L , and C . The combination of the two crystal blocks forms a rectangular cube. The entrance surface has an area $H \times H$. The length of the crystal is $L = H \tan \theta_A$. The air gap has a thickness C .

7.2.1 Conditions of internal refraction/reflection in calcite

At 589.3nm, the refractive indices of calcite are $n_o=1.659$ and $n_e=1.486$, so the critical angle for the o -ray is $\psi_o=37.08^\circ$ and the critical angle for e -ray, after accounting for the varying n_e , is $\psi_e=42.22^\circ$ in the y - z plane of Figure 7.2, as shown in Figure 7.3. The difference between the critical angle of the o - and e -modes is the key property for the polarizer operation.

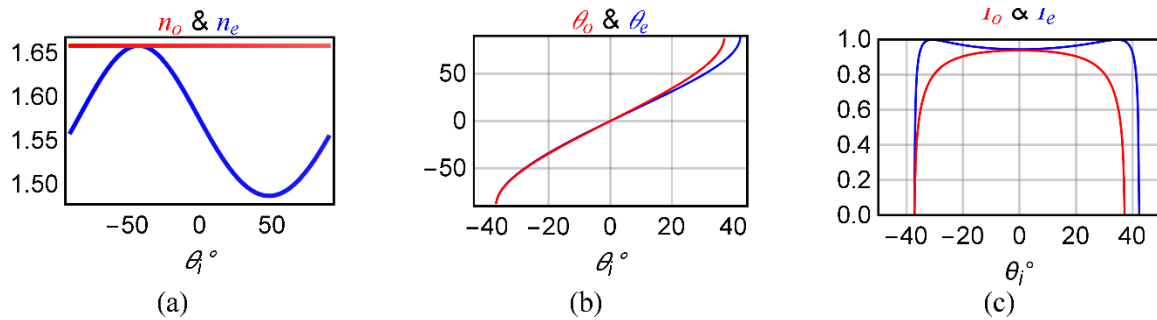


Figure 7.3 The properties of internal reflection at a calcite/air interface as a function of incident angle at the air-gap interface. (a) The refractive index as a function of ray angle in calcite. (b) The refraction angle as a function of incident angle, the o -mode critical angle is 37.08° and e -mode critical angle is 42.22° . (c) The intensity transmission as function of incident angle, where the maximum e -transmission occurs at 34.54° .

Ray paths for internal reflection at a calcite/air interface is depicted in Figure 7.4. When the plane of incidence contained the optic axis, the o -ray refract as s -polarized light, and the e -ray refracts as p -polarized light. As shown in Figure 7.3 (c), the refracted o -ray has decreasing intensity with incident angle, and zero transmission above critical angle. On the other hand, the refracted e -ray has increasing intensity with angle, and 100% transmission at Brewster's angle around 35° , so a smaller θ_A is desirable. As the incident angle continuous to increase, the transmission of e -ray decreases rapidly to zero at critical angle.

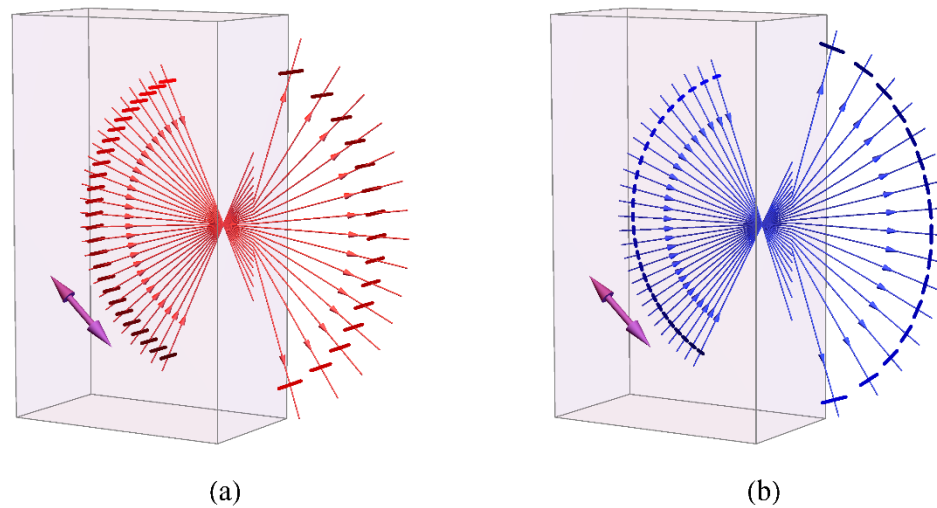


Figure 7.4 *o*- and *e*-rays internally refracts through a calcite/air interface. The incident and exiting polarization orientations are shown at the start and at the end of each ray. (a) The *o*-mode is orthogonal to the optic axis (purple arrow) and (b) the *e*-mode is in the plane of the optic axis. The length of the polarization state represents the transmission coefficient which is also plotted in Figure 7.3 (c). This figure cannot represent the rays with rapidly changing intensity in a small range close to the critical angle.

For light incident on the hypotenuse calcite/air interface of the Glan-Taylor (Figure 7.2) with angles in the range between ψ_o and ψ_e , the *o*-ray (above its critical angle) undergoes TIR and reflects toward the top surface, while the *e*-ray divides into reflected and refracted rays (remains below the critical angle) passes through the air gap; the incident ray splits into reflected and transmitted rays. The *e*-mode in the first crystal couples entirely to the *e*-mode in the second crystal, and exits the polarizer as *y*-polarized light.

7.2.2 Nominal operation at normal incidence

A normal incident ray at 589.3nm refracts through the Glan-Taylor polarizer and divides into the *x*-polarized *o*-mode and the *y*-polarized *e*-mode is shown in Figure 7.5.

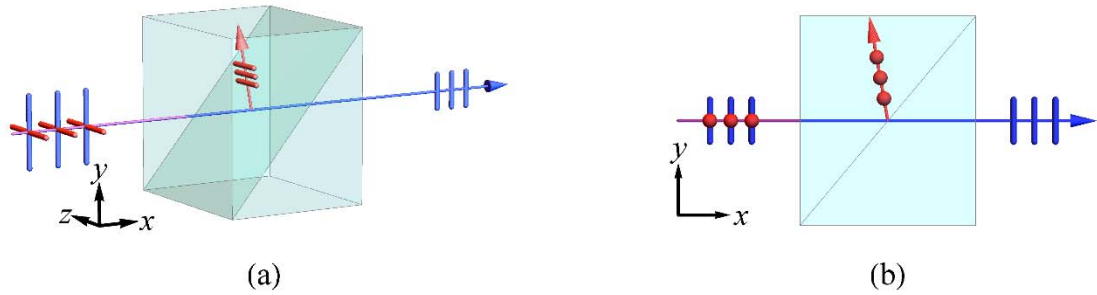


Figure 7.5 For a normal incident ray, the *o*-mode (red) undergoes TIR at the air gap, while the *e*-mode (blue) transmits to the exit surface as vertically polarized light. The *o*-mode either exits through the top surface or is absorbed by a black coating on the top surface. The partial reflections associated with small amplitude are not shown here, for example the partial reflection of the *e*-mode at the hypotenuse.

The desired light path through the polarizer is the *iee*-mode: (*e*)xtraordinary in the first crystal, (*i*)sotropic in the air gap, and then (*e*)xtraordinary in the second crystal. Ray doubling can occur in the second crystal, but in case of normal incidence, when the orientations of the two crystal axes are perfectly aligned, the undesired *ieo*-mode will have zero amplitude.

The polarization ray tracing matrix \mathbf{P}_{eie} of the *iee*-mode for normal incidence is calculated by matrix multiplication of the \mathbf{P} matrices from each of the four interfaces. Table 7.1 shows the \mathbf{P} matrix and cumulative \mathbf{E} field after each interface.

$$\mathbf{P}_{eie} = \begin{pmatrix} 0 & 0 & 0 \\ 0 & 0.891 & 0 \\ 0 & 0 & 1 \end{pmatrix} \quad (7.1)$$

The \mathbf{P}_{eie} corresponds to a *y*-polarizer; the incident *x*-polarized light is completely extinguished. For the incident polarization vector $\mathbf{E}_i = (0, 1, 0)$, the amplitude of the exiting

E field is 0.891 which corresponds to an intensity transmission of 0.793 as calculated in Table 7.2.

Table 7.1 Resultant *e*-mode **P** matrices and electric fields for a normally incident ray through a Glan-Taylor polarizer.

Ray path	P for each individual surface	Cumulative electric field after each surface	Electric field amplitude after each surface
entrance surface	$\mathbf{P}_1 = \begin{pmatrix} 1 & 0 & 0 \\ 0 & 0.804 & 0 \\ 0 & 0 & 1 \end{pmatrix}$	$\mathbf{E}_1 = \begin{pmatrix} 0 \\ 0.804 \\ 0 \end{pmatrix}$	0.804
1 st air gap interface	$\mathbf{P}_2 = \begin{pmatrix} 1 & 0 & 0 \\ 0 & 1.588 & 0.542 \\ 0 & -1.025 & 0.840 \end{pmatrix}$	$\mathbf{E}_2 = \begin{pmatrix} 0 \\ 1.278 \\ -0.825 \end{pmatrix}$	1.521
2 nd air gap interface	$\mathbf{P}_3 = \begin{pmatrix} 1 & 0 & 0 \\ 0 & 0.412 & -0.266 \\ 0 & 0.542 & 0.840 \end{pmatrix}$	$\mathbf{E}_3 = \begin{pmatrix} 0 \\ 0.745 \\ 0 \end{pmatrix}$	0.745
exit surface	$\mathbf{P}_4 = \begin{pmatrix} 1 & 0 & 0 \\ 0 & 1.196 & 0 \\ 0 & 0 & 1 \end{pmatrix}$	$\mathbf{E}_4 = \begin{pmatrix} 0 \\ 0.891 \\ 0 \end{pmatrix}$	0.891

Table 7.2 Resultant transmittance and transmission of *eie*-mode from normal incident is calculated. t_p is the Fresnel coefficient and T_p is the Fresnel transmission.

Ray path	Incident & refraction angles at each surface		Ray index	t_p	$T_p = \frac{n_{out} \cos \theta_{out}}{n_{in} \cos \theta_{in}} t_p^2$
entrance surface	0°	0°	1	0.804	$1.486 \times 0.804^2 = 0.962$
1 st air gap interface	40°	72.84°	1.486	1.890	$\frac{\cos 72.84^\circ}{1.486 \cos 40^\circ} \times 1.890^2 = 0.926$
2 nd air gap interface	72.84°	40°	1	0.450	$\frac{1.486 \cos 40^\circ}{\cos 72.84^\circ} \times 0.4900^2 = 0.926$
exit surface	0°	0°	1.486	1.196	$\frac{1}{1.486} \times 1.196^2 = 0.962$
Total:				$\prod t_p = 0.891$	$\prod T_p = 0.793$

7.2.3 Limited field of view

The Glan-Taylor polarizer is an excellent polarizer within the given FOV, where the undesired polarization component is efficiently redirected by TIR. At incident angles off normal incidence, other undesired modes could present. The FOV of the crystal polarizer is defined as the solid angle within which, only the *eie*-mode is present in the transmitted beam. Within this FOV, the degree of polarization of the exiting light is one. In practice, (1) the TIR of the *o*-mode and (2) the transmission of the *e*-mode for the Glan-Taylor polarizer only occurs within a few degrees around normal incidence, as shown in Figure 7.6, leading to a small FOV which is about $\pm 3.5^\circ$ in the y direction.

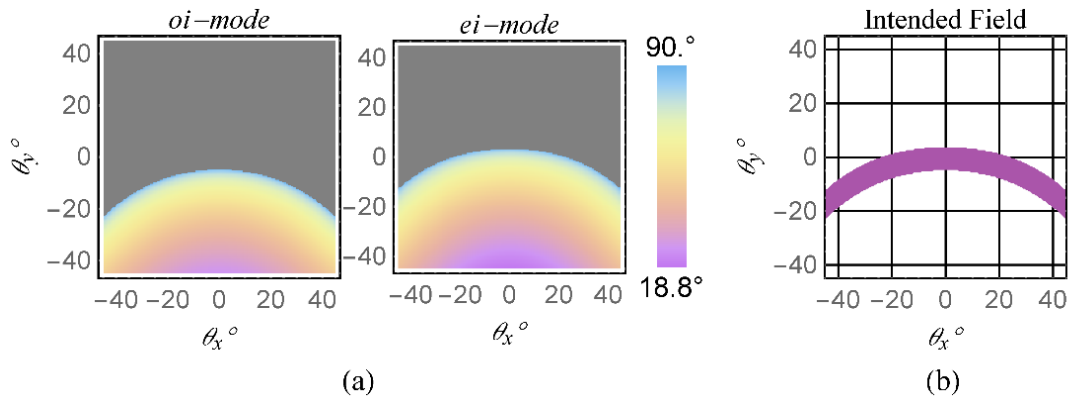


Figure 7.6 (a) The angle of refraction for the *o*- and the *e*-modes at the 1st air gap interface as a function of the incident angle (θ_x , θ_y) at the polarizer's entrance surface. The false color scale indicates the refraction angle, where gray denotes TIR. At the critical angle, light refracts at 90° (light blue). The vertical shift between these two functions for *oi*- and *ei*-modes, is the basis of operation for the Glan-Taylor polarizer, indicating the incident angles where the *o*-mode TIRs while the *e*-mode partially transmits. This shift is responsible for the highly efficient performance of the Glan-Taylor. (c) The intended field for the Glan-Taylor polarizer shown ensures the *o*-mode will TIR at the interface, while the *e*-mode transmits through the polarizer. At $\theta_x=0$, the polarizers field along θ_y ranges from -4.5° to $+3.5^\circ$.

When the angle of incidence at the air gap is below ψ_o , the *o*-mode partially transmits to the second crystal and generates *oie*- and *oio*-modes spoiling the polarizer.

When the angle of incidence at the air gap is greater than ψ_e , the e -mode switches from partially transmitting to TIR, no light reaches the second crystal, and the polarizer goes dark. Also, for an incident rays outside of the y - z plane (θ_x is non-zero), the e -mode generates a small amplitude of eo -mode which leaks through the polarizer as an undesired polarization state in the transmitted light.

The Glan-Taylor polarizer becomes a complicated device outside its small field of view, and users should be prepared for these additional undesired beams, if the incident angular range is not properly limited. Experiments with laser pointers and polarizers easily demonstrate these additional beams.

7.2.4 Multiple potential ray paths for off-axis operation

A polarization ray trace of the Glan-Taylor over a large range of angles is performed to analyze the refractions of all the modes through all the interfaces, taking into account the TIR at the air gap. The calcite is simulated as uncoated, and the Fresnel losses at all surfaces are included. A ray tree depicting all the possible ray paths (coupling between modes) through the polarizer is shown in Figure 7.7.

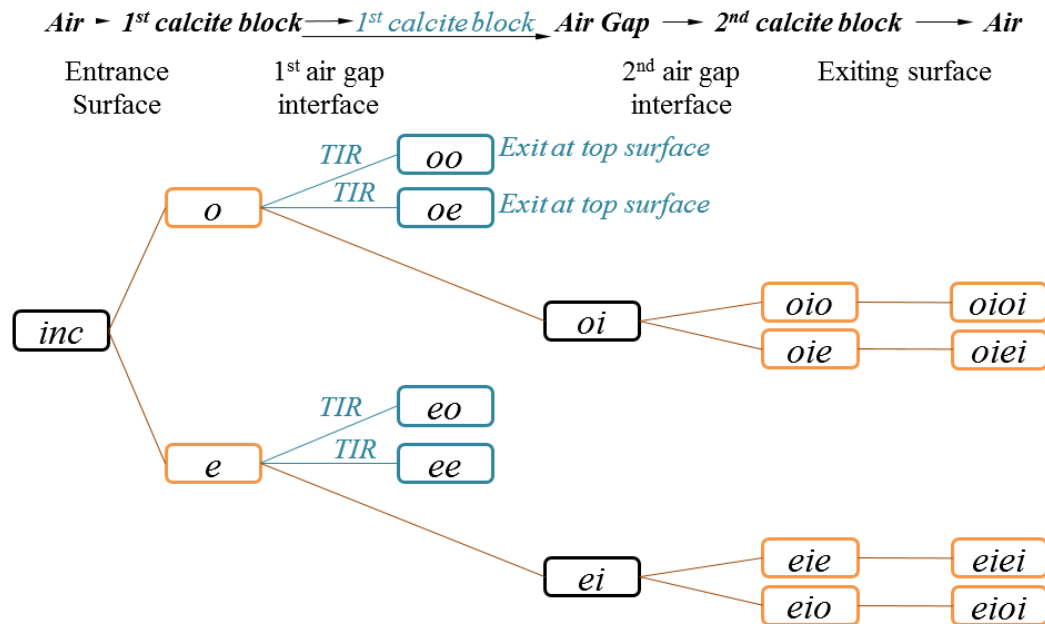


Figure 7.7 A ray tree of all possible ray paths of a ray propagating through a Glan-Taylor polarizer with different mode combinations. The incident ray splits into *o*- and *e*-modes at the entrance surface. Without loss of generality, at the 1st surface of the air gap, both modes can refract through the gap or TIR back to the 1st crystal. For light reflected from the hypotenuse, the rays split further into *oo*- and *oe*-modes or *eo*- and *ee*-modes. These modes may escape through the top surface. Rays transmitted through the air gap further split into *oio*- and *oie*- or *eio*- and *eie*-modes, and exit the polarizer. Up to four exiting modes may occur for a given incident ray, but depending on the incident ray propagation direction, some of these modes have zero amplitude.

The focus of this analysis is refractions not reflections, unless TIR occurs and stop a ray from refracting through the system. The incident light (*inc*) divides into *o*- and *e*-states. At the first crystal's hypotenuse (the birefringent/isotropic interface), each modes reflects into both *o*- and *e*-modes; the coupling of *o* into *e* and *e* into *o* is small. However, this coupling is only zero in the vertical plane, the plane containing the surface normal and the optic axis. Within the air gap between the two crystals, the transmitted rays are in an *isotropic* mode. These rays refract part of their flux into the second crystal, generating *o*- and *e*-rays. Again, coupling from *e* in the first crystal into *o* in the second crystal, or vice versa, is zero only for rays propagating in the vertical plane. The light reflects at the first

hypotenuse is undesired light which will reach the top surface and preferably either escape or be absorbed by a top surface coating. As a ray passes through the air gap (*ei*- or *oi*-mode) into the second crystal, the light splits again into *o*- and *e*-modes. For each incident ray, a maximum of four modes (*iee*, *eio*, *oie*, and *oio*) may emerge from the exit surface.

Total internal reflection from the crystal/air interface is a clever and effective mechanism to redirect the unwanted polarization state out of a ray path. However this mechanism is strongly angle of incidence dependent. As the incident angle increases further from normal incidence, or the desired mode is redirected away from the exit surface, as shown in Figure 7.8 which shows some of the exiting amplitudes for the various modes. As the angle decreases, undesired modes leak to the exiting surface.

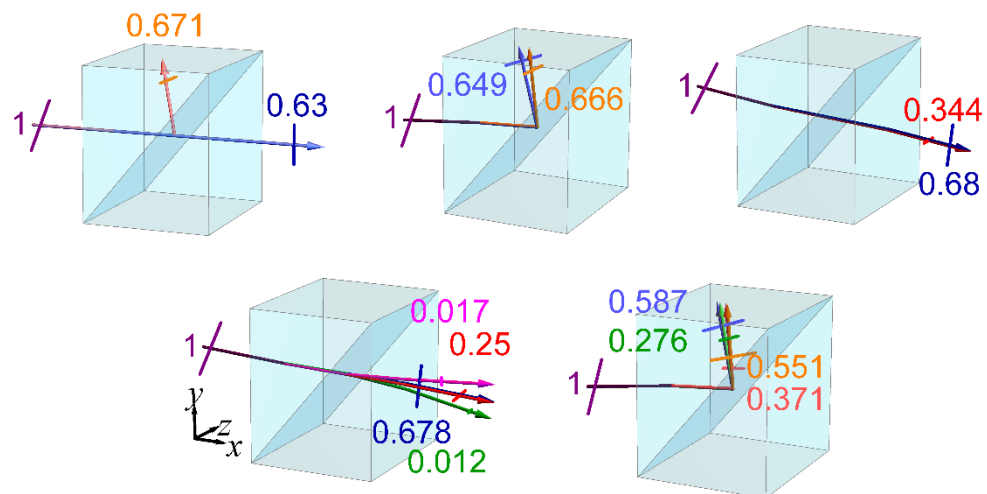


Figure 7.8 Ray traces of several incident angles. Only rays associated with TIR and transmitted through the air-gap are shown. The top left is normal incidence. The incident rays for the top two ray trace on the right are tilted along the *y* axis with incident $\mathbf{k}=(0, 0.087, 0.996)$ in air and $(0, -0.122, 0.993)$. The incident rays in the third row are tilted in both the *x* and *y* directions with incident $\mathbf{k}=(0.104, -0.104, 0.989)$ and $(0.104, 0.104, 0.989)$. All incident beams are 45° linearly polarized with amplitude of one. The resultant *iee*- (blue), *eio*- (green), *oie*- (magenta), *oio*- (red), *ee*- (light blue) and *oo*- (orange), *eo*- (green), and *oe*- (coral) polarizations are shown with their corresponding amplitude.

Tilting the incident ray in the y - z plane induces oo -, ee -, oio -, and eie -modes, while the oe -, eo -, oie - and ioe -modes have zero amplitude since the optic axis is along y axis. As the incident ray is tilted away from the vertical plane in the x direction, the cross-coupling modes, oe -, eo -, oie - and ioe -modes start to linearly gain amplitude. These leakages from the undesired modes cause reduction of the extinction ratio and other aberrations, and affect image quality.

A wavefront converging through the polarizer becomes quite distorted. Figure 7.9 shows a polarization ray trace for a $\pm 45^\circ$ fan of rays in the y - z plane. Parts of the rays are redirected by TIR, while the rest of the eie - and oio -rays transmit through with an uneven spatial distribution. Each ray exits parallel to the incident ray, since refractive indices experienced by the ray in the first and second crystal are equal in this case, but with large sideways displacements, indicating substantial pupil aberration. The individual ray plots for five of the rays in the ray fan are also shown, producing varying ray propagation across the field. Due to the asymmetric geometry of the polarizer in the y - z plane, the exiting wavefronts are also non-symmetric.

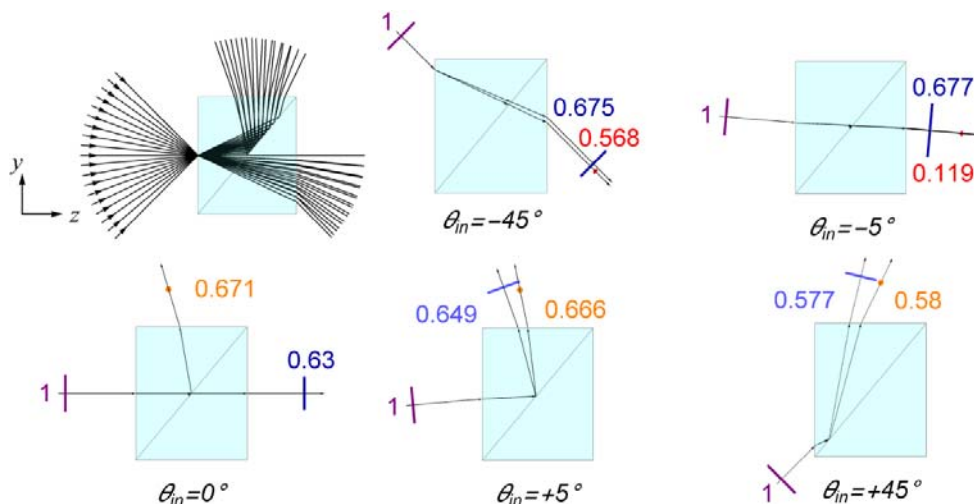


Figure 7.9 Ray paths for a $\pm 45^\circ$ fan of rays in the y - z plane. Details ray paths for five circularly polarized incident rays in the y - z plane are shown for refraction and TIR. (To keep the figures simple, the partial reflection are not shown.) The resultant ie - (blue), io - (red), ee - (light blue) and oo - (orange) polarizations are shown with their corresponding electric field amplitude.

Figure 7.10 contains a similar ray trace to Figure 7.9 but in the x - z plane. The polarizer geometry is symmetric in this plane and therefore the resultant wavefront is symmetric.

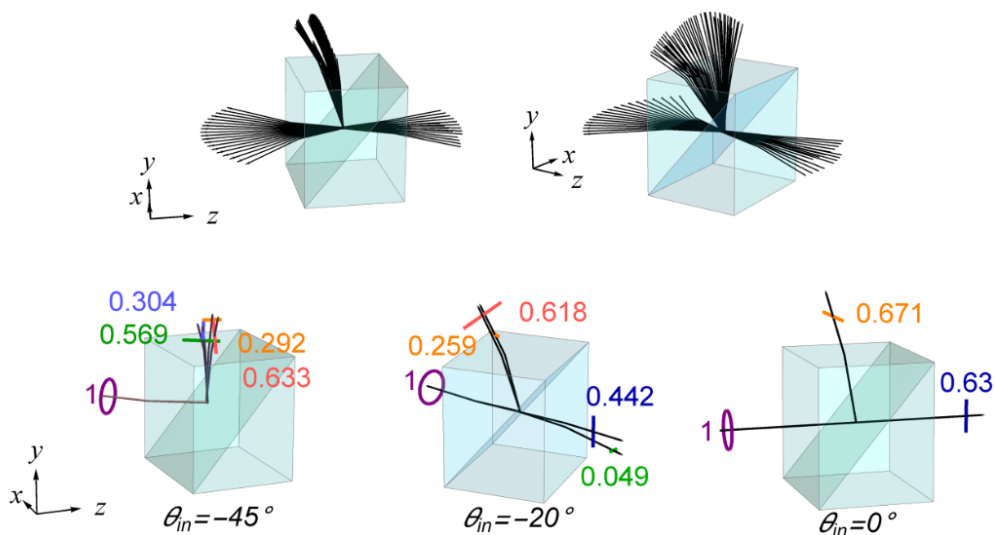


Figure 7.10 A $\pm 45^\circ$ x - z fan of rays through a Glen-Taylor polarizer. Individual rays in the x - z plane at different incident angles with circularly polarized incident ray (purple) with incident angle θ_{in} and an amplitude of 1. The resultant ie - (blue), io - (green), ee - (light blue), oo - (orange), eo - (light green), and oe - (coral) polarizations are shown with their corresponding electric field amplitudes.

These calculations show the desired *iee*-mode is highly apodized due to the large variation of the Fresnel transmission close to critical angle at the hypotenuse, as shown in Figure 7.3 (c). Precision radiometry is thus extremely difficult using this *iee*-beam!

7.2.5 Multiple polarized wavefronts

To understand crystal polarizers, especially in the regions where undesired modes are present, involves calculations to combine the effects of multiple polarized wavefronts. To do this, a spherical wavefront, simulated by a grid of rays, is sent through the polarizer, shown in Figure 7.11 (top), to study the off-axis effects. According to the ray tree in Figure 7.7, four groups of rays are expected for the four exiting modes. These modes are examined individually before combining the wavefronts to determine the overall electric field. The exiting polarization states for each modes are shown in Figure 7.11 (middle, bottom).

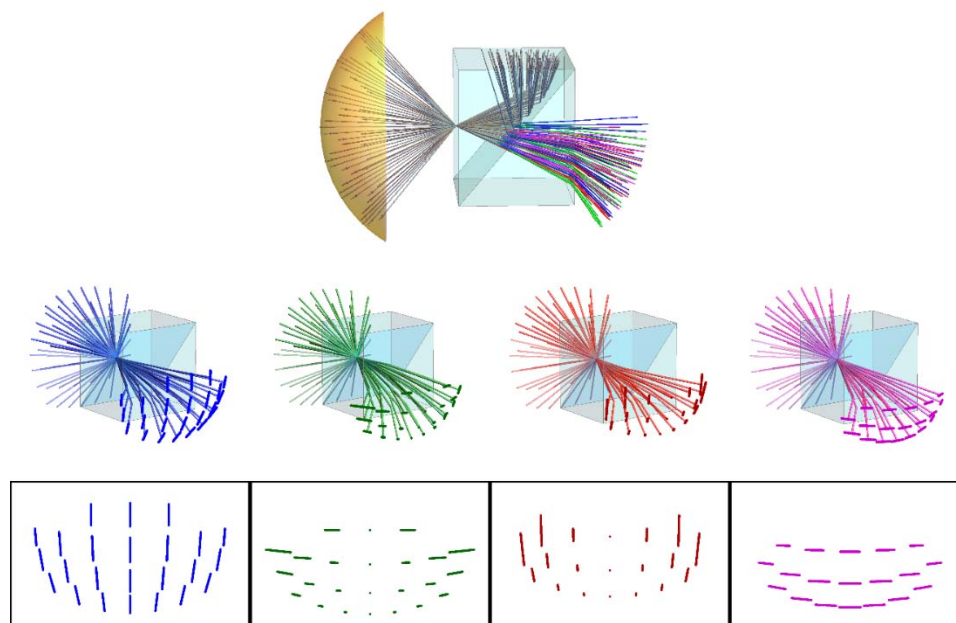


Figure 7.11 (Top) An incident spherical wavefront (yellow) is ray traced for a grid of rays (gray lines) shown within a $\pm 45^\circ$ cone. The wavefront focuses at the entrance of the Glan-Taylor polarizer and diverges into the crystal. Due to ray doubling, four resultant modes, shown in separate colors, pass through the polarizer, exit, and overlap unevenly. The *eie*-mode is blue, *eio*-mode is green, *oie*-mode is red, and *oio*-mode is magenta. (Middle row) The grid of rays for each refracted modes are plotted separately. The exiting polarization states are determined in 3D. Note that only the bottom half of the rays transmit through. The polarization ellipses of each rays are shown in at the end of the ray. (Bottom row) The 3D polarization states scaled by their amplitudes viewed after the crystal.

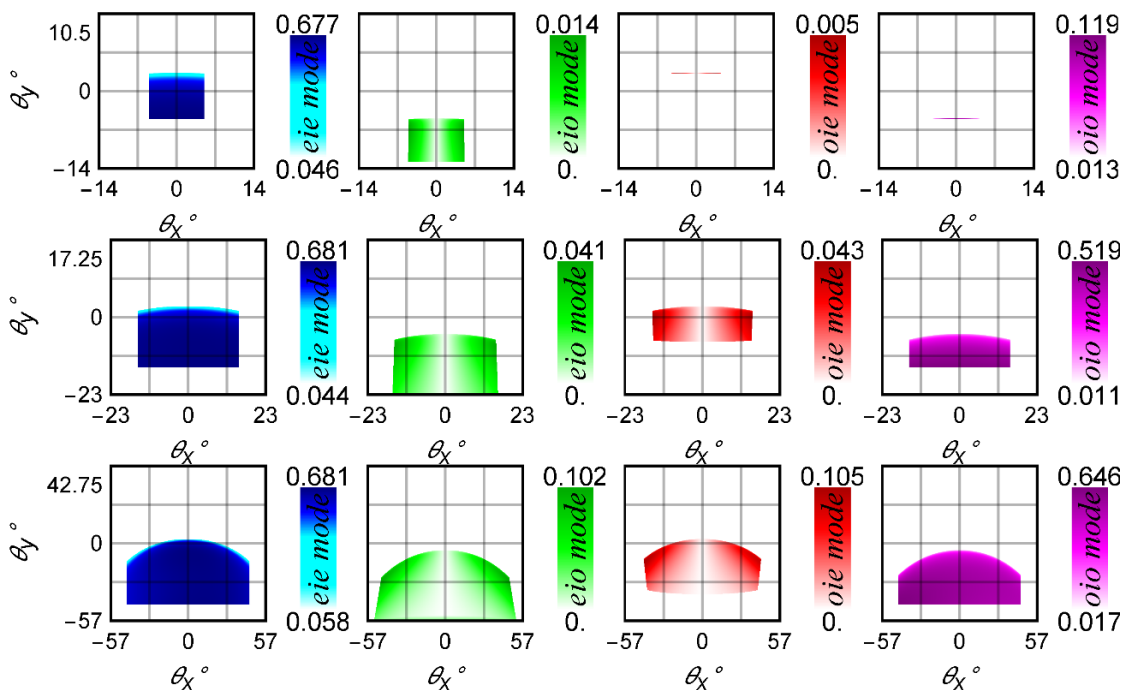


Figure 7.12 The distribution of the electric field amplitudes for each exiting modes in Figure 7.11 as function of exiting angle. The numerical aperture (NA) of the incident beam for each rows are (top) $0.088=\sin 5^\circ$, (middle) $0.259=\sin 15^\circ$ and (bottom) $0.707=\sin 45^\circ$.

The exiting amplitude distributions for three incident beams with $0.088=\sin 5^\circ$, $0.259=\sin 15^\circ$ and $0.707=\sin 45^\circ$ numerical aperture (NA) are shown in Figure 7.12. These incident ray grids are an evenly spaced square grid of rays. None of the four exiting modes maintain the original square outline, and all have large amplitude variations across their fields. The exiting *eie*- and *eio*-modes have the same maximum exiting angle because they have the same critical angle at the air gap. Similarly, all the *eio*- and *oio*-modes have the same maximum exiting angle.

The electric field amplitudes are calculated for 45° linearly polarized incident rays. The desired *eie*-mode is vertically polarized and has higher amplitude towards the bottom of the field where it is approaching Brewster angle, with maximum transmitted amplitude 0.68. The undesired *oio*-mode is horizontally polarized and has increasing amplitude with

increasing NA. For a cone of $\pm 45^\circ$ incident beam, the maximum amplitude of the *oio*-mode reaches 0.65. The amplitudes of both of these modes decrease rapidly towards the TIR boundary, and their ray angles are unchanged after the polarizer because the refractive indices in the first and second crystals are the same. On the other hand, the *oie*- and *eio*-modes can be classified as cross coupling leakages. For rays out of the y - z plane, crossing the air-gap, small amounts of *o* couple into *e* and vice versa. They have small amplitudes, less than 10%, and increase approximately linearly with increasing θ_x . Their angles are different in air, in each crystal, and in air again due to the change of refractive indices, from n_o to n_e and vice versa. For larger NA, these four modes overlap each other after the polarizer, as shown in Figure 7.13.

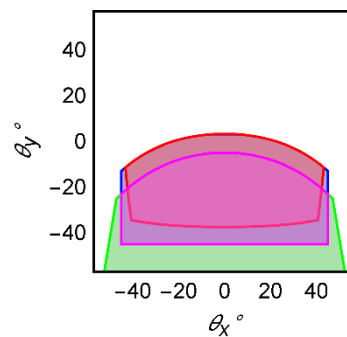


Figure 7.13 The overlap between the four exiting modes for 0.707NA (the bottom row of Figure 7.12), as function of exiting angle.

The *OPLs* of each exiting modes in Figure 7.12 depends on the size of the polarizer. The height of the polarizer in this simulation is 20mm ($H=20\text{mm}$ and $L=16.78\text{mm}$ in Figure 7.2). The *OPLs* are evaluated on a surface 10mm from the center of the polarizer or 1.61mm from the exit surface. The *OPLs* shown in Figure 7.14 are relative to the on-axis *eie*-ray. Because of the large crystal block, the *OPL* contains large values.

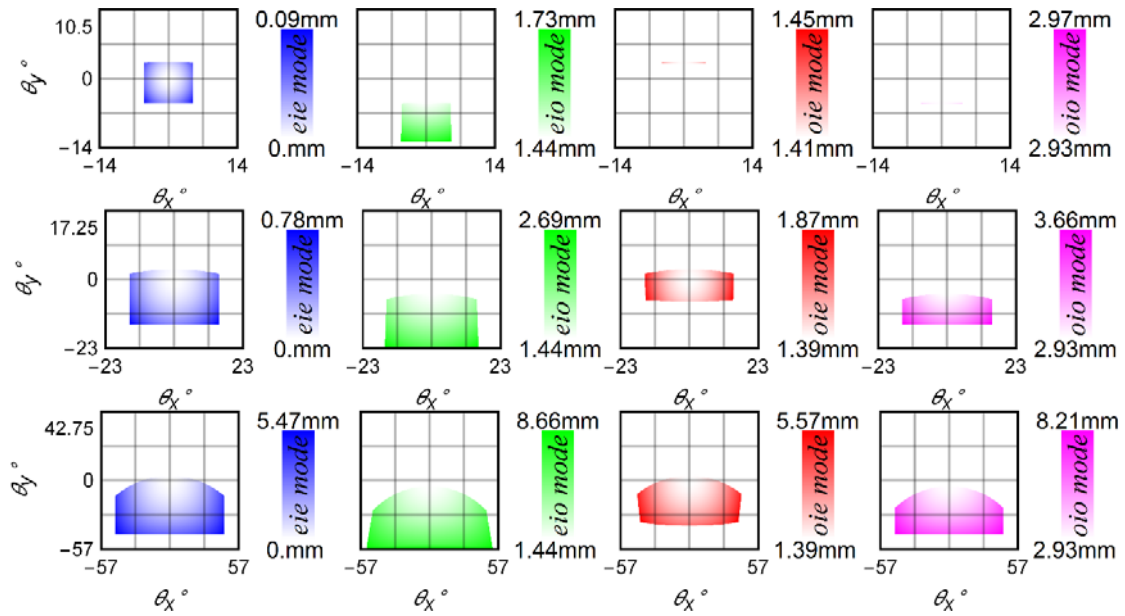


Figure 7.14 OPL of each modes corresponds to the amplitude shown in Figure 7.12, and relative to the OPL of the on-axis eie -ray.

7.3 Polarized wavefronts exiting from the polarizer

To understand the polarizer's performance, the fields of the four exiting modes are combined. The method of Chapter 5 for combining polarized wavefronts represented by irregular grids of rays is applied. The resultant wavefronts from each mode is approximated by resampling each grid of rays onto the same grid. The overall \mathbf{E} field is

$$\mathbf{E}(\theta_x, \theta_y) = \sum_m^M e^{i\frac{2\pi}{\lambda} OPL_m(\theta_x, \theta_y)} \begin{pmatrix} E_{mx}(\theta_x, \theta_y) \\ E_{my}(\theta_x, \theta_y) \\ E_{mz}(\theta_x, \theta_y) \end{pmatrix} \quad (7.2)$$

where OPL_m and \mathbf{E}_m are generated from interpolating the ray parameters in terms of θ_x and θ_y for mode m .

The resultant far field intensity distributions in angle space, calculated by equation (2.27), of the four exiting modes are shown in Figure 7.15 for three incident NA.

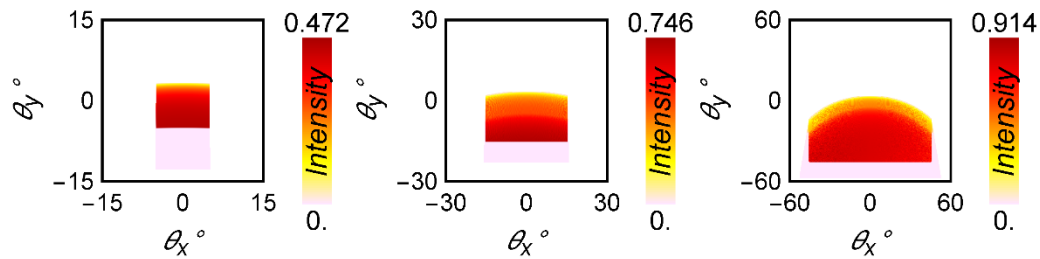


Figure 7.15 The resultant intensity distribution for Figure 7.12 and Figure 7.14. The incident NA for each of them are (left) 0.088, (middle) 0.259 and (right) 0.707. Light pink is chosen to represent the lower intensity.

The resultant intensity drops off toward the top of the field due to the decreasing Fresnel coefficients toward the critical angle of the pure *e*-mode and pure *o*-mode. Both of these modes eventually become zero due to TIR. A faint ghost mode (pink) is observed at the bottom of the field from the *eio*-mode.

These simulation results can be compared with the polarimetric measurement of a Glan-Taylor crystal polarizer shown in Figure 7.16. The measurement shows the angular behavior of the polarizer in the form of a Mueller matrix image measured by a Mueller Matrix Imaging Polarimeter (MMIP) in the Polarization Lab at the University of Arizona¹⁴². The image is acquired over a range of incident angles by illuminating the crystal polarizer with a 0.1NA focused beam from a polarization state generator. After the beam refracts through the crystal polarizer, the transmitted light is collected by a polarization state analyzer. Then an image of the exit pupil of a collection objective lens is formed across a CCD. So, each pixel of the image represents light from a different angle exiting from the crystal polarizer.

The measured irradiance (Figure 7.16 left) shows the polarizer has a decreasing transmittance toward the top of the field, and zero transmittance in 1/3 of the 0.1NA. This

region with zero transmittance corresponds to the TIR of all polarization states at the polarizer's hypotenuse as in the simulation. The measured Mueller matrix image (Figure 7.16 middle) contains the polarization properties of the crystal polarizer, including retardance and diattenuation. It has high signal in the m_{00} , m_{01} , m_{10} , and m_{11} components^{‡‡}, and about zero for the other components. The Mueller matrix image has a form close to

$$\begin{pmatrix} 1 & -1 & 0 & 0 \\ -1 & 1 & 0 & 0 \\ 0 & 0 & 0 & 0 \\ 0 & 0 & 0 & 0 \end{pmatrix} \text{ in } 2/3 \text{ of the } 0.1\text{NA, which corresponds to a vertical polarizer. The}$$

diattenuation image (Figure 7.16 right) is calculated from the Mueller matrix image. It shows high diattenuation within the middle region and about 0.5 diattenuation in a small region at the bottom of the field. This low diattenuation corresponds to the multiple modes overlapping as in the simulation. Due to the aperture of the microscope objective, further leakages from the undesired modes are cropped, and the ghost shadow in the simulation does not reach the detector.

‡‡ The (4×4) 16 elements of the Mueller matrix are $\begin{pmatrix} m_{00} & m_{01} & m_{02} & m_{03} \\ m_{10} & m_{11} & m_{12} & m_{13} \\ m_{20} & m_{21} & m_{22} & m_{23} \\ m_{30} & m_{31} & m_{32} & m_{33} \end{pmatrix}$.

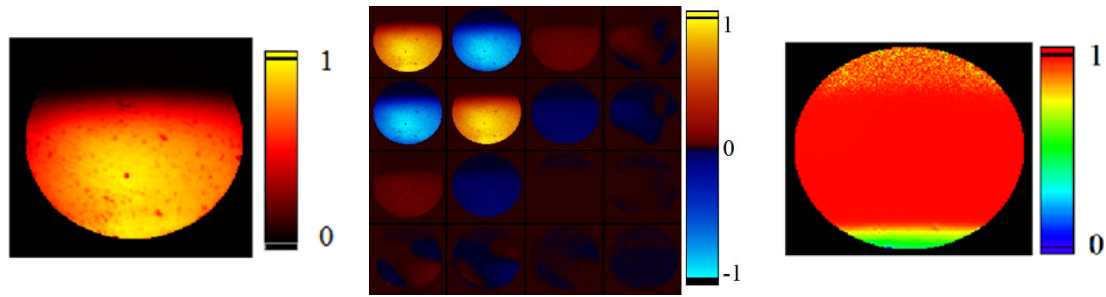


Figure 7.16 Polarimeter measurement of a Glan-Taylor polarizer with a 0.1NA microscope objective pair. (Left) Measured irradiance, (middle) normalized Mueller matrix image, and (right) diattenuation image.

7.4 Aberrations and performance of the Glan-Taylor polarizer

The aberrations of the *iee*-mode (the principal and the only desired mode) and the extinction ratio of the Glan-Taylor polarizer are examined in this section. For the 0.088NA, Figure 7.12 shows how the *oio*-mode hardly overlaps the *iee*-mode at the center $\pm 5^\circ$. The wavefront aberrations of the *iee*-mode can be estimated using the actual *OPLs* distribution shown in Figure 7.14 (top left) which is also shown in Figure 7.17.

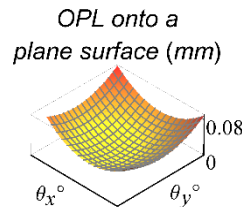


Figure 7.17 The *OPL* function for the *iee*-mode from ray tracing to a flat surface; defocus dominates.

The estimation of the *iee*-aberration is done by Zernike polynomial fitting,

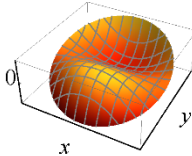
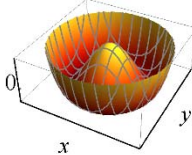
$$OPL(\rho, \varphi) = a_0 P + a_1 T_1 + a_2 T_2 + a_3 D + a_4 A_1 + a_5 A_2 + a_5 S \quad (7.3)$$

where $(P, T_1, T_2, D, A_1, A_2, S)$ are the form of the aberrations presented in Table 7.3, a 's are the aberration coefficients, ρ is normalized pupil coordinate, and $\tan \varphi = \varphi_x / \varphi_y$ is the

pupil angle measured counterclockwise from the x axis. The Zernike fit to 9 terms produces about $0.3\mu\text{m}$ error from higher order aberrations.

Table 7.3 Zernike coefficients for the eie -wavefront for system with 0.088NA.

Zernike Aberration		a coefficients of the eie -wavefront (waves)
Piston, P	a_0	38.067
Tip, T_1	$a_1 (\rho \cos \theta)$	0.018
Tilt, T_2	$a_2 (\rho \sin \theta)$	0
Defocus, D	$a_3 (2\rho^2 - 1)$	38.052
Astigmatism 1, A_1	$a_4 (\rho^2 \sin 2\theta)$	0
Astigmatism 2, A_2	$a_5 (\rho^2 \cos 2\theta)$	-7.198
Coma 1, C_1	$\rho (3\rho^2 - 2)\sin \theta$	0

Coma 2, C_2	$\rho (3\rho^2 - 2)\cos \theta$		0.0197
Spherical, S	$a_6 (6\rho^4 - 6\rho^2 + 1)$		-0.037

After subtracting the piston, tilt and defocus, the residual wavefront of the *eie*-mode, shown in Figure 7.18, is primarily astigmatism.

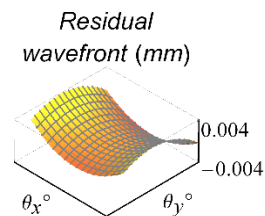


Figure 7.18 Wavefront of *eie*-mode after removing piston, tilt and defocus.

A figure of merit for polarizer performance is the extinction ratio,

$$\text{Extinction Ratio} = \frac{\text{Intensity}_{\text{co-polarized}}}{\text{Intensity}_{\text{cross-polarized}}}, \quad (7.4)$$

the ratio of the transmission of the co-polarized system to the cross-polarized system for unpolarized incident light. For sheet polarizers, the cross-polarized system is two polarizers with their transmission axes crossed, and the co-polarized system is two polarizers with their transmission axes in the same orientation.

Two configurations are considered (Figure 7.19) for calculating the extinction ratio for a pair of Glan-Taylor co- and cross- polarizers. At normal incidence, the co-polarized

system produces a vertically polarized ray, and the cross-polarized system blocks all incident light. Therefore the extinction ratio at normal incidence is infinite.

The advertised FOV of commercial Glan-Taylor polarizer is stated to be around 3° to 5° at $0.5 \mu\text{m}^{143}$. A $\theta_y=3^\circ$ incident ray shown in Figure 7.19 (right) creates 4 exiting modes in the cross-polarized configuration (extinction) and 5 exiting modes in the co-polarized configuration (adding the desired mode). As the off-axis ray propagates through polarizers, therefore the cross-polarized system leaks light at this angle light. The extra light carries only a small flux at this small field, but this drastically decreases the extinction ratio.

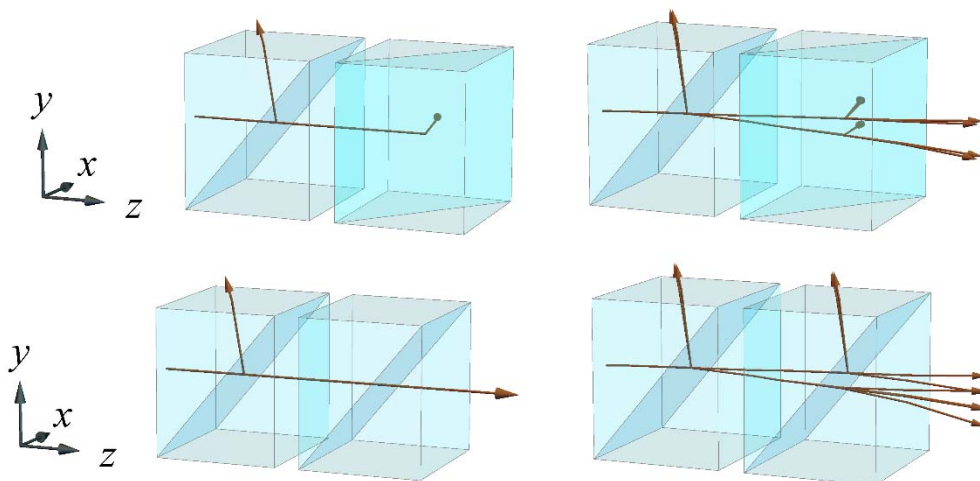


Figure 7.19 Polarizer configurations for calculating extinction of Glan-Taylor polarizers. (Left) A normal incident ray propagates through the (top) cross and (bottom) co-polarized systems. (Right) An off-axis ray with $\theta_y=3^\circ$ incident angle propagates through the two systems, where light leaks through the cross-polarized system while more rays split through the co-polarized system.

Both of these two polarizer systems have four blocks of calcite with eight birefringent interfaces, so they potentially yield 2^4 or a total of 16 possible exiting modes, as shown in Figure 7.20. These 16 rays involve all possible couplings between o - and e -modes. When the ray enters the air gap between the crystals, it does not split, and this mode

is represented by i , for isotropic air. So, the 16 possible exiting modes are: $eieieie$, $eieieio$, $eieioie$, $eieioio$, $eioieie$, $eioieio$, $eioioie$, $ieoioio$, $oieieie$, $oieieio$, $oieioie$, $oieioio$, $oioieie$, $oioieio$, $oioioie$, and $oioioio$.

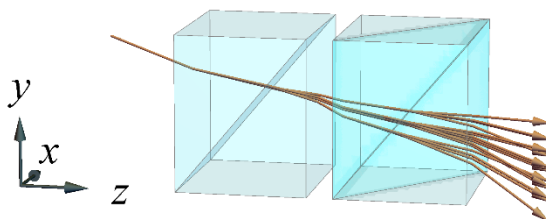


Figure 7.20 A ray propagates through a co-polarized system with 4 crystals. Beyond $\theta_y = -10^\circ$, one incident ray produces 16 exiting rays.

The performance of the Glan-Taylor polarizer is first examined for a square grid of incident rays with 0.05NA. At this small NA, there are 4 exiting modes for the cross-polarized system, and 6 exiting modes for the co-polarized system. Figure 7.20 shows the locations for all the resultant modes at far field. The number of exiting modes increases with increasing field for this system.

The flux of the exiting beam near the optical axis (z axis) is dominated by the pure e -modes for co- and crossed-Glan-Taylor prisms. The four exiting modes from the cross-polarized system propagates in four distinct directions, and results in four wavefront patches which do not overlap. On the other hand, three of the six modes from the co-polarized system have the same exiting propagation vector and overlap right below the dominant $eieieiei$ -wavefront, as shown in Figure 7.21. Exiting rays from the same mode produce a smooth wavefront; this is not the case for rays across different modes. Therefore, as in the last section, each mode is treated individually before combining them.

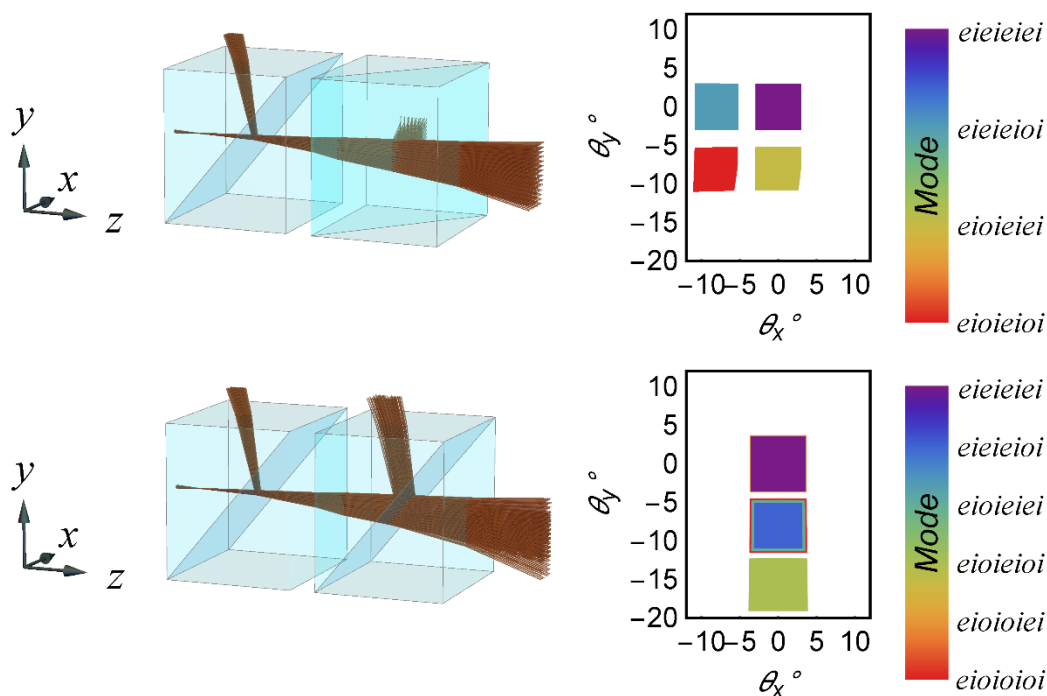


Figure 7.21 (Left) A grid of rays with 0.05NA propagates through the cross and co-polarized systems, where rays leak through for non-normal incident rays. (Right) The exiting modes are divided into groups by different colors and are plotted as function of exiting angles. In the co-polarized system, $eieieie$ -mode dominates the center of the field.

The polarization amplitude of each modes exiting the cross and co-polarized system are shown individually in Figure 7.22 and Figure 7.23 as a function of exiting angle. In the cross-polarized system, a Maltese cross like pattern is observed for both the $eieieie$ - and $eieieio$ -modes, with the $eieieioi$ -mode carrying the least energy. The $eioieie$ - and $eioieio$ -modes have zero amplitude for incident rays along the y - z plane. These amplitudes increase with incident angle away from the y - z plane. These four modes appear at distinct areas of the exit surface, where the $eieieie$ -mode stays at the center of the optical axis, and all the other modes are displaced. From the co-polarized system, the dominant extraordinary mode has rapidly decreasing amplitude, apodization, with increasing θ_y . The rest of the five

exiting modes displaced from the center have minimum amplitude with zero θ_x component, and increases with θ_y .

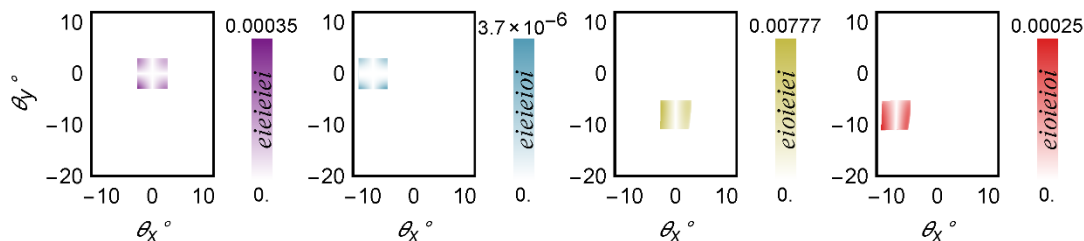


Figure 7.22 Polarization amplitudes through the cross-polarized system with 0.05NA for each resultant mode expressed in the exiting angle coordinates.

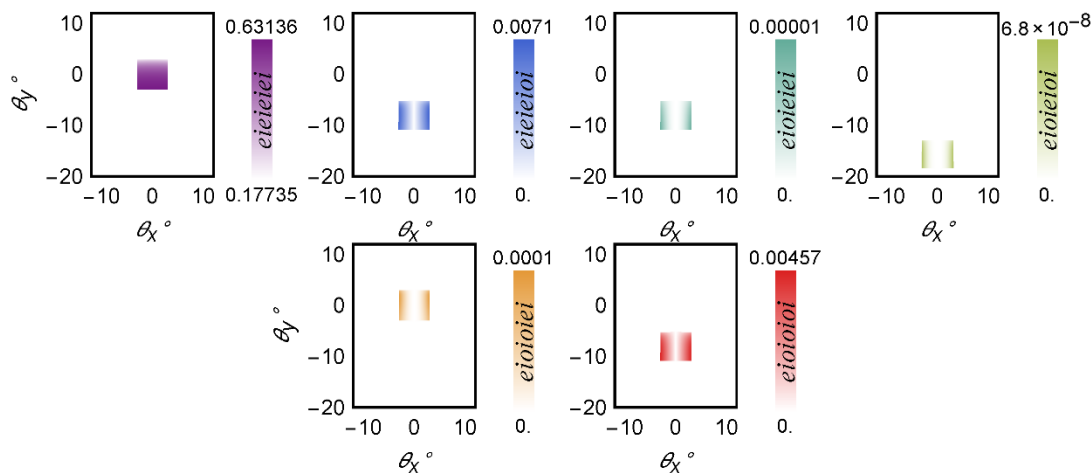


Figure 7.23 Polarization amplitudes through the co-polarized system with 0.05NA for each resultant mode in exiting angle coordinates.

The combined intensity distributions at the far field for both of the systems are shown in Figure 7.24, where part of the energy is redirected away from the center of the field. The highest intensity leaks in the cross-polarized system is the *eiowie*-mode, which is just below the centered pure *e*-mode. Special care is necessary to prevent this significant mode from interfering an optical system's performance.

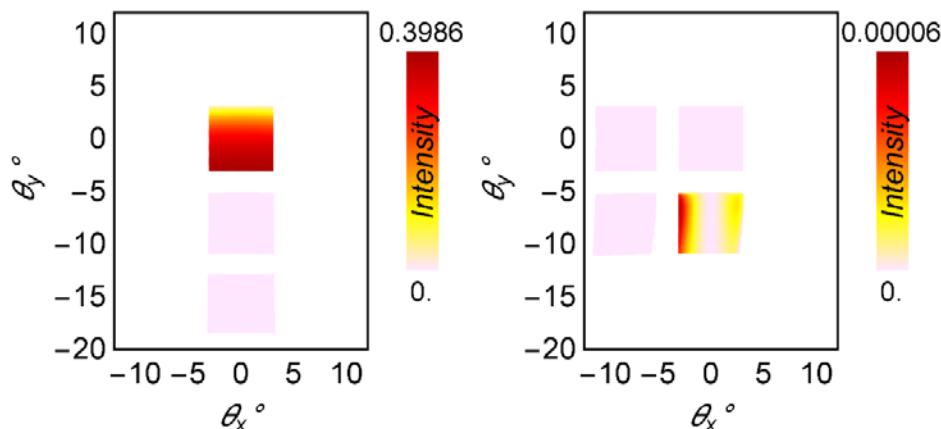


Figure 7.24 Resultant electric field intensity at the exit surface of the (left) co and (right) cross-polarized systems with 0.05NA.

The extinction ratio will be calculated for a $\pm 3^\circ$ FOV, as shown in Figure 7.25, where the pure e -mode dominates. The extinction ratios are highly dependent on the incident angle.

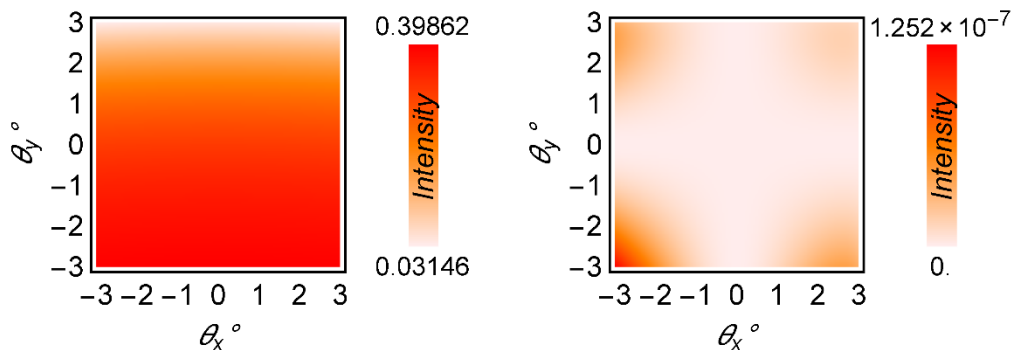


Figure 7.25 The intensity distribution at the center $\pm 3^\circ$ in the far field for the (left) co and (right) cross-polarized systems. The Maltese cross pattern represents the light leakage from off-axis rays in the cross-polarized system. The co-polarized system has decreasing amplitude toward the $+y$ direction.

The ratio of these two systems yields the extinction ratio distribution shown in Figure 7.26.

The highest extinction ratio, essentially infinite in simulation with ideal polarizers and monochromatic light, is observed at normal incidence (shown by the center point) and along the x and y direction (zero θ_x and/or θ_y). This is because the intensity at those regions

in Meltese cross leakage of the crossed-polarized system are zeros. Outside those regions, the extinction ratio drops off rapidly with increasing angles to about 10^5 .

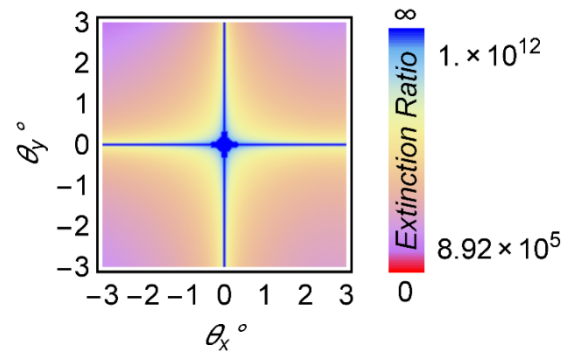


Figure 7.26 Extinction ratio map for $\pm 3^\circ$ square illumination. The highest extinction ratio is at normal incidence, and along the x and y directions.

Next, a similar analysis is performed for a 0.1NA. The exiting modes have more overlap than the 0.05NA, as shown in Figure 7.27. The co-polarized system has a decreasing transmission toward the $+y$ direction and only transmits light up to $+3^\circ$ due to TIR. In the cross-polarized system, the center $\pm 6^\circ$ region is highly affected by the overlapping modes. The low Meltese cross leakage is boosted by the light couplings from the overlapped modes; the abrupt changes of intensity is the sign of overlapped modes. Also, the crossed-polarized system does not transmit light beyond $+3^\circ$ in both x and y directions. The extinction ratio is undefined when the co-polarized system has zero intensity which is when $\theta_y > +3^\circ$. It is infinity when the cross-polarized system has zero intensity at normal incidence and $\theta_x > +3^\circ$. At the mode overlapping regions ($\theta_x \sim -6$, $\theta_x \sim +3$, and $\theta_y \sim -6$) of the cross-polarized system, the extinction ratio drops to 0.13. The minimum extinction ratio of the remaining area is ~ 3000 which is lower than that for the 0.05NA in Figure 7.26.

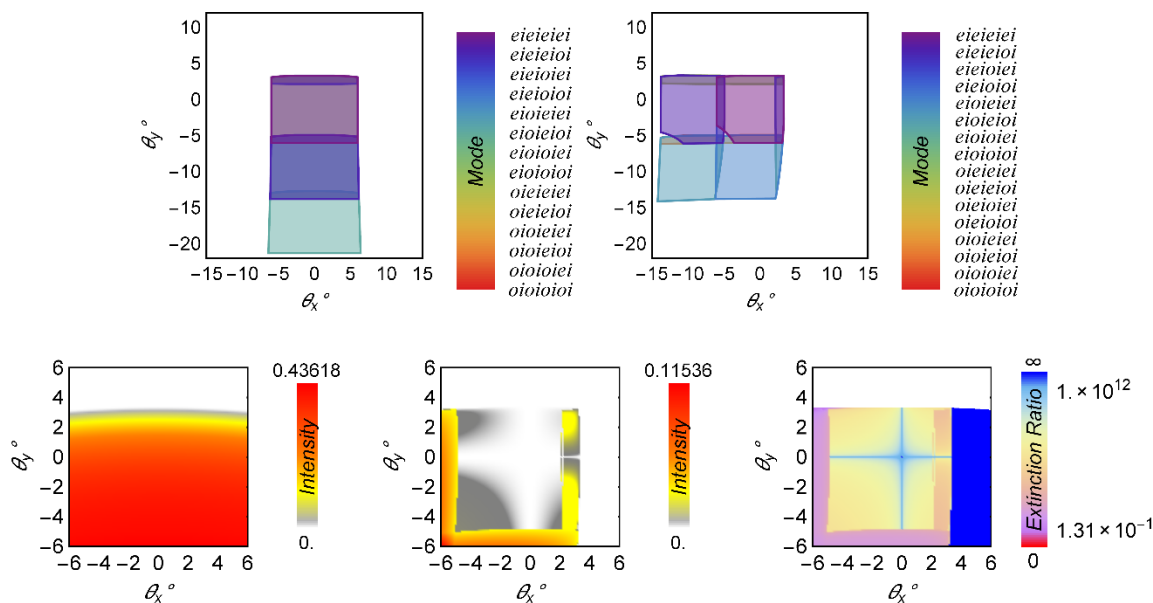


Figure 7.27 Analysis for a $\pm 6^\circ$ incident beam. (Top) The mode overlapped after the co and cross-polarized systems. (Bottom, left & middle) The exiting intensity within $\pm 6^\circ$ exiting angle for the co- and cross-polarized systems. (Bottom, right) Overlapping mode is visible in the extinction ratio plot.

7.5 Conclusions

This chapter showed a complex method to analyze complex optical components with anisotropic materials. All the significant modes generated from ray doubling are considered, which reveals the high performance crystal polarizer – Glan-Taylor prism – is highly sensitive to incident angle. Also, incident beams with various NAs through the polarizer, and the multiple exiting modes were simulated. The light leakage from undesired modes have increasing effects with increasing FOV. The Glan-Taylor polarizer shows interesting wavefront and polarization aberrations due to the non-rotationally symmetric geometry of the component. For small FOV, the center region is dominated by the extraordinary mode which has residual astigmatism due to the uniaxial crystal and rapidly decreasing intensity towards critical angle. The undesired modes propagating through the anisotropic materials should be aware of to avoid the unexpected energy leakage.

Additionally, a more complex configurations of the prisms, co- and cross- crystal polarized systems, are studied and the performance of the Glan-Taylor crystal polarizer decreases drastically when operating outside of the intended FOV. Similar configurations can be found in interferometers with co-and crossed-beam-splitters, such as Heterodyne interferometer¹⁴⁴ and other multi-channel interferometers^{145,146,147}, and similar light leakage could be observed and affect the resultant fringe visibility.

CHAPTER 8 RAY TRACING ELEMENTS WITH STRESS BIREFRINGENCE

8.1 Introduction to stress birefringence

Stress induced birefringence is common and often unavoidable in optical systems. The associated retardance is generally undesirable, changing the wavefront aberration and polarization aberration in complex patterns. Thus it is very useful to be able to ray trace elements with stress birefringence to assess the impact and calculate tolerances. This chapter will discuss polarization ray tracing through lenses with stress birefringence, where stress is described by arrays of stress tensors in CAD file.

Scottish physicist David Brewster¹⁴⁸ discovered stress induced birefringence in isotropic substances in 1816; this phenomenon is also addressed as mechanical birefringence, photoelasticity, and stress birefringence. Stress is present in optical systems in two different forms, mechanically induced or residual. Mechanical stress results from physical pressure, vibration, or thermal expansion and contraction. It often arises from mounts squeezing or applying force to elements. Such a property of an optical material is referred to as photoelasticity¹⁴⁹. Residual stress is a permanent stress inside an element, independent of external forces. It commonly occurs during fabrication of injection molded lenses or when glass is poorly annealed. As material cools from liquid to solid, stress can easily become frozen into the material, particularly when the outer surface solidifies before the inner material. Stress is also generated during the annealing process due to variation of chemical composition within a melt. Either form of stress alters the material's molecular structure slightly, some molecules are closer than equilibrium, others further apart, changing the optical properties in the direction of the stress, and induces birefringence.

Isotropic materials with stress induced birefringence behave as spatially varying weakly uniaxial or biaxial materials. This induced birefringence is readily observed with interferometers^{150,151} and polariscopes^{152,153}, as shown in Figure 8.1.

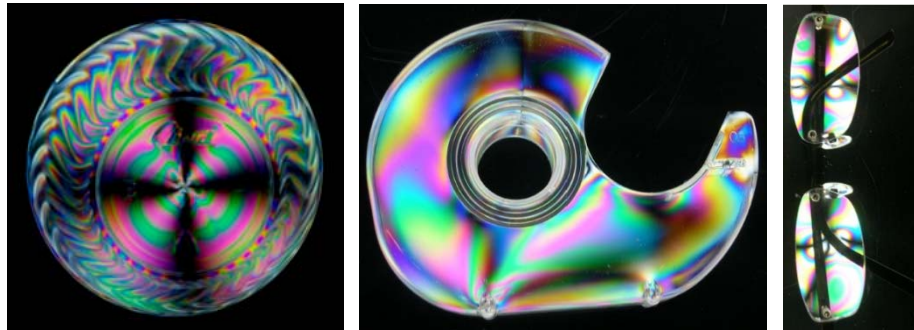


Figure 8.1. The colors in these plastic cup, plastic tape dispenser, and prescription eye glasses placed between crossed polarizers indicate large amounts of spatially varying stress.

The colorful patterns of materials with stress birefringence between crossed polarizers is due to the wavelength dependent nature of the retardance. Transparent isotropic optical elements will exhibit temporary birefringence when subjected to stress and revert to isotropic when the stress is released. An example is the glass rectangle subjected to stress by tightening a screw against one edge in Figure 8.2.

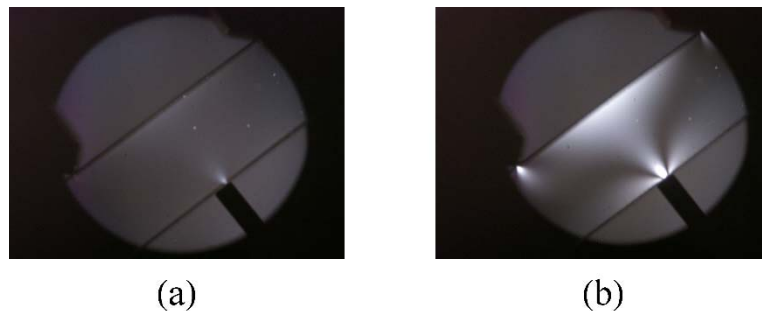


Figure 8.2 (a) An isotropic glass plate placed in an optical mount and viewed between crossed polarizers. (b) The same glass plate as a screw is tightened against the glass at the bottom. Due to the stress created, induced birefringence has caused significant leakage between crossed polarizers.

Stress birefringence can be intentional, for example in tempered glass and photoelastic modulators. In general optical elements, it is undesirable. For example, the stress which is common in injection molded lenses added to the wavefront aberrations and causes polarization aberrations, thus increasing the size of the points spread function, and degrading the image.

8.2 Stress birefringence in optical systems

In most optical designs, tolerance analysis is required to ensure high performance of the system in the desired environment. The analysis can be done, for example, by understanding the allowable induced birefringence. Some typical birefringence tolerances on lenses and glass blanks are 2nm/cm for critical applications such as photolithography systems, polarimeters and interferometers, 5nm/cm in precision optics, 10nm/cm for microscope objectives, and 20nm/cm for eyepieces, viewfinder, and magnifying glasses^{154,155}. More lenses are made from plastic these days due to its low cost and ease of fabrication. However, plastic optics more easily suffer stress birefringence, which easily occurs during injection molding and cooling. Molding parameters such as the pressure applied to the resin in a mold, the time spent in the mold, and the rate the molded lens cool are often adjusted to minimize stress birefringence, but completely eliminating it is difficult.

It is useful but complicated to simulate stress induced birefringence in polarization ray tracing, because the stress effects are directional and change through the volume. This chapter presents the mathematical description of stress and its relationship to optical birefringence. Methods to translate the non-uniform stress information of optical

components to retardance and the algorithms to use this information for polarization ray tracing through stress components will be explained. The finite-element model of example plastic lenses will be analyzed using retardance maps, Jones pupil images and polarization point spread matrices to visually demonstrate the induced birefringence and its effects.

8.3 Effects of stress birefringence on material properties

The stress birefringence can be described mathematically. When stress is applied to an object, the material deforms slightly as atoms reposition themselves in response to applied forces, as shown in Figure 8.3. The stress discussed in this chapter induces small changes in atomic and molecular positions, but causes negligible change in the material's physical shape. This applied stress, contact stress, or principal stress is characterized by the force applied in $\text{kg}\cdot\text{m}\cdot\text{s}^{-2}$ or Newton (N) to the relevant cross sectional area; the resulting stress is given in units of N/m^2 or Pascals (Pa). For a material such as glass or clear plastic, compression increases the refractive index in the compressive stress direction; atoms move closer together in this direction but move further apart in the perpendicular plane. Conversely, tension decreases refractive index in the tensile stress direction as atoms expand along this axis. For small stress, after releasing the force, the glass returns to an isotropic state. This is referred to as elastic deformation. Above some threshold, irreversible changes to the molecular arrangements occur, and the object cannot return to its original shape. For example, glass may shatter or a plastic lens may become dented.

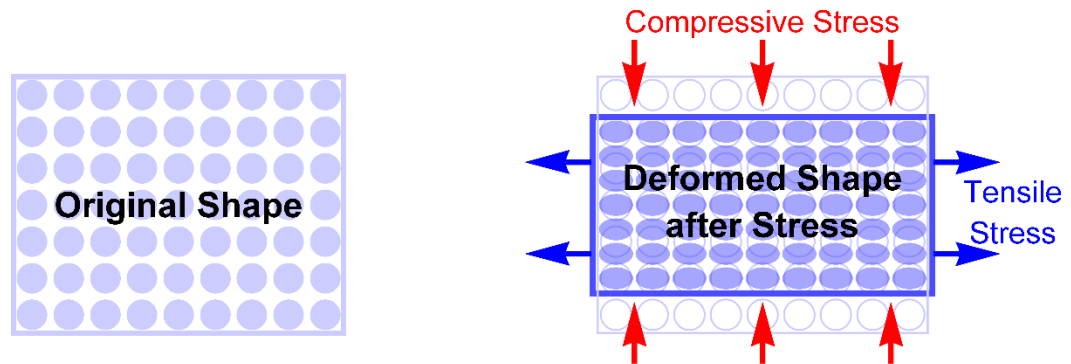


Figure 8.3 Stress on an object results in compressive stress and tensile stress. (Left) The original shape of an object. (Right) When stress is applied to the object, the shape of the object deformed. The deformation of the object shown is exaggerated to visualize the effect of compressive and tensile stress.

Stress induces a small changes in a material's refractive index with Δn less than 1.

Typically, a 15MPa stress yields a Δn in the order of 0.0001 for glass, as shown in Figure 8.4.

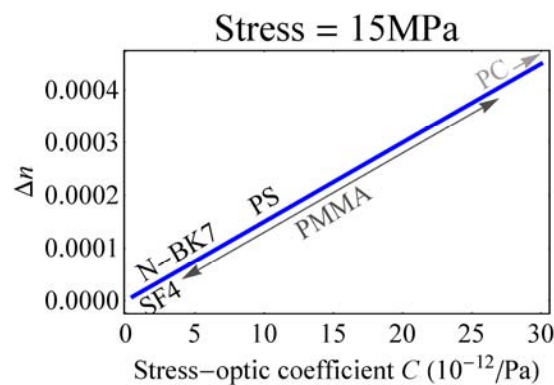


Figure 8.4 The change of refractive index Δn plotted as a function of material stress-optic coefficient C for 15MPa applied stress, where $\Delta n = C \cdot \text{Stress}$. Glasses such as N-BK7 and SF4 have $C < 5$. Polymers, such as Polymethylmethacrylate (PMMA), Polystyrene (PS), and Polycarbonate (PC), have larger C which vary in a large range with temperature.

When an external force is applied along one direction to an isotropic piece of glass, it becomes a uniaxial material with its optic axis along the direction of external force. Application of a second force along a different direction causes the glass to become a

biaxial material. These stresses alter the dielectric tensor of the material. Therefore the stressed optical element is simulated as an anisotropic material. A real optical component generally has varying stress throughout its volume, such as Figure 8.1 and Figure 8.2, so stress birefringence should be simulated as a spatially varying anisotropic material.

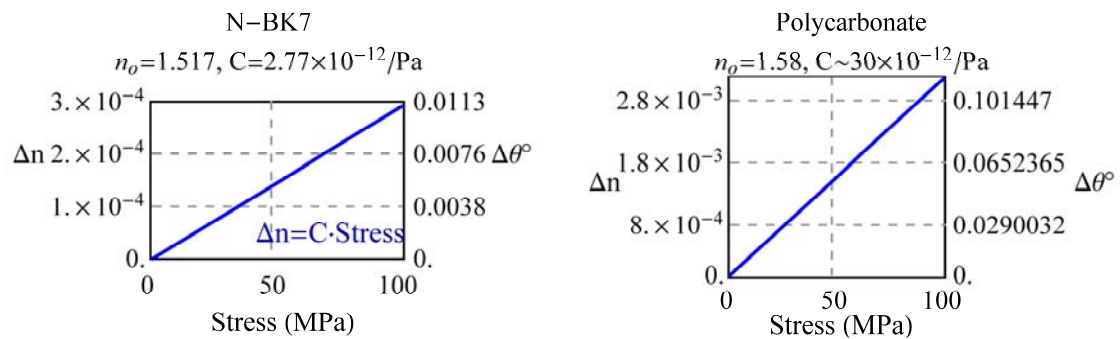


Figure 8.5 Refractive index change Δn and its corresponding ray split $\Delta\theta$ as a function of applied stress for glass N-BK7 (left) and polymer polycarbonate (right). The ray split is calculated with algorithms presented in Chapter 2.

Figure 8.5 shows the very small change in refractive index (Δn) due to typical stress induced birefringence for N-BK7 and polycarbonate (PC), which results in a negligibly small amount of ray doubling ($\Delta\theta^\circ$), so the two split modes propagate very close to each other. Since a few wavelengths of ray separation in a ray trace is insignificant and would usually not affect the accuracy of many calculations, this ray doubling can be safely ignored. The induced birefringence of the two modes can be modeled as retardance along a single ray path. And, the refraction is typically modeled based on Snell's Law using the unstressed refractive index.

8.4 Ray tracing in stress birefringent components

Algorithms will now be developed for simulating stress birefringence in polarization ray tracing. Its effects on image formation, fringe visibility, and other optical metrics can be

calculated. The applied stress and its induced retardance have a linear relationship. Therefore, the stress induced birefringence can be represented as spatially varying linear retarder. \mathbf{P} matrices are used to keep track of stress induced retardance along ray paths. The following sections will describe the algorithms which take the stress of an optical material as input and calculate the resultant retardance experienced by light rays.

8.4.1 Anisotropic stress model

When multiple stresses are applied to an isotropic material in different directions, the stressed component becomes biaxial. The applied stress is represented as a 3×3 stress tensor \mathbf{S} , defined in terms of normal stresses σ and shear stresses τ in (x, y, z) coordinate system,

$$\mathbf{S} = \begin{pmatrix} \sigma_{xx} & \tau_{xy} & \tau_{xz} \\ \tau_{xy} & \sigma_{yy} & \tau_{yz} \\ \tau_{xz} & \tau_{yz} & \sigma_{zz} \end{pmatrix}. \quad (8.1)$$

\mathbf{S} contains 6 stress tensor coefficients, σ_{xx} , σ_{yy} , σ_{zz} , τ_{xy} , τ_{xz} , and τ_{yz} ^{156,157,158,159,160}, which represent the force per unit area from different directions in three dimensions. The amount of deformation in the optic relative to the original shape due to \mathbf{S} is characterized by the strain tensor $\mathbf{\Gamma}$,

$$\mathbf{\Gamma} = \begin{pmatrix} \gamma_{xx} & \gamma_{xy} & \gamma_{xz} \\ \gamma_{xy} & \gamma_{yy} & \gamma_{yz} \\ \gamma_{xz} & \gamma_{yz} & \gamma_{zz} \end{pmatrix}, \quad (8.2)$$

where γ 's are the strain tensor coefficients. The material refractive index is represented as a 3×3 dielectric tensor $\mathbf{\epsilon}$ (introduced in Chapter 2). Isotropic materials have an refractive

index n_o , and a dielectric tensor $\boldsymbol{\epsilon}_o$ ($n_o^2 \times$ identity matrix), which changes and becomes non-diagonal $\boldsymbol{\epsilon}$ when external stress is applied in arbitrary directions,

$$\boldsymbol{\epsilon}_o = \begin{pmatrix} n_o^2 & 0 & 0 \\ 0 & n_o^2 & 0 \\ 0 & 0 & n_o^2 \end{pmatrix} \rightarrow \boldsymbol{\epsilon} = \begin{pmatrix} n_{xx}^2 & n_{xy}^2 & n_{xz}^2 \\ n_{xy}^2 & n_{yy}^2 & n_{yz}^2 \\ n_{xz}^2 & n_{yz}^2 & n_{zz}^2 \end{pmatrix}. \quad (8.3)$$

where n_o is the unstressed refractive index. Similarly, the impermeability tensor, the inverse of $\boldsymbol{\epsilon}_o$, also changes from a diagonal tensor to a non-diagonal tensor with external stress as

$$\boldsymbol{\eta}_o = \boldsymbol{\epsilon}_o^{-1} = \begin{pmatrix} 1/n_o^2 & 0 & 0 \\ 0 & 1/n_o^2 & 0 \\ 0 & 0 & 1/n_o^2 \end{pmatrix} = \begin{pmatrix} \eta_o & 0 & 0 \\ 0 & \eta_o & 0 \\ 0 & 0 & \eta_o \end{pmatrix} \rightarrow \boldsymbol{\eta} = \begin{pmatrix} \eta_{xx} & \eta_{xy} & \eta_{xz} \\ \eta_{xy} & \eta_{yy} & \eta_{yz} \\ \eta_{xz} & \eta_{yz} & \eta_{zz} \end{pmatrix}. \quad (8.4)$$

Stress alters the index ellipsoid from spherical to ellipsoidal. From equations (2.34) and (2.31),

$$u = \frac{1}{2} \mathbf{E} \cdot \mathbf{D} = \frac{1}{2} \left(\frac{D_x^2}{n_x^2} + \frac{D_y^2}{n_y^2} + \frac{D_z^2}{n_z^2} \right) \text{ and } 1 = \frac{\left(\frac{D_x}{\sqrt{2u}} \right)^2}{(n_x)^2} + \frac{\left(\frac{D_y}{\sqrt{2u}} \right)^2}{(n_y)^2} + \frac{\left(\frac{D_z}{\sqrt{2u}} \right)^2}{(n_z)^2}.$$

So,

$$\begin{aligned} \frac{x^2}{n_o^2} + \frac{y^2}{n_o^2} + \frac{z^2}{n_o^2} &= x^2 \eta_o + y^2 \eta_o + z^2 \eta_o = 1 \\ &\downarrow \\ \eta_{xx} x^2 + \eta_{yy} y^2 + \eta_{zz} z^2 + 2\eta_{xy} xy + 2\eta_{xz} xz + 2\eta_{yz} yz &= 1 \end{aligned} \quad (8.5)$$

where $x = \left(\frac{D_x}{\sqrt{2u}} \right)$, $y = \left(\frac{D_y}{\sqrt{2u}} \right)$ and $z = \left(\frac{D_z}{\sqrt{2u}} \right)$, and u is the energy density of the light field.

The links between the stress/strain and their optical effect on isotropic, non-magnetic, and non-absorbing material are given by the 6×6 stress optic tensor \mathbf{C} and strain optic tensor $\mathbf{\Omega}$,

$$\mathbf{C} = \begin{pmatrix} C_1 & C_2 & C_2 & 0 & 0 & 0 \\ C_2 & C_1 & C_2 & 0 & 0 & 0 \\ C_2 & C_2 & C_1 & 0 & 0 & 0 \\ 0 & 0 & 0 & C_3 & 0 & 0 \\ 0 & 0 & 0 & 0 & C_3 & 0 \\ 0 & 0 & 0 & 0 & 0 & C_3 \end{pmatrix} \quad \text{and} \quad \mathbf{\Omega} = \begin{pmatrix} p_1 & p_2 & p_2 & 0 & 0 & 0 \\ p_2 & p_1 & p_2 & 0 & 0 & 0 \\ p_2 & p_2 & p_1 & 0 & 0 & 0 \\ 0 & 0 & 0 & p_3 & 0 & 0 \\ 0 & 0 & 0 & 0 & p_3 & 0 \\ 0 & 0 & 0 & 0 & 0 & p_3 \end{pmatrix} \quad (8.6)$$

for the unidirectional symmetric structure of isotropic materials and polymers. \mathbf{C} is a function of the stress optic coefficients, C_1 and $C_3 = C_1 - C_2$ with unit inverse Pascals (1/Pa). $\mathbf{\Omega}$ is a function of the strain optic coefficients, p_1 and p_2 with $p_3 = (p_1 - p_2)/2$. These stress/strain optic coefficients are directly related to each other through the Young's modulus E and Poisson's ratio ν as:

$$C_1 = \frac{n_0^3}{2E} (p_1 - 2\nu p_2) \quad \text{and} \quad C_2 = \frac{n_0^3}{2E} [p_2 - \nu(p_1 + p_2)]. \quad (8.7)$$

Then matrix $\mathbf{\Omega}$ and \mathbf{C} relate the strain and stress to material refractive index as:

$$\Delta\boldsymbol{\eta} = \begin{pmatrix} 1/n_{xx}^2 - 1/n_o^2 \\ 1/n_{yy}^2 - 1/n_o^2 \\ 1/n_{zz}^2 - 1/n_o^2 \\ 1/n_{xy}^2 \\ 1/n_{yz}^2 \\ 1/n_{xz}^2 \end{pmatrix} = \boldsymbol{\Omega} \begin{pmatrix} \gamma_{xx} \\ \gamma_{yy} \\ \gamma_{zz} \\ \gamma_{xy} \\ \gamma_{yz} \\ \gamma_{xz} \end{pmatrix} \quad \text{and, } \Delta\boldsymbol{\eta} = \mathbf{C}_o \begin{pmatrix} \sigma_{xx} \\ \sigma_{yy} \\ \sigma_{zz} \\ \tau_{xy} \\ \tau_{yz} \\ \tau_{xz} \end{pmatrix} \quad \text{or} \quad \begin{pmatrix} n_{xx} - n_o \\ n_{yy} - n_o \\ n_{zz} - n_o \\ n_{xy} \\ n_{yz} \\ n_{xz} \end{pmatrix} \approx -\mathbf{C} \begin{pmatrix} \sigma_{xx} \\ \sigma_{yy} \\ \sigma_{zz} \\ \tau_{xy} \\ \tau_{yz} \\ \tau_{xz} \end{pmatrix}. \quad (8.8)$$

Table 8.1 contains a set of strain and stress optic tensor coefficients C_1 and C_2 . The stress optic tensor coefficients for plastic are typically larger than glass, which means an equivalent stress applied on plastic yields a larger change of refractive index than glass. More compressible materials have a larger response in general. Polycarbonate (PC) is a very strong polymer, but generally has high stress induced birefringence. So PC is avoided in application where stress is a problem, but is popular in eye glasses for its strength.

Table 8.1 Refractive index n_o , strain optic coefficients (p_1 and p_2), Young's modulus E , Poisson's ratio ν , and stress optic tensor coefficients (C_1 and C_2) for glasses and plastics at 633nm.

Materials	n_o	p_1	p_2	E (GPa)	ν	C_1 ($10^{-12}/\text{Pa}$)	C_2 ($10^{-12}/\text{Pa}$)
Corning 7940 fused silica ^{158,161}	1.46	0.121	0.270	70.4	0.17	0.65	4.50
Corning 7070 glass ¹⁶¹	1.469	0.113	0.23	51.0	0.22	0.37	4.80
Corning 8363 glass ¹⁶¹	1.97	0.196	0.185	62.7	0.29	5.41	4.54
Al_2O_3 ¹⁵⁸	1.76	-0.23	-0.03	367	0.22	-1.61	0.202
As_2S_3 ¹⁶¹	2.60	0.24	0.22	16.3	0.24	72.5	59.1
Polystyrene ¹⁶²	1.57	0.30	0.31	3.2	0.34	53.9	62.0
Lucite ^{162, 163}	1.491	0.30	0.28	4.35	0.37	35.4	24.9
Lexan ^{162,163}	1.582	0.252	0.321	2.2	0.37	13.0	98.1

From equation (8.8), the stressed impermeability tensor is $\boldsymbol{\eta} = \boldsymbol{\eta}_o + \Delta\boldsymbol{\eta}$ which can be converted to a dielectric tensor in the principle coordinate system. When $\boldsymbol{\eta}$ is expressed

in its principle coordinates, it is a diagonal matrix with its eigenvalues (L_1, L_2, L_3) along the diagonal,

$$\boldsymbol{\eta}_{\text{principle}} = \begin{pmatrix} L_1 & 0 & 0 \\ 0 & L_2 & 0 \\ 0 & 0 & L_3 \end{pmatrix}, \text{ so } \boldsymbol{\varepsilon}_{\text{principle}} = \begin{pmatrix} 1/L_1 & 0 & 0 \\ 0 & 1/L_2 & 0 \\ 0 & 0 & 1/L_3 \end{pmatrix}. \quad (8.9)$$

The dielectric tensor in principle coordinates is rotated from the global coordinate system as

$$\boldsymbol{\varepsilon} = \mathbf{R}^{-1} \cdot \boldsymbol{\varepsilon}_{\text{principle}} \cdot \mathbf{R}, \quad (8.10)$$

where \mathbf{R} is $(\mathbf{v}_1 \ \mathbf{v}_2 \ \mathbf{v}_3)$ whose columns are the eigenvectors of $\boldsymbol{\eta}$.

Stress applied to uniaxial or biaxial crystals requires additional stress optic coefficients than the one shown in equation (8.6), which are related to the other strain coefficients. Their stress optic tensor require more non-zero components to account for interactions between off-diagonal $\boldsymbol{\varepsilon}$ components in both shear and normal stress^{156,164,165}.

Using the results in equations (8.8) to (8.10), we obtain the stressed dielectric tensor that alters the polarization properties of a ray in a way similar to a biaxial dielectric tensor. As described in Chapter 2, when a ray passes through a stressed biaxial material, it splits into two modes with orthogonal electric field vectors \mathbf{E}_1 and \mathbf{E}_2 which carry two different refractive indices n_1 and n_2 . The following assumptions are made to simplify the calculation of the stressed \mathbf{P} matrix:

(1) The applied stress only causes small changes to the refractive index. So, refraction into and out of an element is accurately calculated by Snell's law using the unstressed refractive index.

(2) Ray doubling is ignored since the two modes exiting the stress birefringent material are essentially on top of each other, as shown in Figure 8.5, and the path is well modeled by a single ray traced from the entrance to exiting surfaces. Therefore $\hat{\mathbf{k}} \approx \hat{\mathbf{S}}$ and $\hat{\mathbf{D}} \approx \hat{\mathbf{E}}$.

Using these assumptions, the refracted propagation vector \mathbf{k} is calculated as

$$n_i \sin \theta_i = n_o \sin \theta_o \quad \text{and} \quad \mathbf{k} = \frac{n_i}{n_o} \mathbf{k}_i + \left(\frac{n_i}{n_o} \cos \theta_i - \cos \theta_o \right) \hat{\mathbf{n}}, \quad (8.11)$$

where n_i and n_o are the incident and unstressed refractive indices, θ_i and θ_o are incident and refraction angles, \mathbf{k}_i is the incident propagation vector, and $\hat{\mathbf{n}}$ is the surface normal. The refractive index and electric field vector for the two modes are calculated with the method described in section 2.4. By combining the anisotropic constitutive relation in equation (2.5) and the Maxwell equations, the eigenvalue equation for \mathbf{E} is

$$\left[\boldsymbol{\varepsilon} + (n \mathbf{K})^2 \right] \mathbf{E} = 0, \quad (8.12)$$

where $\mathbf{K} = \begin{pmatrix} 0 & -k_z & k_y \\ k_z & 0 & -k_x \\ -k_y & k_x & 0 \end{pmatrix}$ and $\hat{\mathbf{k}} = (k_x, k_y, k_z)$ is the propagation direction within the

stressed material. For non-zero \mathbf{E} ,

$$\left| \boldsymbol{\varepsilon} + (n \mathbf{K})^2 \right| = 0 \quad (8.13)$$

with two refractive index solutions, n_1 and n_2 corresponding to the two eigenmodes. Then \mathbf{E}_1 and \mathbf{E}_2 are obtained through the singular value decomposition of $[\boldsymbol{\varepsilon} + (n \mathbf{K})^2]$ with n_1 and n_2 . Their Poynting vectors are the cross product of the electric and magnetic vectors,

$$\mathbf{S} = \frac{\mathcal{R}e[\mathbf{E} \times \mathbf{H}^*]}{|\mathcal{R}e[\mathbf{E} \times \mathbf{H}^*]|}, \quad (8.14)$$

where

$$\mathbf{H} = n \mathbf{K} \cdot \mathbf{E}. \quad (8.15)$$

The \mathbf{P} matrix of the ray within the stressed material is a linear retarder. It maps vectors

$(\hat{\mathbf{E}}_1, \hat{\mathbf{E}}_2, \hat{\mathbf{S}})$ to $(\hat{\mathbf{E}}_1 e^{i\frac{2\pi}{\lambda}n_1d}, \hat{\mathbf{E}}_2 e^{i\frac{2\pi}{\lambda}n_2d}, \hat{\mathbf{S}})$. So,

$$\mathbf{P}_{\text{stressed}} = \begin{pmatrix} \hat{\mathbf{E}}_1 e^{i\frac{2\pi}{\lambda}n_1d} & \hat{\mathbf{E}}_2 e^{i\frac{2\pi}{\lambda}n_2d} & \hat{\mathbf{S}} \end{pmatrix} (\hat{\mathbf{E}}_1 \quad \hat{\mathbf{E}}_2 \quad \hat{\mathbf{S}})^T, \quad (8.16)$$

where λ is the wavelength of the light, and d is the distance the light travels inside the material.

8.4.2 Spatially varying stress

In optical elements with stress birefringence, the stress usually varies in a complex way. For example, when plastic optical elements are manufactured by injection molding, stress from lens mounts and vacuum windows create complex spatially varying stress birefringence, like Figure 8.1. Mechanical engineering software packages, such as *SigFit*¹⁶⁶, calculate the stress distributions within mechanical parts due to forces such as bolting items together, welding, and gravity. This finite element modeling (FEM) of

stresses and many other parameters such as vibration characteristics are part of the mechanical design process. The resultant stress distribution is calculated at a discrete set of data points, thus the designation finite element. For injection molding, other software packages such as *Moldflow* and *Timon3D*^{167,168,169} analyze the complex physical process of injection molding by simulating the flow of the viscous melted plastic into a heated mold, the non-uniform cooling of the mold and part, the solidification under high compression, and the separation of the lens from the mold. Modeling has improved efficiency and quality in plastic lens molding to incorporate new polymers and meet the high demand in high-quality electronics, consumer products, and automobiles industry¹⁷⁰. In both cases, mechanical stresses and molding stresses, the distribution of stress inside a 3D object is expressed as an array of 3×3 stress tensors. Figure 8.6 shows the 3×3 symmetric stress tensor distribution on the surface of an injection molded lens, where high stress variations are observed in the diagonal elements.

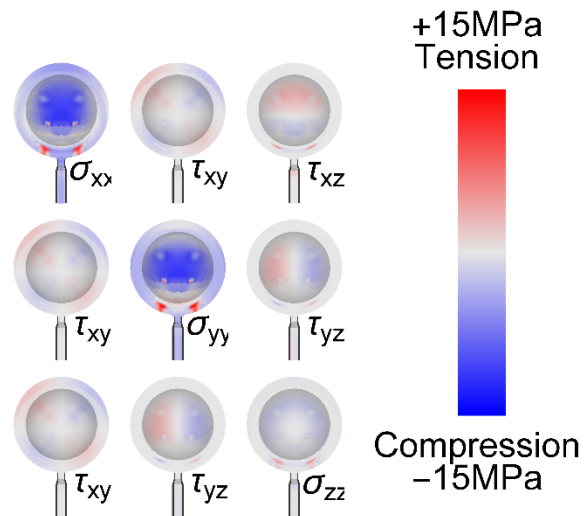


Figure 8.6 The 3×3 stress tensor distribution of an injection molded lens. Red indicates tension, blue indicates compression, and gray indicates zero stress. The plastic entered the lens mold from the bottom at the region called the gate. The cylinder of plastic extending from the bottom of the lens is for handling the lens, which will be removed by a robotic saw. When the cylinder is removed, the lens falls into packaging for delivery.

To simulate polarization change through an optical element with spatially varying stress involves four general steps listed below. They calculate *OPL*, retardance, and \mathbf{P} matrices for a finite element stress model.

- (1) Extract the element's optical shape,
- (2) Calculate the optical path of a ray inside the element,
- (3) Extract the stress information along that optical path, and
- (4) Convert the stress optical distribution into a retarder \mathbf{P} matrix.

8.4.3 Refraction and reflection at stress birefringent intercepts

Although the storage details of a 3D object with stress vary between CAD systems, the idea is similar; the goal is to discretize a continuous region to a finite numbers of sub-domains. In general, an object stored in a CAD file is using numerous simple building blocks or finite elements, such as cuboids or tetrahedrons. Each element is specified by its

vertices or nodes. A cuboid requires eight nodes, and a tetrahedron requires four nodes as shown in Figure 8.7 (a). Nodes for elements are spaced in a semi-regular grid; all the nodes are at the finite elements' corners. With tetrahedron building blocks, the surface of the resultant 3D object can be expressed in surface triangles, as shown in Figure 8.7 (b) and (c).

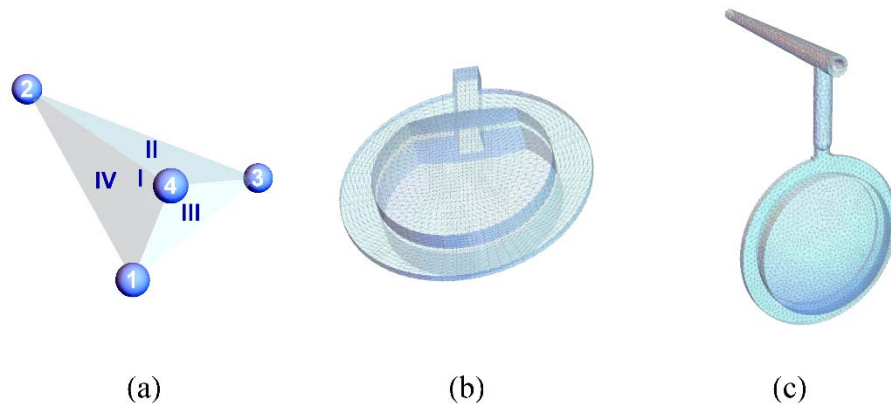


Figure 8.7 (a) A tetrahedron element has four vertices (1, 2, 3, and 4) and four surfaces (I, II, III, and IV). (b) and (c) are surface plots of two different injection molded lens structures. The surfaces are represented by surface triangles.

Refraction and reflection are performed using the unstressed refractive indices and the surface triangles at the object surface extracted from a CAD file. Each surface triangle has its surface normal specified in global coordinate systems. For a given triangle, two vectors are calculated by taking the differences between the triangle vertices. The cross product of these two vectors is the surface normal. For a given ray, a ray intercept is calculated using the algorithm in the reference 171. Figure 8.8 shows the refraction of a ray grid refracts through an injection molded lens. Using the ray intercept routine and Snell's law, a set of collimated rays converge after refracting from the lens surfaces.

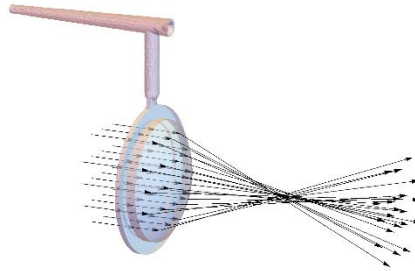


Figure 8.8 Refraction through an injection molded lens uses surface triangles and Snell's law to calculate ray intercepts. The figure shows a simulation of collimated rays converging through the lens.

8.5 Polarization ray tracing P matrix for stress birefringent model

Stress information is usually contained in CAD files as an array of stress tensors, each with six stress coefficients, σ_{xx} , σ_{yy} , σ_{zz} , τ_{xy} , τ_{xz} , τ_{yz} in equation (8.8). A stress tensor is assigned to each element building block. When a ray propagates through a lens or a 3D object, the ray passes through multiple elements and experiences varying stress tensors along the ray segment. Usually each stress tensor is associated with the center of one element block as shown in Figure 8.9. Thus for an object comprised of A element blocks, the stress file provides A stress data points distributed throughout the object's volume. The light ray propagates through this cloud of points and interpolation can estimate the stress at arbitrary locations along the ray.

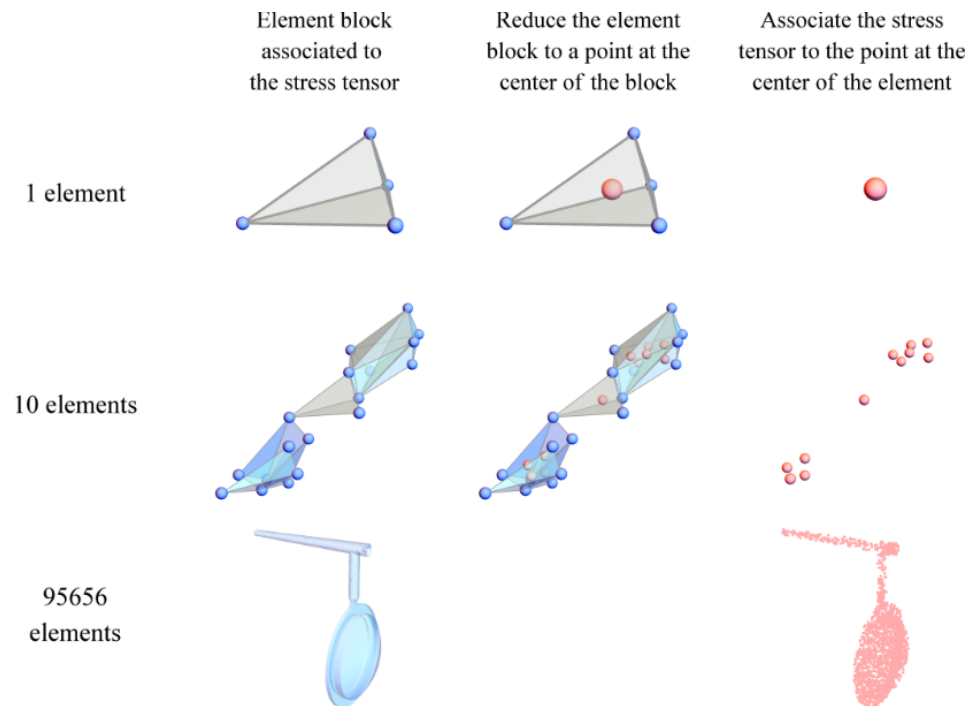


Figure 8.9 A tetrahedron element defined by four corners (top row, left column) is reduced to one data point, shown as a red point at the center of the element. Eleven tetrahedrons shown in the middle row are reduced to eleven data locations. The last row shows all 95,656 tetrahedrons of an object are reduced to 95,656 data locations, each of them are associated with a stress tensor.

The stress component σ_{xx} of an example injection molded lens is shown in Figure 8.10. It is common that most of the stress is concentrated in a thin layer at the surfaces. A stress tensor map with all nine components of another example lens is shown in Figure 8.11 with the magnitude of the stress shown in the color scale. Higher stress is observed around the gate (where the plastic melt flow into the mold) and the flange (an annular structure around the outside of the lens for mounting) of the plastic lens.

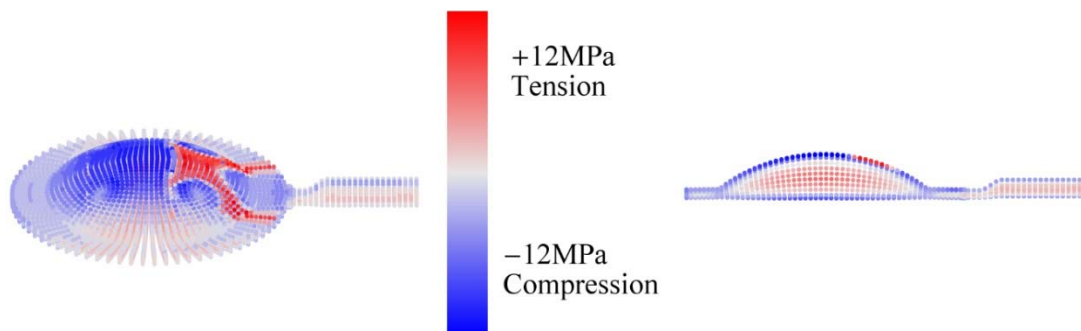


Figure 8.10 Two views of the stress tensor coefficient σ_{xx} from the CAD file of an injection molded lens.

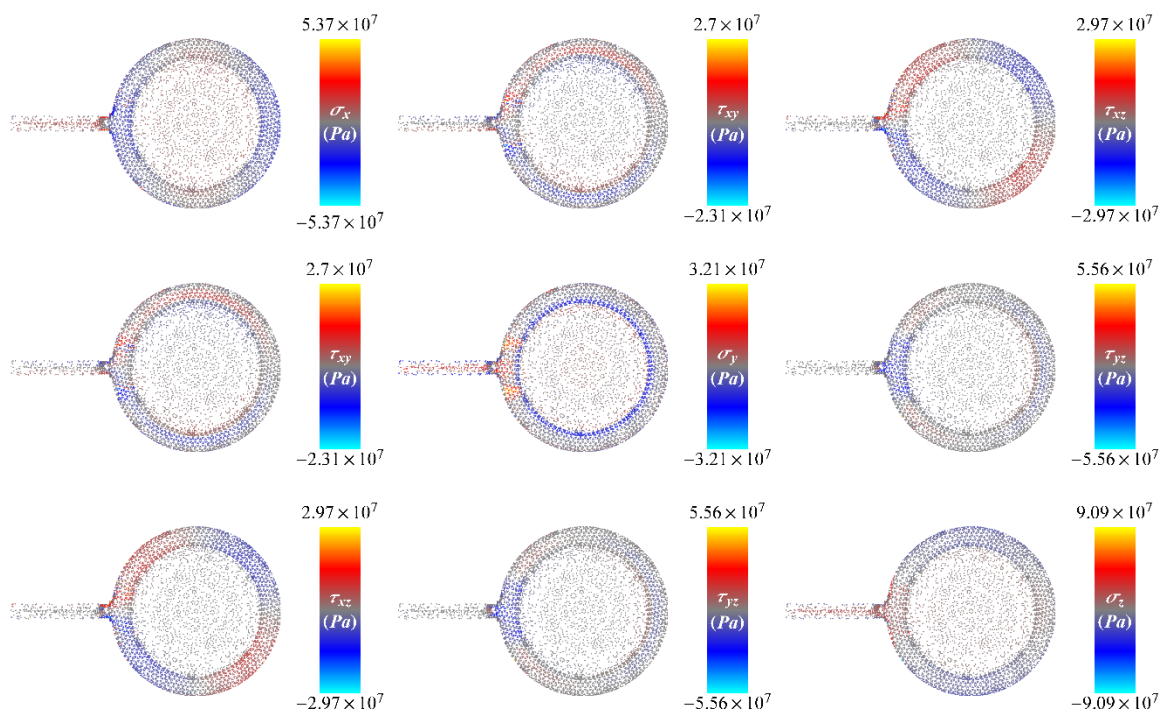


Figure 8.11 Stress tensor maps for the 9 components are plotted across an object cross section in color scale.

When a ray propagates through material with spatially varying stress, it experiences retardance change along the ray path. This is similar to a ray propagating through a spatially varying birefringent material, so the ray path is modeled as a stack of constant biaxial materials as shown in Figure 8.12. The Figure 8.12 (left) shows a spatially varying birefringent layers with a rotating optic axis and changing retardance magnitude. Such

spatially varying behavior is simulated by dividing the material into thin slabs along the ray path as shown in Figure 8.12 (right). Each of the slabs represent a constant biaxial material with its unique optic axis orientation and retardance magnitude.

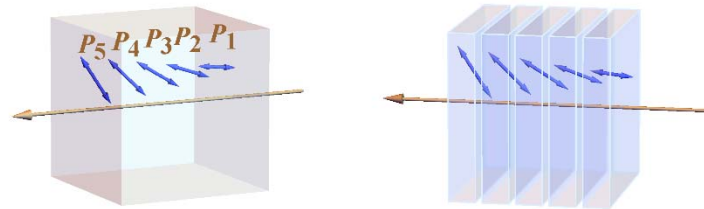


Figure 8.12 For a single ray, a spatially varying biaxial material (left) can be simulated as a stack of constant biaxial slabs (right). A different stack is calculated for each ray.

The concept of slicing a ray path into segments through a material is applied to the stress data shown in Figure 8.13. (a) Along a ray path, a ray passes many stress data points. (b) The ray path is then divided into steps. (c) A step is very unlikely to be on top of a data point. (d) The stress tensor at each step is the weighted average of the three closest data points. (e) A \mathbf{P} matrix is calculated for the step from the stress tensor. The data point closest to the step contributes more than the data point further away from the step. The number of steps should be chosen to be sufficiently large to model spatial variation of the stress birefringence and ensure accurate results.

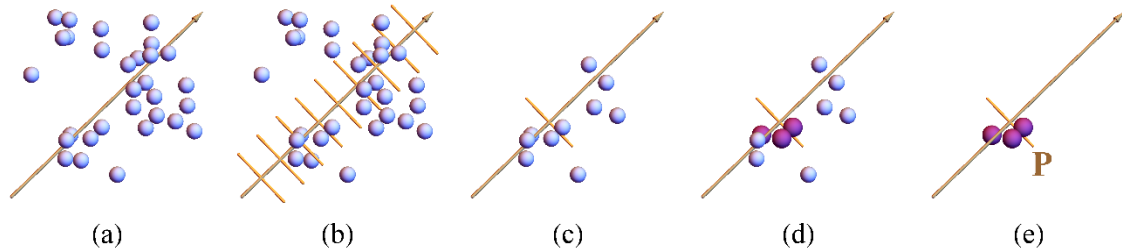


Figure 8.13 The ray path inside the spatially varying biaxial material is divided into steps. Interpolation is used to obtain stress information at each step. (a) A ray passes near many stress data points shown in light blue along its ray path. (b) The ray path is then divided into steps shown as orange parallel lines along the ray path. (c) It is unlikely that the step exactly intersects any data point. (d) The N closest data points, three are highlighted in purple, are used to interpolate the stress for the step. (e) A \mathbf{P} matrix is calculated for the step from the stress tensor, the ray direction, and the step length.

The stress grid is intended to well sample the spatial stress variation such that the change between nearby modes is small. In this limit the stress can be interpolated. However, for more rapidly vary stresses, higher order equations could be needed, and interpolation would be performed on the retardance magnitude and retardance orientation separately.

The method to calculate the weighted average stress is similar to the interpolation algorithm shown in section 5.6. Consider a set of 3×3 stress tensors ($\mathbf{S}_1, \mathbf{S}_2, \dots, \mathbf{S}_a, \dots, \mathbf{S}_A$) at A data locations ($\mathbf{r}_{s1}, \mathbf{r}_{s2}, \dots, \mathbf{r}_{sa}, \dots, \mathbf{r}_{sA}$) describing the stress distribution of an object. A ray propagates through the object and its ray path within the stressed object is evenly divided into N steps ($\mathbf{r}_1, \mathbf{r}_2, \dots, \mathbf{r}_n, \dots, \mathbf{r}_N$). The distance between each step is d . At step n , the Q closest data points are ($\mathbf{r}_{n1}, \mathbf{r}_{n2}, \dots, \mathbf{r}_{nq}, \dots, \mathbf{r}_{nQ}$) with stress tensors ($\mathbf{S}_{n1}, \mathbf{S}_{n2}, \dots, \mathbf{S}_{nq}, \dots, \mathbf{S}_{nQ}$). Q is chosen to produce a reasonable stress estimation at a location other than the A data points. $Q=3$ is sufficient for the examples shown in this chapter. These data points are

a distance $(|\bar{r}_{n1}|, |\bar{r}_{n2}|, \dots, |\bar{r}_{nQ}|) = (|\mathbf{r}_{n1} - \mathbf{r}_n|, |\mathbf{r}_{n2} - \mathbf{r}_n|, \dots, |\mathbf{r}_{nQ} - \mathbf{r}_n|)$ away from step n . The stress at step n is interpolated from this data. One interpolation equation is

$$\mathbf{S}_n = \sum_{q=1}^Q A_q \mathbf{S}_q, \quad (8.17)$$

where

$$A_q = \frac{(|\bar{r}_{nq}| + 10^{-17})^{-2}}{\sum_{q=1}^Q [(|\bar{r}_{nq}| + 10^{-17})^{-2}]} \quad (8.18)$$

is scaling factor based on distance $|\bar{r}_{nq}|$ and has a maximum of 1. A_q emphasizes \mathbf{S}_q when it is very near point r_n and deemphasizes points further away. If r_n is exactly on top of r_{nq} , $|\bar{r}_{nq}| = 0$ and $A_q \approx 1$. When r_n is away from any one data point, A_q includes effects from the closest Q data points.

Each of the steps behaves as a linear retarder whose effect is represented by a \mathbf{P} matrix. The stressed \mathbf{P}_n matrix corresponding to step n is calculated using methods described in section 8.4.1 and equation (8.16) with average \mathbf{S}_n in equation (8.17). The net effect of the sequences of retardances is obtained by multiplying the \mathbf{P} matrices. For all N steps, the cumulative stressed \mathbf{P} matrix is

$$\mathbf{P}_{\text{stress}} = \prod_{n=1}^N \mathbf{P}_{N-n+1}. \quad (8.19).$$

To represent a ray refracting into the stress material, propagating through the stressed material, and refracting out of the material, the total \mathbf{P} matrix is

$$\mathbf{P}_{\text{out}} \cdot \mathbf{P}_{\text{stress}} \cdot \mathbf{P}_{\text{in}} \quad (8.20)$$

where \mathbf{P}_{in} and \mathbf{P}_{out} are isotropic \mathbf{P} matrices calculated as described in section 3.3 with the unstressed refractive index for the incident and exiting surfaces.

8.6 Example: Polarization ray tracing for a plastic injection molded lens

There are many ways to analyze ray tracing results for systems containing stress birefringence, such as the polarization state change or birefringence change. The most common figure of merit is retardance. Retardance magnitude and fast axis orientation across the pupil give insight into the stress location, orientation, and magnitude. In most optical systems, a quarter of a wave of retardance yields a significant amount of aberrations, causing noticeable image degradation in the point spread function.

The simulation methods described in section 8.4 and 8.5 are applied to calculate the retardance induced by an injection molded lens with stress shown in Figure 8.14. The complete 3×3 stress tensor of this lens is shown in Figure 8.11.

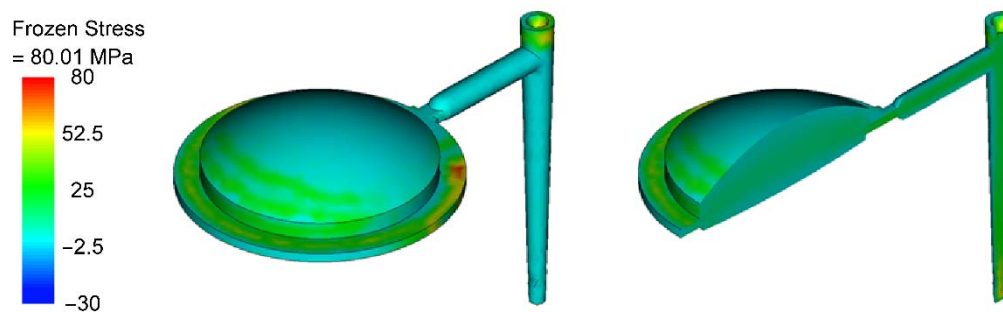


Figure 8.14 The stress images of the injection molded lens (the same lens as in Figure 8.11) with a cut away through the CAD variation file.

A collimated grid of rays is traced through this stressed lens. The retardance variation across the lens is calculated from the ray tracing \mathbf{P} matrices and plotted in Figure 8.15.

Rapid variation of retardance appears on the flange and the gate of the lens. The retardance is lower at the center and slightly higher towards the edge. This lens is also simulated in a polariscope with crossed polarizers. The light leakage through the polariscope is due to the shape of the lens as well as the stress induced retardance.

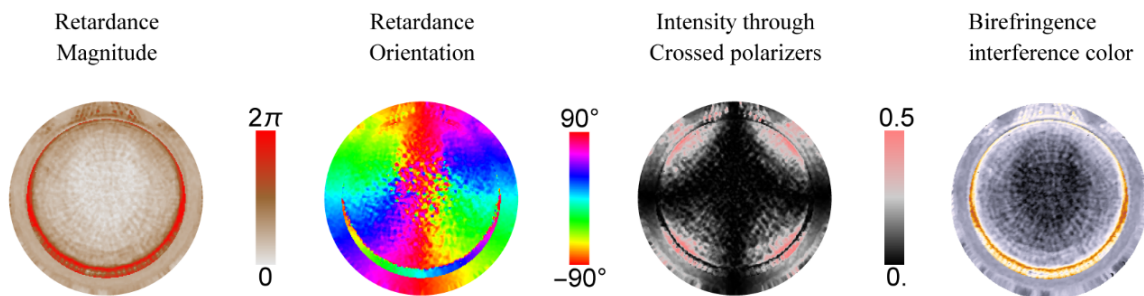


Figure 8.15 Retardance magnitude, retardance orientation, and polariscope images from a polarization ray trace for an injection molded lens of Figure 8.14. The gate of the lens is located at the top of the lens shown.

Injection molded DVD lenses are sensitive to stress induced polarization since the DVD signal is routed with two passes through a polarization beam splitter. The signal is degraded by stress induced aberrations. Too much degradation causes the bit error rate to increase. Without stress, the lens has zero retardance and performs as a conventional ray trace would predict; with stress, the lens has non-zero induced retardance. The stress induced retardance of an example DVD pick up lens across the pupil is shown in Figure 8.16.

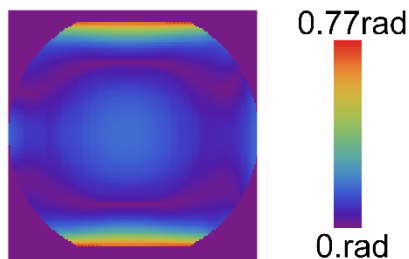


Figure 8.16 Stress induced retardance of a DVD pick up lens across the pupil.

The DVD pick up lens configuration in Figure 1.6 is illuminated through then images through a polarizing beam splitter. The image quality is evaluated by its polarizing point spread matrix (section 1.6). The point spread functions (PSF) is presented in the form

of $\begin{pmatrix} x \rightarrow x & y \rightarrow x \\ x \rightarrow y & y \rightarrow y \end{pmatrix}$. In Figure 8.17 for the example DVD lens, the main PSF components

xx and yy are nearly Airy disks for the unstressed lens (Figure 8.17 left) with a small amount of light coupled into the off-diagonal elements xy and yx . When the polarization ray trace analysis is repeated with the stress data, the main xx and yy components are only slightly affected, but much more light is now coupled into the orthogonal polarization states, as shown by the off diagonal elements xy and yx .

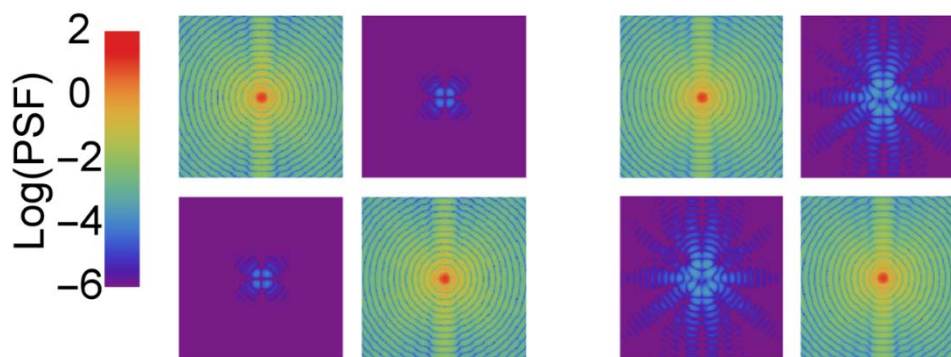


Figure 8.17 Point spread functions of polarized light through the un-stressed lens (left) and the stressed lens (right) in log scale.

As the stress continuously increases, the xx and yy images become less and less like an Airy disk, and the leakages between x and y -polarizations continuously increase. At extreme levels of stress, illustrated in Figure 8.18, the lens loses its ability to form an image.

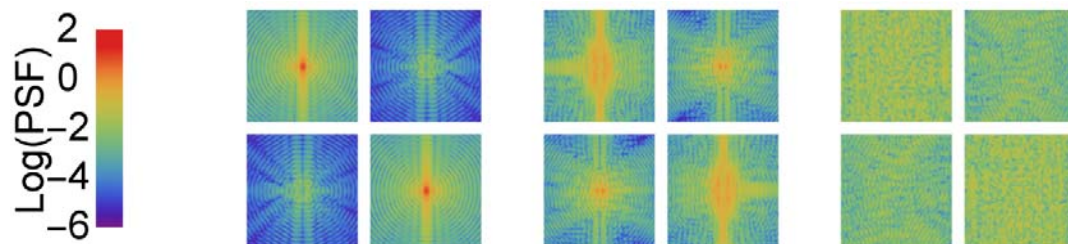


Figure 8.18 Point spread functions of polarized light refracting through a stressed lens with 10, 100, and 1000 times the stress shown in Figure 8.17.

8.7 Conclusions

Stress in optical elements impacts performance. Methods for the simulation of stress birefringence was presented in this chapter. Complex stress distributions are modeled as a varying anisotropic material with spatially varying dielectric tensor. To ray trace through stress birefringent components, the induced birefringence along a ray path was simulated as cascade of \mathbf{P} matrices for short ray segments. The stresses simulated in this chapter was assumed to be small and induces negligible ray doubling. Therefore, the small ray segment within the stress material was represented by a normal refraction through a linear retarder with retardance related to the orthogonal modes calculated with the algorithms shown in Chapter 2, Chapter 3 and Chapter 4. Then the effects of the stress on the optical system was evaluated by the point spread functions calculated from the stress induced polarizing pupil.

Stress birefringence can be measured and observed by polariscopes and Mueller matrix polarimeters. Other birefringence measurement methods are also developed for

higher accuracy and shorter processing time using photoelastic modulators, optical heterodyne interferometry¹⁷², phase shifting techniques¹⁷³, and near-field optical microscopes (NSOM)¹⁷⁴. Being able to analyze and simulate the effects of the stress in optical elements is very important for industrial inspection, product control and tolerance analysis for precision optical system. Using the stress simulation to predict the product performance can optimize the tradeoff between the processing time and the product quality in manufacturing without expensive cost of trial and error.

Anisotropic material requires more complex stress optic tensor and strain optic tensor to describe its directional dependent change induced by external stress, but similar algorithms described in this chapter still apply to model the optical performance. Also, the ray tracing method, modeling optical components with spatially varying optical properties, can apply to simulate gradient index optic, liquid crystal, and other similar optical elements.

CHAPTER 9 CONCLUSIONS AND FUTURE WORK

9.1 Work accomplishment in Polaris-M

This goal of this dissertation is to extend the polarization ray tracing calculus to incorporate anisotropic materials. Some of this work was funded by the Science Foundation Arizona (SFAz), a Technology & Research Initiative Funding (TRIF) imaging fellowship, and the NALUX Corporation. With the funding, a polarization ray tracing program, Polaris-M, was developed at the Polarization Lab in the University of Arizona. Besides implementing the algorithms to handle anisotropic optical materials in Polaris-M, research was performed into data structure to systematically manage the multiplicity of rays generated by anisotropic elements. These structures needed to handle many special cases unique to anisotropic interactions: inhibited refraction, total internal reflection, and conical refraction. Algorithms for evaluating imaging quality of an optical system are also implemented in Polaris-M, so that polarization image formation can be calculated with anisotropic elements.

Many ray tracing examples were developed to test the validity of the algorithms where possible against published data. An early presentation on the Polaris-M algorithms was presented at the International Optical Design Conference (IODC) 2010 at Jackson Hole, Wyoming, USA¹⁷⁵. Many more complex analyses have been performed since then, such as the modeling of crystal polarizers, crystal retarders and optical components with stress induced birefringence.

Other analyses utilizing advanced Polaris-M features include the modeling of solid corner cube, compensating polarization aberrations between fold mirrors, and a detailed

evaluation of the PSF of a Cassegrain telescope. The solid corner cube modeling was presented at the International Optical Design Conference (IODC) 2014 at Kohala Coast, Hawaii, USA and demonstrated the polarization skew aberration resulting from geometrical aberration⁶. Fold mirrors are common optical components used in many optical systems for compactness, but they are often a significant source of polarization aberrations. The polarization aberrations (diattenuation and retardance) of a metallic fold mirror for a spherical wavefront can be partially compensated by using multiple fold mirrors oriented as crossed-mirror configuration, as shown in reference 176. An astronomical Cassegrain telescope followed by a fold mirror was analyzed using Polaris-M⁵ where it is shown how the astronomical image, particularly its point spread function (PSF), is affected by polarization aberrations. It also shows how a wavefront correction system cannot optimally correct the wavefront aberrations for all polarizations simultaneously. Thus the polarization aberration will interfere with exoplanet imaging. Such effects have important implications for high-contrast imaging, coronagraphy, and astrometry with their stringent PSF image symmetry and scattered light requirements, so a vector-wave or polarization optimization is recommended.

Many other ray tracing examples were developed using Polaris-M and were not included in this dissertation. These examples include simulation of PSF of biaxial waveplate, a realistic model of retarder (varying retardance with angle), realistic models of dichroic polarizers and wire grid polarizers, and diffractive grating analysis of blazed gratings, echelle gratings, and optically active gratings.

Many other science modules for Polaris-M were also developed by my colleagues (Greg Smith, Karlton Crabtree, Garam Young, Paula Smith, Hannah Noble, and Michihisa Onishi) since 2008. These science modules include isotropic thin films, biaxial thin films, stress birefringence, rigorous coupled wave analysis (RCWA) for anisotropic grating calculations, bi-directional scattering model for polarized light, and interfacing with polarimeter measurement.

As a research ray tracing program, Polaris-M would benefit from more ray tracing examples with confirmation against measurement where possible to further validate the current science modules. For example, it would be interesting to test some of the science module with metamaterials with negative refractive index and other new photonic materials. Further future development of Polaris-M is outlined in section 9.3.

9.2 Summary of modeling optical system with anisotropic components

My contributions to accurately analyze the subtle effects of anisotropic optical components on optical systems have been demonstrated in this dissertation in the following order: (1) polarization ray tracing through a series of uncoated anisotropic optical interfaces, (2) automating ray doubling and carrying the polarization effects related to the multiple wavefronts along their ray paths from the entrance to the exit pupils of an optical system (3), calculating polarizing parameters (diattenuation, retardance, and Jones pupil) across the exit pupil for individual or combined polarized wavefronts, and (4) analyzing the resultant image quality where aberrations from each polarized wavefronts are apparent. The polarization aberrations of the wavefronts for each eigenmode can be studied

individually before combining them to examine their effects across the exit pupil as well as at the image plane.

The automated ray doubling algorithm accommodates the exponentially growing number of ray segments per anisotropic elements as a result of anisotropic ray doubling. The resultant ray data for each ray intercept and ray segment are organized in a ray tree structure, as shown in Figure 9.1. The polarization properties at each ray interface and along each ray segment are represented by \mathbf{P} matrices; the polarization evolution along a ray path is represented by series of \mathbf{P} matrices. The cumulative \mathbf{P} matrix fully characterizes the polarizations of each ray path, and evaluates the exiting polarization states by operating on any incident states.

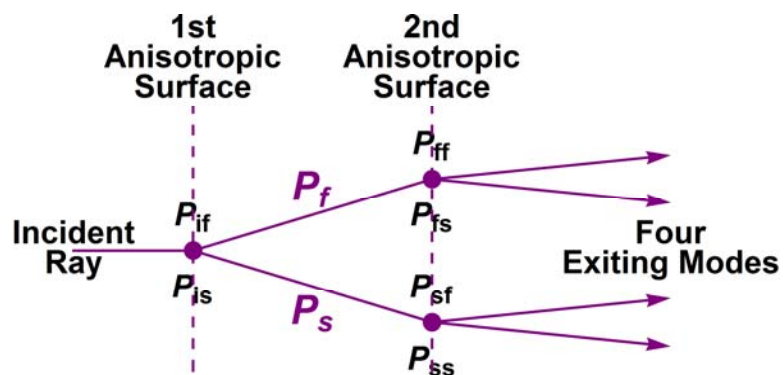


Figure 9.1 Ray tree for system with two anisotropic surfaces. The incident ray split into two modes at the 1st intercept. These two modes split again at the 2nd anisotropic interface and result in four exiting modes. The surface interactions are represented by \mathbf{P}_{if} , \mathbf{P}_{is} , \mathbf{P}_{ff} , \mathbf{P}_{fs} , \mathbf{P}_{sf} , and \mathbf{P}_{ss} . The phase changes due to propagation are represented by \mathbf{P}_f , \mathbf{P}_s . The polarization of the first exiting mode is represented by the \mathbf{P} matrices along the first ray path, which is the matrix multiplication of $\mathbf{P}_{ff} \cdot \mathbf{P}_f \cdot \mathbf{P}_{if}$.

The procedures of anisotropic ray trace demonstrated in this dissertation and the corresponding analysis of imaging quality for polarized light are summarized in Figure 9.2.

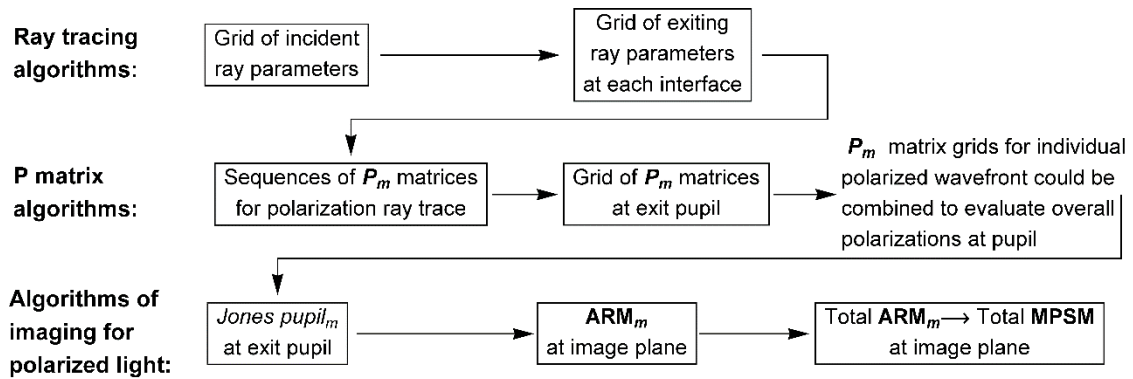


Figure 9.2 Summary of anisotropic ray tracing and imaging analysis of multiple polarized wavefronts. Subscript m indicates the m^{th} eigen-polarized wavefront. The total **MPSM** is the summation of **ARM_m** of all the overlapped modes.

Although the algorithms presented in this dissertation describe ray tracing through uncoated anisotropic interfaces, the **P** matrix algorithms for handling multiple exiting rays can be applied to other light-surface or light-material interactions with ray multiplying effects. For example, Polaris-M handles isotropic and anisotropic diffraction gratings (a module developed by Michihisa Onishi¹⁷⁷ calculates amplitude coefficients for anisotropic gratings) and surfaces coated with anisotropic thin films (another module developed by Paula Smith¹⁷⁸ calculates amplitude coefficients for coated anisotropic interfaces). Also, liquid crystal cells can be simulated as both (1) layers of retarders using the calculation for anisotropic bulk materials as in Chapter 2 or (2) using the more accurate multilayer interference model for anisotropic thin films. The goal of these ray tracing algorithms involves calculating the polarization change in terms of eigenpolarizations, ray direction change, and the associated *OPL*. By placing these ray parameters in the **P** matrix using the algorithms in Chapter 3 and Chapter 4, the polarization effects of many different types of surfaces can be evaluated together in one optical system, an extremely useful tool for optical design and optimization. For example, one application is biaxial multilayer films

matched with liquid crystal cells for field of view (FOV) enhancement in liquid crystal displays.

9.3 Further work

Any optical design program is incomplete; there is always more physics and analysis to be incorporated. This section mentions some of my thoughts from the last few years. The polarization ray tracing calculus utilized throughout this dissertation is a high level ray tracing method used to systematically perform ray propagation in a global 3D coordinate system. There are many areas of optical modeling can be explored and further implemented in Polaris-M, for example the specification of the light source polarization, development of merit functions for the optimization of anisotropic optical systems, and methods for tolerancing such systems.

Many design questions involve the spatial and temporal coherence of the light source, and how this should be incorporated during the interference of wavefronts (combination of polarized wavefronts). Coherence describes the ability of \mathbf{E} fields to interfere with each other when added together^{179,180}. If the rays are fully incoherent, the Mueller matrix formalism applies and ray flux is added incoherently. If rays are fully coherent, the polarization ray tracing or Jones formalism applies and \mathbf{E} fields are added coherently. These are relatively straight forward. Partial coherence calculation involves much more computationally intensive calculations than the incoherent and coherent cases, and computer programming methods to perform large but meaningful calculations should be explored.

Straight forward evaluation of coherence integrals can involve 10^2 , 10^3 , 10^4 , or more computation, putting such calculations out of reach of reasonable computers and computation times. Examples are found in Chapter 10 of reference 9 (equation 46 in section 10.6.3) and other references^{181,182,183,184,185}. Further techniques to describe changes in coherence during propagation as well as methods for combining partially coherent rays are worth exploring.

The image formation algorithms need to be improved to handle combination of multiple polarized images for on- and off-axis point object. To perform computer optimization and tolerancing on optical system with anisotropic materials, new types of merit function to characterize the image quality for the multiple wavefronts are needed. The optimization variables and constraints need to be defined carefully so that specifications and constraints are met (such as the system should operate within the small FOV of the crystal polarizer) and the system remains manufacturable (such as components do not have negative thickness, clearances are maintained and components do not block beams).

In computer ray tracing, an optical system having N optimization variables is often regarded as a point in an N -dimensional space. Optimization uses numerical algorithm to iteratively find the minimum of the nonlinear error function that depends on N variables, starting from the initial configuration¹⁸⁶. It is important that the merit function is smooth. If it is bumpy, the system can get stuck many places far from the desired minima. The evaluation of complex functions with double (or arbitrary) precision arithmetic yields irregularity, typically around 10^{-17} of the value, which are a small problem. Combining a

large number of algorithms and calculations into a merit function or constraint can result in significantly bumpy or irregular high dimensional surfaces. The goal is that the system performance be stable with small amount of perturbations. For optical systems with moderate complexity, due to the high dimensionality of the parameter space, the nonlinearity of the merit function, and the many nonlinear constraints, there is no guarantee that the mathematical global minimum can be found in a reasonable period of time. But with long processing time, algorithms such as the escape function method¹⁸⁷, simulated annealing¹⁸⁸, and global synthesis¹⁸⁹, algorithms can find solutions that are considerably better than those found by local optimization. Although further research for improving global optimization algorithms is still necessary, an optimization method (global or local) should be implemented and explored with Polaris-M, to allow design and research into the limit of anisotropic components optimization with respect to manufacturing errors as well as image quality.

APPENDIX A RMS FOCUS

Due to aberrations, a group of rays propagating to an image plane might not converge to a single point, as shown in Figure A.1. In this case, the location of the focal plane can be defined as the point where all the rays converge to the smallest RMS spot size. This RMS focus minimizes the root mean square of all the ray intercepts relative to the center of the RMS spot.

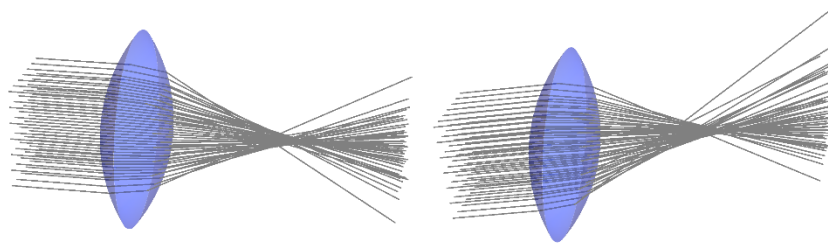


Figure A.1 A collimated beam focuses through a lens. Due to aberrations, the rays never coincide at a single point. (Left) On-axis beam. (Right) Off-axis beam.

The minimum RMS focus is calculated by the ray parameters of all the converging rays at the last optical surface (Z) before the focus. These parameters of the grid of rays are the ray locations ($\mathbf{r}_1, \mathbf{r}_2, \dots, \mathbf{r}_m, \dots, \mathbf{r}_M$) with ray directions ($\hat{\mathbf{S}}_1, \hat{\mathbf{S}}_2, \dots, \hat{\mathbf{S}}_m, \dots, \hat{\mathbf{S}}_M$).

(1) Locate the average axis which is orthogonal to the plane of RMS focus. This average

axis passes through the average ray location $\mathbf{r}_{\text{Mean}} = \frac{1}{M} \left(\sum_{m=1}^M \mathbf{r}_m \right)$ and lies in the direction

of the average ray direction $\mathbf{S}_{\text{Mean}} = \frac{1}{M} \left(\sum_{m=1}^M \hat{\mathbf{S}}_m \right)$, as shown in Figure A.2.

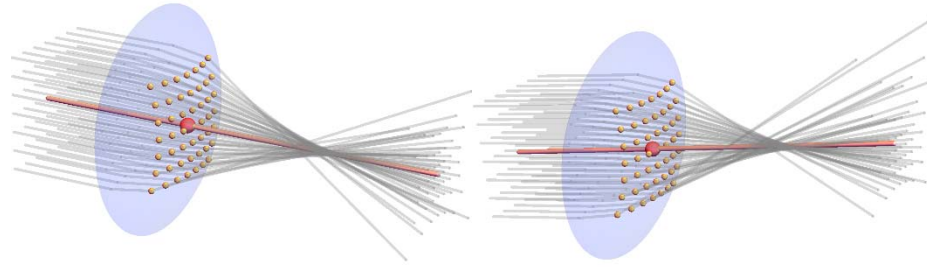


Figure A.2 The ray intercepts on the last surface before focus are shown in yellow. The average of these ray intercepts \mathbf{r}_{Mean} is shown in red. The average axis \mathbf{S}_{Mean} is shown as a pink line passing through \mathbf{r}_{mean} . (Left) On-axis beam. (Right) Off-axis beam.

There is a family of planes orthogonal to the average axis, as shown in Figure A.3. One of these planes is potentially the plane containing the best focus.

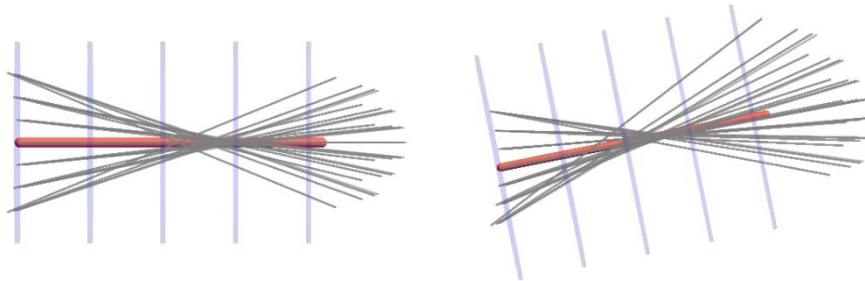


Figure A.3 Potential planes of focus (light blue) orthogonal to average axis (pink). (Left) On-axis beam. (Right) Off-axis beam.

(2) The potential plane of best focus is t_n away from \mathbf{r}_{Mean} along the average axis. The ray intercept of this potential plane of any ray on the last surface with $(\mathbf{r}_m, \mathbf{S}_m)$ is:

$$\mathbf{r}_{m,n} = \mathbf{r}_m + \hat{\mathbf{S}}_m t_{m,n}$$

where

$$t_{m,n} = \frac{(\mathbf{r}_{\text{Mean},n} - \mathbf{r}_m) \cdot \hat{\mathbf{S}}_{\text{Mean}}}{\hat{\mathbf{S}}_m \cdot \hat{\mathbf{S}}_{\text{Mean}}}$$

and the average axis intercept to that plane of best focus is $\mathbf{r}_{\text{Mean},n} = \mathbf{r}_{\text{Mean}} + \hat{\mathbf{S}}_{\text{Mean}} t_n$.

Therefore

$$\mathbf{r}_{\mathbf{m},n} = \mathbf{r}_{\mathbf{m}} + \hat{\mathbf{S}}_{\mathbf{m}} \frac{[(\mathbf{r}_{\text{Mean}} + \hat{\mathbf{S}}_{\text{Mean}} t_n) - \mathbf{r}_{\mathbf{m}}] \cdot \hat{\mathbf{S}}_{\text{Mean}}}{\hat{\mathbf{S}}_{\mathbf{m}} \cdot \hat{\mathbf{S}}_{\text{Mean}}}.$$

These ray intercepts for each of these potential planes of best focus are shown in Figure A.4.

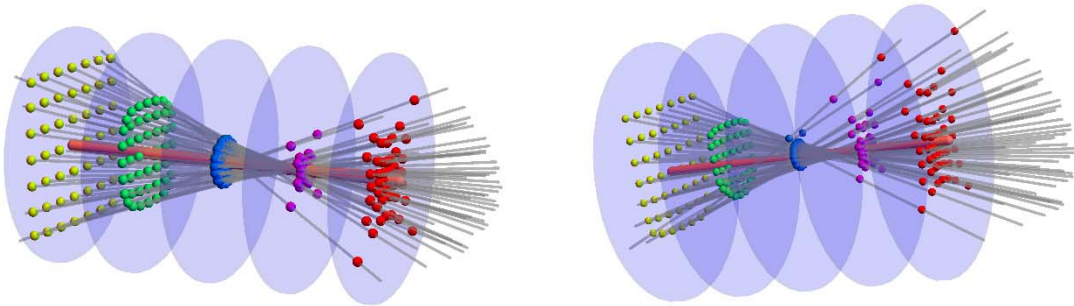


Figure A.4 Ray intercepts (colored points) of the grid of rays on each potential planes of best focus (blue). (Left) On-axis beam. (Right) Off-axis beam.

(3) At each potential best focus plane, the distance between each intercept and the average

axis is $dist(t_n) = |\mathbf{r}_{\mathbf{m},n} - \mathbf{r}_{\text{Mean},n}|$ which is a function of t_n only.

(4) The root mean square of these distances for all rays is

$$dist_{rms}(t_n) = \sqrt{\frac{1}{N} \sum_{n=1}^N dist^2}.$$

(5) The minimum $dist_{rms}$ with $t_{n,min}$ corresponds to the minimum RMS spot radius.

So, the best focus is at $\mathbf{r}_{\text{Mean}} + \hat{\mathbf{S}}_{\text{Mean}} t_{n,min}$.

APPENDIX B LOCAL COORDINATE SYSTEMS

The polarization states on a spherical wavefront or wavefront with small deviations from a spherical wavefront can be described most unambiguously in 3D global coordinates. However, it is frequently necessary to convert the 3D data onto a 2D plane, such as onto computer screen or onto a printed page, to communicate the polarization effects on the 2D transverse plane. The polarization aberrations are commonly represented by the Jones pupil, which is the 2×2 Jones matrix in pupil coordinates. This Jones pupil is commonly used in industry and can be generated from ray tracing output. This Appendix defines two common pupil coordinate systems for each 3D polarization state on a spherical wavefront to transform onto the 2D Jones pupil.

The first coordinate basis is called the Dipole system. Consider a ray emerging from the origin $(0, 0, 0)$ with ray direction $\mathbf{k}=(x, y, z)$; the local x and y basis are

$$\mathbf{x}_{\text{local}} = \left(-\frac{y}{\sqrt{x^2 + y^2}}, \frac{x}{\sqrt{x^2 + y^2}}, 0 \right) \text{ and } \mathbf{y}_{\text{local}} = \left(-\frac{xz}{\sqrt{x^2 + y^2}}, -\frac{yz}{\sqrt{x^2 + y^2}}, \sqrt{x^2 + y^2} \right).$$

The dipole system with singular poles along the y axis is shown in Figure B.1.

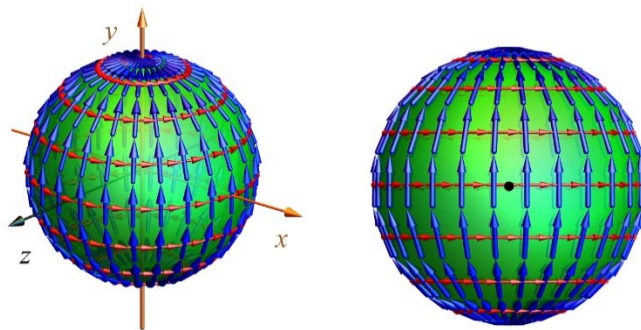


Figure B.1 Dipole coordinate system has local x and y axes along the latitude and longitude of a spherical wavefront.

The singularities at $\pm y$ represent an undefined basis. A spherical wavefront that propagates through an optical system has its chief ray aligned with the z direction shown in Figure B.1, and it is rare to have to include the ray propagating in the $\pm y$ direction. The dipole coordinate system best depicts the polarizations of spherical wavefronts emerging from linear polarizers.

The second coordinate basis is called the Double pole system. Instead of the two singularities in the dipole system, the double pole system has both of the singularities wrapped to a single point at $-z$. This double pole system is shown in Figure B.2.

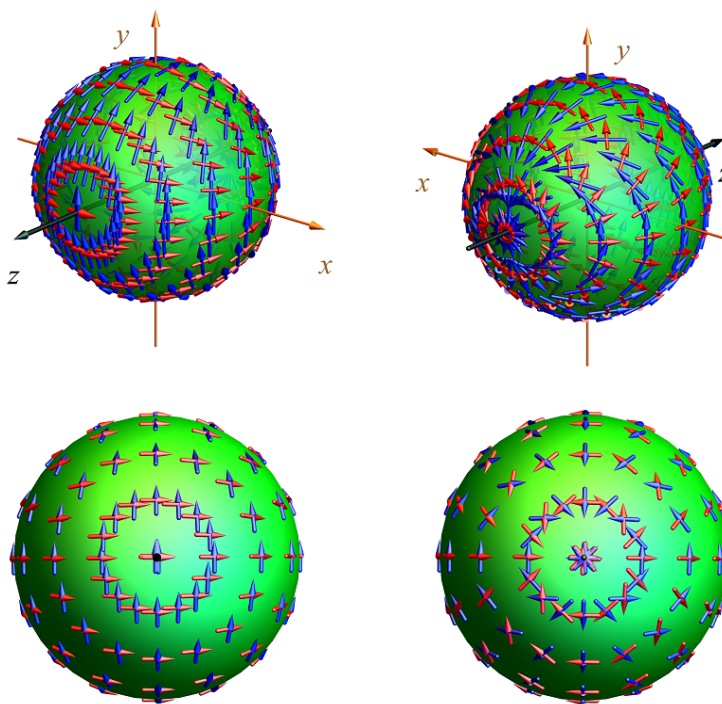


Figure B.2 Double pole local coordinate system with one double singularity at $-z$. (Left) Viewing toward the opposite end of the singular double pole, the basis vectors have a nice nearly uniform distribution. (Right) Near the double pole, the basis vectors rotate rapidly by 720° .

Similar to the dipole system, the chief ray of a spherical wavefront is aligned with $+z$. To fully specify the coordinate basis, the chief ray propagating to $z=(0, 0, 1)$ is set to have a

local x axis $(1, 0, 0)$. Then the local y for this ray is $\mathbf{k}_{\text{local}} \times \mathbf{x}_{\text{local}} = (0, 1, 0)$. In this double pole coordinate system, all the other \mathbf{k} 's have the following basis vectors:

$$\mathbf{x}_{\text{local}} = \left(z + \frac{y^2}{1+z}, -\frac{xy}{1+z}, -x \right) \text{ and } \mathbf{y}_{\text{local}} = \left(-\frac{xy}{1+z}, z + \frac{x^2}{1+z}, -y \right),$$

except at the double pole $(-z)$, where the basis coordinates are undefined. Although the front side of the double pole sphere is smoother than the dipole sphere, the basis changes rapidly around the singularity on the $-z$ side of the double pole sphere. The double pole basis depicts the polarization of light exiting an ideal lens.

APPENDIX C BIAXIAL REFRACTION AND REFLECTION PROPERTIES WITH CRYSTAL AXES ALONG XYZ AXES

The transmission and reflection properties of the anisotropic surface are studied in this Appendix. Consider a biaxial crystal made of KTP with principal refractive indices $(n_F, n_M, n_S) = (1.786, 1.797, 1.902)$ whose principal axes are oriented along the (x, y, z) axes.

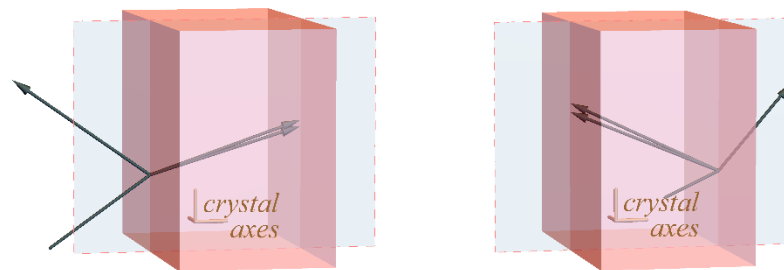


Figure C.1 External (left) and internal (right) reflection and refraction of biaxial interface.

The external and internal reflection and refraction properties are calculated with the algorithm in section 2.4 for wavelength 500 nm through different incident angles. Figure C.1 (left) shows the external reflection and refraction at an isotropic/anisotropic interface of air/KTP. Part of the light reflects back to air with s - and p -polarizations, and part of the light refracts into KTP as $fast$ - and $slow$ -modes in different directions. Figure C.1 (right) shows the internal reflection and refraction at an anisotropic/isotropic interface of KTP/air. Part of the light reflects back into the KTP with $fast$ - and $slow$ -modes in different directions, and part of the light refracts into air with s - and p -polarizations. To simplify the analysis, the xyz aligned crystal axes allow the s -polarization to couple entirely to the $fast$ -mode and the p -polarization to couple entirely to the $slow$ -mode. Performing the calculations at different angles of incidence yields the following results.

Figure C.2 plots the amplitude coefficients of the air/KTP interface, which are the case of external dielectric reflection/refraction. In reflection, the s -polarization reflectance increases with angle, while the reflectance of p -polarized light decreases to zero at around 60° . In refraction, due to the orientation of the crystal axis, p -polarized light couples entirely to the *slow*-mode and the s -polarization couples entirely to the *fast*-mode.

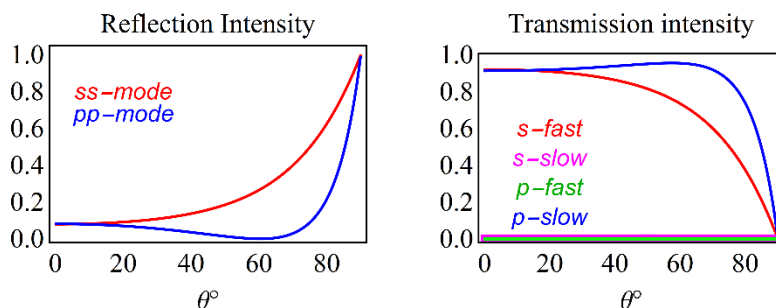


Figure C.2. Reflection and transmission coefficients at the air/KTP interface.

Figure C.3 shows a fan of incident rays, from 0 to 70° , reflecting from the air/KTP interface. In Figure C.3 (right), the reflected polarization of the s -polarized light has a π phase shift, while the p -polarized state in Figure C.3 (left) turns around when passing through the Brewster's angle. Around normal incidence, both polarizations have the same reflectance. Approaching Brewster's angle, their reflectance difference increases, thus their reflected diattenuation also increases.

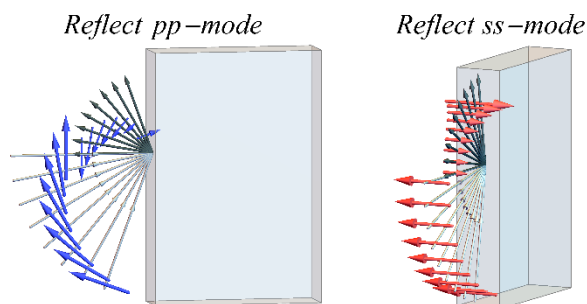


Figure C.3 A fan of rays externally reflect from an air/biaxial interface. The gray arrows are the incident \mathbf{k} vectors. The black arrows are the corresponding reflected \mathbf{k} vectors. The blue and red arrows are the polarization ellipses, showing the evolution of the electric field, where the arrow head indicates the start of the electric field evolution in time. All the incident polarizations have the same magnitude. The length of the polarization arrows indicate the intensity of the reflected light, but are adjusted slightly for visualization.

In refraction, the crystal axis orientations of the biaxial KTP are oriented to have non-zero intensity p -slow and s -fast modes. The other two possible modes, p -fast and s -slow, have zero coupling. These two refracted modes, p -slow and s -fast, have different \mathbf{S}_t . The phase of the polarization is unchanged upon refraction, as shown in Figure C.4, thus the refracted retardance for this uncoated interface is zero. As the incident angle increases, the transmission decreases while the reflection increases.

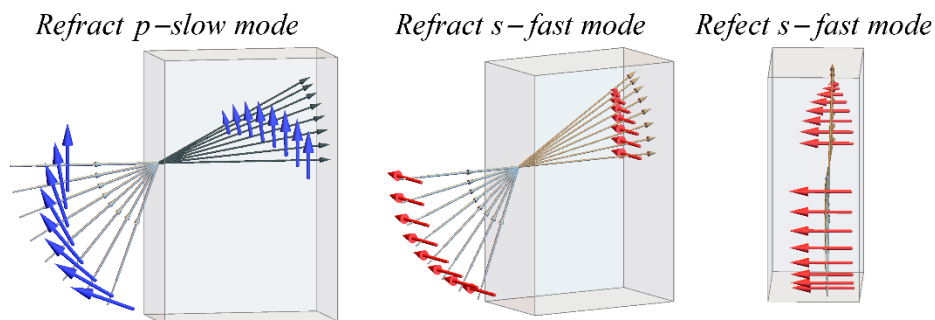


Figure C.4 A fan of rays externally refract through an air/biaxial interface. The gray arrows are the incident \mathbf{k} vectors. The black and brown arrows are the refracted \mathbf{S} vectors for the $slow$ - and $fast$ -modes. The blue and red arrows are the polarization ellipses of p -slow couplings and s -fast couplings.

Consider a left circularly polarized light propagating to the air/KTP interface at various angles, as shown in Figure C.5. The reflected polarizations are elliptically polarized. Around normal incidence, the incident and reflected polarizations evolve in the same direction viewing in 3D; left circularly polarized light reflects as right circularly polarized light. As the incident angle approaches Brewster's angle, the reflected polarization elongates towards the s -polarization. When it reaches Brewster's angle, the reflected p component is zero, and the reflected light becomes completely s -polarized. Above the Brewster's angle, the reflected polarization starts to gain ellipticity again, but in the opposite helicity than below Brewster's angle; left circular light reflects as left circularly polarized light.

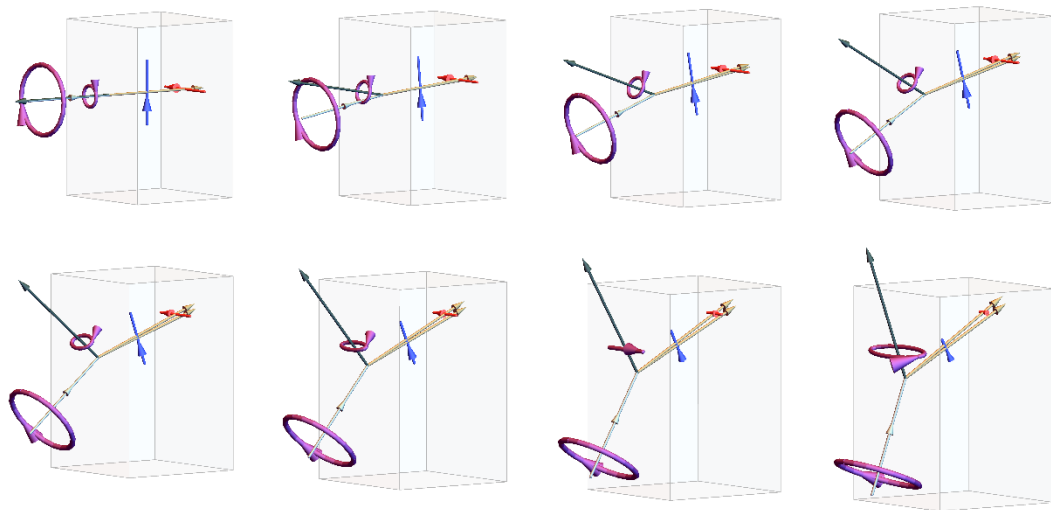


Figure C.5 Left circularly polarized light is incident on the air/biaxial interface. The gray, black and brown arrows are the incident, reflected and refracted rays, respectively. The purple ellipses are the incident and reflected polarizations. The red and blue arrows are the refracted *fast*- and *slow*-modes.

Figure C.6 shows the internal reflection/refraction intensities of the example KTP/air interface. In reflection, the *fast*-mode couples entire to the reflected *fast*-mode with

Brewster's angle just below 30° , the *slow*-mode couples entirely to the reflected *slow*-mode, and the *fast-slow* and *slow-fast* couplings are zero. This anisotropic surface has critical angle for the *slow*-mode that is smaller than the critical angle for the *fast*-mode.

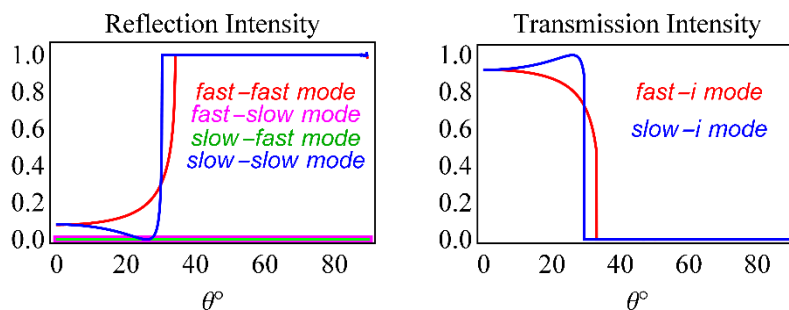


Figure C.6 Internal reflection and transmission coefficients at the KTP/air interface.

The polarizations of the internal reflection are shown in Figure C.7. The incident *fast*- and *slow*-modes lie orthogonal to and in the plane of incidence, respectively. Below the critical angle, most energy transmits, while the low energy reflected light undergoes a π phase shift. Above the critical angle, the reflected intensity increases drastically due to TIR, with a changing phase shift.

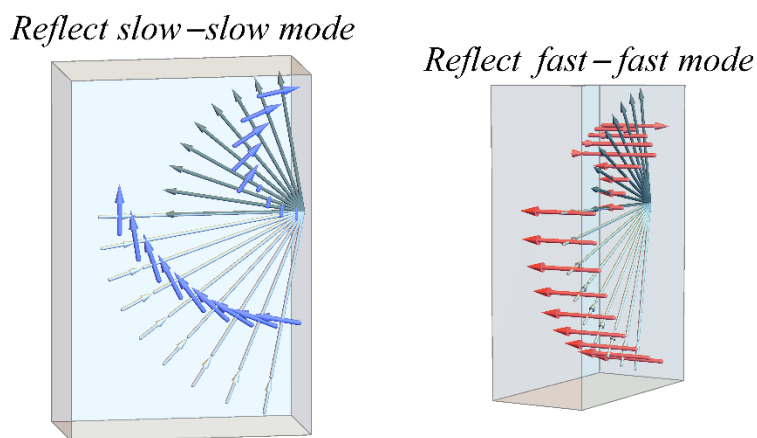


Figure C.7 A fan of rays internally reflect from a biaxial/air interface. The gray arrows are incident \mathbf{k} vectors. The black arrows are reflected \mathbf{k} vectors. The blue arrows are the incident and reflected polarizations of *slow*-modes. The red arrows are the incident and reflected polarizations of *fast*-modes.

In Figure C.8, the polarizations refracted through the uncoated surface have zero phase change. The *slow*-mode couples to *p*-polarized light in the plane of incidence, while the *fast*-mode couples to *s*-polarized light orthogonal to the plane of incidence.

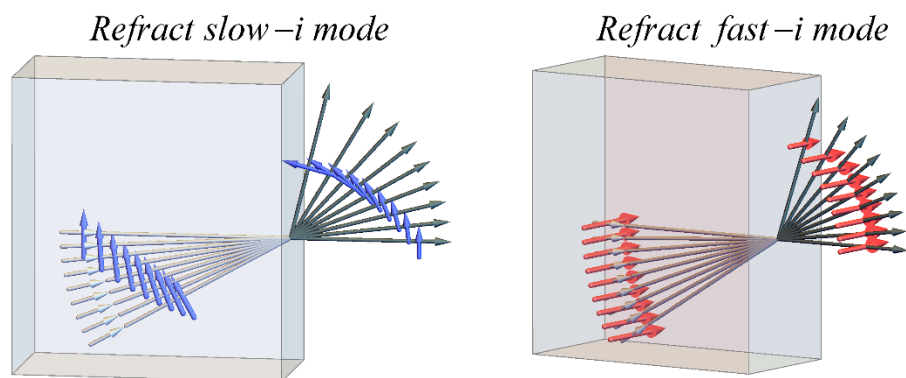


Figure C.8 A fan of rays internally refract through a biaxial/air interface. The gray arrows are incident \mathbf{k} vectors. The black arrows are refracted \mathbf{k} vectors. The blue arrows are the incident and refracted polarizations of *slow*-modes. The red arrows are the incident and refracted polarizations of *fast*-modes.

REFERENCES

- ¹R. A. Chipman, "Polarization analysis of optical systems I," *Opt. Eng.* **28**, 90-99 (1989).
- ²R. A. Chipman, "Polarization analysis of optical Systems II," *Proc. SPIE* **1166**, 79-99 (1989).
- ³H. Kuboda and S. Inoué, "Diffraction images in the polarizing microscope," *J. Opt. Soc. Am* **49**, 191-198 (1959).
- ⁴J. O. Stenflo, "The measurement of solar magnetic fields," *Rep. Prog. Phys* **41**, 865-889 (1978).
- ⁵James Breckinridge, W. S. T. Lam, R. Chipman, "Polarization Aberrations in Astronomical Telescopes: The Point Spread Function," *Publications of the Astronomical Society of the Pacific* **127**, (2015).
- ⁶G. Young, W. T. Lam, and R. A. Chipman, "A Review of Skew Aberration, the Intrinsic Polarization Aberration in High NA Optical Systems," in *Classical Optics 2014*, OSA Technical Digest (online) paper ITu1A.4 (OSA, 2014).
- ⁷M. Mansuriper, "Effects of High-numerical-aperture Focusing on the State of Polarization in Optical and Magneto-optical Data Storage Systems", *Appl. Opt.* **30** (22), 3154-3162 (1991).
- ⁸T. J. Bruegge, "Analysis of Polarization in Optical Systems," *Proc. SPIE* **1166**, 165-176 (1989).

-
- ⁹M. Born and E. Wolf, *Principles of Optics*, 6th Ed., (Pergamon, 1980).
- ¹⁰J. P. McGuire and R. A. Chipman, "Polarization Aberrations 1. Rotationally symmetric optical systems," *Applied Optics* **33** (22), 5080-5100 (1994).
- ¹¹R. A. Chipman, "Polarization Aberrations," PhD Dissertation, University of Arizona (1987).
- ¹²James P. McGuire and Russell A. Chipman, "Diffraction image formation in optical systems with polarization aberrations. I: Formulation and example," *J. Opt. Soc. Am. A* **7**, 1614-1626 (1990).
- ¹³James P. McGuire and Russell A. Chipman, "Diffraction image formation in optical systems with polarization aberrations. II: Amplitude response matrices for rotationally symmetric systems," *J. Opt. Soc. Am. A* **8**, 833-840 (1991).
- ¹⁴Dola Roy Chowdhury, Kallol Bhattacharya, Ajay K. Chakraborty, and Raja Ghosh, "Polarization-based compensation of astigmatism," *Appl. Opt.* **43**, 750-755 (2004).
- ¹⁵Michael Shribak, Shinya Inoué, Rudolf Oldenbourg, "Polarization aberrations caused by differential transmission and phase shift in high-numerical-aperture lenses: theory, measurement, and rectification," *Opt. Eng.* **41** (5), 943-954 (2002).
- ¹⁶J. O. Stenflo, "The measurement of solar magnetic fields," *Rep. Prog. Phys* **41**, 865-889 (1978).
- ¹⁷J. P. McGuire and R. A. Chipman, "Polarization Aberrations in Optical Systems", *Proc. SPIE* **818**, 240-245 (1987).

-
- ¹⁸E. W. Hansen, "Overcoming Polarization Aberrations in Microscopy," Proc. SPIE **891**, 190-197 (1988).
- ¹⁹R. A. Chipman and L. J. Chipman, "Polarization aberration diagrams," Opt. Eng. **28** (2), 100-106 (1989).
- ²⁰M. Shrieback, S. Inoue and R. Oldenbourg, "Polarization aberrations caused by differential transmission and phase shift in high-numerical-aperture lenses: theory, measurement and rectification," Opt. Eng. Bellingham **41**, 943 (2002).
- ²¹A. Beckley and T. Brown, "Imprinting Aberrations in the Stokes Parameters of a Focal Spot, " in International Optical Design Conference and Optical Fabrication and Testing, OSA Technical Digest (CD), paper IWA5 (OSA, 2010).
- ²²J. L. Pezzanitti and R. A. Chipman, "Mueller matrix imaging polarimeter," Opt. Eng. **34**, 6 (1995).
- ²³S. McEldowney, D. Shemo and R. Chipman, "Vortex retarders produced from photo-aligned liquid crystal polymers," Opt. Express **16**, 7295-7308 (2008).
- ²⁴R. C. Jones, "A New Calculus for the Treatment of Optical Systems," J. Opt. Soc. Am., **31**, 488-493, 493-499, 500-503 (1941), **32**, 486-493 (1942), **37**, 107-110, 110-112 (1947), **38**, 671-685 (1948), **46**, 126-131 (1956).
- ²⁵S. Lu and R. Chipman, "Homogeneous and inhomogeneous Jones matrices," J. Opt. Soc. Am. A **11**, 766-773 (1994).

-
- ²⁶Russell A. Chipman, "Mechanics of polarization ray tracing," Proc. SPIE **1746**, 62 (1992).
- ²⁷Garam Yun, Karlton Crabtree, and Russell A. Chipman, "Three-dimensional polarization ray-tracing calculus I: definition and diattenuation," Appl. Opt. **50**, 2855-2865 (2011).
- ²⁸Garam Yun, Stephen C. McClain, and Russell A. Chipman, "Three-dimensional polarization ray-tracing calculus II: retardance," Appl. Opt. **50**, 2866-2874 (2011).
- ²⁹Garam Yun, "Polarization ray tracing," PhD Dissertation, University of Arizona (2011).
- ³⁰Garam Yun, Karlton Crabtree, and Russell A. Chipman, "Skew aberration: a form of polarization aberration," Opt. Lett. **36**, 4062-4064 (2011).
- ³¹Garam Young, Russell A. Chipman, "Skew aberration analysis," Proc. SPIE **8550**, (2012).
- ³²Erasmus Bartholin, *Experiments on birefringent Icelandic crystal (Acta historica scientiarum naturalium et medicinalium)*, Translated by Thomas Archibald, (Danish National Library of Science and Medicine, 1991).
- ³³Jed Z. Buchwald and Mordechai Feingold, *Newton and the Origin of Civilization* (Princeton University Press, 2013).
- ³⁴Jed Z. Buchwald, *The Rise of the Wave Theory of Light: Optical Theory and Experiment in the Early Nineteenth Century* (University of Chicago Press, 1989).

³⁵W. Nicol, *Edinb. New Phil. J.* **6**, pp. 83, 1828-1829, as quoted in A. Johannsen, *Manual of Petrographic Methods*, 2nd ed. Hafner pp.158 (New York, 1968); (originally published in 1918).

³⁶Richard T. Glazebrook, "LI. On Polarizing Prisms," *Philosophical Magazine Series 5*, **15** (95), 352-362 (1883).

³⁷P. Glan, *Carl's Repert.* **16**, 570 (1880).

³⁸Silvanus P. Thompson, "XLIV. On a New Polarizing Prism," *Philosophical Magazine Series 5*, **12** (76), 349-351 (1881).

³⁹Silvanus P. Thompson, "LXV. Note on some New Polarizing Prisms," *Philosophical Magazine Series 5*, **21** (133), 476-480 (1886).

⁴⁰Silvanus P. Thompson, "LII. Twin Prisms for Polarimeters," *Philosophical Magazine, Series 5*, **24** (150), 397-401 (1887).

⁴¹Silvanus P. Thompson, "On the Nicol Prism and its modern varieties," *Proceedings of the Optical Convention*, 215-235 (1905).

⁴²G. Szivessy, *Geiger-Scheel Handbuch d. Physik* **20**, 113 (1928).

⁴³C. D. West and R. Clark Jones, "On the Properties of Polarization Elements as Used in Optical Instruments. I. Fundamental Considerations," *J. Opt. Soc. Am.* **41**, 976-980 (1951).

⁴⁴H. E. Bennett and J. M. Bennett, "Chapter 10 Polarization," in *Handbook of Optics*, W. G. Driscoll and W. Vaughan, eds. (McGraw-Hill, New York, 1978).

-
- ⁴⁵Arijit Saha, Kallol Bhattacharya, and Ajoy Kumar Chakraborty, "Achromatic quarter-wave plate using crystalline quartz," *Appl. Opt.* **51**, 1976-1980 (2012).
- ⁴⁶Anna-Britt Mahler, Stephen McClain, and Russell Chipman, "Achromatic athermalized retarder fabrication," *Appl. Opt.* **50**, 755-765 (2011).
- ⁴⁷D. Clark, "Achromatic halfwave plates and linear polarization rotators," *J. Mod. Opt.* **14**, 343-350 (1967).
- ⁴⁸J. M. Beckers, "Achromatic Linear Retarders," *Appl. Opt.* **10**, 973-975 (1971).
- ⁴⁹P. Hariharan, "Achromatic and apochromatic halfwave and quarterwave retarders," *Opt. Eng.* **35**, 3335-3337 (1996).
- ⁵⁰S. Pancharatnam, "Achromatic combinations of birefringent plates," *Proc. Indian Acad. Sci. A*, **41**, 130-136 (1955).
- ⁵¹Julia Craven-Jones, Brandyn M. Way, Michael W. Kudenov, and Jeffrey A. Mercier, "Athermalized channeled spectropolarimetry using a biaxial potassium titanyl phosphate crystal," *Opt. Lett.* **38**, 1657-1659 (2013).
- ⁵²J. H. H. Rietjens, F. Snik, D. M. Stam, J. M. Smit, G. van Harten, C. U. Keller, A. L. Verlann, E. C. Laan, R. ter Horst, R. Navarro, K. Wielinga, S. G. Moon, R. Voors, "SPEX: The Spectropolarimeter for planetary exploration," *International Conference on Space Optics 2010*, Rhodes, Greece (2010).
- ⁵³Frans Snik, Theodora Karalidi, Christoph U. Keller, "Spectral modulation for full linear polarimetry," *Applied Optics* **48** (7), 1337-1349 (2009).

⁵⁴Leica DMRD (DIC) shared by NEON ja on Aug. 2007, from Shishitsuka-Pond, Tsuchiura, Ibaraki Pref., Japan, http://en.wikipedia.org/wiki/Differential_interference_contrast_microscopy#mediaviewer/File:Microsterias_radiata.jpg (accessed on January 2015)

⁵⁵Karen M. Twietmeyer, “GDx-MM: An Imaging Mueller Matrix Retinal Polarimeter,” PhD Dissertation, University of Arizona (2007).

⁵⁶Reed M. Jost, Joost Felius and Eileen E. Brich, “High sensitivity of binocular retinal birefringence screening for anisometropic amblyopia without strabismus,” *Journal of American Association for Pediatric Ophthalmology and Strabismus* **18**, e5-e6 (2014).

⁵⁷“What is Light?” Chapter 3: Applications of Light: CDs and DVDs, Canon Science Lab, http://www.canon.com/technology/s_lab/light/003/06.html (accessed on January 2015)

⁵⁸Orestes N. Stavroudis, “Ray-Tracing Formulas for Uniaxial Crystals,” *J. Opt. Soc. Am.* **52**, 187-189 (1962).

⁵⁹William Swindell, “Extraordinary-ray and -wave tracing in uniaxial crystals,” *Appl. Opt.* **14**, 2298-2301 (1975).

⁶⁰Maria C. Simon, “Ray tracing formulas for monoaxial optical components,” *Appl. Opt.* **22**, 354-360 (1983).

⁶¹Maria. C. Simon, Karin. V. Gottschalk, “Waves and rays in uniaxial birefringent crystals,” *Optik* **118**, 457-471 (2007).

-
- ⁶²Quan-Ting Liang, "Simple ray tracing formulas for uniaxial optical crystals," *Appl. Opt.* **29**, 1008-1010 (1990).
- ⁶³Yanyang Wang, Liang Liang, Hong Xin, and Lei Wu, "Complex ray tracing in uniaxial absorbing media," *J. Opt. Soc. Am. A* **25**, 653-657 (2008).
- ⁶⁴Wei-Quan Zhang, "General ray-tracing formulas for crystal," *Appl. Opt.* **31**, 7328-7331 (1992).
- ⁶⁵Gary D. Landry and Theresa A. Maldonado, "Complete method to determine transmission and reflection characteristics at a planar interface between arbitrarily oriented biaxial media," *J. Opt. Soc. Am. A* **12**, 2048-2063 (1995).
- ⁶⁶C.-J. Chen, A. Lien, and M. I. Nathan, " 4×4 and 2×2 matrix formulations for the optics in stratified and biaxial media," *J. Opt. Soc. Am. A* **14**, 3125-3134 (1997).
- ⁶⁷Yanyang Wang, Peng Shi, Hong Xin, and Lei Wu, "Complex ray tracing in biaxial anisotropic absorbing media," *J. Opt. A: Pure Appl. Opt.* **10** (2008).
- ⁶⁸Stephen C. McClain, Lloyd W. Hillman, and Russell A. Chipman, "Polarization ray tracing in anisotropic optically active media. I. Algorithms," *J. Opt. Soc. Am. A* **10**, 2371-2382 (1993).
- ⁶⁹Stephen C. McClain, Lloyd W. Hillman, and Russell A. Chipman, "Polarization ray tracing in anisotropic optically active media. II. Theory and physics," *J. Opt. Soc. Am. A* **10**, 2383-2393 (1993).
- ⁷⁰D. Goldstein, *Polarized Light*, 3d Ed. (CRC Press, 2010).

-
- ⁷¹Eugene Waluschka, "Polarization Ray Tracing," Proc. SPIE **0891**, Polarization Considerations for Optical Systems (1988).
- ⁷²L. B. Wolff and D. J. Kurlander, "Ray Tracing with Polarization Parameters," IEEE Computer Graphics and Appl. **10** (6), 44-55 (1990).
- ⁷³W. Urbanczyk, "Optical Imaging Systems Changing the State of Light Polarization," Optik **66**, 301-309 (1984).
- ⁷⁴W. Urbanczyk, "Optical Transfer Functions for Imaging Systems Which Change the State of Light Polarization," Opt. Acta. **33**, 53-62 (1986).
- ⁷⁵R. Dorn, S. Quabis, and G. Leuchs, "Sharper focus for a radially polarized light beam," Phys. Rev. Lett. **91**, 233901 (2003).
- ⁷⁶Y. Tu, X. Wang, S. Li, and Y. Cao, "Analytical approach to the impact of polarization aberration on lithographic imaging," Opt. Lett. **37**, 2061-2063 (2012).
- ⁷⁷Yasuyuki Unno, "Influence of birefringence on the image formation of high-resolution projection optics," Appl. Opt. **39**, 3243-3252 (2000).
- ⁷⁸A. Yariv, and P. Yeh, *Optical Waves in Crystals*, (Wiley, New York, 1984).
- ⁷⁹Masud Mansuripur, *Field, Force, Energy and Momentum in Classical Electrodynamics*, Bentham e-Books, (Bentham Science Publishers, 2011).
- ⁸⁰Masud Mansuripur, "CH16 The Ewald-Oseen extinction theorem" in *Classical Optics and its Applications*, 2nd Ed. (Cambridge University Press, 2009).

-
- ⁸¹William J. Tropic, Michael E. Thomas, and Eric W. Rogala, “CH₂ Properties of Crystal and Glasses” in *Handbook of Optics*, Michael Bass ed., 3rd Ed., Vol. 4. (McGraw-Hill 2009).
- ⁸²M. C. Pujol, M. Rico, C. Zaldo et al., “Crystalline structure and optical spectroscopy of Er³⁺-doped KGd(WO₄)₂ single crystals,” *Applied Physics B-Lasers and Optics* **68** (2), 187-197 (1999).
- ⁸³V. G. Dmitriev, G. G. Gurzadyan, D. N. Nikogosyan, *Handbook of Nonlinear Optical Crystals*, 2nd edition, (Springer,1997).
- ⁸⁴V. A. Dyakov et al, “Sellmeier equation and tuning characteristics of KTP crystal frequency converters in the 0.4-4.0 μm range,” *Sov. J. Quantum Electron.* **18**, 1059 (1988).
- ⁸⁵ <http://www.aotk.com/proImg/Birefringent%20Crystals.pdf> (accessed on January 2015)
- ⁸⁶M. Emam-Ismael, “Spectral variation of the birefringence, group birefringence and retardance of a gypsum plate measured using the interference of polarized light,” *Optics & Laser Tech.*, **41** (5), 615-621 (2009).
- ⁸⁷Condon, E. U., “Theories of optical rotatory power,” *Rev. Mod. Phys.* **9**, 432-457 (1937).
- ⁸⁸Gary D. Landry and Theresa A. Maldonado, “Complete method to determine transmission and reflection characteristics at a planar interface between arbitrarily oriented biaxial media,” *J. Opt. Soc. Am. A* **12**, 2048-2063 (1995).
- ⁸⁹M. C. Simon, “Internal total reflection in monoaxial crystals,” *Appl. Opt.* **26**, 3878-3883 (1987).

-
- ⁹⁰M. C. Simon, and R, M, Echarri, "Inhibited reflection in uniaxial crystal," *Opt. Lett.* **14**, 257-259 (1989).
- ⁹¹M. Mansuripur, "Analysis of multilayer thin-film structures containing magneto-optic and anisotropic media at oblique incidence using 2x2 matrices," *Journal of Applied Physics* **67** (10), 6466-6475 (1990).
- ⁹²I. Abdulhalim, "2×2 Matrix summation method for multiple reflections and transmissions in a biaxial slab between two anisotropic media," *Optics Communications*, **163**, 9-14 (1999).
- ⁹³I. Abdulhalim, "Analytic propagation matrix method for linear optics of arbitrary biaxial layered media," *J. Opt. A: Pure Appl. Opt.* **1**, 646 (1999)
- ⁹⁴Khashayar Mehrany and Sina Khorasani, "Analytical solution of non-homogeneous anisotropic wave equations based on differential transfer matrices," *J. Opt. A: Pure Appl. Opt.* **4**, 624 (2002).
- ⁹⁵Kamil Postava, Tomuo Yamaguchi and Roman Kantor, "Matrix description of coherent and incoherent light reflection and transmission by anisotropic multilayer structures," *Appl. Opt.* **41**, 2521-2531 (2002).
- ⁹⁶W. R. Hamilton, *Trans. Roy. Irish Acad.* **17**, 1 (1833).
- ⁹⁷H. Lloyd, *Trans. Roy. Irish Acd.* **17**, 145 (1833).
- ⁹⁸Masud Mansuripur, CH21 in *Classical Optics & Its Applications*, (Cambridge University Press, 2002).

-
- ⁹⁹D. L. Portigal and E. Burstein, "Internal Conical Refraction," *J. Opt. Soc. Am.* **59**, 1567-1573 (1969).
- ¹⁰⁰E. Cojocar, "Characteristics of Ray Traces at the Back of Biaxial Crystals at Normal Incidence," *Appl. Opt.* **38**, 4004-4010 (1999).
- ¹⁰¹William D. Nesse, *Introduction to Optical Mineralogy*, 3rd Ed., (Oxford University Press, 2004).
- ¹⁰²Ernest E. Wahlstrom, *Optical Crystallography*, 3rd Ed., (Wiley, 1960).
- ¹⁰³Bahaa Saleh and Malvin Teich, *Fundamentals of Photonics*, 2nd Ed., (Wiley, 2007)
- ¹⁰⁴John Wilson and John Hawkes, *Optoelectronics an introduction*, 3rd Ed., (Prentice Hall Europe, 1998).
- ¹⁰⁵María C. Simon and Karin V. Gottschalk, "Waves and rays in uniaxial birefringent crystal," *Optik* **118**, 457-470 (2007).
- ¹⁰⁶Dennis H. Goldstein, "Chapter 24 Anisotropic Materials" in *Handbook of Optical Engineering*, Eds. Daniel Malacara and Brian J. Thompson, (New York, NY, USA, CRC Press, 2001).
- ¹⁰⁷S. Y. Lu, "An interpretation of polarization matrices," PhD Dissertation, University of Alabama at Huntsville (1995).
- ¹⁰⁸Russell A. Chipman, Wai Sze T. Lam, Garam Young, *Polarized Light and Optical Systems* (CRC Press, pending publication in 2016).

-
- ¹⁰⁹David B. Chenault and Russell A. Chipman, "Measurements of linear diattenuation and linear retardance spectra with a rotating sample spectropolarimeter," *Appl. Opt.* **32**, 3513-3519 (1993).
- ¹¹⁰Karasik, A. Ya, and V. A. Zubov. *Laser interferometry principles* (CRC Press, 1995).
- ¹¹¹Eric P. Goodwin and James C. Wyant, *Field Guide to Interferometric Optical Testing* (SPIE, 2006).
- ¹¹²Prasad L. Polavarapu, ed. *Principles and applications of polarization-division interferometry*, (John Wiley & Sons, 1998).
- ¹¹³Matthew P. Rimmer and James C. Wyant, "Evaluation of large aberrations using a lateral-shear interferometer having variable shear," *Applied optics* **14**, 142-150 (1975).
- ¹¹⁴Charles M. Vest, *Holographic interferometry* (New York, John Wiley and Sons, Inc., 1979).
- ¹¹⁵Pramod K. Rastogi, *Holographic interferometry*, Vol. 1. (Springer, 1994).
- ¹¹⁶Charles L. Adler and James A. Lock, "Caustics due to complex water menisci," *Appl. Opt.* **54**, B207-B221 (2015)
- ¹¹⁷Maximino Avendaño-Alejo, "Caustics in a meridional plane produced by plano-convex aspheric lenses," *J. Opt. Soc. Am. A* **30**, 501-508 (2013).
- ¹¹⁸H. Noble, E. Ford, W. Dallas, R. A. Chipman, I. Matsubara, Y. Unno, S. McClain, P. Khulbe, D. Hansen, and T. D. Milster, "Polarization synthesis by computer-generated

holography using orthogonally polarized and correlated speckle patterns,” *Opt. Lett.* **35**, 3423-3425 (2010).

¹¹⁹H. Noble, W. Lam, W. Dallas, R. Chipman, I. Matsubara, Y. Unno, S. McClain, P. Khulbe, D. Hansen, T. Milster, “Square-wave retarder for polarization computer-generated holography,” *Appl. Opt.* **50**, 3703-3710 (2011).

¹²⁰ *Optical Shop Testing*, 2nd Ed., Daniel Malacara, Ed., (John Wiley & Son, Inc. 1992).

¹²¹Xiepeng Geng and Peng Hu, “Spatial Interpolation Method of Scalar Data Based on Raster Distance Transformation of Map Algebra,” *IPTC*, Intelligence Information Processing and Trusted Computing, International Symposium, 188-191 (2010).

¹²²I. Amidror, “Scattered Data Interpolation Methods for Electronic Imaging Systems: A Survey,” *J. Electronic Imaging*, **2** (11), 157-176 (2002).

¹²³S. J. Owen, “An Implementation of Natural Neighbor Interpolation in Three Dimensions,” Master's thesis, Brigham Young University (1992).

¹²⁴D. Shepard, “A Two-Dimensional Interpolation Function for Irregularly Spaced Data,” *Proc. 23rd Nat'l Conf.*, 517-524 (1968).

¹²⁵William T. Vetterling, William H. Press, Saul A. Teukolsky, and Brian P. Flannery, *Numerical Recipes Example Book C (The Art of Scientific Computing)* (Cambridge University Press, 1993).

¹²⁶N. S. Lam, “Spatial interpolation methods review,” *The American Cartographer* **10**, 129-149 (1983).

-
- ¹²⁷D. Shepard, "A two-dimensional interpolation function for irregularly-spaced data," Proc. 23rd National Conference ACM, ACM, 517-524 (1968).
- ¹²⁸P. S. Kelway, "A scheme for assessing the reliability of interpolated rainfall estimates," Jour. Hydrology **21**, 247-267 (1974).
- ¹²⁹N.O.A.A., "National Weather Service River Forecast System forecast Procedures," TM NWS HYDRO-14, US Department of Commerce, Washington DC (1972).
- ¹³⁰J. J. Kaluarachchi, J. C. Parker and R. J. Lenhard, "A numerical model for areal migration of water and light hydrocarbon in unconfined aquifers," Adv. Water Resour. **13**, 29-40 (1990).
- ¹³¹D. F. Watson and G. M. Philip, "A refinement of inverse distance weighted interpolation, Geo-Processing," **2**, 315-327 (1985).
- ¹³²D. G. Krige, *A statistical approach to some mine valuations and allied problems at the Witwatersrand*, Master's thesis, the University of Witwatersrand (1951).
- ¹³³Jean Duchon, "Splines minimizing rotation invariant semi-norms in Sobolev spaces," p85-100 in *Constructive Theory of Functions of Several Variables* (Oberwolfach, 1976).
- ¹³⁴Warren J. Smith, *Modern Optical Engineering*, 3rd Ed. (McGraw-Hill, 2000).
- ¹³⁵Jose Luis Vilas, Luis Miguel Sanchez-Brea, and Eusebio Bernabeu, "Optimal achromatic wave retarders using two birefringent wave plates," Appl. Opt. **52**, 1892-1896 (2013).

-
- ¹³⁶H. E. Bennett and J. M. Bennett, "Chapter 10 Polarization." in *Handbook of Optics*, Ed. W. G. Driscoll and W. Vaughan, 1st edition. (McGraw-Hill, New York, 1978).
- ¹³⁷J. M. Bennett, "Chapter 3 Polarizers." in *Handbook of Optics Vol. II*, Ed. M. Bass, 2nd edition. (McGraw-Hill, New York, 1995).
- ¹³⁸J. M. Bennett, "Chapter 13 Polarizers." in *Handbook of Optics Vol. I*, Ed. M. Bass, 3rd edition. (McGraw-Hill, New York, 2010).
- ¹³⁹Del Mar Photonics Newsletter, http://www.dmphotonics.com/rutile_coupling_prism.htm (accessed on January 2015)
- ¹⁴⁰Greyhawk Optics, <http://greyhawkoptics.com> (accessed on January 2015)
- ¹⁴¹J. F. Archard, and A. M. Taylor, "Improved Glan-Foucault prism," *J. Sci. Instrum.* **25** (12), 407-409 (1948).
- ¹⁴²Neil A. Beaudry, Yanming Zhao, and Russell Chipman, "Dielectric tensor measurement from a single Mueller matrix image," *J. Opt. Soc. Am. A* **24**, 814-824 (2007).
- ¹⁴³Karl Lambrecht Corporation, <http://www.klccgo.com/glantaylor.htm> (accessed on 2015 March).
- ¹⁴⁴S. F. Jacobs and D. Shough, "Thermal expansion uniformity of Heraeus-Amersil TO8E fused silica," *Appl. Opt.* **20**, 3461-3463 (1981).
- ¹⁴⁵Chii-Chang Chen, Hung-Da Chien, and Pi-Gang Luan, "Photonic crystal beam splitters," *Appl. Opt.* **43**, 6187-6190 (2004).

-
- ¹⁴⁶Mladen Pavičić, “Spin-correlated interferometry with beam splitters: preselection of spin-correlated photons,” *J. Opt. Soc. Am. B* **12**, 821-828 (1995).
- ¹⁴⁷Laure Kaiser, Erna Frins, Bernhard Hils, Leonid Beresnev, Wolfgang Dultz, and Heidrun Schmitzer, “Polarization analyzer for all the states of polarization of light using a structured polarizer,” *J. Opt. Soc. Am. A* **30**, 1256-1260 (2013).
- ¹⁴⁸David Brewster, “On the effects of simple pressure in producing that species of crystallization which forms two oppositely polarized images, and exhibits the complementary colors by polarized light,” *Phil. Trans. R. Soc. Lond.* **105**, 60-64 (1815).
- ¹⁴⁹E. G. Coker and L. N. G. Filon, *Treatise on Photoelasticity* (Cambridge U. P., London, 1931).
- ¹⁵⁰George Birnbaum, Earl Cory, and Kenneth Gow, “Interferometric Null Method for Measuring Stress-induced Birefringence,” *Appl. Opt.* **13**, 1660-1669 (1974).
- ¹⁵¹Eugene R. Cochran and Chiayu Ai, “Interferometric stress birefringence measurement,” *Appl. Opt.* **31**, 6702-6706 (1992).
- ¹⁵²A. V. Appel, H. T. Betz, and D. A. Pontarelli, “Infrared Polariscopes For Photoelastic Measurement of Semiconductors,” *Appl. Opt.* **4**, 1475-1478 (1965).
- ¹⁵³Wei Su and John A. Gilbert, “Birefringent properties of diametrically loaded gradient-index lenses,” *Appl. Opt.* **35**, 4772-4781 (1996).

¹⁵⁴R. K. Kimmel and R. E. Park, *ISO 10110 Optics and Optical Instruments – Preparation of drawings for optical elements and systems: A User’s guide*, Optical Society of America, (Washington, DC., 1995).

¹⁵⁵ISO/DIS 10110-part 2; Preparation of drawings for optical elements and systems; Material Imperfections–Stress birefringence (1996).

¹⁵⁶Amnon Yariv and Pochi Yeh, *Optical Waves in Crystals: Propagation and Control of Laser Radiation*, 319-329 (John Wiley and Sons, 1984).

¹⁵⁷Douglas A. Pinnow, “Elastooptical Materials” in “CRC Handbook of Lasers with Selected Data on Optical Technology,” ed. Robert J. Pressley, Cleveland, OH: The Chemical Rubber Company (1971).

¹⁵⁸M. Huang, “Stress Effects on the Performance of Optical Waveguides,” *International Journal of Solids and Structures* **40**, 1615-1632 (2003).

¹⁵⁹K. Doyle, V. Genberg and G. Michaels, “Numerical Methods to Compute Optical Errors Due to Stress Birefringence,” *Proc. of SPIE* **4769**, 34-42 (2002).

¹⁶⁰S. He, T. Zheng and S. Danyluk, “Analysis and Determination of the Stress-Optic Coefficients of Thin Single Crystal Silicon Samples,” *Journal of Applied Physics*, **96**, 3103-3109 (2004).

¹⁶¹N. F. Borrelli and R. A. Miller, “Determination of the Individual Strain-Optic Coefficients of Glass by an Ultrasonic Technique,” *Appl. Opt.* **7**, 745-750 (1968).

-
- ¹⁶²Robert E. Newnham, *Properties of Materials: Anisotropy, Symmetry, Structure* (Oxford University Press, 2004).
- ¹⁶³Roy M. Waxler, Deane Horowitz, and Albert Feldman, "Optical and physical parameters of Plexiglas 55 and Lexan," *Appl. Opt.* **18**, 101-104 (1979).
- ¹⁶⁴M. Zgonik, P. Bernasconi, M. Duelli, R. Schlessler, P. Günter, M. H. Garrett, D. Rytz, Y. Zhu, X. Wu, "Dielectric, elastic, piezoelectric, electro-optic, and elasto-optic tensors of BaTiO₃ crystals," *Physical review B* **50** (9), 5941(1994).
- ¹⁶⁵R. B. Pipes, J. L. Rose, "Strain-optic law for a certain class of birefringent composites," *Experimental Mechanics* **14** (9), 355-360 (1974).
- ¹⁶⁶*SigFit* is a product of Sigmadyne, Inc., Rochester, NY.
- ¹⁶⁷R. Y. Chang and W. H. Yang, "Numerical simulation of mold filling in injection molding using a three-dimensional finite volume approach," *Int. J. Numer. Methods Fluids* **37**, 125-148 (2001).
- ¹⁶⁸Huai En Lai and Pei Jen Wang, "Study of process parameters on optical qualities for injection-molded plastic lenses," *Appl. Opt.* **47**, 2017-2027 (2008).
- ¹⁶⁹Y. Maekawa, M. Onishi, A. Ando, S. Matsushima, and F. Lai, "Prediction of birefringence in plastics optical elements using 3D CAE for injection molding," *Proc. SPIE* **3944**, 935-943 (2000).
- ¹⁷⁰Louis Manzione, *Applications of Computer Aided Engineering in Injection Molding* (Oxford University Press, 1988).

-
- ¹⁷¹Tomas Möller and Ben Trumbore, “Fast, minimum storage ray-triangle intersection,” *Journal of Graphics Tools*, **2** (1), 21-28 (1997).
- ¹⁷²Rüdiger Paschotta, “Optical Heterodyne Detection,” *Encyclopedia of Laser Physics and Technology* at http://www.rp-photonics.com/optical_heterodyne_detection.html (accessed on January 2015)
- ¹⁷³E. Hecht, *Optics* (Addison-Wesley, 2002).
- ¹⁷⁴Y. Oshikane et al., “Observation of nanostructure by scanning near-field optical microscope with small sphere probe,” *Sci. Technol. Adv. Mater*, **8** (3), 181 (2007).
- ¹⁷⁵Wai Sze T. Lam, S. McClain, G. Smith, and R. Chipman, “Ray Tracing in Biaxial Materials,” in *International Optical Design Conference and Optical Fabrication and Testing*, OSA Technical Digest (CD) (OSA, 2010).
- ¹⁷⁶Wai Sze Tiffany Lam and Russell Chipman, “Balancing polarization aberrations in crossed fold mirrors,” *Appl. Opt.* **54**, 3236-3245 (2015).
- ¹⁷⁷Michihisa Onishi, “Rigorous Coupled Wave Analysis for Gyrotropic Materials,” PhD Dissertation, University of Arizona (2011).
- ¹⁷⁸Paula K. Smith, “Characterizing Dielectric Tensors of Anisotropic Materials from a Single Measurement,” PhD Dissertation, University of Arizona (2013).
- ¹⁷⁹Colin J. R. Sheppard, “Partial polarization in three dimensions,” *J. Opt. Soc. Am. A* **28**, 2655-2659 (2011).

¹⁸⁰M. R. Dennis, “Geometric interpretation of the three-dimensional coherence matrix for nonparaxial polarization,” *J. Opt. A* **6**, S26-S31 (2004).

¹⁸¹D. L. Marks, B. J. Davis, S. A. Boppart, and P. S. Carney, “Partially coherent illumination in full-field interferometric synthetic aperture microscopy,” *Journal of the Optical Society of America. A, Optics, Image Science, and Vision* **26** (2), 376-386 (2009).

¹⁸²Shalin B. Mehta and Colin J. R. Sheppard, “Partially coherent image formation in differential interference contrast (DIC) microscope,” *Optics Express* **16** (24), 19462-19479, (2008).

¹⁸³Eric C. Kintner, “Method for the calculation of partially coherent imagery,” *Appl. Opt.* **17**, 2747-2753 (1978).

¹⁸⁴Michael S. Yeung, Derek Lee, Robert S. Lee, Andrew R. Neureuther, “Extension of the Hopkins theory of partially coherent imaging to include thin-film interference effects,” *Proc. SPIE* **1927**, Optical/Laser Microlithography, 452 (1993).

¹⁸⁵R. Martinex-Herrero and A. Durán, “Relation between the object and its image for partially coherent and quasi-monochromatic illumination,” *Optica Acta: International Journal of Optics* **28** (1), (1981).

¹⁸⁶Florian Bociort, Optical System Optimization in *Encyclopedia of Optical Engineering*, 1843-1850 (Marcel Dekker, NY, 2003).

¹⁸⁷Masaki Isshiki, Hiroki Ono, Kouichi Hiraga, Jun Ishikawa and Suezou Nakadate, “Lens Design: Global Optimization with Escape Function,” *Optical Review* **2** (6), 463-470 (1995).

¹⁸⁸S. Kirkpatrick, C. D. Gelatt, M. P. Vecchi, "Optimization by Simulated Annealing," *Science* **220** (4598), 671-680 (1983).

¹⁸⁹L. N. Hazra and S. Chatterjee, "A Prophylactic Strategy for Global Synthesis in Lens Design," *Optical Review* **12** (3), 247-254 (2005).